NATIONAL OIL CORPORATION
LIBYAN PETROLEUM INSTITUTE

PETROLEUM RESEARCH JOURNAL

New Insights on Mesozoic Depositional Sequences and Hydrocarbon Systems, from Jiffarah Escarpment to Libyan Offshore Basins .....
Ibrahim Y. Mriheel 1

Depositional Environments of the Upper Ordovician, Mamuniyat Formation, NW Mrzuq Basin, SW Libya .....
Nuri Mohamed Fello 9

Microfacies Analysis and Paleoenvironmental trends of the Paleocene Farrud and Marbuk Reservoirs, Concession 11, West Sirt Basin, Libya .....
Nisreen Agha, Amin Gheith, Salah El-Beialy, Haitham El-Atfy and Waleed Shukri 17

Multi-Well Sand Production Prediction Study to Support Field Development plan, Lower Acacus Formation, Area 47, Ghadamis Basin .....
M. S. Gheddida, C. Sorge, M. El Mabrouk1, A. A. Fituri, A. V. Der Berken 37

Characterization of Libyan Crude Oils and its Heavy Fractions .....
Abdurazag A. Shebli and Alhadi A. Elakrimi 49

Exothermic Chemical Treatment (ECT), Towards Optimizing Heavy Crude Production of Al Haram Field, Concession 47, Sirt Basin, Libya, Using ECT Technology .....
Abdelgader Kernaf and Ales Mrkva 59

Displacement of heavy Oil by Carbon Dioxide in a Tube .....
Mohammed Almabrouk A. Ahmad and Parthasakha Neogi 65

Analytical Modelling of Attenuation of Volatile Petroleum Hydrocarbons in the Vadose Zone .....
Elazhari Ali, Abdulmagid1, Russell Davenport and David Werner 75

Thermal Analysis of a Clad Pipe using Simulation .....
Hala Y. Hamad 81

Optimal Design and Simulation of Solar Photovoltaic Powered Cathodic Protection for Underground Piplines in Libya ...
Dr. Mustafa A. Al-Refai 89

Modeling and Prediction of High Temperature Oxidation of Steels used in Petroleum Refinery Heaters .....
Naji Abdelwanis, Abdelrahman S. Sultan, Omar M Elmabrouk, and Farag A. Maetouq 99

Investigation of Wax Deposition Development in Sarir-Tobruk Pipline .....
Hamza E.Almansour, Sabri M. Mrayed and Ezeddine E. Zorgani 107

Naphtha Catalytic Reformer Hybrid Modeling .....
Isam A. B. Salem and Shams Khaled 119

Cause and Control of Sulfur Trioxide Formation in Waste Gas Thermal Incinerator .....
W. Alzamzam, W. Alfaghi and S. Almabrouk 123

A Case Study of Production of Value-Added Liquid Products from Natural Gas of Mellitah Gas Plant using GTL Technology: A Techno-Economical Study .....
Iftikhar Ahmad, Fauzi Elshawesh and Ahmed Souleman 127

Preliminary Techno-Economic Feasibility Study for Establishing a 250mm LB/YR Polystyrene Plant .....
Eltwaty, A. I, Escandarani, S.S., Akaza, Y. M., Elhouni, M. A., and Alwefally, M. O. 133

Integration of Airborne Wind Energy with the Oil and Gas Industry .....
Youssef Elshebani 141

Critical Success Factors for Successful Libyan Oil and Gas Projects .....
Abdulbaset A. Frefer, Mahmoud M. Matoug and Haleema H. Omer 147

A Framework for Enhancing the Decision Making Processes to Develop Oil and Gas Fields within some Libyan Operating Oil and Gas Companies .....
Hanan Zawam Aburas and Dr. Rajab Abdullah Hokoma 157

VOLUME 24 - (2019)

Libyan Petroleum Institute
P.O. Box 6431, Tripoli
State of Libya

PETROLEUM RESEARCH JOURNAL

Journal of the
Libyan Petroleum Institute
Tripoli
State of Libya

NATIONAL OIL CORPORATION
LIBYAN PETROLEUM INSTITUTE

Chairman

DR. MANSOUR EMTIR

Editor-in-Chief

MAHMOUD T. ELBAKAI

Associate Editors

DR. NURI M. FELLO
DR. ALHADI A. ELAKRIMI
DR. ALSIDDIEK M.ALABOAB

Co-ordinator

ABDULMAGID A. ELMRYED

New Insights on Mesozoic Depositional Sequences and Hydrocarbon Systems, from Jiffarah Escarpment to Libyan Offshore Basins 1

Depositional Environments of the Upper Ordovician, Mamuniyat Formation, NW Mrzuq Basin, SW Libya 9

Microfacies Analysis and Paleoenvironmental trends of the Paleocene Farrud and Marbuk Reservoirs, Concession 11, West Sirt Basin, Libya 17

Multi-Well Sand Production Prediction Study to Support Field Development plan, Lower Acacus Formation, Area 47, Ghadamis Basin 37

Characterization of Libyan Crude Oils and its Heavy Fractions 49

Exothermic Chemical Treatment (ECT), Towards Optimizing Heavy Crude Production of Al Haram Field, Concession 47, Sirt Basin, Libya, Using ECT Technology 59

Displacement of heavy Oil by Carbon Dioxide in a Tube 65

Analytical Modelling of Attenuation of Volatile Petroleum Hydrocarbons in the Vadose Zone 75

Thermal Analysis of a Clad Pipe using Simulation 81

Optimal Design and Simulation of Solar Photovoltaic Powered Cathodic Protection for Underground Piplines in Libya 89

Modeling and Prediction of High Temperature Oxidation of Steels used in Petroleum Refinery Heaters 99

Investigation of Wax Deposition Development in Sarir-Tobruk Pipline 107

Naphtha Catalytic Reformer Hybrid Modeling 119

Cause and Control of Sulfur Trioxide Formation in Waste Gas Thermal Incinerator 123

A Case Study of Production of Value-Added Liquid Products from Natural Gas of Mellitah Gas Plant using GTL Technology: A Techno-Economical Study 127

Preliminary Techno-Economic Feasibility Study for Establishing a 250mm LB/YR Polystyrene Plant 133

Integration of Airborne Wind Energy with the Oil and Gas Industry 141

Critical Success Factors for Successful Libyan Oil and Gas Projects 147

A Framework for Enhancing the Decision Making Processes to Develop Oil and Gas Fields within some Libyan Operating Oil and Gas Companies 157

Copyright © 2019 by Libyan Petroleum Institute (LPI)
Published by the Libyan Petroleum Institute (LPI), Tripoli, Libya

All rights Reserved
No part of this publication may be reproduced or transmitted in any form or by any means, electronically or mechanically including photocopying, recording or any information storage or retrieval system, without prior permission from the copyright holders.

Printed by Gutenberg Press Limited - Malta

FOREWORD

On behalf of the Libyan Petroleum Institute, I have the pleasure to introduce the 24th issue of the Petroleum Research Journal to the scientific community which has many interesting scientific papers. The publication of this Journal is intended to enhance existing knowledge and to promote available means of exchanging scientific information of interest on both national and international levels.

This issue consists of selected papers from over 90 topics presented at the conference held in Benghazi in November 2018 and organized by NOC.

I would like to thank the members of the editorial committee for their successful efforts in getting this issue in the present form. I, also, take this opportunity to invite local and foreign researchers to contribute in the development of this Journal. I hope they will find their contributions in future issues of this Journal encouraging and professionally rewarding.

Dr. Mansour Emtir
LPI, Chairman of Management Committee

EDITORIAL

This issue of the Petroleum Research Journal No. 24 is a continuation of series volumes issued by the Libyan Petroleum Institute (former Petroleum Research Centre) that commenced in 1984 as a news letter, converted to Journal since 1989.

This volume is special and important to the petroleum industry in Libya as it consists of 19 papers selected from over 90 papers presented at the Oil and Gas Conference, held in Benghazi, Libya in November 2018, which was organized by National Oil Corporation (NOC) of Libya. The selection was done totally under the responsibility of the conference's Scientific Committee.

All papers represented herein were edited but not reviewed and, therefore, the ideas expressed by the authors are of course their own.

We would like to express our thanks to all members of the Scientific Committee of the conference mentioned above for showing interest to publish the selected articles in our journal.

Appreciation is due to management's committees of both National Oil Corporation (NOC) of Libya and Libyan Petroleum Institute (LPI) for giving permission and financial support to publish this volume.

At last but not least, LPI, NOC managements and editors would like to call upon scientists, environmentalists, policy-makers, leaders of industry and each one of you to be part of reshaping the next era of energy.

The Editors

EDITORS' NOTE

With reference to the paper by El-Zaroug, El-Harbi and Gammudi entitled 'Palynological Analysis of Cutting Samples from Well A1-177/01, Murzuq Basin' published in Petroleum Research Journal, 22, p. 67 (2016), the editors regret that Figure 2 of the mentioned paper was incorrectly inserted within this paper by mistake. The presented figure belongs to a different paper by the same author. So, we now wish to apologize to our readers for any distress caused and attach the correct figure at the end of this issue no. 24.

PETROLEUM RESEARCH JOURNAL

Editorial Policies

The Petroleum Research Journal (Petroleum Res. J.) is a multi-disciplinary scientific technical journal published periodically by the Libyan Petroleum Institute. The aim of the journal is to publish articles classified as original papers, short communications and reviews of both practical and theoretical interests, which deal with scientific and technical advances in the fields of geology, geophysics, geochemistry, chemistry, petroleum and chemical engineering. Subject matter should be relevant to hydrocarbon exploration, evaluation and industry. The opinions and views expressed by the authors in their contributions are solely their responsibility.

- Ideas of the preliminary results of investigation, that have not advanced yet to the point at which they warrant publication as a full paper, may be submitted for publication as short communications. Other types of contributions such as discussions, book reviews and conference reports may also be submitted.

- Manuscripts may be submitted in Arabic or in English. Manuscripts in Arabic require English abstract.

- Manuscripts are accepted with the understanding that they have not been published elsewhere, and are not currently under consideration by another journal nor will be submitted to another journal. Manuscripts accepted for publication are the copy right of the journal.

- Manuscripts are processed by the Editor-in-Chief. Three copies of each submitted manuscript are sent to the appropriate Associate Editor for technical review. The Associated Editor will seek evaluation from three reviewers qualified to judge value of the paper, collect the reviews received, synthesize their contents and make a recommendation to the Editor-in-Chief concerning the acceptability of the manuscript. The final decision on a paper's disposition is then made by the Editorial Committee and communicated to the author(s) by the Editor-in-Chief.

- Twenty five free reprints of each published paper will be supplied to the author.

Instructions to Authors

Conformity to the following instructions is a prerequisite for consideration:

1. Manuscripts should be submitted with a letter stating (1) that the contents have not been published elsewhere; and (2) that the paper is not being submitted elsewhere.

2. Manuscripts should be submitted in electronic format in Microsoft Word (.doc) on CD-ROM, which must be checked with up-to-date virus scanner. Manuscripts may also be submitted via e-mail.

3. Alternatively, an original copy for each manuscript can be sent to the Editor-in-Chief of the Journal. However, the final revised version of the accepted manuscript must be submitted in electronic format as described above.

4. A title page should accompany the text, which includes: (a) paper title which should be informative and brief; (b) all authors' full names; (c) all affiliations clearly indicated; (d) key words (up to six) characterizing the subject material; and (e) the name, post and e-mail addresses, and telephone and FAX numbers of the corresponding author.

5. Computer illustration, including photographs (which must be kept to a minimum), charts and diagrams, must be submitted in high resolution format, and must be at least 300 dpi. Submit each illustration as separate file and indicate its location within the manuscript. Non-computer illustrations should be submitted in 21x28cm format. They should accompany the manuscript but should not be inserted in the text.

6. Illustrations are to be referred to as "Figures" and should be numbered consecutively in the order in which they are referred to in the text. They should be designed to go across a single or double column width of the journal page. Brief captions should be provided to make the figures as informative as possible.

7. All hand line drawings should be made with black drawing on white paper (preferably tracing paper). The authors' last name should be written in the margins (or on back) for identifications.

8. Non-computer photographs should be glossy prints. The authors last name and identification, as to which is the top of the photo, is to be written in pencil on the back.

9. A list of figures and table captions are to be typed on a separate page and attached to the end of the manuscript. List the figure number in the form "Fig. 1".

10. In the manuscript, principal headings should be typed at the centre of the page in capital letters. Headings of the text, first lower rank should be typed in small letters (first letters of the headings and proper nouns are to be capitalized). The following text should begin on the next line. For headings of second lower rank, underline and place a dash after the headings, and follow with text on the same line.

11. All references should be grouped at the end of the paper, under the heading REFERENCES, either alphabetically or numbered in the order they appear in the text. For a given author referred to more than once, use chronological listings with a suffix (a, b, etc.) to distinguish references of the same year. In the list of references, the following order and punctuation should be observed:

For references to a paper from journals:
- author(s) name (last name first, initials),
- year of publication,
- title (capitalize first word):
- journal name (abbreviate conforming to world list of scientific periodicals), volume number should be in bold; journal name and/or book title in italics.
- Page number (followed by beginning and ending page numbers).

Example:
Lagha, S. (1997). Petrography of the Triassic Phosphorites in the Gharyan Area, N.W. Libya. *Petroleum Res. J.*, **9**, 45-50.

For reference books:
- author(s) name (as above).
- year of publication
- title (capitalize all words of the title).
- publisher (firm name).

Example:
Tucker, M.E. (1981). *Sedimentary Petrology: An Introduction*. Blackwell Scientific, 251 p.

For references to a paper within a book:
- author(s) name
- Year of publication,
- Title of paper/(followed by)
- Editor(s) name(s)
- Title (of book):
- Page range,
- Publisher.

Example:
El-Bakai, M.T. (1996). Diagnesis and diagenetic History of the Lidam Formation, N.W. Sirt Basin In: M.J. Salem, A.S. El-Hawat and A.M. Sbeta (eds.) *The Geology of Sirt Basin*, **I**, 83-97. Elsevier, Amsterdam.

12. All correspondence should be addressed to:

Editor-in-Chief
Petroleum Journal
Libyan Petroleum Institute P.O. Box: 6431
Tripoli
State of Libya
Tel: 4830022/27 – 4836821/24
Fax: (21) 4830031
e-mail address: m.elbakai@lpilibya.com
Web-site: www.lpilibya.com

NEW INSIGHTS ON MESOZOIC DEPOSITIONAL SEQUENCES AND HYDROCARBON SYSTEMS, FROM JIFFARAH ESCARPMENT TO LIBYAN OFFSHORE BASINS

Ibrahim Y. Mriheel*

Abstract: This paper provides the results of outcrop data analyses across the Jiffarah Escarpment (JE). A new Mesozoic stratigraphic scheme and sequence stratigraphic framework are proposed which could be used both in the Libyan onshore and offshore. Chronostratigraphic chart has been constructed across the JE, in E-W direction. The chart demonstrates the way in which depositional sequences and sedimentation history vary across the JE via time. The exposed stratigraphic succession at JE ranges in age from Middle Triassic to Late Cretaceous. This Mesozoic succession represents two second-order sequences (Triassic to Middle Jurassic; and Cretaceous), both depositional sequences are bounded by major tectonic unconformities. The lower sequence (**SI**) is bounded by the Hercynian unconformity at the base of the Triassic and MFS of **SI** is placed in the Bathonian. The Cretaceous sequence (**SII**) is bounded by the Cimmerian-Austrian unconformities at the base and the Albine unconformity at the top. Deposition of the JE Mesozoic mega-sequences took place during several rifting phases effecting the Mediterranean basins, starting from Triassic and passing through the Jurassic and terminated during Early Cretaceous. The region witnessed compressional phases during the Albine Orogeny which lead to uplifting and erosion of wide areas along northern African margin. Stratigraphic correlations made on Mesozoic sequences reveal a complex sequential organization and also account for the impact of the Hercynian uplift and paleotopography on eastward truncations of Triassic-Middle Jurassic sequence. Post Albian deposits developed on a smoothed topography associated with a regional transgression and can be easily correlated over the JE. Reservoir and source rocks potential of the outcropping Triassic-Cretaceous sequences along JE reveal the importance of the deeper thermogenic petroleum systems located in the subsurface of the adjacent Gabes-Tripoli Basin. The exposed Miocene sequence along eastern JE represent good analogue to the proven biogeneic Neogene gas system in the adjacent Mediterranean basins and support the assumption of discovering similar plays in the Libyan offshore basins.

Keywords: Mesozoic Sequences, HC Systems, Jiffarah Escarpment (JE), Libyan Offshore Basins.

INTRODUCTION

The focal of this study encompasses new documentation of the stratigraphic scheme of the JE. The new stratigraphic scheme addresses the implementation of sequence stratigraphy approach in the subdivision of the outcropping rock units along JE (Figs. 1 and 2). Although the existence of valuable sedimentological and stratigraphic studies (Hinnawy & Cheshitev, 1975: Hammuda *et al*, 2000), no attempt has been made to upgrade the classical stratigraphy of the JE. This has contributed negatively on the correlation between the onshore sections and sub-cropping offshore sequences in adjacent basins. Hence, the outcomes are serious damage to the paleogeaographic reconstruction and augmented obstacles in the understanding of the geological history evolution of the region are persisted.

In this study, a review of previously published stratigraphic studies within these units is used to better constrain their dating. Stratigraphic correlations were based on studied outcrop sections along JE. Reconstruction of the temporal and spatial evolution illustrates a better constraint on the geologic history of the Jiffarah region.

* National Oil Corporation, Tripoli-Libya.
Email: imriheel@noc.ly

REGIONAL GEOLOGY AND TECTONIC SETTING

JE is a major topographic feature in the northwestern part of Libya (Fig.1). Jiffarah Uplift represents an arch between the Jiffarah Plain to the north and Ghadamis basin toward the south. In Libya, the JE is oriented in west-east direction and extends for about 350 km from Al Khumus to the Tunisian border. Towards Tunisia, the escarpment is known as the Dahar Plateau, and changes its orientation in a north-south trend. The JE delimits the Jiffarah Plain and rises above sea level to about 800m (Gharyan area).

The Mesozoic sequences exposed in the JE range in age from Triassic to Late Cretaceous. Sedimentation continued during Triassic-Early Cretaceous over a vast region in Jiffarah, however, a progressive truncation of Mesozoic sequences toward the east may be ascribed to both palaeotopgraphic and tectonic controls (Echikh, 1998; Bouaziz *et al*, 2002; Dardour *et al*, 2004 and Underdown *et al*, 2007). Prior to the Hercynian Orogeny, all western Libyan basins Jiffarah, Ghadmis and Murzug were forming single Paleozoic north-south trending basin. The Hercynian Orogeny inverted the northern Ghadamis basin into a prominent east-west arch which was extensively eroded during the Permian, exposing the Precambrian core of Pharusian rocks (Hallett, 2002).

In Triassic times the arch had been greatly reduced in elevation and Triassic-Jurassic and Early Cretaceous sediments were deposited over the rifted Mesozoic Jiffarah Arch and Ghadamis basin. The arch was also covered by the Late Albian-Turonian transgression and deposition of marine sediments continued probably, till the Late Eocene time. The Jiffarah Arch was reactivated during mid-Tertiary in response to the closing of the Tethys. It was subjected to uplifting accompanied by strike–slip faulting along the Al Azizyah Fault and Libyan coastal fault system.

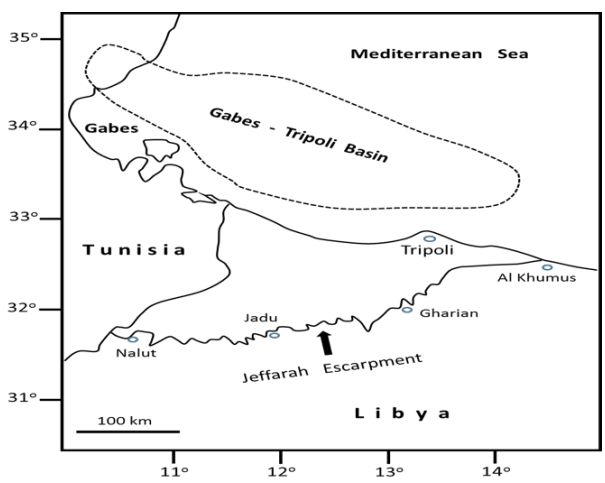


Fig. 1. Location map of the study area.

The current body and topography of the escarpment are the end result of the Alpine tectonic events (volcanic eruptions, uplifting and erosions). The Alpine orogenic event, the latest period of tectonism affecting the Jiffarah and western Libyan Palaeozoic basins, was caused by collision of the Africa-Arabia plate with Europe during latest Cretaceous-Eocene time (Boote *et al*, 1998; Guiraud *et al*, 2005). Exhumation related to this tectonic event is greatest over the uplifted basin margins to the south Gargaf and Tihemboka archs and east Nafusah Uplift (Underdown *et al*, 2007). Eocene tectonism also witnessed volcanic eruptions and lava flows near Gharyan region, and volcanism has continued till recent times. The advent of the Miocene, probably witnessed a major escarpment formation, and outcropping of Mesozoic rocks on the escarpment and in few places in the Jiffarah Plain. The formation of this escarpment has been considered as a retreating fault scarp, its shape and extension is controlled by the Al Aziziyah Fault (Lipparini, 1940 and Miller, 1971).

SEQUENCE STRATIGRAPHY OF THE MESOZOIC SEQUENCES

The exposed stratigraphic succession at JE ranges in age from Middle Triassic to Late Cretaceous (Fig. 2). This Mesozoic succession represents two second-order sequences (Triassic to Middle Jurassic; and Cretaceous), both depositional sequences are bounded by major tectonic unconformities. The older sequence boundary of SI is at the Hercynian unconformity at the base of the Triassic and MFS of SI is placed in the Bathonian. The base of younger sequence (SII) is at the Hauterivian-Cenomanian boundary, coincident with the Cimmerian-Austrian unconformities and MFS SII is placed in the Turonian (Fig. 2). The main tectonic unconformities or sequence boundaries bounding the second order sequences are defined below:

Sequence Boundaries

The lower and upper sequences are interrupted by two major tectonic unconformities along the JE.

They are known to geologist as Cimmerian and Austrian unconformities.

The Cimmerian Orogeny began 200–150Ma (Jurassic), when the Cimmerian plate collided with the North and South China blocks, closing the Paleo-Tethys Ocean between them and forming mountains. According to (Guiraud *et al*, 2005), tectonic deformations are recorded along most North African basins during the Jurassic-Cretaceous transition. This event is known as Cimmerian unconformity and probably occurred coevally with the tectonic activity in south-eastern Europe (Bodin *et al*, 2010).

The Austrian event, records a short-lived unconformity during the Early Cretaceous (Aptian) at the base of Kiklah Formation (Bodin *et al*, 2010) whereas, the Cimmerian unconformity has been applied at the base of Cabow Formation by the same authors. The Austrian tectonic event corresponds to the change of the relative motion and the initiation of the convergence of Africa relative to Europe (Dewey *et al*, 1989 and Rosenbaum *et al*, 2002).

The impact of Jurassic-Cretaceous unconformities on spanning of the sedimentary hiatus across JE can be summarized as follows:

In the western parts of the JE, the unconformity produces a sedimentary hiatus spanning the Oxfordian to Valanginian (164-134Ma & Fig. 2). In the central parts (Gharian area), the unconformity produces a sedimentary hiatus spanning the Sinemurian to Aptian (191-128Ma & Fig. 2). While, in the eastern parts of the region, the unconformity produces a sedimentary hiatus spanning the Rhaetian to Cenomanian (209-100Ma & Fig. 2). The impact of these tectonics on the sedimentary gab durations are varied widely across the JE. It records time duration of 30Ma, 63Ma and 109Ma at western, central and eastern parts of the JE respectively.

Stratigraphic correlations made on Mesozoic sequences reveal a complex sequential organization and also account for the impact of the Hercynian uplift and paleotopography on eastward truncations of Triassic-Middle Jurassic sequence. Post Early Cretaceous deposits developed on a smoothed

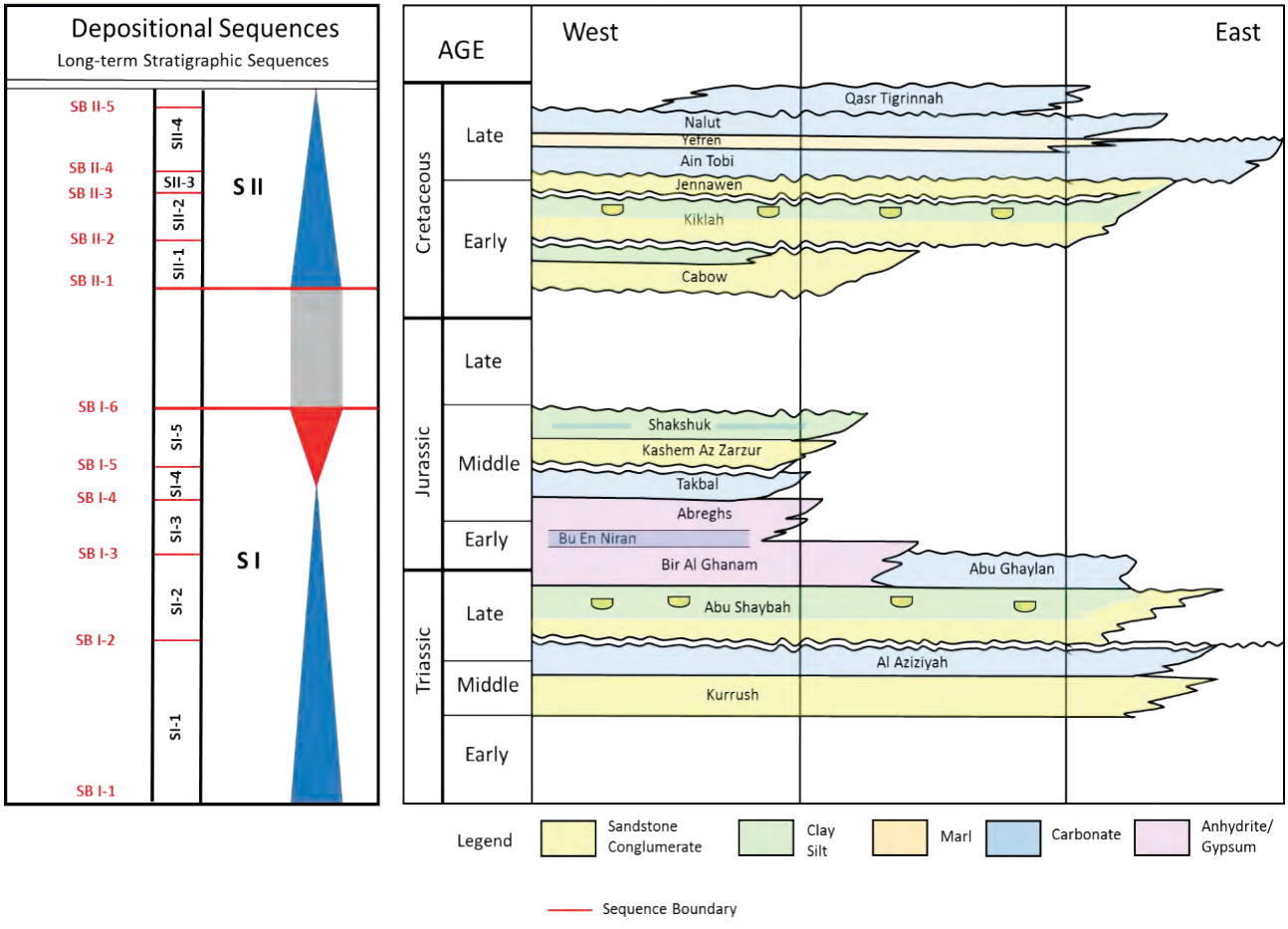


Fig. 2. A new stratigraphic scheme and sequence stratigraphic framework for the Mesozoic sequences outcropping along Jiffarah Escarpment.

topography associated with a regional transgression and can be easily correlated over the JE. The main second order sequences are defined as follows:

The Older Sequence

The lower sequence is essentially a second order transgressive–regressive (T/R) sequence and is comprised of mixed siliciclastics, carbonate and evaporite facies (Fig. 2). This sequence can be further subdivided into five T/R cycles and are developed during rifting phases of the Mediterranean Sea. Along the East-West transect of the JE, Sequences SI-1 and SI-2 are widely developed, whilst sequences SI-3, SI-4 and SI-5 are truncated toward the eastern flanks of the scarp (Fig. 2), indicating paleohigh control and significant erosion due to the tectonic unconformities (i.e. Cimmerian and Austrian). The exposed part of the lower sequence consists of marginal marine sisliciclastic and carbonate ramp facies of Middle Triassic (Anisian-Carnian) of Kurrush (Ras Hamia) and Al Aziziyah formations. This in turn grade upwards into the Late Triassic (Norian-early Rhaetian) fluvial facies of Abu Shaybah Formation which passes upwards into Late Triassic-Early Jurassic (Rhaetian-Sinemurian) shallow shelf carbonate facies of Abu Ghaylan Formation. This facies changes laterally to the west into the evaporites of the Bir Al Ghanam Formation. This unit is followed by the deposition of the Middle Jurassic (Bathonian) carbonate and shale facies of the Takbal Formation. The Bathonian Takbal facies marks the time of maximum flooding (TMF) of this sequence (Fig. 2). The first cycle is terminated by the deposition of the Middle Jurassic (Bathonian-Callovian) regressive sequence, showing an overall progradational stacking pattern and comprising of fluvial to marginal marine siliciclastic of Kashem Az Zarzur Formation that grade upward into mixed shallow marine siliciclastics and carbonates of the Shakshuk Formation (Fig.2).

The sequence is more than 1000m thick in Yefren-Jadu area, reflecting a period of relatively high accommodation. The older second-order sequence consists of fife sequences. They vary in thickness from 100 to 400m. They are defined as follows:

SI-1: The base of this sequence is taken in the lower part of the early Triassic (Scythian), Bir El Jaja Formation basal transgressive marine siliciclastic facies grading upwards into the Middle Triassic (Anisian-Ladinian) marginal marine, mixed siliciclastic and carbonate facies of Ouled Chebbi and Kurrush (Ras Hamia) formations. These in turn grade upwards into the Late Triassic (Late Ladinian-Carnian), shallow carbonate ramp facies of Al Aziziyah Formation. The transgressive to highstand parts of the sequence are represented by the Al Aziziyah Formation. The top of this sequence corresponds with the top of the Carnian Stage (Fig. 2).

SI-2: This sequence has a well-developed, lowstand-thick sandstone at the base of the Abu Shaybah Formation. The regionally identifiable floodplain shale represents the transgressive phase of the third-order sequence (Fig. 2). Locally, the Abu Shaybah Formation, overlain by few meters of marginal marine siliciclastics in the end of TST. Most of the highstand parts of the sequence are represented by the Bir Al Ghanam evaporites and its eastward equivalent Abu Ghaylan carbonates. The age of this sequence is likely Norian to Rhaetian, possibly as young as Sinemurian.

SI-3: The sequence extends from the Sinemurian through the Bajocian and comprises upper parts of the Bir Al Ghanam and whole section of the Bu En Niran and Abreghs formations (Fig. 2). There is a significant evaporate TST and HST components in this sequence, marking the change from siliciclastic to dominantly evaporate deposition in the western part of the study area. The Bu En Niran carbonate facies represents the TMF of this sequence. This sequence is more than 400m thick in the area, reflecting a period of relatively high accommodation. Toward the eastern parts i.e. in Gharyan area (e.g. only the carbonates of Abu Ghaylan Formation are present).

SI-4: This sequence is 22m thick in the Takbal village, comprising limestone and clay, and having retrogradational stacking pattern (i.e above the evaporite deposits of Abreghs Formation). The regionally identifiable Takbal carbonate and clay represents the transgressive phase of this third-order sequence and marking the TMF of the whole older sequence (Fig. 2). The sequence SI-4 is likely Bathonian in age.

SI-5: There is a significant siliciclastic regressive component in this sequence, showing an overall progradational stacking pattern and comprising of fluvial to marginal marine siliciclastic of Kashem Az Zarzur Formation that grades upward into mixed shallow marine siliciclastics and carbonates of the Shakshuk Formation (Fig. 2). Its age is likely Bathonian to Callovian, as defined by biostratigraphic data.

The Younger Sequence

The upper mega sequence is represented by the Cretaceous second-order incomplete transgressive sequence (Fig. 2). Within the Cretaceous sequence, four 3rd order T/R sequences were identified. The younger second-order depositional sequence extends from the Valanginian to Turonian, comprising Cabow, Kiklah, Jennawen, Ain Tobi, Yefren, Nalut and part of the Qasr Tigrinah formations (Fig. 2). The Qasr Tigrinnah shale represents the TMF of the sequence. The basal Cretaceous fluvial siliciclastic facies of Cabow and Kiklah formations are organized into two 3rd order sequences that form sequences SII-1 and SII-2.

A return to marine conditions by Late Albian resulted in deposition of sequence SII-3 of the Jennawen marginal marine siliciclastics facies (Fig. 2), lying unconformably on the Kiklah Formation and form an overall 3rd order transgressive trend where a maximum flooding surface occurs within the upper most deposits. Transgression continued during Late Cretaceous, as carbonates deposition become increasingly significant (Fig. 2). The overall sequence II-4 represents transgressive succession, forming backstepping shallow-marine carbonates and marl of Ain Tobi, Yefren, Nalut and Qasr Tigrinnah formations (Fig. 2). The TMF of this sequence coincides with the deposition of regional Turonian source rocks in G-T Basin and Tunisia.

In many parts of Jiffarah Scarp, above the Early Cretaceous regressive successions Cabow and Kiklah deposits, Both sequences II-3 & II-4 show backstepping character and are formed of marginal-marine Jennawen sediments and shallow-marine carbonates and marl of Ain Tobi, Yefren, Nalut and Qasr Tigrinnah formations.

SEQUENCES HC SOURCE POTENTIAL AND RESERVOIR ROCKS

The exposed Mesozoic sequences along JE provide clear vision on the HC potential for their subcropping analogue, encountered at greater depths in adjacent offshore basins (e.g. Gabes-Tripoli Basin). Selected examples explaining the case are illustrated in (Figs. 3-5).

Older sequence HC Source & Reservoirs

Deep-outer ramps Triassic (Carnian) shales of Al Aziziyah Formation are possible source rocks in the southern Gabes-Tripoli Basin (Mriheel, 2014). Triassic (Norian-Early Rhaetian) sandstones of

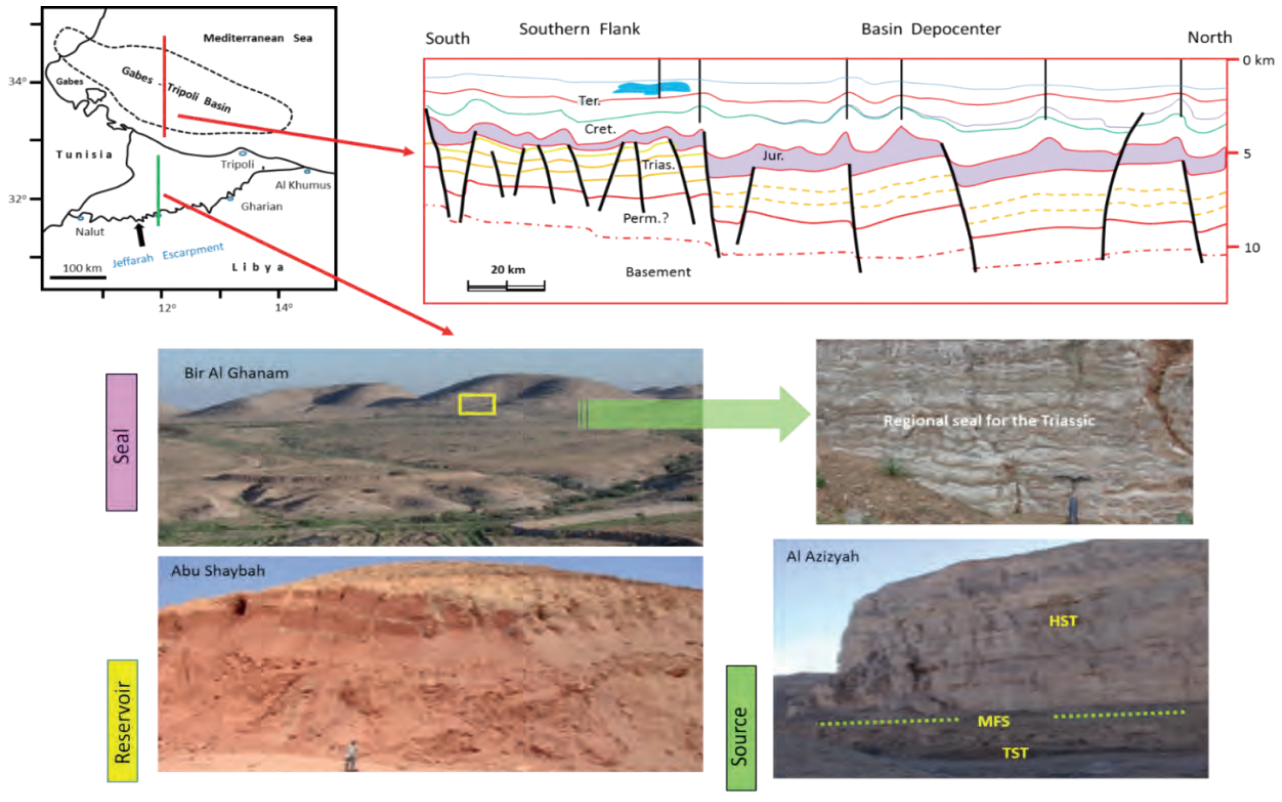


Fig. 3. Map, cross-section and field photos showing extension of Triassic petroleum play elements from outcrop to Libyan offshore.

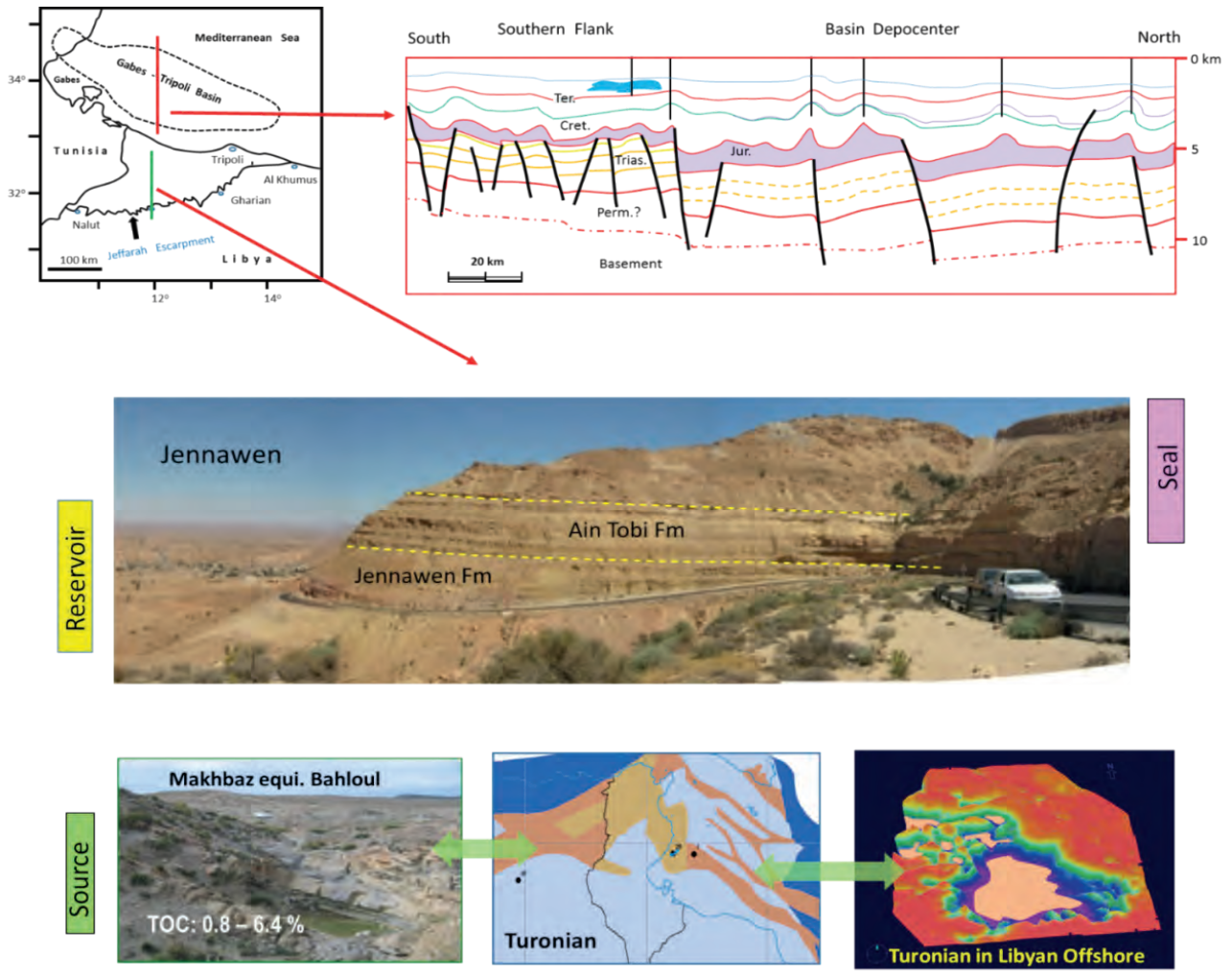


Fig. 4. Map, cross-section and Field photo showing extention of Cretaceous petroleum play elements from outcrop to Libyan offshore.

Abu Shaybah Formation are potential reservoirs both in Libyan and Tunisian offshores (Fig. 3). Triassic deposits are proven source rocks in eastern Sirt Basin. Middle Jurassic (Bathonian) shales and carbonates represent a time of significant maximum flooding and are considered as possible source rocks in the offshore basins. Equivalent Bathonian-early Callovian Khattaba Formation is source rock for oil in the Western Desert of Egypt (Keeley and Massoud, 1998). Triassic-Jurassic carbonate build-ups are principle reservoir in the Gulf of Gabes (Carr, 2003).

Younger Sequence HC Source and Reservoirs

Early Cretaceous (Aptian-Albian) Nubian lacustrine shales are source rocks in the eastern Sirt Basin. Early Cretaceous deposits are reservoirs in the eastern Sirte Basin and Gulf of Gabes. Important petroleum Late Cretaceous source rock in Gapes-Tripoli Basin is Makbaz Formation (equivalent to the Tunisian Bahloul Formation). Turonian marine deposits are source rocks in the eastern Sirt Basin. Late Cretaceous marine deposits are source rocks in Sirt Basin and in Gulf of Gabes. Late Cretaceous carbonates and siliciclastics are major reservoirs in Sirte Basin. Late Cretaceous sediments are reservoirs in Gulf of Gabes (Carr, 2003). The richness of the Late Cretaceous source rock section, availability of carbonate and clastic reservoirs and encouraging basin modelling (Fig. 4) results suggest that much more oil could be found in the transgressive Jennawen sandstones and Alalgah and Makbaz carbonate reservoirs (Mriheel, 2017).

Other Sequences HC Source and Reservoirs

The newly proposed biogenic gas system of the Oligocene-Early Miocene (Mriheel, 2017) reveals the existence of interesting accumulations in the

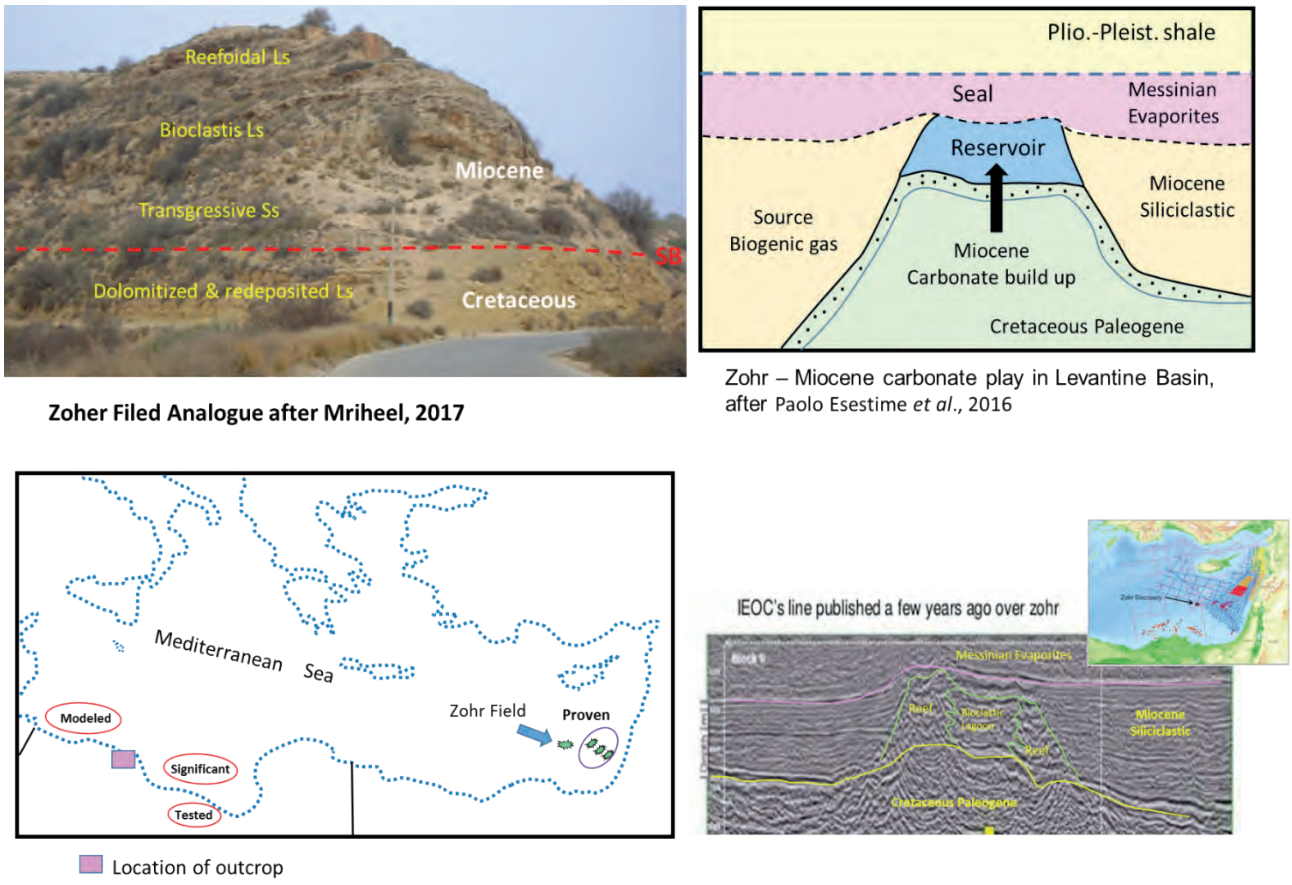


Fig. 5. Miocene biogenic gas play in Levantine and outcropping Miocene sequence above Cretaceous unconformity supports of similar plays in Libyan offshore.

Dirbal Formation sealed laterally and on top by the shales and marls of the Ras Abd Jalil Formation and Al Mayah Formation respectively. Future exploration must not neglect these spectacular carbonate build-ups both in the Gabes-Tripoli Basin and in the Sirt Basin offshore.

The Middle-Upper Miocene reefoidal carbonates of the Alkhums Formation (Fig.5) represent excellent analogue to the Zohar field at the Egyptian offshore where huge gas has recently been discovered. Furthermore, this newly proposed biogeneic gas system open new doors for gas exploration within the transgressive Oligocene sandstones in the onshore of the Sirt Basin.

CONCLUSIONS

A new stratigraphic framework for the Mesozoic succession in JE has been constructed. The stratigraphy is divided into two second-order sequences (older and younger) and key sequence stratigraphic surfaces for both sequences have been defined.

The older sequence boundary of SI is at the Hercynian unconformity at the base of the Triassic and MFS of SI is placed in the Bathonian. The base of younger sequence (SII) is at the Hauterivian-Cenomanian boundary, coincident with the Cimmerian-Austrian unconformities and MFS SII is placed in the Turonian. This sequence framework is intended to provide a basis for future in-depth analysis and further subdivisions of the succession. The outcomes of this framework synthesis will encourage younger geoscientists to carry out more detailed studies and consequently, help in recognition of the impacts of the global and relative sea level changes on sequences development of the region.

ACKNOWLEDGEMENT

The author wishs to thank the management of the National Oil Corporation for the sponsorship and permission to publish the data and interpretations in this paper. Thanks are also extended to Dr. Mahmoud Elbakai for the editorial work and reviewing of the manuscript.

REFERENCES

Bodin, S.; Petitpierre, L.; Wood, J.; Elkanouni, I. and Redfern, J. (2010). Timing of Early to Mid-Tectonic Phases along North Africa: New Insights from the Jeffara Escarpment (Libya-Tunisia). *Journal of North Africa earth Sciences*, **58**: 489-506.

Boote, D. R. D.; Clark-Lowes, D. D. and Traut, M. W. (1998). Palaeozoic Petroleum Systems of North Africa. In: *Petroleum Geology of North Africa* (Ed. by: D. S. MacGregor, R. T. J.; Moody and D .D. Clark-Lowes). *Geological Society of London, Special Publication*, **132**: 7-68.

Bouaziz, S.; Barrier, E.; Soussi, M.; Turki, M. M. and Zouari, H. (2002). Tectonic Evolution of the Northern African Margin in Tunisia from Paleostress Data and Sedimentary Record. *Tectonophysics*, **357**: 227-253.

Carr, I. (2003). A Sequence Stratigraphic Synthesis of the North African Mesozoic. *Jour.Petr. Geol*., **26**: 133-152.

Dardour, A. M.; Boote, D. R. D. and Baird, A. W. (2004). Stratigraphic Controls on Palaeozoic Petroleum Systems, Ghadames Basin, Libya. *Jour. Petr. Geol*., **27**: 141-162.

Dewey, J. F.; Helman, M. L.; Turco, E.; Hutton, D. W. H.; and Knott, S. D. (1989). Kinematics of the Western Mediterannean. In: *Alpine Tectonics* (Ed. by: M. P. Coward, D. Dietrich, R. G. Park). *Geol. Soc. Am., Spec. Publ*., **45**: 265-283.

Echikh, K. (1998). Geology and Hydrocarbon Occurrences in the Ghadames Basin, Algeria, Tunisia, Libya. In: *Petroleum Geology of North Africa* (Ed. by: D. S. MacGregor, R. T. J.; Moody and D .D. Clark-Lowes). *Geological Society of London, Special Publication*, **132**: 109-129.

El Hinnawy M. and Cheshitev, G. (1975). Geological Map of Libya 1:250,000, Sheet Tarabulus, NI 33-13, *Explanotary booklet. Industrial Research Centre*, Libya.

Guiraud, R.; Bosworth, W.; Thierry, J.; and Delplanque, A. (2005). Phanerozoic Geological Evolution of Northern and Central Africa: An Overview. *Journal of African Earth Sciences*, **43**: 83-143.

Hallett, D. (2002). Petroleum Geology of Libya: Amsterdam, the Netherlands, Elsevier: 503p.

Hammuda, O. S.; Sbeta, A. M. and D. Worsley, D. (2000). Field Guide to the Mesozoic Succession of Jabal Nafusah, NW Libya: *Sedimentary basins of Libya-Second symposium: Geology of Northwest Libya*: 50p.

Keeley, M. L. and Massoud, M. S. (1998). Tectonic Controls on the Petroleum Geology of Eastern North Africa. In: *Petroleum Geology of North Africa (Ed. by: D. S. MacGregor, R. T. J*.; Moody and D .D. Clark-Lowes). *Geological Society of London, Spec. Publ*., **132**: 265-281.

Lipparini, T. (1940). Tectonica e Geomorfologia dela Tripolitania. *Boll. Soc. Geol. Ital*., **59**: 221-301.

Miller, V. C. (1971). A Preliminary Investigation of the Geomorphology of the Jebel Nefusa. In: *Proceedings of the 1st symposium on the Geology of Libya* (ed. C. Gray). Fac. Sci. Univ. Libya, Tripoli: 365-386.

Mriheel, I. Y. (2014). Paleogeography and Sedimentation History of the Western Libya Offshore, Central Mediterranean In: *The International Conference and Exhibition, Am. Assoc. Petrol. Geologists*, Istanbul, Turkey, (Extended Abstract): 9p.

Mriheel, I. Y. (2017). New Petroleum Plays Assessment Using Sequence Stratigraphy and Basin Modeling Techniques, Libyan Offshore. Presented at the *First Conference of Applied Sciences*, Alzintan, Faculty of Science, Libya.

Rosenbaum, G.; Lister, G. S. and Duboz, C. (2002). Relative Motions of Africa, Iberia and Europe During Alpine Orogeny. *Tectonophysics*, **359**: 117-129.

Underdown, R.; Redfern, J.; and Lisker, F. (2007). Constraining the Burial History of the Ghadames Basin, North Africa: An Integrated Analysis Using Sonic Velocities, Vitrinite Reflectance Data and Apatite Fission Track Ages. *Basin Research*, **19**: 557-578.

DEPOSITIONAL ENVIRONMENTS OF THE UPPER ORDOVICIAN, MAMUNIYAT FORMATION, NW MURZUQ BASIN, SW LIBYA

Nuri Mohamed Fello*

Abstract: The Murzuq Basin, SW Libya, is one of a series of Palaeozoic intracratonic sag basins on the North African Saharan Platform. The structural fabric of the basin was developed during the Late Proterozoic Pan-African Orogenic event, which has strongly influenced the stratigraphy and depositional patterns within the predominantly Palaeozoic clastic basin-fill.

The Upper Ordovician (Ashgillian) Mamuniyat Formation is the primary reservoir target in three oilfields A, B and H within Repsol Oil Operations Concession area NC115, on the NW flank of the Murzuq Basin. A major problem with the Mamuniyat is the location of the sediment provenance, due to the lack of adequate subsurface and outcrop data, and the relationship and controls on sediment flux, and the depositional systems. Petrographic data derived from sandstone samples from cored intervals through the Mamuniyat Formation show that they are mainly sublitharenites, with some quartz arenites and litharenites. Compositional data for the three oilfields indicate that they were derived from a similar parent rock. These same tectonic events influenced facies patterns, sediment deposition and interaction between a variety of shallow water marine and fluvial depositional environments across a NW-SE oriented storm-influenced coastline. Petrography and regional facies patterns suggest that the Mamuniyat sandstones were derived from a nearby, tectonically active, granitic basement source terrain, which was most probably the uplifted Ghat/Tikiumit Arch to the SW of NC 115. Periodic uplift of the basin margin in the SW, and associated base level changes led to the basinward progradation of braided fluvial systems. That was followed by marine transgressive events emanating from Palaeotethys in the northeast. Both the braided fluvial and shallow water marine sandstones of the Mamuniyat Formation are primary hydrocarbon reservoir targets, with the main source and seal being the eustatically controlled Lower Silurian Tanezzuft Shale.

Keywords: Ordovician Succession, Mamuniyat Formation, Murzuq Basin, SW Libya.

INTRODUCTION

The Murzuq Basin of SW Libya (Fig. 1) forms one of a series of Palaeozoic intracratonic sag basins on the Saharan Platform. The structural fabric, imposed on the North Africa continental lithosphere during the Late Proterozoic Pan-African Orogenic event, played an important role in controlling subsequent structural and stratigraphic evolution of the basin (Thomas, 1995). The basin, which covers an area of some 350,000km2, is sub-circular in shape and clearly visible on satellite photographs of SW Libya. During Early Palaeozoic times, NNW trending horst and graben structures developed, which extended as far as the eastern Ennedi Mountains in Chad and the northern and central parts of Niger. The horst and graben structures are filled with siliciclastic continental and shallow water marine sediments (Klitzsch, 2000).

Thus, Early Palaeozoic tectonism effectively controlled the distribution of the main fluvial-shallow marine reservoir interval of Upper Ordovician (Ashgillian) age, in several oil fields. The Murzuq

Basin is a Palaeozoic structural element filled with strata of Cambrian to Carboniferous age, including several hundred meters of Lower Silurian Tanezzuft Shale that locally has excellent to fair source rock potential (Fello and Turner, 2001).

Repsol's NC115 Concession, which lies on the northwest flank of the Murzuq Basin, is located

*National Oil Corporation, Exploration Department, P.O. Box: 2655, Tripoli – Libya. E-mail address: nfello@noc.ly

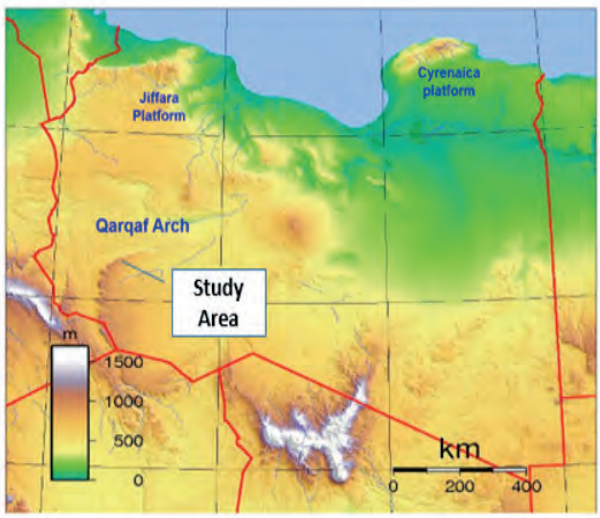


Fig. 1. Location map of the study area in NW Murzuq Basin, SW Libya.

some 1,330 km SW of Tripoli and covers an area of 25,850 km2. The main focus of this study is the Upper Ordovician (Ashgillian) Mamuniyat Formation, which is the primary reservoir target in three oilfields A, B and H within the Repsol Concession area NC115 (Fig. 2). The subsurface occurrence of the Mamuniyat sandstone is 20-170m thick, but with a regional thickening towards the northeast towards the Gargaf Arch (Pierobon, 1991).

A problem with the Mamuniyat Formation is the location of the sediment provenance, and the relationship and controls on sediment flux and the depositional systems, due to the lack of adequate subsurface and outcrop data. This study is based on core photographs and samples from more than 310m (1016ft) of conventional core from 12 oil wells distributed throughout the three oilfields A, B and H (Fig. 2). Wells A8, B2 and H4-NC115 are type section wells, which provide core coverage of the Mamuniyat Formation of over 134m in A8-NC115, 126m in B2-NC115 and 54m in H4-NC115. In addition we have also worked on a number of additional exploration and development oil wells, to provide further information and constraints on lateral facies variations between the three main oilfields.

STRATIGRAPHIC FRAMEWORK

The Murzuq Basin succession unconformably overlies Precambrian crystalline basement. It consists predominantly of Palaeozoic sediments with lesser amounts of Mesozoic and Cenozoic sediments (Fig. 2), which attain a maximum thickness in the central part of the basin of over 3500m. However, the complete succession is only preserved at outcrop in a few areas due to regional erosion during the Caledonian and Hercynian Orogenic events. The present structural framework of the basin is largely a result of successive, superimposed tectonic events related to the Taconic, Caledonian and Hercynian orogenies. Although tectonic activity continued to influence the basin until post Eocene times (Fig. 3). As a result the basin exhibits a variety of structural styles, fault patterns and traps. The early to mid Palaeozoic structural relief comprises a system of NNW to N striking horst troughs developed during Cambrian to Early Ordovician times. These form wide elongate troughs that became the routes for long-distance transgression to the south or southeast, whenever the northern part of Gondwana was transgressed by the sea.

Consequently, these structurally low areas were covered by relatively thick sequences of marine strata during highstand, whereas during periods of regression, they become the sites of nearshore marine or continental sedimentation. In contrast intervening uplifted horst areas were subject to reduced sedimentation and/or erosion (Klitzsch, 2000).

SEDIMANTARY FACIES ASSOCIATIONS AND ENVIRONMENTS

The Mamuniyat Formation can be divided into three main facies associations, each of which comprises a number of constituent facies, defined on the basis of their lithology, sedimentary structures and trace fossils. These facies associations are interpreted to represent two main depositional environments: braided fluvial and marine (Fello,

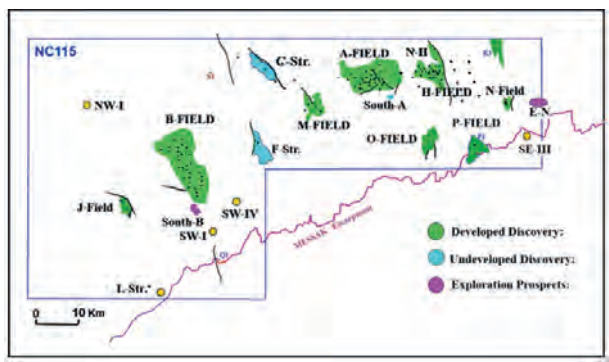


Fig. 2. Location map of the main oil fields in NC115 Concession, Murzuq Basin.

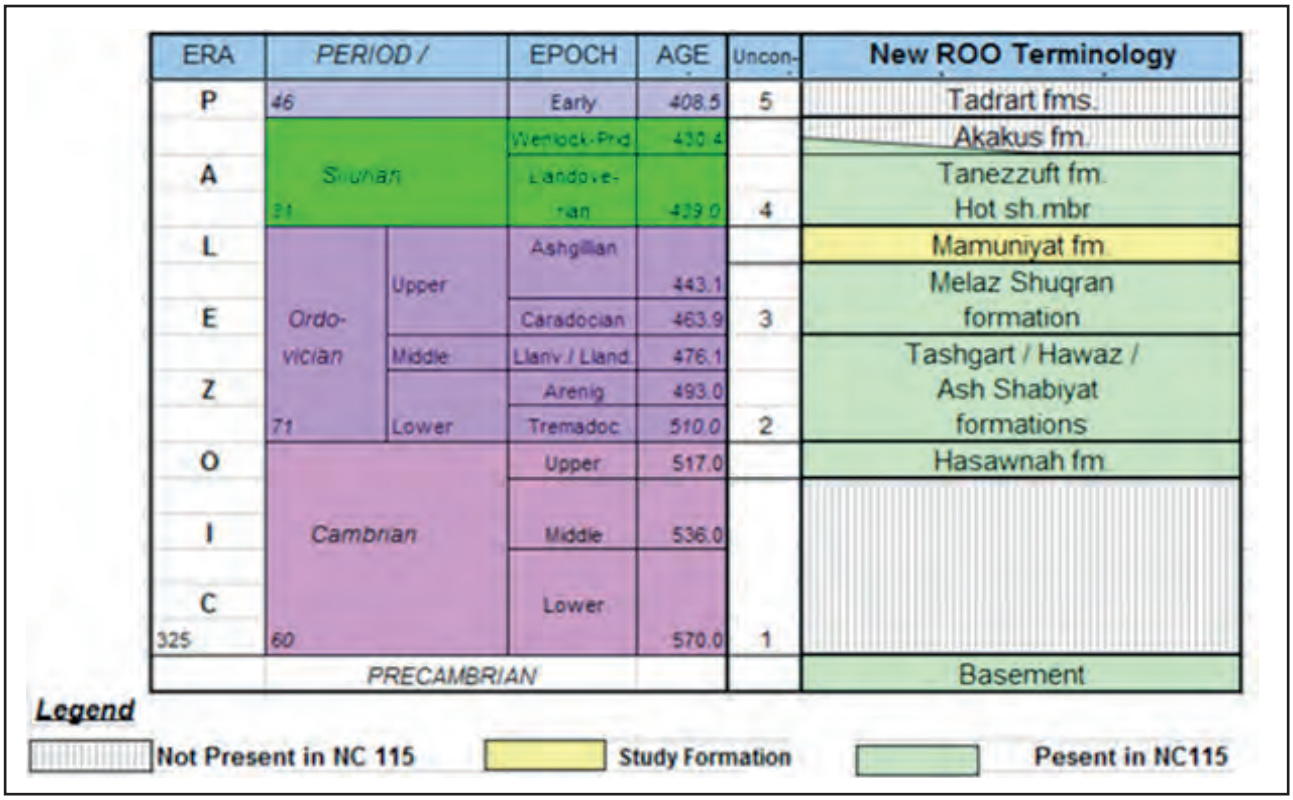


Fig. 3. Stratigraphic column of the study section within NC115 area, NW Murzuq Basin, SW Libya.

2001). Fig. 4 summarises the facies associations, their constituent facies, and depositional environments. The facies associations are described and interpreted below based on the terminology of Miall (1996).

Alluvial Plain Facies Association

Description: This facies association is restricted to the Upper Member (M1) of the Mamuniyat Formation (Fig. 4) in the southwest part of NC115 Concession.

It is restricted to the B-Field where it makes up most of the reservoir interval, especially in type well B2-NC115 (Fig. 2). This facies association is represented by the cored interval from 1402m to 1430 m. It is represented by course- to very coarse-grained sandstone with rare coarse-grained siltstone interbeds. The sandstones are poorly sorted, and mainly sublitharenite in composition. A characteristic feature of this facies association is that it forms thick packages of sandstone beds ranging from 10cm to 15cm in thickness, which show a fining-upward trend from very coarse and coarse-grained sandstone to very coarse and medium-grained sandstone (Fig. 4). The dominant sandstones, and individual beds of siltstone can be traced throughout all the wells in the B-Field (32 wells), over a distance of some 10km. Two locally developed types of fining-upward sequence occur as following:

1) Scoured, intraclast-strewn surface, overlain by coarse- to very coarse-grained, medium- to small-scale trough cross-bedded sandstone passing up into fine-grained ripple cross-laminated and horizontally-laminated sandstone with some siltstone; and
2) Medium- to fine-grained, large-scale planar cross-bedded sandstone in which individual sets decrease in scale upwards are overlain by fine-grained sandstone containing small trough cross-bedding. The sandstone beds show an upward increase in thickness with a concomitant decrease in the abundance of pebbles, horizontal lamination and ripple cross-lamination, which is confined to the upper part of the sandstone beds.

The sedimentary structures are dominated by medium-scale, trough cross-bedding from 10 to 25cm thick. Soft sediment deformation structures are rare, but some laterally more continuous horizons showing fluid escape structures are common in the southwest part of the study area in the B-Field (Fig. 2). Some sandstones contain

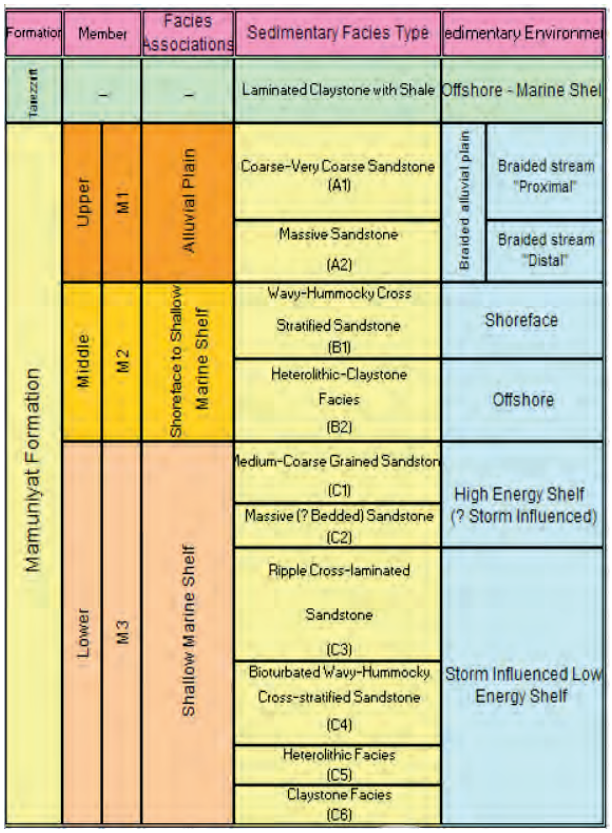


Fig. 4. General characteristics of the fluvial and shallow marine facies within the Mamuniyat Formation, NC115 Concession.

low-angle truncation surfaces that can be traced laterally for several tens of metres, as well as laterally discontinuous minor erosional scour surfaces. In addition, the rare micaceous siltstone units form laterally discontinuous lenses, and contain *Tigillites* burrow forms incised by the sandstones.

In the lowermost part of the alluvial plain facies association, the sandstone is mostly structureless and sedimentary structures are very rare, where present they consist of planar and trough cross-bedding, flat bedding and ripple cross-lamination with individual ripple sets from 0.02m to 0.5m thick. Flame structures are also present and rare subvertical fractures, possibly enhanced by coring, which were open to silica cement. Moreover, the sandstones also contain a few stylolites with the orientation of some of the sutured seams generally parallel to bedding. Thus, the stylolite axes are perpendicular to the primary bedding surface (Bauerle *et al*, 2000). The thinly bedded siltstones, which range from 1cm to 5cm in thickness, are mainly confined to the lowermost part of this facies association, and contain sub-angular to sub-rounded intraclasts of fine to medium-grained sandstone.

Interpretation: The coarse-grain size, planar and trough cross-bedding, small fining-upward and coarsening-upward sequences within multistoried, truncated packages are most consistent with a braided fluvial depositional environment for this facies association.

Direct analogous outcrops of this facies association have not been found in the SW Murzuq Basin (Herzog, 1997). The upward increase in bed thickness, grain-size, and the scale of cross-bedding provides a measure of proximity to detrital clastic influx and the source area. The fine- to medium-grain size, better sorting and limited thickness of the sandstones within the lower part, compared to the upper part, suggest that the sedimentary properties of the sandstone change continuously away from the basin edge. Enabling the depositional setting of the Upper Mamuniyat Formation to be divided into an upper braided plain (proximal) and lower braided plain (distal). The lowermost part of the Upper Mamuniyat sandstone was deposited in a zone of decreased gradient and stream power with increased entrapment of fine-grained detritus. This suggests that they were deposited further away from the source area than the uppermost part of the Upper Mamuniyat Formation. However, the textural uniformity of the sandstones could be related to the nature of the sediment available at the source area (Ghat/Tikiumit Arch) located to the southwest of NC115 Concession.

The sedimentary structures and alluvial architecture of this facies association are similar to those observed in the Platte-type and shallow, perennial, sandbed braided river models of Miall (1996). This interpretation is consistent with the abrupt transition from very coarse-grained to medium-grained sandstone, the low ratio of siltstone to sandstone and lack of fossils. Intimate interbedding of pebbly sandstone and coarse to very coarse sandstone, plus the occasional presence of thin siltstones within the upper part indicate that changes in discharge were both frequent and extreme. In the Upper Member of the Mamuniyat Formation, the grain-size variations within lenticular beds indicate lateral as well as vertical changes in current velocities (Fello and Turner, 2001). The presence of a monotypic *Tigillites* ichnofabric in the alluvial plain facies association may indicate the periodic establishment of paralic environmental conditions. However, present data is extremely limited and the significance and regional extent of this ichnofabric is uncertain.

The variation in thickness of the sandstone is probably a function of temporal fluctuations in flow regime and flow depth during deposition. The overall lithological characteristic patterns of sedimentation and lack of evidence of subaerial exposure are consistent with a year round rainfall, relatively high runoff, and perennial braided streams.

Shoreface to Shallow Marine Shelf Facies Association

Description: This facies association has been found only in the southwest part of the study area within the B-Field. It is restricted to the middle Member (M2) of the Mamuniyat Formation (Fig. 4). This facies association is represented by the cored interval from 1430m to 1456m in type well B2-NC115. The entire thickness is about 26m, and comprises fine- to medium-grained sandstones with black shales (Fig. 4).

The uppermost part of this facies association is dominated by hummocky cross-stratified sandstone (HCS), particularly in type section well B2-NC115 (Fig. 3). The HCS consists of fine-to medium-grained sandstone and is generally overlain by concordant laminae, with interbedded cross-bedding and ripple-cross laminated sandstone. Internally, the HCS sandstones are coarse-grained and display flat, low angle cross-bedding, which can be braced laterally for hundreds of meters within the B-Field (Herzog, 1997). Glauconitic sandstone, an important constituent of the fine-grained sandstones, is found associated with the hummocky cross-stratified package in the middle Mamuniyat Formation. The HCS sandstone beds are usually sharply based, sometimes with small-scale scours and erosion into the underlying sandstone. The position of the hummocks above erosional depressions is similar to the stratification described by Surlyk and Noe-Nygaard (1991) from Jurassic sandstones in Denmark. Furthermore, the HCS sandstones contain sparse *Cruziana* bioturbation and vertical burrows (? *Skolithos*). These burrows occur mostly as narrow tubes up to 3cm long and 2mm wide. The most characteristic burrows are *Tigillites* (Selley, 1996). The lowermost part of the middle Mamuniyat Formation (M2) is dominated by heterolithic-claystone, particularly in type section well B2-NC115. It is mainly composed of black shale (Radioactive Shale) and subordinate fine-grained sandstones with rare coarse-grained siltstone (Fello, 2001).

The black shales are intercalated with wavy, rippled, light grey to reddish-brown siltstone to fine-grained sandstone beds. The entire succession shows a general fining-upward trend and passes sharply upwards into fine-grained-sandstone, siltstone and shale. The black shales are well compacted/indurated, carbonaceous, micaceous, and fissile, and form laminae-sets 0.5cm to 3cm thick. The heterolithic-claystone forms beds, which range from 5cm to 10cm in thickness. These are tabular and sharply based, with small-scale ripple and/or parallel-laminations. Furthermore, the intense bioturbation throughout the heterolithic-claystone, has destroyed the primary structures and homogenized the sediment. The heterolithic-claystone also contains plant material preserved on lamination planes parallel to fissility (Fello and Turner, 2001).

Interpretation: The wavy-hummocky cross-stratified sandstone is interpreted as the middle/ intermediate shoreface of a nearshore zone, influenced by two alternate hydraulic regimes; traction and suspension (Ghosh, 1991). The HCS is thought to result from episodic storm wave activity and wave-generated surges. Variations of the HCS beds described herein can be explained in terms of amalgamated HCS. The various features of the HCS were produced by both oscillatory and combined oscillatory/unidirectional flows that prevailed during various stages of individual storms (Cheel and Leckie, 1992). The abundance and orientation of cross-bedding point to deposition from low flow regime traction currents. The fine grain-size, however, shows these currents to have had significantly lower velocities than those which deposited the overlying braided alluvial plain sandstones of the alluvial plain facies association. The occurrence of tabular planar cross-beds and the absence of channelling indicate that these were open flow currents not confined by channel banks.

Both vertical *Skolithos* burrows, *Cruziana* and the *Tigillites* ichnofacies, indicate that deposition occurred in a shallow marine setting. The medium-grained sandstone with occasional coarse-grained siltstones and some fine glauconitic sandstone within the wavy-hummocky cross-stratified sandstone are interpreted as storm- and wave dominated shelf sediments deposited near fair-weather wave base. The scarcity of wave-produced features suggests relatively minor wave influence between storm events (Selley, 1996). The offshore shallow marine environment is sedimentologically complex because of the number of different processes, which operate within it. Relative to other sediment, the products of these processes are poorly known because of the

physical difficulties involved in studying them and because of the present disequilibrium of continental shelves. On the NW flank of the Murzuq Basin, particularly in the B-field, the highly radioactive shales in the middle Mamuniyat Member, are mainly confined to localized palaeotopographic lows (valleys, erosional or structural depressions) or to broad areas flanking highs such as in the A and H-Fields in the northeast part of Concession NC115 (Fello, 2001).

Shallow Marine Shelf Facies Association

Description: This facies association forms the bulk of the lower Mamuniyat Formation (M3, Fig. 3). It occurs in the three oilfields of the study area, and is represented by the cored interval from 1408m to 1541m in type well A8-NC115, the cored interval from 1456m to 1528m in type well B2-NC115 and the cored interval from 1475m to 1529m in type well H4-NC115. The entire facies association comprises sandstone, characterized by a coarsening-upward trend marked by alternations of fine- to medium-grained and minor coarse-grained sandstone, and subordinate coarse-grain siltstone with claystone. The uppermost part of this facies association consists of medium- to coarse-grained, mostly sublitharenite sandstone, which locally contains small amounts of glauconite. Massive sandstones beds occur within 12m thick succession, which comprises less than 10% of the facies association. The individual beds of massive sandstone are often structureless in appearance, and generally homogeneous, occasionally exhibiting pebbly-stringers and indistinct lamination. The whole succession is referred to as the massive sandstone complex. The middle part of this facies association contains ripple cross-lamination and bioturbated sandstone beds. In the ripple cross-laminated sandstone the amount of burrows normally increases upward. The burrows are predominantly horizontal, < 1cm in diameter, and filled with light grey siltstone and/or very fine sandstone. Moreover, a few small narrow vertical burrows, < 1cm long, belonging to the *Skolithos* and *Cruziana* ichnofacies, also occur in the sandstone (1457m in type well B2-NC115). The lowermost part of the Mamuniyat Formation mainly consists of claystone deposits. This interval of claystone exhibits soft-sediment deformation structures. However, bioturbation is locally present in this succession and decreases upward concomitant with increased parallel lamination (Fello, 2001).

Interpretation: The alternation of fine-to medium-grained sandstones with coarse-grained siltstone and claystone throughout the lower Mamuniyat Formation shows that the environment was one of fluctuating current strengths. Mud, silt, and probably some of the thinnest sand laminae were deposited directly from suspension, but in the thicker sandstones bedload transport resulted in the development of bedforms, and primary sedimentary structures (Fig. 5). The absence of high angle cross-stratification in the fine-grained sandstones may be due to the narrow range of flow power, especially under condition of decreasing current strength.

Medium- to coarse-grained sandstone shows a range of storm-generated wave and current features, which indicate that the normal, quieter background sedimentation was overprinted by episodic storm conditions. Vertical changes in sedimentary structures and grain-size indicate changes in wave and current energy (Turner, 1980). The individual shale beds within the lower Mamuniyat Formation may have formed during a minor transgression and increased water depth. Ripple cross-lamination is the dominant physical sedimentary structure formed in the nearshore according to Fello (2001). The most common situation is one of ripple cross-laminated sandstone intercalated with siltstones and shales. The interlaminated sandstone and shale beds suggest variable depositional conditions and periodic higher energy currents affecting a normally quiet-water environment (Hein *et al*, 1991). The abundance of *Skolithos* and *Cruziana* within ripple cross-laminated sandstone indicate that deposition occurred in a

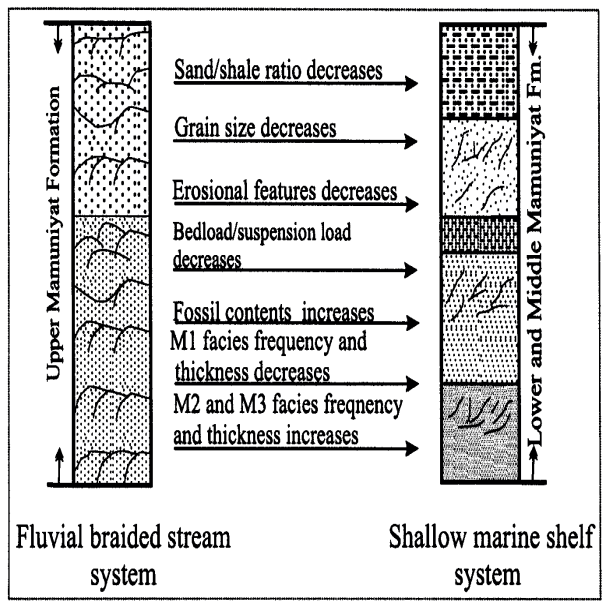


Fig. 5. General characteristics of the fluvial and shallow marine facies within the Mamuniyat Formation NC115 Concession.

shallow marine setting. As noted by Fello (2001), the abundance of fine glauconitic sandstone is also a good indication of marine setting. The occurrence of burrowing and bioturbation within wavy-hummocky cross-stratified sandstone suggests a more-protected environment, possibly periods of reduced current activity with alternations of current and biogenic structures related to their differential energy level. The contact between the bioturbated sandstone and the wavy-hummocky cross-stratified sandstone is interpreted to represent fair-weather wave base of the shallow marine environment, with the presence of bioturbation indicating a relatively low-energy environment with slow rate of sediment input (Fig 5). Claystone deposits show subtle changes in colour from darker shale to lighter sandstone/siltstone indicating periodic changes in sedimentation rates from relatively slow to fast. Furthermore, the laminae commonly have sharp bases and locally diffuse tops, features characteristic of shelf storm deposits.

DEPOSITIONAL MODEL

Depositional conditions were variable during deposition of the Upper Ordovician (Ashgillian) Mamuniyat sandstones on the northwest flank of the Murzuq Basin, particularly the increasingly continental aspect of the facies associations upwards through the succession; a factor which has left its impact on both source and reservoir potential. The basement rocks of the massif areas surrounding the southwestern part of the study area appear to have acted as a clastic source for the Mamuniyat Formation and were only intermittently reached by marine transgressive events from Palaeotethys in the northeast. Based on facies associations the Mamuniyat Formation on the NW flank of the Murzuq Basin is interpreted to have been deposited in braided fluvial and marine depositional environments (Fello and Turner, 2001).

The Mamuniyat sandstones display seaward progradation (coarsening-upward package), and basinward-thinning (clastic wedge) to the northeast, accompanied by a change from fluvial to marginal marine and neritic marine environments. Significant thickness variations reflect a strong tectonic control on sedimentation (Thomas, 1995; Fello, 2001). Laterally the Mamuniyat sandstone shows changes in grain-size, lithology and sedimentary structures. These changes are fundamentally linked to the gradient decrease in passing outward from the source terrain, with concomitant decrease in stream capacity and competence. Although the sedimentary properties change continuously away from the basin edge, the depositional setting of the Mamuniyat Formation can be divided into an upper braidplain (proximal), a lower braidplain (distal), shallow marine shelf and nearshore marine environment (Fig. 6).

CONCLUSION

1- Deposition of the Upper Ordovician (Ashgillian) Mamuniyat Formation on the NW flank of Murzuq Basin occurred within a braided alluvial plain and shallow marine setting. Repetition of fluvial and marine sandstones is attributed to interaction of the fluvial and marine environments cross a NW-SE oriented coastline in response to episodes of progradation and transgression.

2- The NC115 Concession is unlike other Palaeozoic basins in Libya in that, there is no direct evidence of a glacial influence on deposition during Upper Ordovician (Ashgillian) times (Turner, 1980; Fello, 2001).

3- Compositional data indicates that the Mamuniyat sandstones in the three oilfields, were derived from a similar parent rock, but with differences in modal composition, textural attributes and porosity of the lower, middle and upper Members of the Mamuniyat Formation. This is attributed to tectonic activity and source area uplift.

4- Facies associations suggest that these same tectonic events also influenced sediment deposition and interaction between shallow marine and fluvial depositional systems, with the

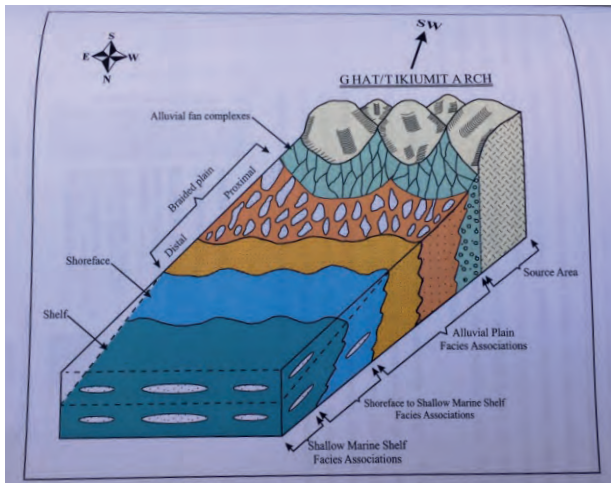


Fig. 6. General Depositional Model for Upper Ordovician, Mamuniyat Formation, NC115 Concession, NW Murzuq Basin, SW Libya.

marine shelf subjected to frequent storms (Fello and Turner, 2001). The Mamuniyat sandstones were derived from a nearby, tectonically active, granitic basement source terrain, which was most probably the uplifted Ghat/Tikiumit Arch some 150km to the SW of NC 115 Concession.

5- The Upper Ordovician Sequence (Ashgillian) Mamuniyat Formation shows an increased marine influence toward the northeast. It is dominated by proximal braided stream deposits in the southwest giving way to fluvial-marginal marine and shelf deposits in the northeast. Poor correlation within the Mamuniyat sandstone is a function of its complex stratigraphy, due mainly to a series of rapid, changes in sea-level and increases in regional tectonism (Fello, 2001).

ACKNOWLEDGEMENT

This paper is based on part of the main author Ph.D. Thesis submitted to the University of Durham, United Kingdom. Sincere appreciation is expressed to my supervisor Dr. Brian Turner for his assistance throughout the project. Dr. Fello should also like to thank the National Oil Corporation and Akakus Oil Operations (Repsol), for their financial support and encouragement throughout this study, and for permission to publish the results of this work.

REFERENCES

Bauerle, G.; Bornemann, O.; Mauthe, F. and Michalzik, D. (2000). Origin of Stylolites in Upper Permian Zechstein Anhydrite (Gorleben Salt Dome, Germany). J. Sediment. Res., **70**: 726-737.

Cheel, R. J. and Leckie, D. A. (1992). Coarse-Grained Storm Beds of the Upper Cretaceous Chungo Member (Wapiabi Formation), Southern Alberta, Canada. J. Sed. Petrol., **62**: 933-945.

Fello, N. M. (2001). Depositional Environments, Diagenesis and Reservoir Modelling of Concession NC115, Murzuq Basin, SW Libya. *Unpublished PhD thesis*, University of Durham, Durham, England: 330p.

Fello, N. M. and Turner, B. R., (2001). Provenance Analysis, Tectonism and Shifting Depositional System in the NW Part of the Murzuq Basin, Libya: Implication for Hydrocarbon Prospectivity. *21st International Association Sedimentology (IAS) meeting of Sedimentology, Abstract*, Davos, Switzerland.

Ghosh, S. K. (1991). Palaeoenvironmental Analysis of the Late Proterozoic Nagthat Formation, NV Kumaun Lesser Himalaya. *India. Sediment. Geol*., **71**: 35-45.

Hein, F. J.; Robb, G. A.; Wolberg, A. C. and Longstaffe, F. J. (1991). Facies Descriptions and Associations in Ancient Reworked (? Transgressive) Shelf Sandstones: Cambrian and Cretaceous Example. *Sedimentology*, **38**: 405-431.

Herzog, U. (1997). Technical Report for the Geological Field Trip to Ghat/Tikiumit Arch, and Qarqaf Arch. Repsol Oil Operations: *Guidebook*: 27p.

Klitzsch, E. H. (2000). The Structural Development of the Murzuq and Kufra Basins-Significance for Oil and Mineral Exploration. In: Geological Exploration in Murzuq Basin (Ed. by: M. A. Sola and D. Worsley (Eds.), Elsevier Science: 143-150.

Miall, A. D. (1996). The Geology of Fluvial Deposits, Sedimentary Facies, Basin Analysis and Petroleum Geology: 582p.

Pierobon, E. S. T. (1991). Contribution to the Stratigraphy of the Murzuq Basin, SW Libya. In: The geology of Libya (Ed. by: M. J. Salem and M. N. Belaid), Academic Press London, **V. 6**: 1767-1784.

Selley, R. C. (1996). Ancient Sedimentary Environments and Their Subsurface Diagnosis (*4th Edition*). Chapman and Hall, London: 300p.

Surlyk, F. and Noe-Nygaad. (1991). Sand Bank and Dune facies Architecture of a Wide Intracratonic Seaway: Late Jurassic-Early Cretaceous Raukev Formation, Jameson Land, East Greenland. In: *The Three-Dimensional Facies Architecture of Terrigenous Clastic Sediments, and its Implication for Hydrocarbon Discovery and Recovery* (Ed. by: A. D. Miall and N. Tyler), **V. 7**: 261-276.

Thomas, D. (1995). Geology, Murzuq Oil Development Could Boost SW Libya Prospects. *Oil and Gas Jour*., **V. 5**.: 41-46.

Turner, B. R. (1980). Palaeozoic Sedimentology of the Southeastern Part of Al Kufrah Basin, Libya: A Modal for Oil Exploration. In: *The Geology of Libya* (Ed. by: M. J. Salam and M. T. Busrewil)., **V. II**: 351-374. Academic press, London.

MICROFACIES ANALYSIS AND PALEOENVIRONMENTAL TRENDS OF THE PALEOCENE FARRUD AND MABRUK RESERVOIRS, CONCESSION 11, WEST SIRT BASIN, LIBYA

Nisreen Agha*, Amin Gheith**, Salah El-Beialy**, Haitham El-Atfy** and Waleed Shukri**

Abstract: Investigation of thin sections taken from representative core samples under the petrological microscope reveals common petrographic and mineralogical characteristics with distinct faunal assemblages allow establishing the microfacies associations and deducing the paleoenvironmental trends of the Paleocene Farrud and Mabruk rock units. Recognition of the early and post diagenetic processes particularly dolomitization and micritization as well as dissolution and precipitation of spary drusy calcite as a newmorphism process affecting the reservoir rocks is established. The microfacies trends detected from the investigation of 46 core samples from Farrud Member (Lower Paleocene) representing six wells; QQQ1-11, GG1-11, LLL1-11, RRR1-11, RRR40-11 and RRR45-11 indicate that the deposition was started within the realm of shallow supratidal and intertidal subenvironments followed by deeper environments of the shelf bays with maximum sea level during inner shelf environment where fossiliferous bioclastic packstone dominated. The microfacies associations determined in 8 core samples from two wells LLL1and RRR40 representing Mabruk Member (Upper Paleocene) indicate paleoenvironmental trends marked by sea level fluctuations accompanied with a relatively marine shelf bay conditions intervened with short-lived shallow intertidal and supratidal warm coastal sedimentation. As a result dolostone, evaporitic dismicrites and gypsiferous dolostone of supratidal characters were deposited.

Keywords: Farrud and Mabruk memebers, Paleocene, microfacies associations, diagenesis, sea level oscillation, and depositional environments.

INTRODUCTION

The Sirt Basin is the youngest sedimentary basin in Libya, one of Africa's most productive petroleum basins, and the world's 13th largest petroleum province. The vast majority of hydrocarbons recovered from Libya have been exploited in the basin, making it of a great economic importance and attracting the attention of many explorationists and petroleum companies. The Sirt Basin is separated structurally, by the Zelten platform into the west Sirt Basin (the focus of this study) and the east Sirt Basin (Hallett, 2002). The area of study is located onshore north-central Libya, west Concession 11, west of the Sirt Basin. The present paper focuses on Concession 11 (Fig. 1A), which is located in the Zallah Trough in the west of the basin (Figs. 1B and C). This concession includes many giant oil fields (Table1). In this paper, we will deal with the microfacies description of 54 core samples retrieved from Paleocene time, Sirt Basin, NW Libya. The microfacies trends detected from the investigation of 46 core samples from Farrud Member (Lower Paleocene) representing six wells; QQQ1-11, GG1-11, LLL1-11, RRR1-11, RRR40-11 and RRR45-11 and 8 core samples representing Mabruk Member (Upper Paleocene) were investigated from two wells LLL1and RRR40 (Table 2).

LITHOSTRATIGRAPHY

Stratigraphically, Abadi (2002) classified the deposits of the Sirt Basin into pre-rift (Cambro-Ordovician), syn-rift (Upper Cretaceous-Eocene) and post-rift (Oligo-Miocene).The pre-rift and post-rift deposits were dominated by clastics, whereas

*Harouge Oil Operations, Petroleum Engineering Department, Tripoli, Libya.
**Geology Department, Faculty of Science, Mansoura University, Egypt.
Corresponding author: nisreenagha9@gmail.co.com

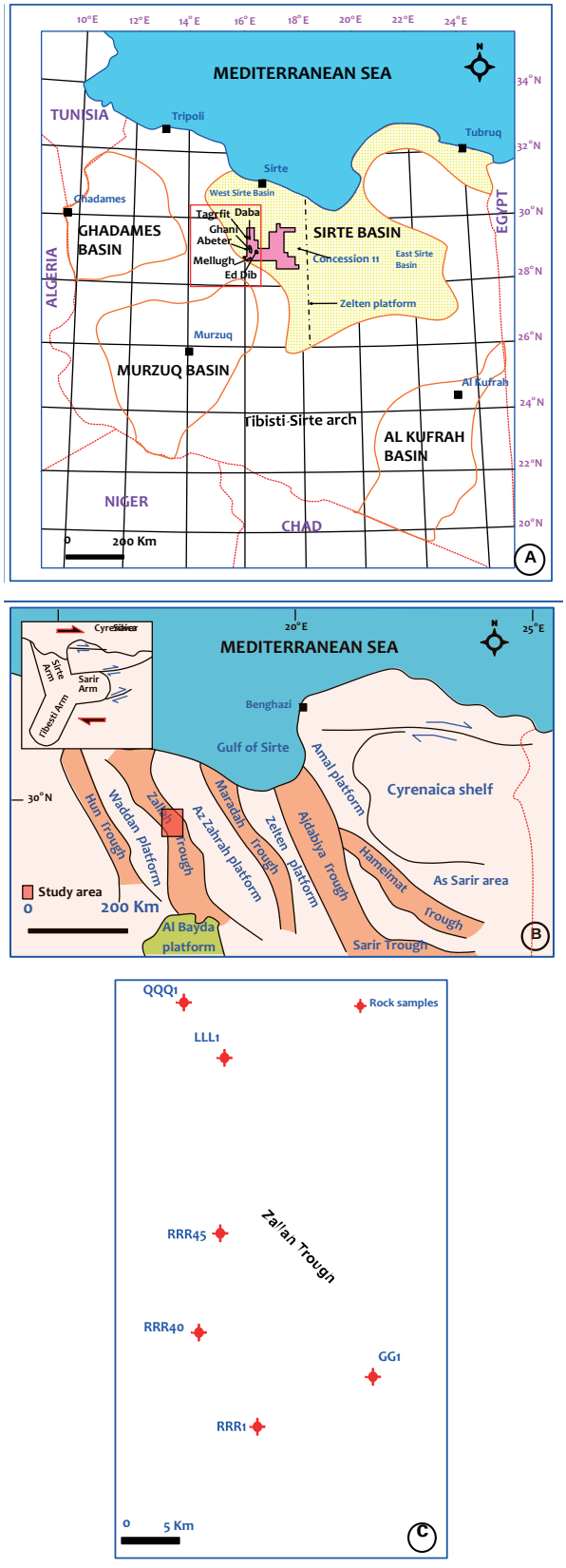


Fig. 1. A. location map of the study area in Concession 11, western Sirt Basin, northern Libya; B: the main structural elements in the Sirt Basin; Fig.1.C, the location of wells studied. Figure after Ahlbrandt (2001), Hallett (2002), and Abadi *et al* (2008).

the syn-rift (Cretaceous- Eocene) sediments were dominated by non-clastics (Fig. 2). The floor of the Sirt Basin is a major unconformity, above which a thick sequence of Late Cretaceous to Recent sediments overlies. The present study is focused on the syn-rift deposits because of the availability of samples and their economic importance as reservoir rocks in the study area. The Paleocene sediments in the Sirt Basin start at the base with the Danian Hagfa Formation. This is followed upward with the Montian Beda Formation and terminated with the Landenian Dahra, Zelten and the lower Kheir formations. The target in this paper is Beda Formation that is consists mainly of various interbedded limestone lithofacies with subordinate dolomite and calcareous shale. The Beda Formation is subdivided into three members from base to top as follow: (1) Thalith Member, (2) Farrud Member, and (3) Mabruk Member. The last two members will be considered in the present study due to their economic importance as reservoir rocks in the study area. The Farrud Member consists of a regressive carbonate depositional cycle at the base, whereas in its upper part fine grained sediments, grade upward to coarser-grained sediments. The latter were deposited in shallower and more agitated water (HOO, 2009). This is followed upward by the deposition of the Mabruk Member (HOO, 2009).

STRUCTURAL FRAMEWORK

The Sirt Basin is one of the important structural features in north Libya. The Sirt Basin is heavily fractured with major faults resulting in a number of major NW-SE trending grabens (Fig. 1B). These are from NW to SE: the Dur al Abd, Zallah, Abu Tumayam, Maradah, Ajdabiya, and Hameimat. The platforms on the intervening horst blocks are from the west to east: Waddan Platform, Az Zahrah-Al Hufrah, Al Bayda, Zelten, and Al Jahamah platforms (Abadi, 2002).

TECTONIC FRAMEWORK

The North African region was subjected to diachronous rifting with subsequent post-Mesozoic continental collision, leading to the development of basins with complex histories. A number of different tectonic domains existed, with each basin having a unique tectonic history (Carr, 2003). The Sirt Basin is a major intracratonic rift system on the north central African Plate and comprises a complex

Table 1. List of the studied wells in the giant oilfields, Concession 11, west Sirt Basin, NW Libya.

Well name	Field	Coordinates		Pay zone	Age	Total depth (ft)
		Lat	Lon			
QQQ1	Tagrfit	29° 17′ 25″	17° 23′ 52″	Farrud	Paleocene	9490
LLL1	Daba	29° 15′ 10″	17° 26′ 06″	Farrud	Paleocene	10361
RRR45	Ghani	29° 61′ 34″	17° 27′ 14.5″	Farrud	Paleocene	6300
RRR40	Ghani	28° 59′ 38.06″	17° 25′ 37.7″	Farrud	Paleocene	8300
RRR1	Ghani	28° 57′ 41.0″	17° 28′ 0.0″	Farrud	Paleocene	6160
GG1	Ed- Did	28° 59′ 34″	17° 34′ 08″	Gir (Facha)	Eocene	10989

of horsts and grabens that began to develop during the latest Jurassic-Early Cretaceous. The tectonic evolution of the Sirt Basin involved thermal arching and repeated phases of rifting that culminated in the Late Cretaceous and Paleocene to Early Eocene, which were followed by thermal subsidence from Late Eocene onwards (Abadi, 2002). The sedimentary succession of the Sirt Basin reflects its tectonic and structural evolution, which is closely related to the opening of the Atlantic Ocean and the convergence of the Tethys in Mesozoic and Tertiary times (Gras and Thusu, 1998).

The Sirt Basin area experienced stretching and down faulting during the Cretaceous. Large scale subsidence and block faulting began in the latest Jurassic/Early Cretaceous (Abugares, 2007). The faults in the Sirt Basin are reactivated during the Late Cretaceous and continuously into the Early Paleocene and Late Eocene, where volcanic activity is resumed in post-Eocene times. This is believed to have been concurrent with movement along major basement fault zones situated outside the Cretaceous rift on the western side of the Sirt Basin. The subsidence of the Sirt Basin reached a maximum during Paleocene/ Eocene time (Gumati and Kanes, 1985).

MATERIAL AND METHODS

This paper focuses on 6 wells located in Concession11, western Sirt Basin (Fig. 1 A; Table1). Fifty-four rock samples were cut for thin sections using a cut-off saw and ground flat before being impregnated with Epoxy Resin (Table 2). The samples were mounted on glass slides ground and polished using Carbide Grit until they were about 0.03mm thick. Subsequently, the sections were covered with glass cover slips. The standard polarizing microscope Olympus BX51 (E330-ADU1.2X) in plane polarized light (PPL) and between Cross Nicols (XPL) was used for thin sections petrographic analysis and photomicrographs were taken digitally. The focus was to recognize diagenetic components and cements in addition to the identification fossil contents.

A brief review of carbonate classifications was first given by Folk (1959, 1962) based upon their orthochemical and allochemical components, as well as, their textural class.

On the other hand, Dunham's (1962) used a limestone textural and compositional classification; which was modified later on (Embry and Klovan, 1971). Subsequently Flügel (1982, 2004) and Wilson (1975) summarized the standard microfacies types (26 SMF) and facies zones (9 FZ) to identify their related depositional environments. A wide usage of the microfacies analysis took place due to the great progress in oil and gas exploration.

RESULTS AND DISCUSSION

Microfacies Characteristics of Lower Paleocene Farrud (Selandian) Member

Forty-six thin sections have been examined from 6 wells including the following: QQQ1 (9 samples), LLL1 (8 samples), RRR45 (11 samples), RRR40 (5 samples), RRR1 (8 samples), and GG1 (5 samples). This member is the most important one in the studied wells because it acts as a reservoir rock in the studied concession. The investigated facies from the above member are described as follow:

Table 2. List of the studied Paleocene samples in six wells, Concession 11, west Sirt Basin, NW Libya.

Sample No.	Well name	Age	Sample type	Depth (ft)	Rock unit
1	RRR40	Paleocene (Selandian)	Core	5968	**Mabruk Member**
2	RRR40	Paleocene (Selandian)	Core	5972	**Mabruk Member**
3	RRR40	Paleocene (Selandian)	Core	5978	**Mabruk Member**
4	RRR40	Paleocene (Selandian)	Core	5989	**Mabruk Member**
5	LLL1	Paleocene (Selandian)	Core	5280	**Mabruk Member**
6	LLL1	Paleocene (Selandian)	Core	5289	**Mabruk Member**
7	LLL1	Paleocene (Selandian)	Core	5297	**Mabruk Member**
8	LLL1	Paleocene (Selandian)	Core	5298	**Mabruk Member**
9	RRR40	Paleocene (Selandian)	Core	6090	**Farrud Member**
10	RRR40	Paleocene (Selandian)	Core	6032	**Farrud Member**
11	RRR40	Paleocene (Selandian)	Core	6035	**Farrud Member**
12	RRR40	Paleocene (Selandian)	Core	6041	**Farrud Member**
13	RRR40	Paleocene (Selandian)	Core	6048	**Farrud Member**
14	RRR1	Paleocene (Selandian)	Core	5951	**Farrud Member**
15	RRR1	Paleocene (Selandian)	Core	5954	**Farrud Member**
16	RRR1	Paleocene (Selandian)	Core	5970	**Farrud Member**
17	RRR1	Paleocene (Selandian)	Core	5981	**Farrud Member**
18	RRR1	Paleocene (Selandian)	Core	5984	**Farrud Member**
19	RRR1	Paleocene (Selandian)	Core	5993	**Farrud Member**
20	RRR1	Paleocene (Selandian)	Core	5994	**Farrud Member**
21	RRR1	Paleocene (Selandian)	Core	6003	**Farrud Member**
22	RRR45	Paleocene (Selandian)	Core	5832	**Farrud Member**
23	RRR45	Paleocene (Selandian)	Core	5837	**Farrud Member**
24	RRR45	Paleocene (Selandian)	Core	5840	**Farrud Member**
25	RRR45	Paleocene (Selandian)	Core	5850	**Farrud Member**
26	RRR45	Paleocene (Selandian)	Core	5857	**Farrud Member**
27	RRR45	Paleocene (Selandian)	Core	5861	**Farrud Member**
28	RRR45	Paleocene (Selandian)	Core	5874	**Farrud Member**
29	RRR45	Paleocene (Selandian)	Core	5898	**Farrud Member**
30	RRR45	Paleocene (Selandian)	Core	5944	**Farrud Member**
31	RRR45	Paleocene (Selandian)	Core	5949	**Farrud Member**
32	RRR45	Paleocene (Selandian)	Core	5959	**Farrud Member**
33	GG1	Paleocene (Selandian)	Core	5668	**Farrud Member**
34	GG1	Paleocene (Selandian)	Core	5670	**Farrud Member**
35	GG1	Paleocene (Selandian)	Core	5713	**Farrud Member**
36	GG1	Paleocene (Selandian)	Core	5723	**Farrud Member**
37	GG1	Paleocene (Selandian)	Core	5798	**Farrud Member**
38	QQQ1	Paleocene (Selandian)	Core	5402	**Farrud Member**
39	QQQ1	Paleocene (Selandian)	Core	5404	**Farrud Member**
40	QQQ1	Paleocene (Selandian)	Core	5405	**Farrud Member**
41	QQQ1	Paleocene (Selandian)	Core	5406	**Farrud Member**
42	QQQ1	Paleocene (Selandian)	Core	5410	**Farrud Member**
43	QQQ1	Paleocene (Selandian)	Core	5418	**Farrud Member**
44	QQQ1	Paleocene (Selandian)	Core	5420	**Farrud Member**

Table 2. Cont.

45	QQQ1	Paleocene (Selandian)	Core	5422	**Farrud Member**
46	QQQ1	Paleocene (Selandian)	Core	5429	**Farrud Member**
47	LLL1	Paleocene (Selandian)	Core	5304	**Farrud Member**
48	LLL1	Paleocene (Selandian)	Core	5314	**Farrud Member**
49	LLL1	Paleocene (Selandian)	Core	5317	**Farrud Member**
50	LLL1	Paleocene (Selandian)	Core	5322	**Farrud Member**
51	LLL1	Paleocene (Selandian)	Core	5326	**Farrud Member**
52	LLL1	Paleocene (Selandian)	Core	5331	**Farrud Member**
53	LLL1	Paleocene (Selandian)	Core	5335	**Farrud Member**
54	LLL1	Paleocene (Selandian)	Core	5337	**Farrud Member**

Dolostone association/Dolomite wackestone (Figs. 3A & B, samples 46, 45, 42, 39, QQQ1 well): This microfacies shows medium-sized, equigranular, euhedral to subhedral dolomite crystals as a common groundmass. Many dolomite crystals are stained with dark brown ferruginous matter. The abundance of uni-sized homogeneous rhomboid dolomite crystals suggests that deposition took place within arid tidal flats (Selley, 1980; Reading, 1996). This microfacies resembles SMF23 and FZ9 (Wilson, 1975; Flügel, 2004).

Anhydrite dolostone association/Anhydrite dolomite wackestone (Figs. 3C & D, samples 44, 43, 41, QQQ1 well): It shows medium-sized, mosaic ehudral dolomite crystals as a groundmass. No allochemes present. Most pore spaces and fissures are filled with anhydrite crystal laths with radiating habit, as it is distinguished from gypsum by its higher relief and stronger birefringence. This association suggests deposition within arid, evaporitic supratidal setting. The presence of anhydrite facies indicates super saturated saline-rich sources together with high temperature conditions (Adams *et al*, 1984). It resembles SMF23 and FZ9 (Wilson, 1975; Flügel, 2004).

Evaporite pelloidal dolostone association/ Evaporite dolomitized wackstone (Fig. 3E, sample 40, QQQ1well): Fine to medium-grained rhombic recrystallized dolomite crystals, and abundant pelloidal allochemes composed of micrite lacking any recognizable internal structure. The micritic pellets sometimes show recrystallization of mosaic rhombic dolomite in the internal structure. Some laths of anhydrite and gypsum filling a cavity, occupy fissures and voids as a new diagenetic alteration. The abundance of uni-sized homogeneous rhomboid dolomite crystals indicates deposition within evaporitic, tidal flats and/or supratidal setting. The high salinity within the lagoon allowed no fauna to flourish. This association is similar to SMF23 and FZ8 (Wilson, 1975; Flügel, 2004).

Evaporite (anhydrite) association (Fig. 3F sample 38, QQQ1 well): Recrystallized coarse granular mosaic and large fibrous crystals of anhydrite arranged in parallel orientation. The evaporite facies suggests close nearness to super-saturated saline-rich sources of high intertidal-supratidal flats, together with high temperature conditions (Kinsman, 1969).

Micritized biodolomite association/Biodolomite wackstone (Fig. 3G, sample 37, GG1 well): Compact mosaic anhedral crystals of dolomite embedded in a micritic matrix. The crystal fabric is tightly interlocked with some rhombic-shaped dolomite. Poorly-preserved bivalves and foraminifera are recorded and replaced by mosaic calcite. Ferrugineous materials are seen as clouds staining many parts of dolomite and surrounding the micritized fossils. Deposition within shallow restricted supratidal marine setting is suggested for the present association. This facies is in accordance with SMF23 and FZ9 (Wilson, 1975; Flügel, 2004).

Ostracodal biomicrite association/Ostracodal wackestone (Fig. 3H, sample 36, GG1 well): Turbid micrite with argillaceous and abundant ferruginous materials. The allochems are generally few, represented by different skeletal debris, complete ostracodal shells, few bivalvs and ill-defined foraminiferal chambers are floating in the micritic matrix. Most of the internal cavities of the shells are entirely recrystallized into coarse crystalline mosaic calcite. Deposition prevailed in a relatively shallow marine condition, sluggish

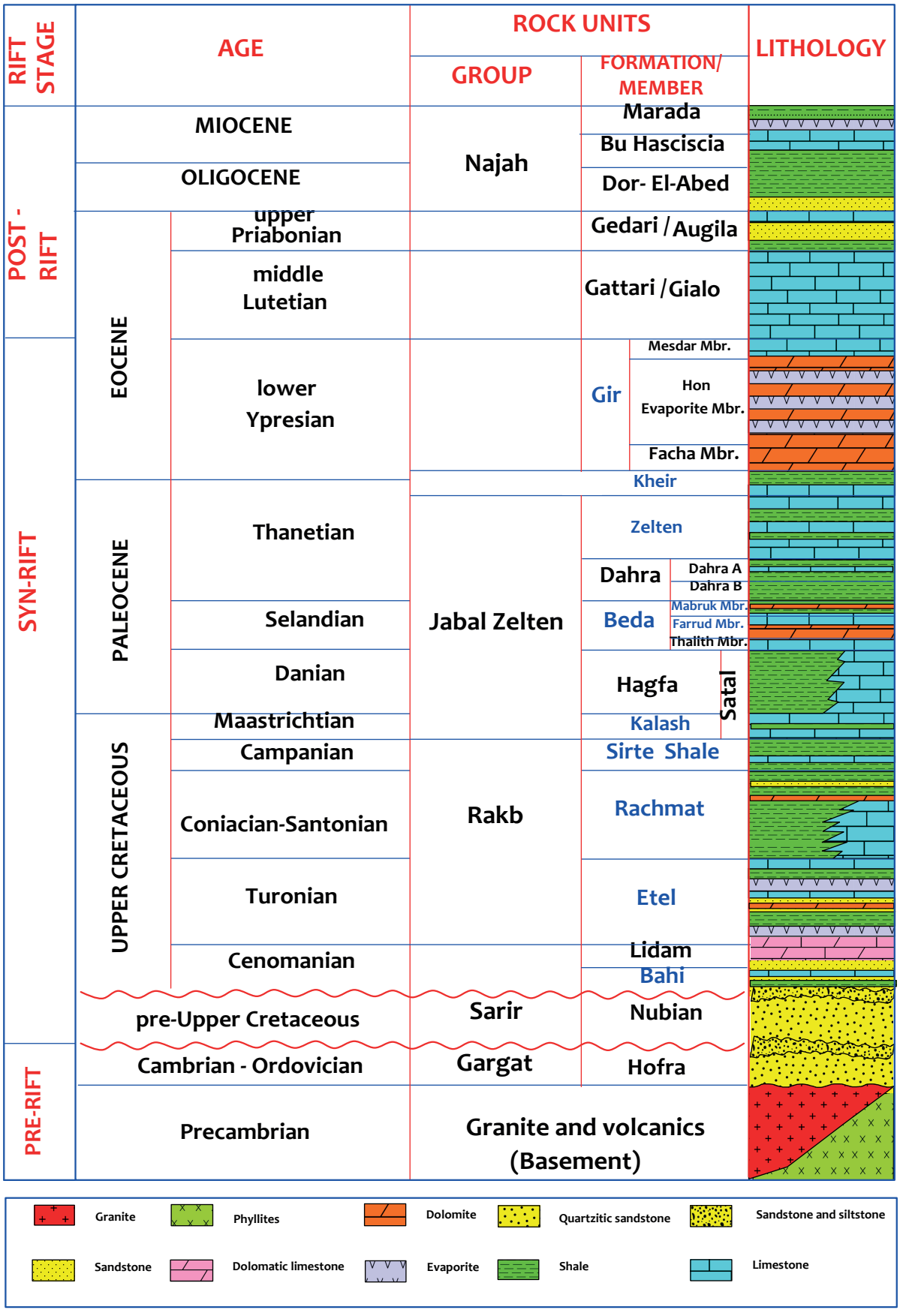


Fig. 2. Generalized lithostratigraphic column for the Concession 11 area, west Sirt Basin, Libya (modified after Barr and Weegar, 1972; Hallett, 2002).

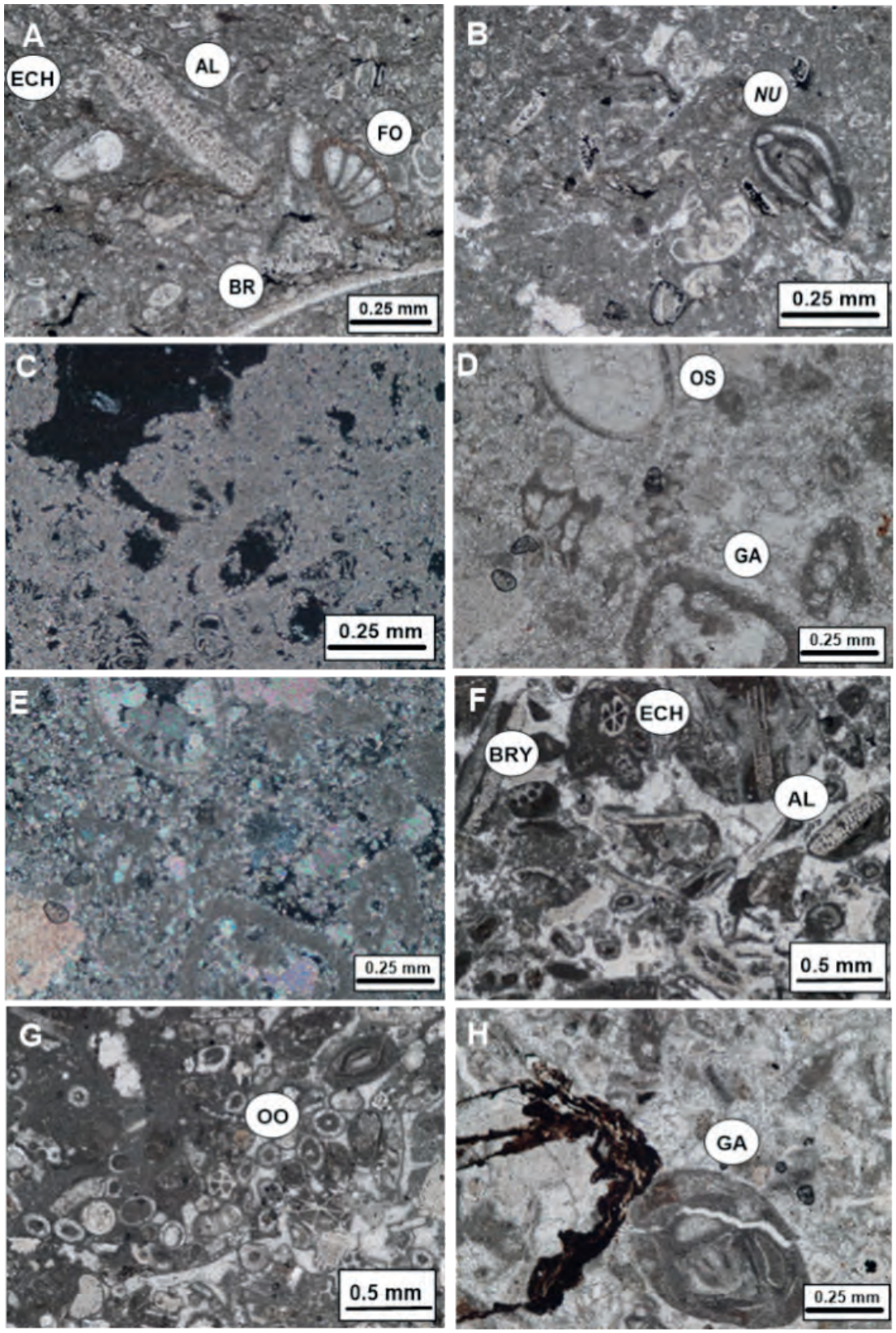


Fig. 3. The Paleocene (Selandian) Farrud Member microfacies; A-B, Dolomite wackestone association, Farrud Member, Paleocene (Selandian), samples 46, 5429 ft, 45, 5422 ft, 42, 5410 ft and 39, 5404 ft, QQQ1 well, XPL. C-D, Anhydrite dolomite wackstone, Farrud Member, samples 44 (5420 ft), 43 (5418 ft) and 41 (5406 ft), QQQ1 well, XPL. E, Evaporite dolomitized wackstone association, sample 40 (5404 ft), QQQ1 well, XPL. F, Evaporite association, sample 38 (5402 ft), QQQ1 well, XPL. G, Micritized biodolomite association, sample 37 (5798 ft), GG1 well, XPL. H, Ostracodal wackestone association. Ostracod shells (OS), sample 36 (5723 ft), GG1 well, XPL.

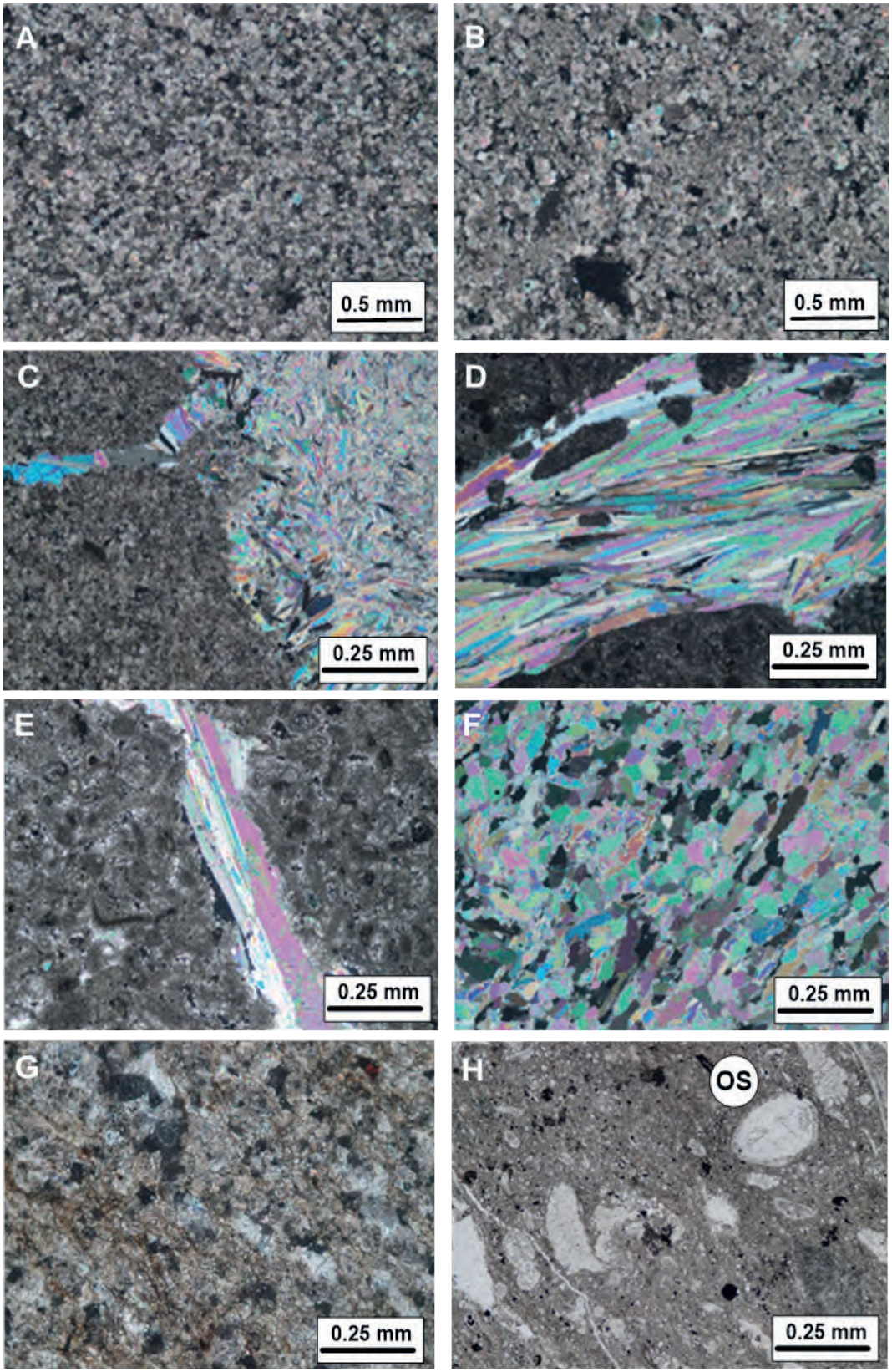


Fig. 4. The Paleocene (Selandian) Farrud Member microfacies; A-B, Foraminiferal bioclastic wackestone association. Foraminiferal (FO), algae (AL), echinoid (ECH), brachiopod (BR) and Nummulites (NU), sample 35 (5713 ft), GG1 well, PPL and XPL. C, Foraminiferal lime mud association, sample 34 (5670 ft), GG1 well, XPL. D-E, Ostracodal foraminiferal dolomitized packstone association. Gastropod (GA) and ostracod shells (OS), sample 33 (5668 ft), GG1 well, PPL and XPL. F-H, Echinoidal oolitic foraminiferal dolomicrite association. Oolite (OO), echinoid spines (ECH), algae (AL), gastropod (GA), bivalve (BI), brachiopod (BR) and bryozoan (BRY), samples 54-50 (5337-5322 ft), LLL1 well, PPL and XPL.

energetic conditions, with fluctuating sea level due to the prevalence of micrite. This microfacies is similar to SMF8 and FZ7 (Wilson, 1975; Flügel, 2004).

Foraminiferal biomicrite association/ Foraminiferal wackestone (Figs. 4A & B, sample 35, GG1 well): Abundant allochems and ill-defined planktonic and benthic foraminiferal chambers are loosely packed. Pelecypod fragments and foliated brachiopods, algae, gastropods commonly float within lime mud micritic matrix. Most allochems boundaries are admixed within the rock matrix assuming a partial micritization. Diagenesis is recorded by recrystallization of mosaic coarse grained calcite within the internal structure of the fossils and inside the empty patches. Deposition took place within relatively quiet, less energetic conditions most likely below wave base conditions (quiet inner-shelf marine conditions). It resemnbles SMF9 and FZ7 (Wilson, 1975; Flügel, 2004).

Foraminiferal biomicrite association/ Foraminiferal lime-mud (Fig. 4C, sample 34, GG1 well): Fine-grained crystalline micrite is the major constituent. Allochems are represented by ill-defined scattered foraminiferal tests. The boundaries of allochems are deformed and admixed within the rock matrix. Diagenesis took place due to micritization. Deposition prevailed in relatively quiet, less energetic conditions below wave base (quiet inner-shelf marine conditions). This facies is similar to SMF9 and FZ7 (Wilson, 1975; Flügel, 2004).

Ostracodal foraminiferal dolostone association/ Ostracodal, foraminiferal packstone (Figs. 4D & E, sample 33, GG1 well): Coarse-grained rhombic dolomite is surrounded by remains of fine-grained crystalline micrite as a major constituent. Allochems represented by complete ostracodal shells, ill-defined foraminiferal chambers, gastropods and carbonate fragment. The internal cavity of the shell is entirely recrystallized into coarse crystalline mosaic calcite. Diagenesis is evidenced by micritization process, well developed mosaic calcite crystals seen inside fossil cavities, indicate active recrystallization. Dolomitization is recorded by the development of dolomite surrounding the allochems at the expense of lime due to the high Mg-rich marine pore-water invading the rock. Deposition took place within relatively intertidal flats under marked shallow marine, less energetic conditions with fluctuating sea level. This facies is similar to SMF12 and FZ6.

Echinoidal oolitic foraminiferal dolomicrite association/Echinoidal, foraminiferal packstone (Figs. 4F-H and Figs. 5A-C, samples 54-50, LLL1 well): Coarse interlocking mosaic dolomite and micrite matrix. Abundant allochems represented by echinoid spines, concentric oolites, pelloids, bryozoans, algae, foraminifera, bivalves, gastropods, brachiopods and shell fragments, cemented by sparry mosaic calcite and/or crystallized dolomites. Diagenesis is caused by the dissolution of micritic matrix and large carbonate fragments replaced by coarse- grained sparry calcite and well developed dolomite. Deposition prevailed within warm, marine setting of fluctuating sea level. An intertidal foreshore lagoonal setting is suggested for this association, which correlates SMF 12 and FZ 6 (Wilson, 1975; Flügel, 2004).

Gypsiferous dolostone association/Gypsum dolomite wackestone (Figs. 5D & E, samples 49-48, LLL1 well): Uni-sized medium-grained mosaic euhedral dolomite crystals. Allochems are rare represented by ill-defined scattered bivalves floating within the dolomitic groundmass. Pale yellow colored patches and irregular lamina of gypsum are seen. The abundance of uni-sized homogeneous rhomboid dolomite crystals suggests deposition within arid, evaporitic tidal flats to supratidal setting. The occurrence of gypsum indicates close nearness to super-saturated saline-rich source together with high temperature conditions. This facies resembles SMF23 and FZ9 (Wilson, 1975; Flügel , 2004).

Foraminiferal dolomitized micrite association/ Foraminiferal dolomitic packstone (Fig. 5F, sample 47, LLL1 well): Fine to coarse dolomitic matrix with abundant compact allochems. The allochems are represented by foraminifera, brachiopods, pelloids and oolites cemented with developed euhedral fine to medium-grained recrystallized dolomite. Some of allochems are totally dissolved and replaced by recrystallized mosaic sparry calcite. The dolomitization is at the expense of micrite due to Mg-rich solution invading the pore spaces of the rock. Deposition took place within a relatively quiet and less energetic lagoonal setting. This facies resembles SMF9 and FZ6.

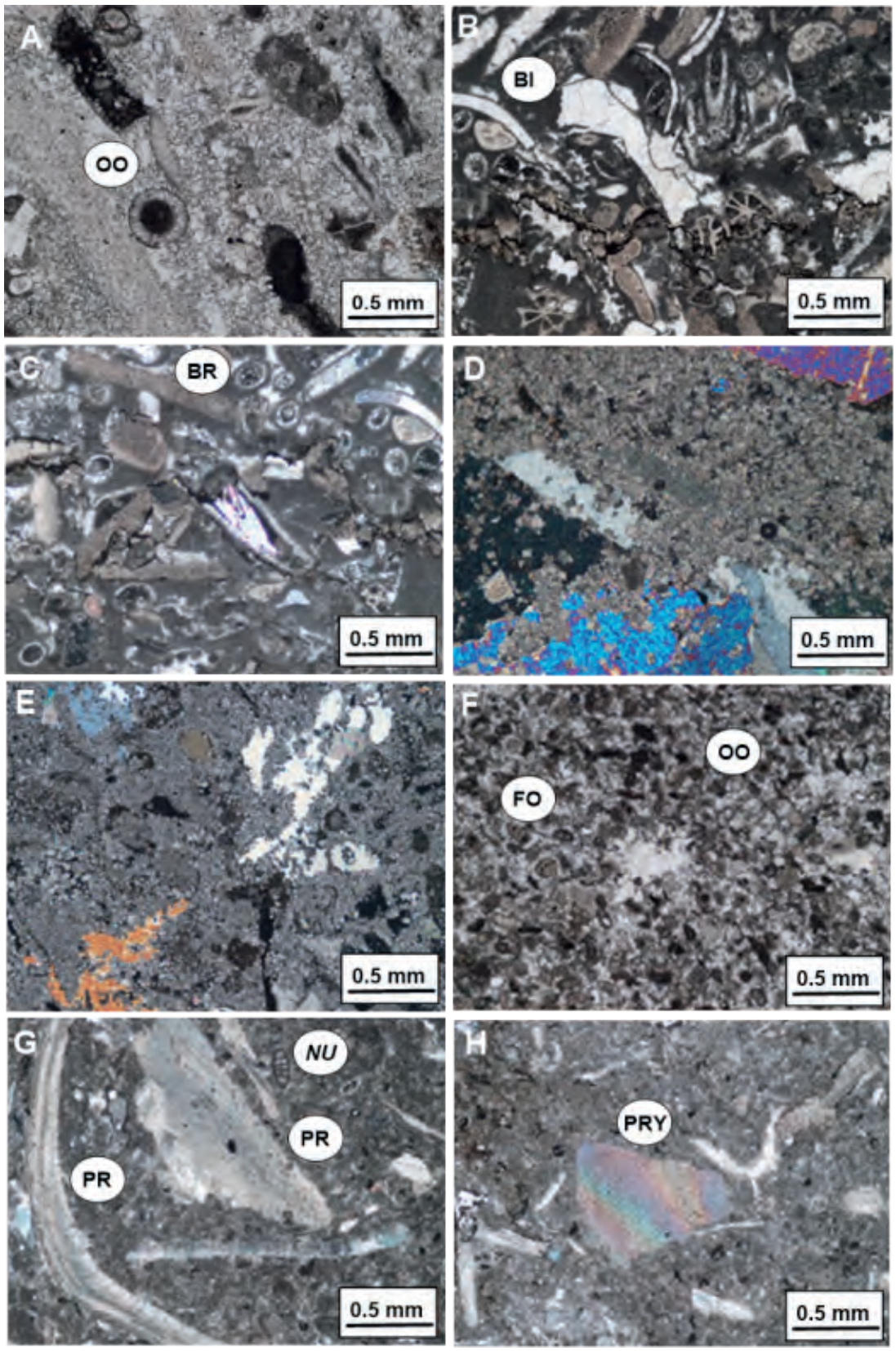


Fig. 5. The Paleocene (Selandian) Farrud Member microfacies; A-C, Echinoidal oolitic foraminiferal dolomicrite association. Oolite (OO), echinoid spines (ECH), algae (AL), gastropod (GA), bivalve (BI), brachiopod (BR) and bryozoan (BRY), samples 54-50 (5337-5322 ft), LLL1 well, PPL and XPL. D-E, Gypsum dolomite wackestone association, samples 49 (5317 ft) and 48 (5314 ft), LLL1 well, XPL. F, Foraminiferal dolomite packestone association. Foraminifera (FO) and oolite (OO), sample 47 (5304 ft), LLL1 well, PPL. G-H, Foraminiferal brachiopod biomicrite association. Nummulites (NU), bivalve (BI), brachiopod (BR) and bryozoan (BRY), sample 21, 6003 ft, RRR1 well, XPL.

Foraminiferal brachiopod biomicrite association/ Foraminiferal bioclasts floatstone (Figs. 5G & H and Fig. 6A, sample 21; Fig. 6B-C, samples 20-18, RRR1 well): Fine-grained cryptocrystalline micritic matrix enriched with allochems of different varieties. The allochems are represented by different foraminiferal tests (miliolids and nummulites), various debris of bivalves and gastropods, oyster and pelecypod fragments. Other allochems include calcareous algae (Halimeda), bryozoa and ostracodal valves, which float in the micritic matrix. The oysters have foliated internal structure with thick shells. Diagenesis is seen due to micritization and dissolution of quartz boundaries replaced by micrite. Sometimes recrystallization of coarse sparry calcite is well developed. Deposition prevailed within relatively quiet, an inner shelf, shallow marine conditions and diminishing energy below wave base level. This facies resembles SMF9 and FZ7 (Wilson, 1975; Flügel, 2004).

Gypsiferous micrite association/Gypsum lime-mudstone (Figs. 6D & E, sample 18, RRR1 well): Lime-mud (micrite) groundmass of very fine cryptocrystalline carbonate materials. Allochems not present. Faint pale yellow colored patches and irregular laminae of gypsum occupying a large area within the matrix. Deposition prevailed in less energetic marine conditions due to dominance of micrite. However, the development of gypsum at the expense of lime-mud indicates saturated saline solution. This occurs under fluctuating sea level conditions into intertidal foreshore lagoonal setting. This association matches SMF23 and FZ8 (Wilson, 1975; Flügel, 2004).

Echinoid oobiosparite association/Oolitic biosparite packstone (Figs. 6F & G, samples 17-16, RRR1 well): Different varieties of allochems are cemented with drusy mosaic equant calcite crystals. Allochems include abundant concentric oolites, echinoids, algae, micrite peloids and foraminifera (e.g. nummulites and miliolids). Most allochems show micritic envelope and the internal cavity of the shells is entirely recrystallized into mosaic calcite.Deposition took place within relatively shallow agitated marine conditions in the outer shelf bays. However, oolites originated within shoals near outer platform margins.This facies is equivalent to SMF15 and FZ8 (Wilson, 1975; Flügel, 2004).

Foraminiferal quartz biomicrite association/ Foraminifertal quartz wackestone (Fig. 6H and Fig. 7A, sample 15, RRR1 well): Dark brown cryptocrystalline argillaceous micritic matrix with few allochems representedby ill-defined foraminifera. Nummulites and miliolids can be seen, although most fossils are altered and replaced by crystalline mosaic quartz. Some patches of the micritic matrix are dissolved and replaced by drusy megaquartz, indicative of slicicfication as a late stage diagenesis. Deposition prevailed within shallow marine conditions under mid to outer shelf setting. This association matches SMF9 and FZ7 (Wilson, 1975; Flügel, 2004).

Evaporite association (Fig. 7B, sample 14, RRR1 well): Medium to fine-grained gypsum and anhydrite laths are arranged in foliated layers and random aggregate structures. Recrystallization of anhydrites shows equant and lath crystals producing coarse granular mosaic and large fibrous crystals. This indicates a direct precipitation of sulphate from water in a relatively tidal flat of diminishing energy conditions. The evaporite facies suggests close nearness to super-saturated saline-rich sources of high intertidal-supratidal flats, together with high temperature conditions (Kinsman, 1969).

Pelagic foraminiferal biomicrite association/ Foraminiferal packstone (Fig. 7C, sample 13, RRR40 well): Fine cryptocrystalline micrite mixed with clay material as matrix. Allochems are grain-supported, represented by ill-defined scattered foraminiferal chambers with deformed boundaries and admixed within the micritic matrix. Allochems consist of dominant microscopic foraminiferal tests, echinoids, ostracods, algae, bryozoa and bivalve fragments. Iron patches and pellets are scattered in the matrix. Most fissures are filled with sparry calcite cement. This kind of microfacies suggests deposition in quiet less energetic marine conditions due to dominance of micrite. Mid to outer shelf marine setting is suggested for this facies. This association matches SMF3 and FZ1 (Wilson, 1975; Flügel, 2004).

Brachipods bivalves biomicrite association/ Brachipod bivalves packstone (Figs. 7D & E, sample 12, RRR40 well): Cryptocrystalline micritic matrix enriched with different varieties of allochems. The allochems include foraminiferal

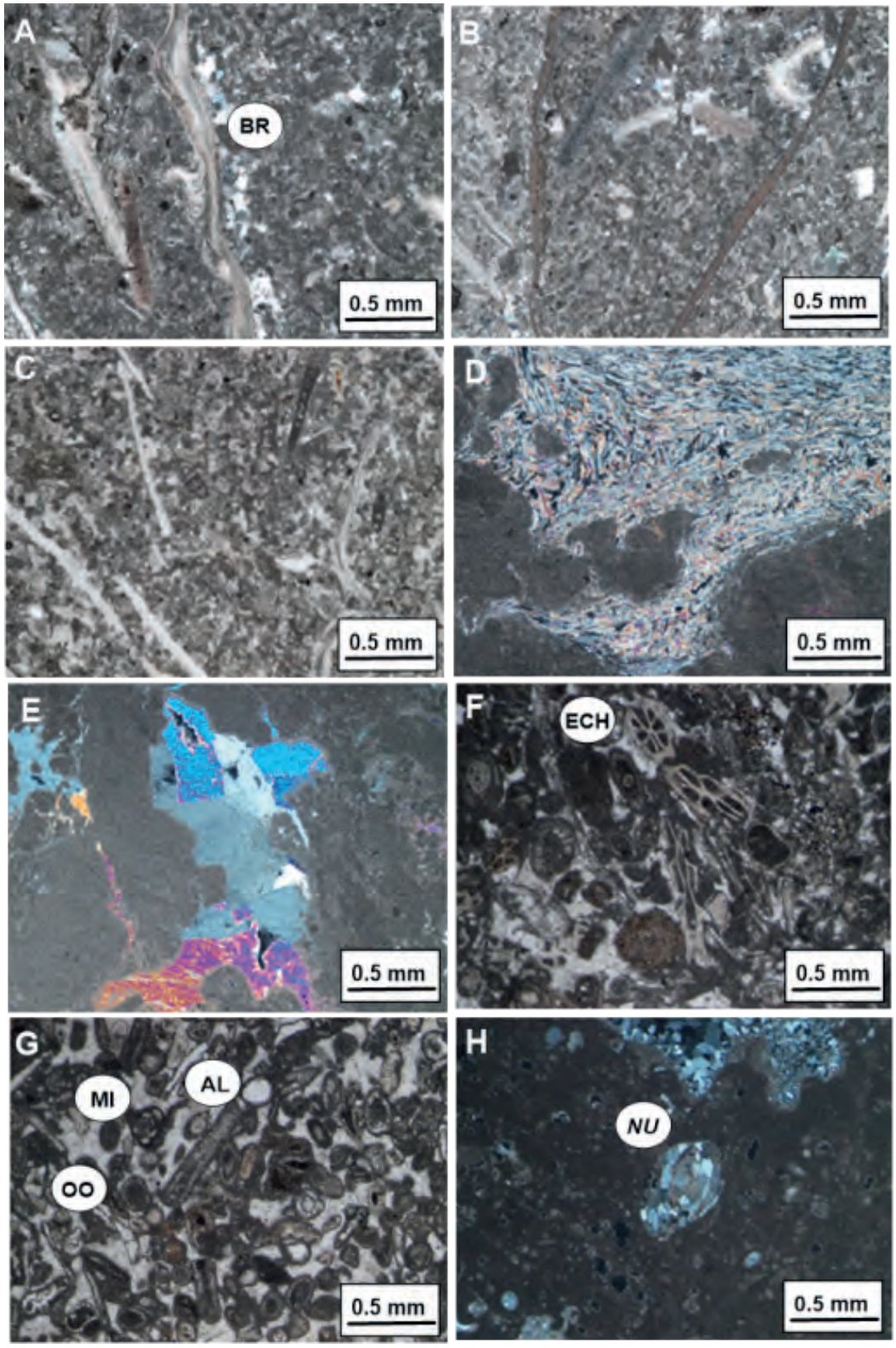


Fig. 6. The Paleocene (Selandian) Farrud Member microfacies; A, Foraminiferal brachiopod biomicrite association. brachiopod (BR), sample 21 (6003 ft), RRR1 well, XPL. B-C, Photomicrographs in PPL showing foraminiferal brachiopod biomicrite association/ foraminiferal bioclasts floatstone, sample 20 (5994 ft) and sample 19 (5993 ft), RRR1 well, PPL. D-E, Gypsiferous micrite association, sample 18 (5984 ft), RRR1 well, XPL. F-G, Echinoid oobiosparte association/oolitic biosparite packstone. Oolite (OO), echinoid (ECH), algae (AL) and miliolid (MI), sample 17 (5981 ft); sample 16 (5970 ft), RRR1 well, XPL. H, Foraminiferal quartz biomicrite association. Nummulites (NU), sample 15 (5954 ft), RRR1 well, XPL.

tests assigned to miliolids, nummulites, and pelagic foraminifera. Other structures include brachiopod fragments, long straight bivalve and gastropod shell fragments, oysters with foliated internal structure, pelecypod fragments, algae (halimeda), brayozoa and ostracodal valves. Deposition took place within relatively quiet, less energetic shallow marine conditions below wave base level and an inner shelf marine setting is suggested. This facies resembles SMF9 and FZ7 (Wilson, 1975; Flügel, 2004) respectively.

Oolitic bivalve algal foraminiferal biomicrite association/Oolitic bivalve foraminiferal packstone (Figs. 7F-H and Fig. 8A, samples 10-11, RRR40 well): Highly fossiliferous, tightly packed bioclasts of sand and pebbly-sized skeletal and non-skeletal debris are admixed in compacted micritic matrix. The allochems encounter concentric and radial oolites, bivalves, algae, foraminifera (nummulites and miliolids), echinoids, bryozoa, brachiopopds and oysters. Dissolution of some patches of the micrite was replaced by coarse-grained mosaic calcite as a common diagenesis. Deposition prevailed in relatively less agitated marine conditions within mid-outer shelf marine setting below wave base as this facies corresponds to SMF12 and FZ6 (Wilson, 1975; Flügel, 2004).

Argillaceous biomicrite association/Brachipod bivalves lime-mudstone (Figs. 8B & C, sample 9, RRR40 well): Cryptocrystalline argillaceous micritic matrix compacted and laminated. The allochems include bivalves, brachiopods, foraminifera, gastropod fragments and algae. Deposition took place in relatively quiet less energetic marine conditions under fluctuating sea level, as evidenced by dominance of micrite/ shale intercalation. Shallow inner shelf bayment is suggested for this facies. This facies resembles SMF9 and FZ7.

Pelagic foramineral argillaceous biomicrite association/Pelagic foraminiferal lime-mudstone (Figs. 8D-F, sample 32, RRR45 well; Fig. 9E, sample 26, RRR45 well): Fine-grained cryptocrystalline argillaceous micritic matrix slightly laminated with scattered poorly-preserved foraminiferal tests, strongly micritzed and admixed with the matrix. Deposition took place in quiet less energetic marine conditions due to dominance of micrite. Mid to outer shelf marine setting is suggested for this facies. This association is concomittant with SMF3 and FZ1 (Wilson, 1975; Flügel, 2004).

Fossiliferous biomicrite association/Foraminiferal bivalves packstone (Figs. 8F-H and Fig. 9A, samples 31-29, RRR45 well; Fig. 9B & C, sample 28, RRR45 well): Argillaceous micritic matrix is enriched in allochems of sand and pebbly sized skeletal and non-skeletal debris. Allochems include foraminifera (nummulites and miliolids), algae, bryozoa, pelecypods, oolites, echinoids, oysters, brachiopods, concentric oolites and gastropods embedded in a carbonate mud matrix. Diagenesis is due to crystallization of coarse-grained sparry mosaic calcite in some patches at the expense of micrite matrix. Deposition might have taken place within less energetic nearness to mid-outer shelf marine setting. This association is close to SMF12 and FZ6 (Wilson, 1975; Flügel, 2004).

Dolomitized dismicrite association/Dolomitized wackestone (Fig. 9D-F, samples 25 & 27, RRR45 well): Petrogtaphically, the rock is entirely composed of fine-grained, non-ferroan subhedral to anhedral dolomite crystals surrounded by micrite. The most common diagenetic event is the development of dolomite at the expense of micrite. Dolomitization took place under Mg-rich marine water that invaded the original dismicrite. Deposition indicates an intertidal foreshore lagoonal setting. This association is concordant with SMF25 and FZ8 (Wilson, 1975; Flügel, 2004).

Gypsiferous dismicrite association/Gypsiferous lime-mudstone (Fig. 9G, sample 24, RRR45 well): This association is entirely composed of framework of fine to very fine-grained micritic matrix. No allochems are seen, however, some fossils show badly preserved. Large area was attacked by sulphate solution that crystallized as irregular, faint pale yellow crystal laths of gypsum which occupy large area within the association. Deposition prevailed in intertidal to lagoonal conditions. This association resembles SMF23 and FZ8 (Wilson, 1975; Flügel, 2004).

Gastropods dolomitized micrite association/ Gastropods dolomitic lime-mudstone (Fig. 9H, sample 23, RRR45 well): Cryptocrystalline micritic matrix with few allochems is formed of ill-defined gastropods, foraminiferal tests and carbonate

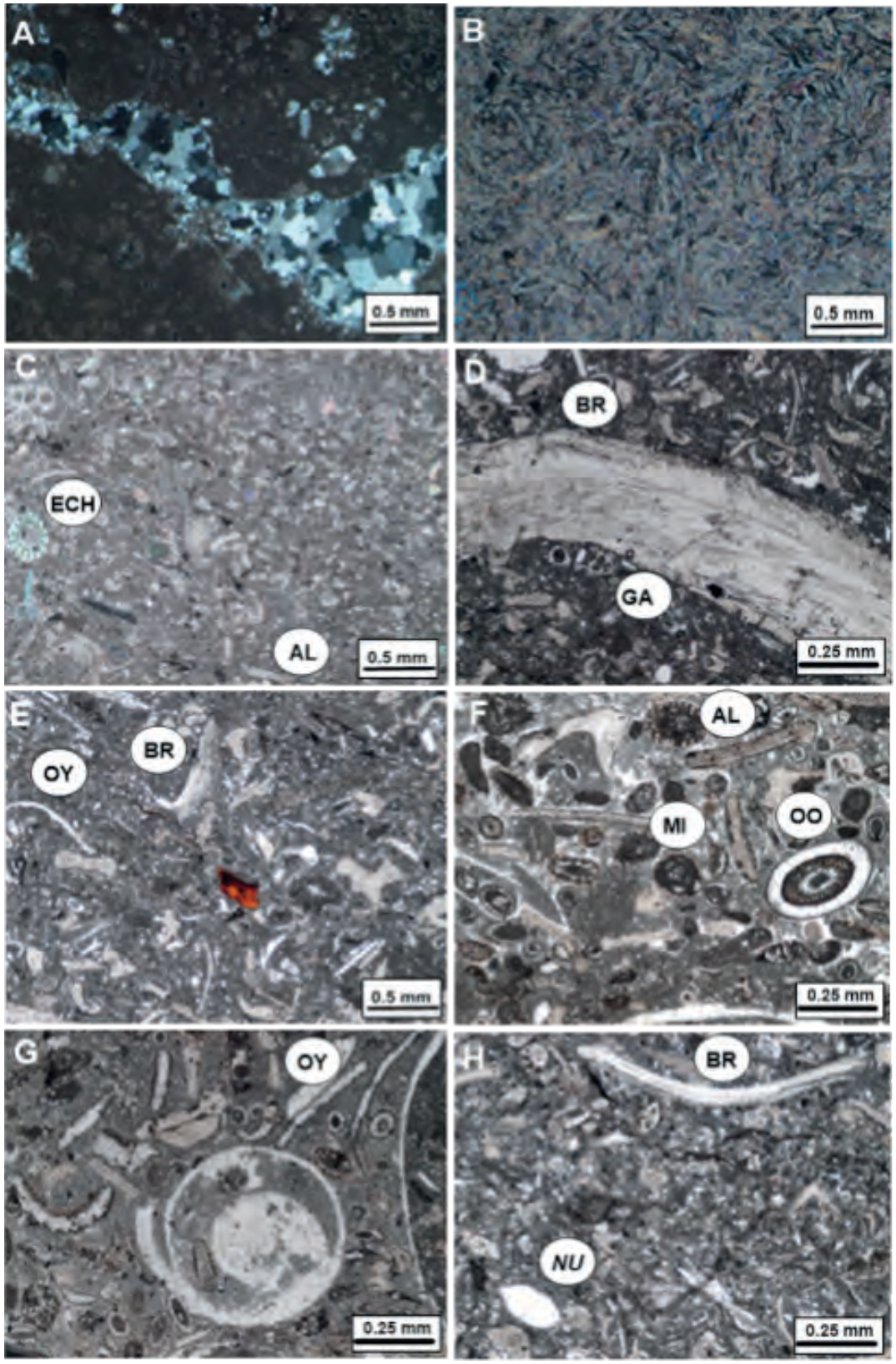


Fig. 7. The Paleocene (Selandian) Farrud Member microfacies; A, Foraminiferal quartz biomicrite association, sample 15 (5954 ft), RRR1 well, XPL. B, Evaporite association, sample 14 (5951 ft), RRR1 well, XPL. C, Pelagic foraminiferal biomicrite association. Echinoid (ECH) and algae (AL), sample 13 (6048 ft), RRR40 well, PPL. D-E, Brachiopods bivalves biomicrite association. Brachiopod (BR), oyster (OY) and gastropod (GA), sample 12 (6041 ft), RRR40 well, PPL. F-H, and Fig. 8. A, Oolitic bivalve algal foraminiferal biomicrite association. Oolite (OO), algae (AL), miliolid (MI), nummulites (NU), brachiopopd (BR) and oyster (OY), samples 11 (6035 ft); sample 10 (6032 ft), RRR40 well, PPL and XPL.

fragments cemented with dolomites. The internal cavity of the shells shows a partial micritization replaced by fine crystallized subhedral dolomite crystals. Deposition took place within warm, saline saturated marine setting. An intertidal foreshore lagoonal setting connected to the open sea is suggested. This association is similar to SMF23 and FZ9 (Wilson, 1975; Flügel, 2004).

Evaporite assiciation (Fig. 10A, sample 22, RRR45 well): Fine crystalline fibrous crystals of faint pale yellow colored anhydrite and gypsum are arranged in foliated aggregates and/or irregular laminas. Deposition took place within intertidal-flat to supratidal setting close to super saturated saline-rich sources associated with high temperature conditions.

Microfacies Characteristics of Lower Paleocene Mabruk (Selandian) Member

Eight thin sections have been examined from the Middle Paleocene Mabruk Member in two wells, namely LLL1 (4 samples) and RRR40 (4 samples). These thin sections can be discussed herein as follow:

Foraminiferal pelloidal biomicrite association/ Foraminiferal pellets wackestone (Fig. 10B, sample 4, RRR40 well): The thin section is composed of microcrystalline micrite as a framework matrix. Allochems are different and dominated by foraminifera chambers floating within the matrix. The allochems strongly admixed into the rock matrix assuming partial micritzation process accompanying the burial. The assimilated allochem boundaries strongly admixed into the rock matrix assume partial micritization process. Rare iron pockets and a few pellets are seen scattered in the association.

Dismicrite association/Lime-mud (Fig. 10C & D, samples 2-3, RRR40 well): The groundmass is made up of lime-mud homogeneous micrite. No allochems are observed. The rock has been subjected to partial sparitization. Deposition prevailed in relatively quiet less agitated marine conditions (tidal flats to inner-shelf lagoon setting) due to dominance of micrite.

Gypsiferous quartz arenite association (Fig. 10E & F, sample 1, RRR40 well): A groundmass is almost entirely composed of crystallized medium to fine-grained anhedral quartz crystals, partially and sometimes completely replaced by secondary sulphate minerals (anhydrite and gypsum). Deposition prevailed within tidal flats invaded by freshwater circulation.

Gypsiferous dolomitized biomicrite association/ Gypsum dolomite wackestone (Figs. 10G-J, samples 6-8, LLL1 well): Medium to coarse-grained crystalline mosaic dolomite crystals replaced most of the biomicrite marix. Ill-defined allochems include foraminiferal tests, echinoids and algae. The groundmass is attacked by a sulphate solution, where fine crystalline fibrous gypsum and anhydrite laths partially replaced dolomite and filling the intergranular molidic porosity. Dolomitization and sulphanization are the most significant diagenetic processes that affected the rock. The abundance of rhomboid dolomite crystals suggests deposition within arid, evaporitic tidal flats, or supratidal setting. This facies matches SMF23 and FZ9 (Wilson, 1975; Flügel, 2004).

Dolostone association/Dolomite floatstone (Fig. 10K, sample 5, LLL1well): A groundmass consists of coarse-grained, crystalline, well developed euhedral stained dolomite crystals. Irregular patches of faint grey gypsum are also observed. The abundance of uni-sized homogeneous rhomboid dolomite crystals suggests primary deposition from shallow restricted supratidal marine setting under high temperature. This association resembles SMF25 and FZ9 (Wilson, 1975; Flügel, 2004).

CONCLUSIONS

Fifty four thin sections were investigated from the two members Farrud (Lower Paleocene) and Mabruk (Upper Paleocene) in six wells; QQQ1, GG1, LLL1, RRR1, RRR40 and RRR45. Sediments of this member consist mainly of limestone and/ or mixed dolomite, evaporite, limestone and argillaceous beds. The microfacies trends detected from the investigation of 46 core samples from Farrud Member indicate that the deposition was started within the realm of shallow supratidal and intertidal subenvironments where dolostone and evaporite facies deposited in the Farrud Member of wells QQQ1, LLL1 and RRR45. While deposition in wells; GG1, RRR1 and RRR40 exhibits different depositional trend where foraminiferal, brachiopods and bivalves biomicrite of different textures vary from lim-mudstone to wackestone and packstone associations. They indicate deposition

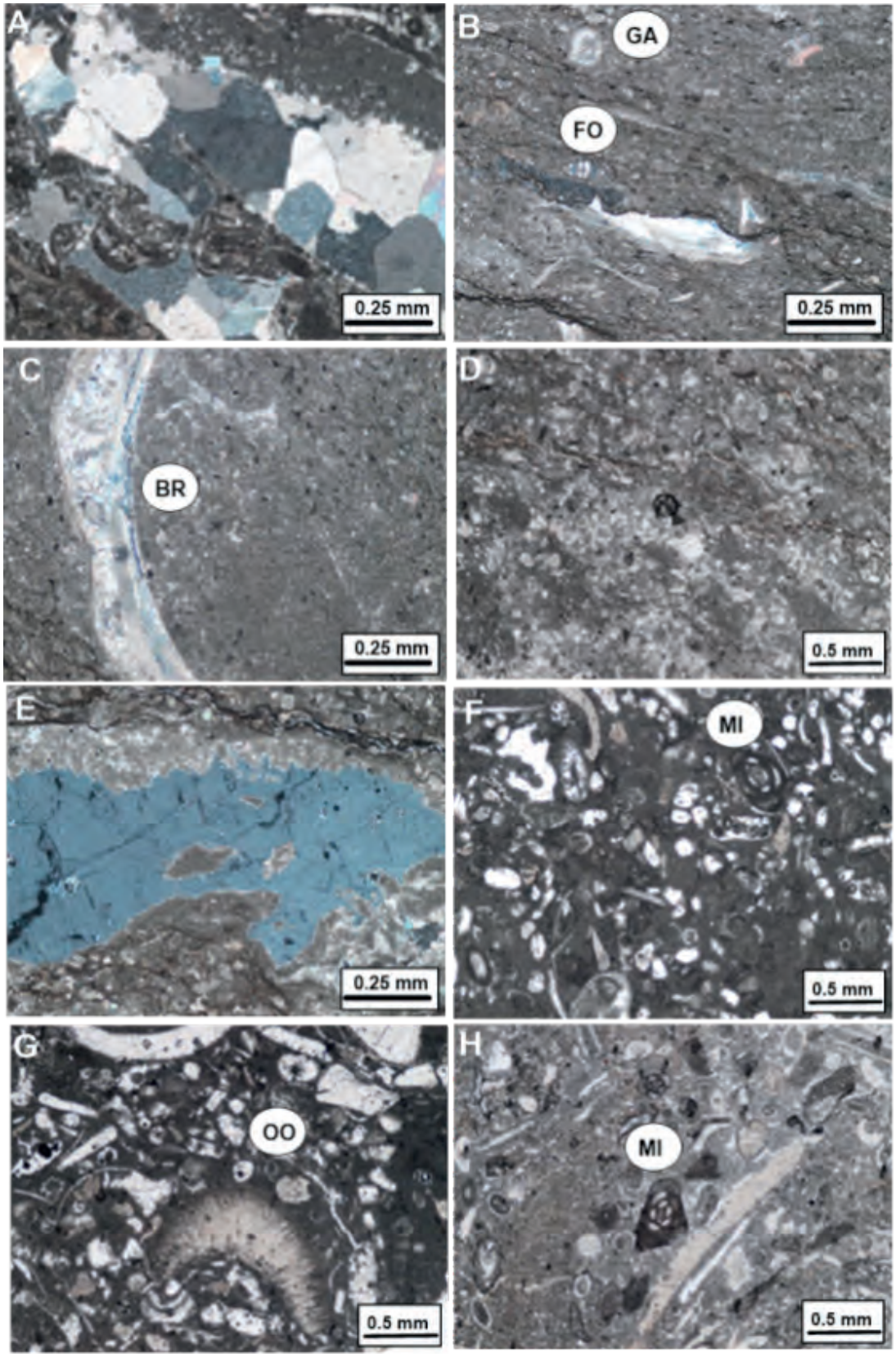


Fig. 8. The Paleocene (Selandian) Farrud Member microfacies; B-C, Brachiopods bivalves lime-mudstone association. Foraminifera (FO), gastropod fragment (GA) and brachiopod (BR), sample 9 (6029 ft), RRR40 well, XPL. D-E, Pelagic foraminiferal argillaceous biomicrite association, sample 32 (5959 ft), RRR45 well, PPL. F-H and Fig. 9. A, Foraminiferal bivalves bioclasts packstone association. Miliolid (MI), oolite (OO), algae (AL), oyster (OY) and gastropod (GA), samples 31 (5949 ft); 29 (5898 ft), RRR45 well, PPL and XPL.

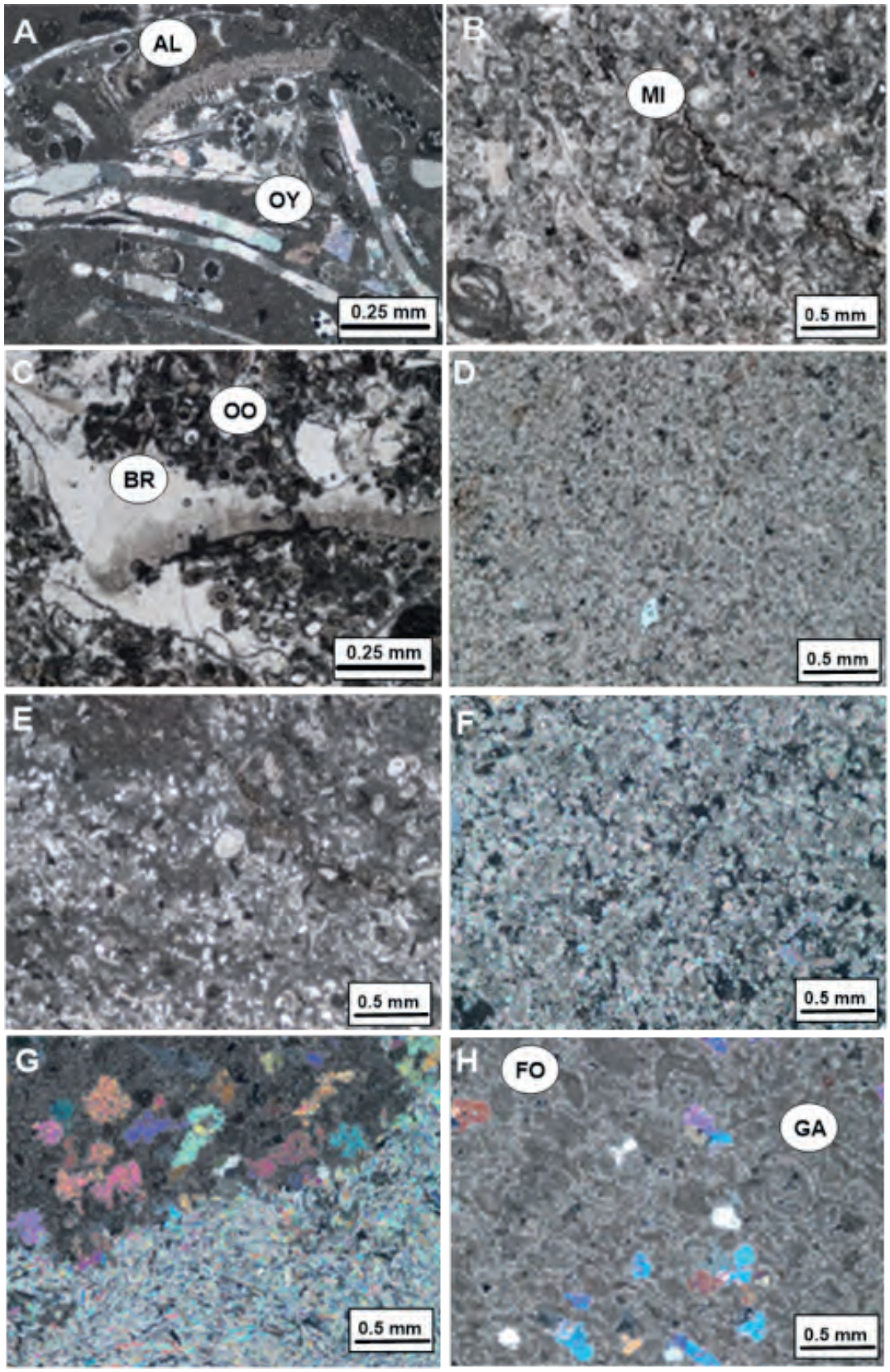


Fig. 9. The Paleocene (Selandian) Farrud Member microfacies; B-C, Foraminiferal bivalves bioclasts packstone association. Brachiopod (BR), oolite (OO) and miliolid (MI), sample 28 (5874 ft), RRR45 well, PPL. D-F, Dolomitization invaded the dismicrite, sample 27 (5861 ft); sample 25 (5850 ft), RRR45 well, PPL. E, Pelagic foraminiferal argillaceous biomicrite association, sample 26 (5857 ft), RRR45 well, PPL. G, Gypsiferous dismicrite association, sample 24 (5840 ft), RRR45 well, XPL. H, Gastropods dolomitized micrite association. Gasstropods (GA) and forminiferal tests (FO), sample 23 (5837 ft), RRR45 well, XPL.

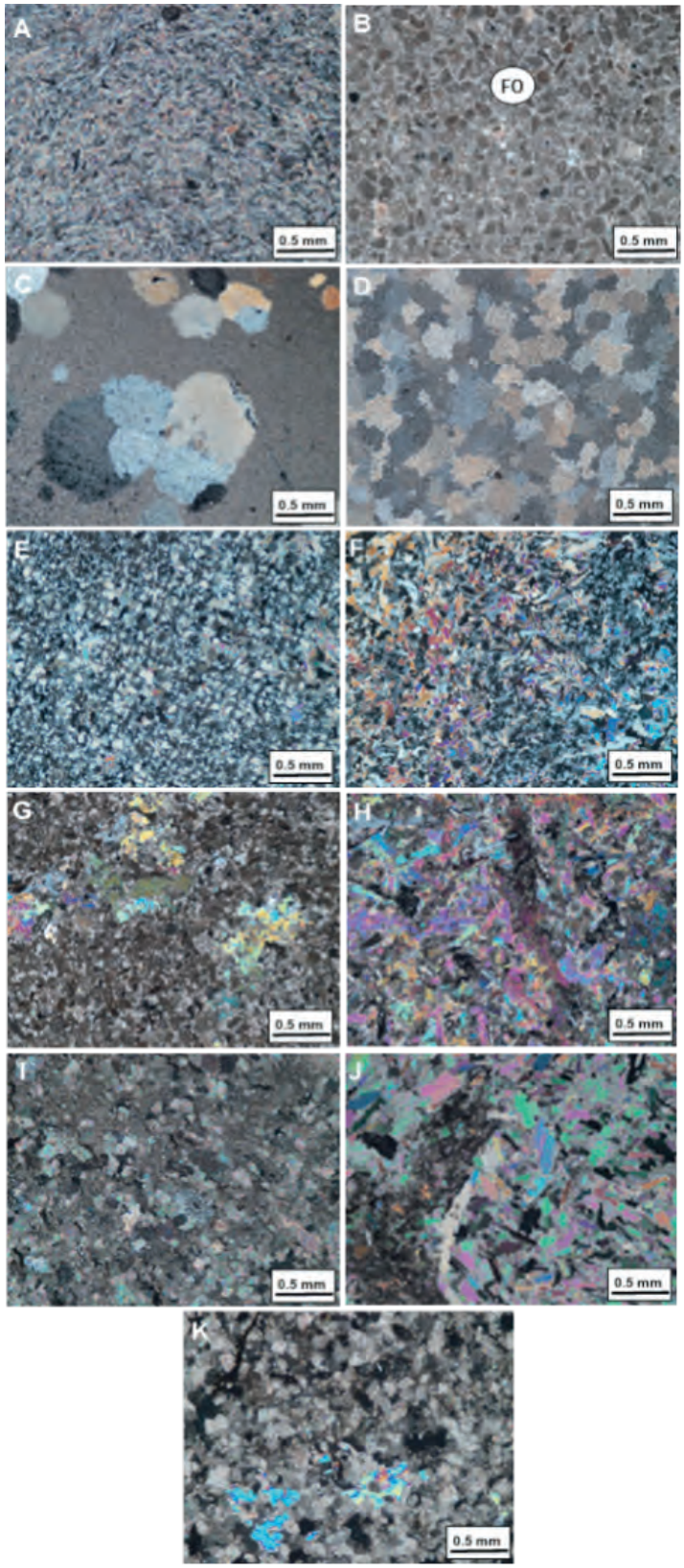


Fig. 10. The Paleocene (Selandian) Farrud Member microfacies; A, Evaporite association, sample 22 (5832 ft), RRR 45 well, XPL. The Paleocene (Selandian) Mabruk Member microfacies; B, Foraminiferal pelloidal biomicrite association. Foraminifera chambers (FO), sample 4 (5989 ft), RRR40 well, PPL. C-D, Dismicrite association, sample 3 (5978 ft); sample 2 (5972 ft), RRR40 well, XPL. E, Gypsiferous quartz arenite association, sample 1 (5968 ft), RRR40 well, XPL. F, Gypsiferous quartz arenite association, sample 1 (5968 ft), RRR40 well, XPL. G-J, Gypsiferous dolomitized biomicrite association, sample 8 (5298 ft); sample 7 (5297 ft); sample 6 (5289 ft), LLL1 well, XPL. K, Dolostone association, sample 5 (5280 ft), LLL1 well, XPL.

in mainly deeper environments of the shelf bays with maximum sea level rise during inner-shelf environment where fossiliferous bioclastic packestone was dominated. On the other hand, some wells exhibit different deposition in Farrud Member probably due to their locations in the basin of deposition. They reflect rapid oscillation of the sea level marked by drop land-ward shift of the sea shore deposition prevailed by supratidal gypsiferous dolostone and numerous ferrugineous materials as clouds staining many parts of dolomite and surrounded the micritized fossils. This situation ends the deposition of the Farrud Member in most of the studied wells. On the other hand, the facies in the northern part of the Concession -11 field indicates deposition in deeper marine setting than in the southern facies.

Mabruk Member (Upper Paleocene) overlies Farrud Member in two wells of the concession 11. It is generally limestone/dolomite dominated facies intercalated with evoporites and thin siliciclastics. Generally, these facies indicate deposition started during a phase of sea level drop resulted in the dominance of shallow intertidal, supratidal facies instead of the marked deeper shelf marine conditions. 8 core samples representing Mabruk Member were investigated from two wells LLL1 and RRR40. Mabruk Member reflects paleoenvironmental trends marked by sea level fluctuations accompanied with a relatively marine shelf bay conditions intervened with short-lived shallow intertidal and supratidal warm coastal sedimentation. As a result dolostone, evaporitic dismicrites and gypsiferous dolostone of supratidal characters were deposited.

ACKNOWLEDGEMENTS

We are indebted to Harouge Oil Operations for the provision of samples, geological information and permission to publish this study.

REFERENCES

Abadi, A. M. (2002). Tectonics of the Sirt Basin. Unpublished PhD Dissertation, Vrije Universiteit, Amsterdam ITC. Enschede, 187p.

Abadi, A. M.; Van Wees, J-D.; van Dijk, P.M. and Cloetingh, S. A. P. L. (2008). Tectonics and Subsidence Evolution of the Sirt Basin, Libya. AAPG Bulletin, 92(8): 993-1027.

Abugares, M. M. (2007). Deposition, Development of the Cretaceous Lidam Formation, SE Sirt Basin, Libya. Unpublished M. Sc. Thesis, Durham University, 217p.

Adams, A. E.; Mackenzie, W. S. and Guilford, C. (1984). Atlas of Sedimentary Rock Under the Microscope. Harlow-Longman Scientific and Technical, John Wiley and Sons, Inc., New York, 104p.

Ahlbrandt, T. S. (2001). The Sirt Basin Province of Libya-Sirte-Zelten Total Petroleum System. U.S. Geological Survey, Bulletin 2202-F: 29p.

Barr, F. T. and Weegar, A. A. (1972). Stratigraphic Nomenclature of the Sirte Basin, Libya. Petroleum Exploration Society of Libya, Tripoli: 179p.

Carr, I. D. (2003). A Sequence Stratigraphic Synthesis of the North African Mesozoic. Jour. Petr. Geol., 26: 133-152.

Dunham, R. J. (1962). Classification of Carbonate Rocks According to Their Depositional Texture. In: Classification of carbonate rocks (Ed. by: W. E. Ham). AAPG Memoir 1: 108-121.

Embry, A. F. and Klovan, J. E. (1971). A Late Devonian Reef Tract on Northeastern Banks Island. N. W. T. Cana. Petr. Geol., Bulletin, 19(4): 730-781.

Flügel, E. (1982). Microfacies Analysis of Limestones. Springer -Verlag, Berlin, 633p.

Flügel, E. (2004). Microfacies of Carbonate Rocks: Analysis, Interpretation and Application. Springer-Verlag, Berlin-Heidelberg-New York, 976p.

Folk, R. L. (1959). Practical Petrographic Classification of Limestone. AAPG, Bulletin, 43: 1-38.

Folk, R. L. (1962). Spectral Subdivision of Limestone Types. In: Classification of carbonate rocks (Ed. by: W. E. Ham). AAPG Memoir 1: 62-85.

Gras, R. and Thusu, B. (1998). Trap Architecture of the Early Cretaceous Sarir Sandstone in the Eastern Sirt Basin, Libya. In: Petroleum Geology of North Africa (Ed. by: D. S. MacGregor; R. T. J. Moody and D. D. Clark-Lowes). Geol. Soc., Spec. Publ. 132: 317-334.

Gumati, Y. D. and Kanes, W. H. (1985). Early Tettiary Subsidence and Sedimentary Facies, Northern Sirt Basin, Libya. AAPG, Bulletin 69(1): 39-52.

Hallett, D. (2002). Petroleum Geology of Libya. Elsevier, Amsterdam, 503p.

Harouge Oil Operations (HOO), Libya (2009). Unpublished Internal report: 80p.

Kinsman, D. J. (1969). Interpretation of Sr+2 Concentration in Carbonate Minerals and Rocks. Jour. Sedi. Petro., 39(2): 486-508.

Reading, H. G. (1996). Sedimentary Environments: Processes, Facies and Stratigraphy, 3rd edn. Blackwell Science, Oxford, 688p.

Selley, R. C. (1980). Ancient Sedimentary Environments. Chapman and Hall, 287p.

Wilson, J. L. (1975). Carbonate Facies in Geologic History. Spring-Verlag, New York, Heidelberg, Berlin, 471p.

MULTI-WELL SAND PRODUCTION PREDICTION STUDY TO SUPPORT FIELD DEVELOPMENT PLAN, LOWER ACACUS FORMATION, AREA 47, GHADAMIS BASIN

M. S. Gheddida*, C. Sorge**, M. El Mabrouk*, A. A. Fituri* and A. V. Der Berken**

Abstract: This work presents the synthesis of an extensive study on sand production prediction conducted on six structures in block 2, Lower Acacus Formation, Area-47 in Ghadamis Basin, Libya. These structures, upon declaring their commerciality, were identified for North Hamada Field Development. Thirteen wells (exploratory and appraisals), have been drilled and tested in these structures. Some of these wells have exhibited sand production phenomena during their initial production tests. A sand production prediction study was performed to investigate and quantify the magnitude of the problem, suggesting proper sand control remedy and optimum completion parameters for cased and open hole scenarios.

Geomechanical Modeling and Wellbore Stability (WBS) Analysis have been performed simultaneously for each well, to assess mechanical properties and stresses that have been used for sanding analysis. A petrophysical and rock physics analysis of log data from all wells allowed to integrate available measurements by means of multi-well workflows utilizing, 1D-geomechanic model, rock physics and completion modules. All analyses confirmed the occurrence of sanding in some critical sections at different reservoir pressure depletion regimes. Predicted sanding tendency on existing wells, was in good agreement, with observations made from DST's.

These results have been used to start planning for the upcoming operation phase. They also constitute the base for the development of an integrated 3D geomechanic reservoir model enabling large scale analysis of the regional sand production phenomena.

Keywords: Area-47, Mechanical earth modeling, Sand production prediction.

INTRODUCTION

Field Location and History

North Hamada Field is located in the North Ghadamis Basin, Libya, approximately 220km South West of Tripoli. The field was discovered in 2005 by Verenex and Medco International Ventures Limited (MIVL) which was operating in Area-47 under Exploration and Production Sharing Agreement (EPSA). The field is divided into 4 blocks with several structures (Oil & Gas) had been proved through exploration wells. The productive structures are mostly located in Block-2 and Block-4 as shown in (Fig.1).

The discovery well is A1-47/02 which penetrated the reservoir main producing sandstone of the Lower Acacus Formation (Silurian). Until very recently, the majority of the exploration focus has been in Block 2 where thirteen (13) wells have been drilled in order to delineate and test the Acacus Formation. Six (6) proven structures designated AL, B, C, D, F and J already have commercial status through final appraisal report document. Those structures have been engaged in field development plan (FDP) and granted to deliver hydrocarbon from several multilayer from bottom to top (Sand 1 to Sand 5). Some of these drilled wells produce sand during the initial DST performed during the exploration phase.

Objectives

The multi-well sand production study was conducted with the intent to determine if the known sand production during the drill steam tests (DST) can be predicted at the reservoir levels and can be produced to the surface facilities. Therefore, the main identified objectives of this study are:

1) Integrate and analyze the existing relevant logs and other field data.

*Nafusah Oil Operation B.V., Tripoli, Libya.
**Schlumberger, Paris, France.

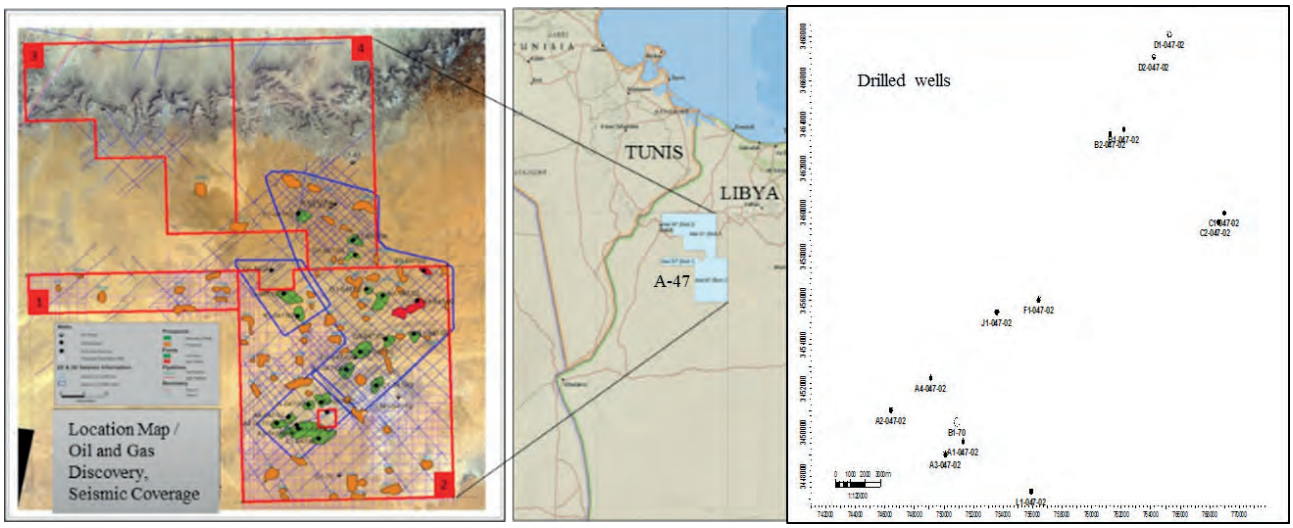


Fig. 1. Location map of the area A 47 and the drilled wells in block 2.

2) Perform 1D Mechanical Earth Models (MEM) for the existing 13 wells.
3) Perform laboratory tests on selective core samples.
4) Refine and calibrate the Mechanical Earth Models, (MEM) using the selected core tests results, existing caliper, drilling data and borehole images.
5) Develop continuous critical drawdown profile for the entire reservoir for different depletion steps and for various completion scenarios.
6) Perform uncertainty analysis on critical drawdown profile and advice on key inputs to reduce the uncertainty.

RESERVOIR LITHOLOGY

The Lower Acacus Formation consists of multilayers of sandstone, shale and siltstone. Units were interpreted to be for the most part with thick beds of sandstone which also display evidence of textural heterogeneity. Siltstone was interpreted to be a gradation of both sandstone and shale units.

The stratigraphic and structure correlation are constructed through all wells in area 47 Block 2 covering AL, J, F and B, C, D structures. Although the separation between structures is big, the sand continuity from well to well can be clearly observed. The stratigraphic sequence is commonly characterized by cyclic progradational parasequence, and good correlation from well to well in the lower zones as supported by seismic.

It gradually becomes more complicated in upper zones from Sand 4 up due to deeper marine influence as indicated by more shale interval intercalation. The base reservoir is defined to exclude non-reservoir zones below the pay zones.

To better characterize the reservoir, the key reservoir zones (Sand 1, Sand 2, Sand 3, Sand 4 and Sand 5) are subdivided into several reservoir subzones as shown in stratigraphic cross section (Fig. 2). Each region is indicated by consistent shale or porosity breaks from well to well and tends to have its own fluid contact. The following is the subdivision of the reservoir zones that represents the structures of the study area A, J, F, B and D that are used for static reservoir modeling.

SAND PRODUCTION PREDICTION

Data Audit and Rock Physics

The main results and initial phase of the study is to audit the available data and examine the rock physic. The relevant data typically includes survey, drilling, logs, laboratory and in-situ test data, geological information.

The available logs show good coverage. A minimum log suite allowing a satisfactory geomechanical modeling. All 13 wells were included and used in the study (Fig. 3). eleven wells have compressional sonic (DTCO) whereas shear sonic (DTSM) is available only on four wells.

Editing were performed to fill the gaps and correct the bad obvious reading. Synthetic logs used where measured data show some reading problems or not existing (Fig. 4). For the overburden, synthetic density

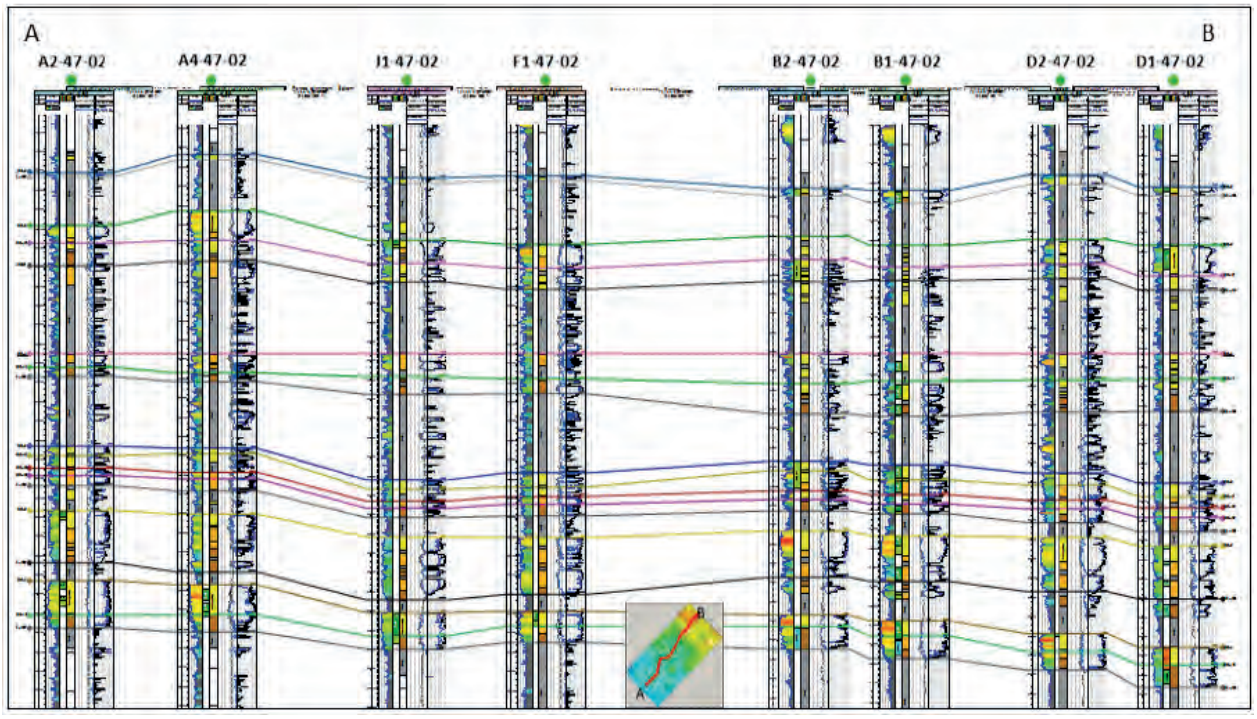


Fig. 2. Lithostratigraphic correlation through the reservoir multilayer.

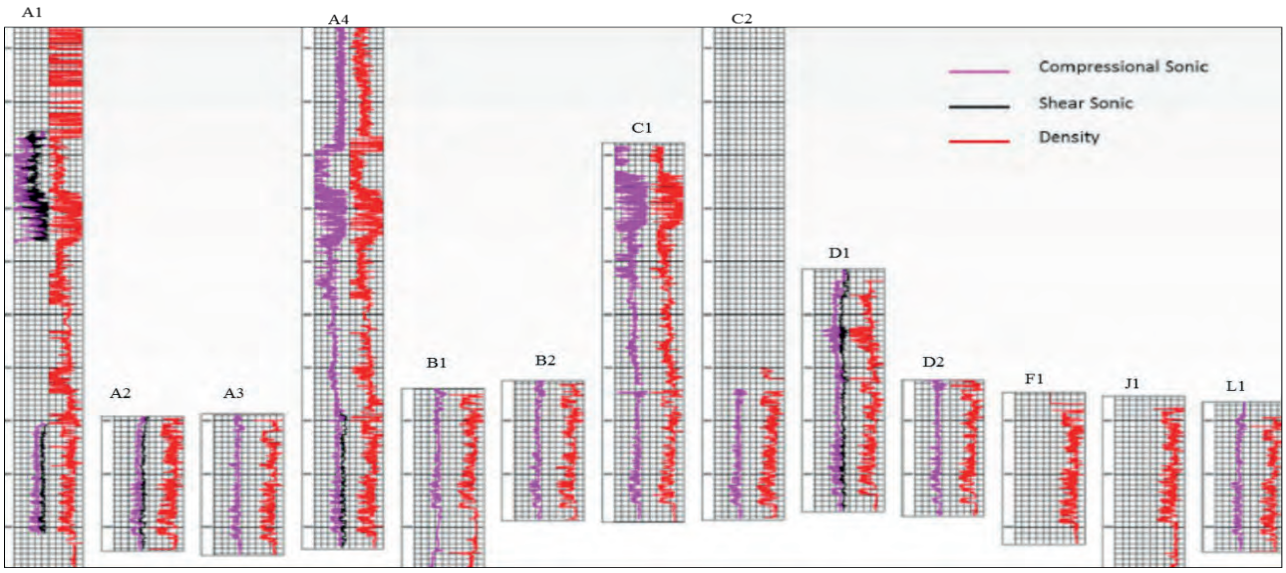


Fig. 3. Shows the provided compressional and share sonic slowness and density in terms of log view. Measured data.

logs have been generated using Gardner relation from literatures for sand and shale.

RHOB_sand= 1.66 Vp0.261

RHOB_shale=1.75Vp0.26

The log view gives a good sketch of log coverage (density) and missed data (share). The cross plots help to test the compatibility of the data from the set of wells and QC the available data which proved to be relatively good. The editing start with compressional sonic. A synthetic curve is generated using Neural Network (NN) technique with logs like measured depth, gamma ray, deep resistivity and neutron porosity as input. The modeled logs are compared to the measured one. Where the condition of the measured log is bad, usually in bad borehole section or not existent, the synthetic log is used in replacement.

The edited compressional sonic is then used as input to edit shear sonic and density log. For overburden (logs are noisier and absence of logs like deep resistivity and neutron porosity) synthetic

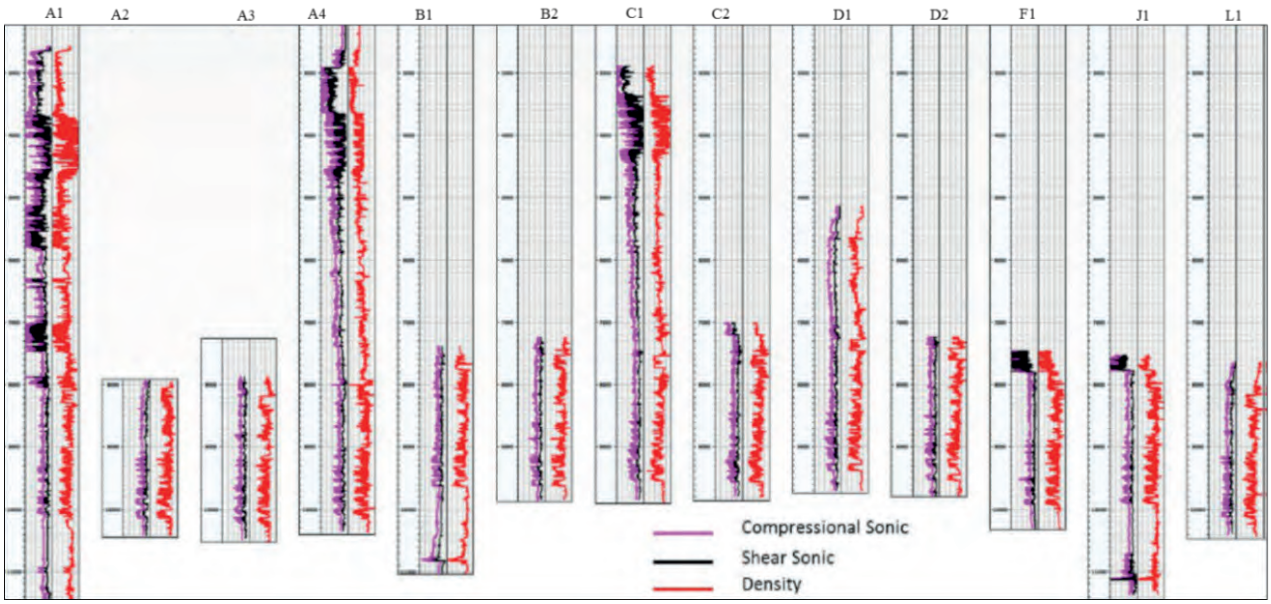


Fig. 4. Shows the measured and edited compressional and share sonic slowness and density in terms of log view.

density is also generated using calibrated Gardner type relations starting from published relations sand and shale. Once all the measured data are edited, shear velocity need to be predicted where missing on the nine wells (Kumar *et al*, 2014). Two methods are tested in parallel:

Calibrated linear relation Greenberg-Castanga (GC) type and Neural Network (NN) with inputs like compressional velocity, gamma ray and deep resistivity. Figures 5 and 6 show the histograms of the difference between measured and synthetic shear and compressional velocities. The neural network is slightly more centered and symmetrical. Therefore; this method is the preferred choice.

The Result of the Audit and Editing: Fig. 7 shows the result and QC of the edited logs for the well A1-47-02 as an example. After editing the whole gaps are filled and the abnormal values replaced. Figures 3, 4 show compressional, shear sonic and density of the thirteen wells respectively before and after editing, all the gaps are filled and the missing data have been generated where the data set are more homogeneous.

It can be observed from, the cross plots of compressional, shear sonic and density color-coded by wells volume of clay (Fig. 8), a graduation from sand to shale in sonic: shale tends to have higher shear sonic and lower compressional sonic than sand. A sort of separation can also be seen on density versus compressional sonic plot: shale tends to have higher density and may be slightly lower compressional sonic than sand.

ROCK MECHANICS LABORATORY TEST AND 1D MECHANICAL EARTH MODELS

Sample Collection and Testing

During this study, the decision was made to analyze core samples from two representative wells. Based on the availability and conditions of the cores, selective intervals were preferred. For this test we provided 22 vertically oriented, sandstone samples, and nine (9) chunks from wells A4-047-02 & D1-047-02 (Table 1). The plugs were prepared by Libyan Petroleum Institute and provided to Schlumberger Reservoir Labs, in Salt Lake City to perform the optimum analysis. The testing program consists of:

- Unconfined compression testing on odorless mineral spirits (OMS) topped-off vertical sandstone samples at room temperature to determine peak compressive strength.
- Triaxial compression testing performed at room temperature with concurrent ultrasonic velocity measurements on OMS topped-off vertical sandstone samples and.
- Petrographic analysis including laser particle size analysis (LPSA) and sieve analysis.

The purpose of testing was

1) To provide strength information for developing a failure locus for the material. With adequate measurements of strength on core samples, and with the availability of supplementary information such as clay content and porosity, logging-based predictions of strength may be possible.

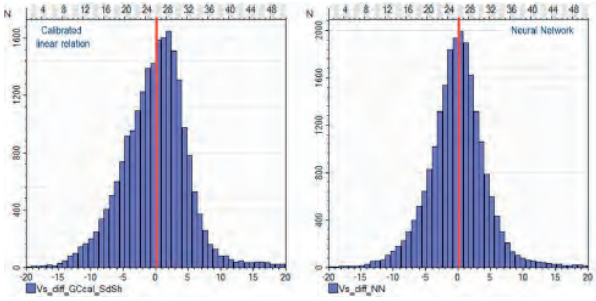


Fig. 5. Shear velocity prediction - histograms of difference between measured log and synthetics.

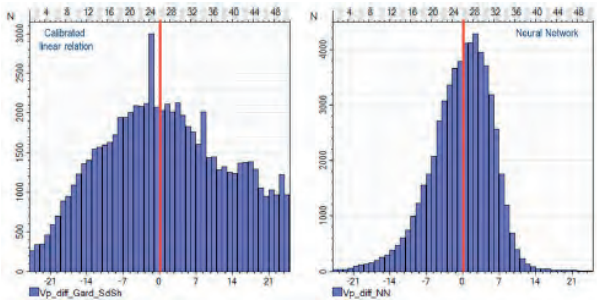


Fig. 6. Compressional velocity prediction -histograms of difference between measured log and synthetics.

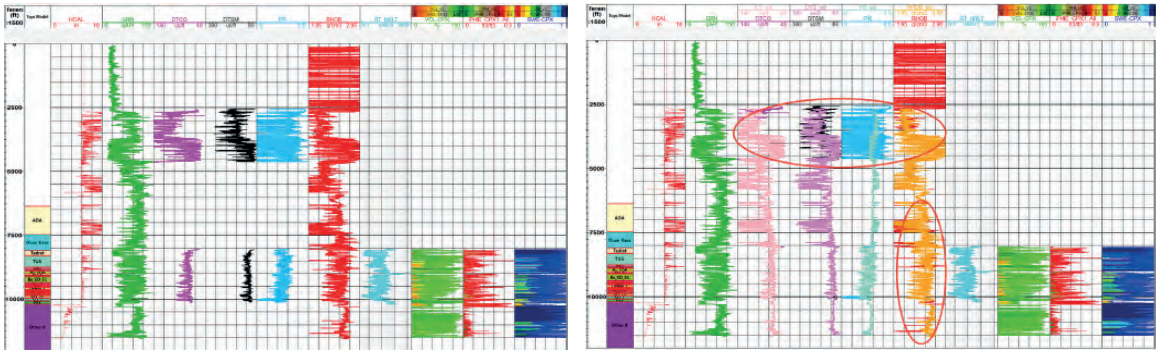


Fig. 7. QC of editing log view, measured data (left) and edited (right)- Well A1-47-02. Circles points out to slightly abnormal reading.

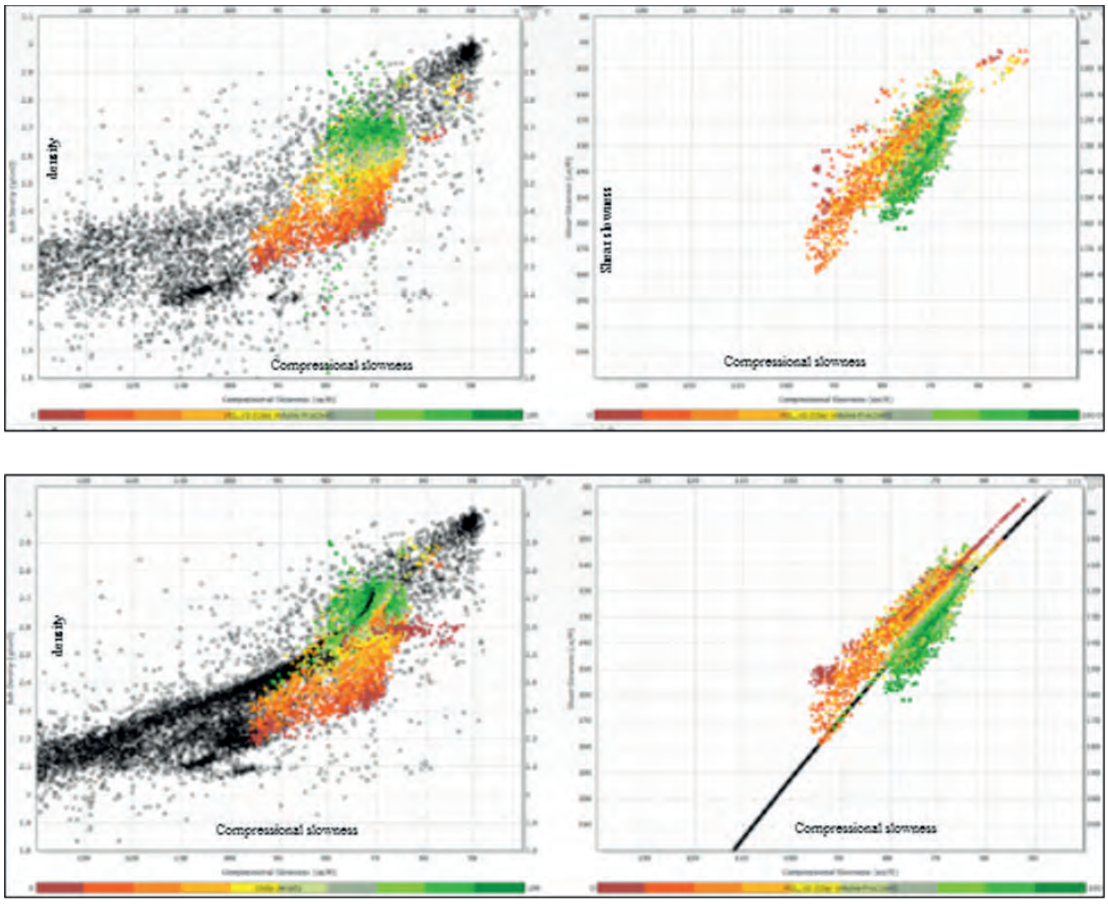


Fig. 8. Cross plot shows the QC of density vs. compressional and shear sonic vs. compressional color-coded by wells volume of clay. Measured (top), Edited (Bottom).

Table 1. Shows the sample material and testing.

Well / Sample ID	Depth (ft)	Approx. Length in	Approx. Diameter in	Scheduled Test 1
A4-047-02				
A4 1-1	9995	2.0	1.0	UCS
A4 1-2	9995	1.8	1.0	TXC w/UVs
A4 1-3	9995	2.0	1.0	TXC w/UVs
A4 1-4	9995	2.0	1.0	TXC w/UVs
A4 2-1	10,022	2.0	1.0	UCS
A4 2-2	10,022	2.0	1.0	TXC w/UVs
A4 2-3	10,022	1.9	1.0	TXC w/UVs
A4 2-4	10,022	2.0	1.0	TXC w/UVs
D1-047-02				
D1 1-1	9006	1.9	1.0	
D1 1-2	9006	1.9	1.0	UCS
D1 2-1	9015	2.0	1.0	TXC w/UVs
D1 2-2	9015	2.0	1.0	TXC w/UVs
D1 2-3	9015	2.0	1.0	TXC w/UVs
D1 3-1	9021	1.7	1.0	UCS
D1 4-1	9027	2.0	1.0	TXC w/UVs
D1 4-2	9027	1.9	1.0	TXC w/UVs
D1 4-3	9027	2.0	1.0	TXC w/UVs
D1 5-1	9033	2.0	1.0	MTXC w/UVs
D1 5-2	9033	2.0	1.0	UCS
D1 6-1	9039	2.0	1.0	Spare
D1 6-2	9039	2.0	1.0	TXC w/UVs
D1 6-3	9039	2.0	1.0	TXC w/UVs
A4-047-02				
A4-1	9995	Chunk – 185 grams	LPSA & Sieve	
A4-2	10,022	Chunk – 197 grams	LPSA & Sieve	
A4-3	10,036	Chunk – 192 grams	Spare	
D1-047-02				
D1-1	9006	Chunk – 189 grams	LPSA & Sieve	
D1-2	9015	Chunk – 199 grams	LPSA & Sieve	
D1-3	9021	Chunk – 183 grams	Spare	
D1-4	9027	Chunk – 199 grams	LPSA & Sieve	
D1-5	9033	Chunk – 196 grams	Spare	
D1-6	9039	Chunk – 199 grams	LPSA & Sieve	

2) To provide static and dynamic mechanical properties information for correlating well-log data. Physical/mechanical response of a material is dependent on the rate at which it is loaded and the applied stress/strain amplitude. Logging-based measurements are in the kilohertz range; whereas, actual physical loading rates acting on a wellbore are generally much slower (pseudo-static). Even hydraulic fracturing (particularly the change in width) is a pseudo-static process. This is the rationale for performing laboratory pseudo-static testing for measurement of Young's modulus (E) and Poisson's ratio (ν), and simultaneously measuring dynamic (high loading rate and low loading magnitude) responses of core samples. This provides information for well-log calibration, to provide realistic deformation parameters (E, ν) for engineering purposes (John *et al*, 2007).
3) Minimize the amount of uncertainty existing in rock strength and grain size distribution, in order to improve the reliability of the Sand Prediction Model in development and to determine grain size and distribution. Based on log derived mechanical properties in situ horizontal and vertical stresses have been estimated at the depth of the samples (Table 2). This estimation has been further calibrated using core test results. Single-stage triaxial compression tests (TXC) with concurrent ultrasonic velocity measurements were performed on suites of vertical samples at varying confining pressures (either 0.5x, 1.0x, or 1.5x the mean effective in-situ stress conditions). Additionally, when material was limited, multi-stage triaxial compression tests (MTXC) were performed on vertical samples at confining pressures equal to 1.0x and 1.5x. From stresses and strains measured during triaxial compression tests, elastic properties and compressive strength were determined for each test specimen. Static values for Young's modulus and Poisson's ratio were calculated using the following equations:

$$Es = \delta\sigma 1 / \delta\varepsilon a$$

$$vs = \delta\varepsilon r / \delta\varepsilon a$$

Where:

Es,	Young's modulus,
σ1,	axial stress,
vs,	Poisson's ratio, and
δεa, δεr	axial and radial strains.

Static Young's modulus and Poisson's ratio correspond to the initial slope of the laboratory tests curves Axial stress vs Axial strain and Radial strain vs. Axial strain, respectively. Results of unconfined and triaxial compression tests are presented in Tables 3 and 4. Dynamic mechanical properties using ultrasonic wave transmission (with 1MHz P- and S-wave transducer) were determined concurrently during all triaxial compressional tests. Comparison of static and dynamic values of Poison's and Young's modulus with increasing confining pressure for vertical samples are shown in Tables 5 and 6. These results allowed establishing the correlation and the corresponding correction to apply in order to drive static Young's modulus.

1D MECHANICAL EARTH MODELS (MEM)

Once the mechanical properties and stresses are derived from the wireline logging data and calibrated against the available measurements of core tests, the geomechanical evaluation process is accomplished by means of well bore stability (WBS, Biniti *et al*, 2015). The drilling integrity analysis is performed, and the results are ready to be used for the sanding analysis.

Mechanical Proporties (elastic and stress)

The rock mechanical properties include the poroelastic properties (Young's modulus E; Poisson's ratio PR), Biot's coefficient (ALPHA)

Table 2. In-Situ stress conditions inferred from preliminary Mechanical Earth Models (MEM). Mean effective stress is defined as (1/3*(Sigh+SigH+SigV)-Pp). Biot's coefficient (ALFA) assumed equal to 1.

Well ID/ Depth ft	Sigh psi	SigH psi	SigV psi	PP psi	Effective Stresses: alpha = 1.0 Vertical psi	Horizontal psi	Mean psi	Confining Pressure Stages (Mean-Eff-Stress) 0.5x in-situ	1.0x in-situ	1.5x in-situ
A4-047-02										
9995	6102	6257	10,598	3998	6600	2182	3654	1827	3654	5482
10,022	6613	6770	10,625	4009	6616	2683	3994	1997	3994	5991
D1-047-02										
9006	6886	7430	9744	3602	6142	3556	4418	2209	4418	6627
9015	5754	5831	9754	3606	6148	2187	3507	1754	3507	5261
9021	6015	6127	9761	3608	6153	2463	3693	1847	3693	5540
9027	6381	6465	9767	3611	6156	2812	3927	1963	3927	5890
9033	6292	6399	9773	3613	6160	2733	3875	1938	3875	5813
9039	5985	6242	9780	3616	6164	2498	3720	1860	3720	5580

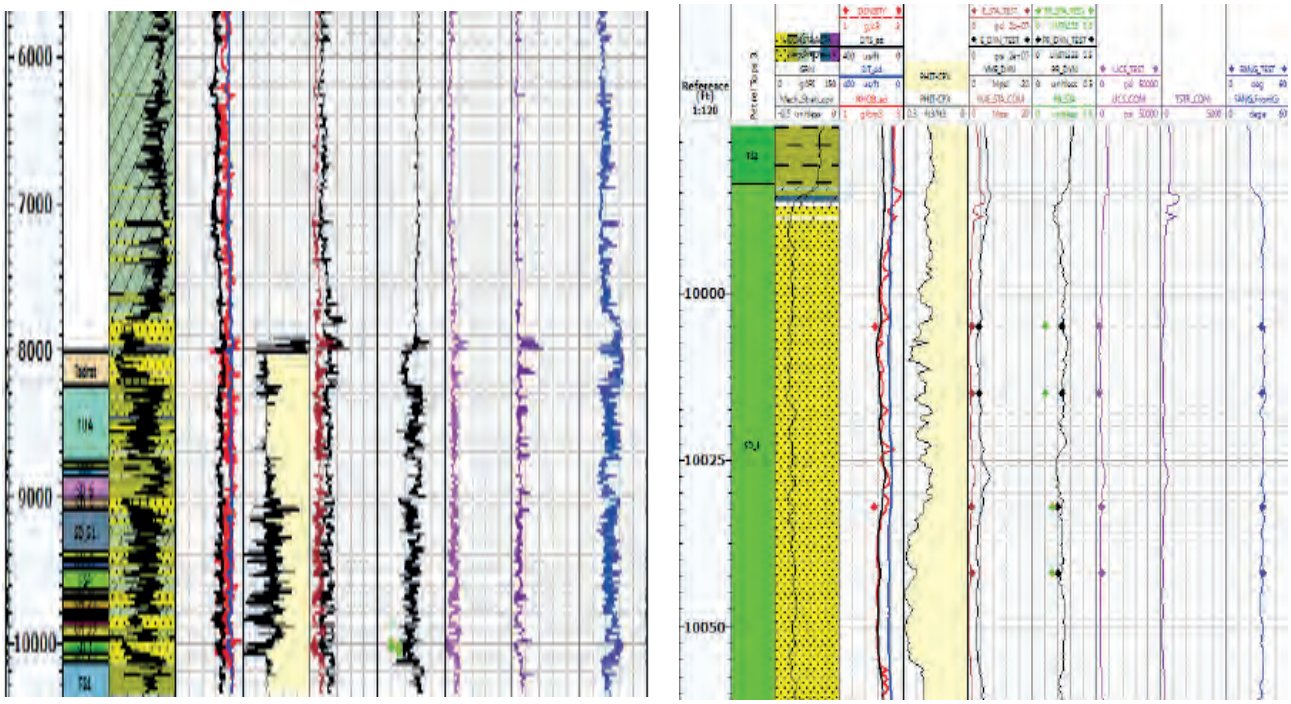


Fig. 9. a) Mechanical properties of well A4. b) Mechanical Properties of well A4.

and rock strength properties (unconfining compressional strength UCS), internal friction angle (FANG) and the tensile strength (TSTR, Gang *et al*, 2011). Log data, notably compressional and shear slowness and rock bulk density, were used to compute dynamic elastic module. Elastic properties computed from the logs are termed dynamic because the sonic measurements are conducted at high frequencies. wellbore deformation or failure is a relatively slow process compared to high frequency wave propagation. The properties computed from core tests considered to be static measurements. Static Young's Modulus correlation has been used to calculate UCS which is the load per unit area at which a cylindrical sample fails in compression without applying confining (cell) pressure.

To check the validity of the mechanical properties estimated in the 1D MEMs and allow a possible calibration, the lab test results of wells A4 has been plotted against in situ stress conditions Fig. 9a and b. A very good match for dynamic and static Young's modulus was observed and no further calibration was required. However; Dynamic Poisson's ration and static one do not seem to have a clear correlation. Consequently, static has been considered equal to dynamic one. High dispersion of experimental data is well known in the literature. It is generally observed that there is no meaningful correlation

between the values of static Poisson's ratio and other mechanical properties or physical property of the rock, expect porosity. High Poisson's ration corresponds to high porosity. UCS has been calibrated (i.e. decreased) to match with the Lab results. TSTR has been assumed equal to 10% of the UCS in the lack of specific laboratory tests. FANG results show good match and no further calibration was required.

Pore Pressure and Overburden Stress

The weight of the overburden sediments compacts the grains and squeezes the water out. The water escapes based on the permeability and rate of burial. In the study area, no evidence of overpressure is recorded in any of the 13 wells in the end of well report (EOWR). This is confirmed by measurements in MDT results. The average gradient of 0.4 psi/ft has been measured. Pore pressure (PP) profile for each well is studied. Only pore pressure of well D1 is shown in (Fig. 10).

The overburden weight per unit area is called overburden or vertical stress. Overburden stress at any given depth is the pressure exerted by the weight of the overlying sediments and can be calculated integrating the density of the overlying sediments (synthetic and measured).

Horizontal Stress

Minimum and maximum horizontal stresses are fundamental input to wellbore stability, they are used to compute failure. Horizontal stresses have been computed considering poroelastic theory involves Young's modulus, Poisson's ratio, Biot's constant (ALPHA) assumed =1, vertical stress, pore pressure.

Minimum horizontal stress also called (closure pressure) can be constrained by leak off test. In the study area, only formation integrity test (FIT) was provided therefore cannot be calibrated. and must be better corroborated by direct measurements from the upcoming drilled wells.

Maximum horizontal stress gradient is somewhat complicated as there isn't a direct measurement that could be used to infer its values. They are generally derived from the MEM and well bore stability (WBS). The result of the stress modeling of each well is studied. Fig. 11 presents the model of well A2 and A4.

Wellbore Stability (WBS) Analysis

The principal stresses around the borehole are used to determine if the borehole wall has failed or not. WBS is caused by two major types of failure, shear or tensile. Shear failure is usually caused by low mud weight; tensile failure is caused by high

Table 3. Summary of Unconfined and Triaxial Compressional Tests of well A4.

Well /sample ID A4-047-02	Depth ft	Bulk Density g/cm3	Confining Pressure psi	Peak Effective compressive strength psi	Effective Residual compressive strength psi	Young's Modulus	Average Poisson Ratio psi
A4 1-1	9995	2.160	0	1985	-	288,100	0.27
A4 1-2	9995	2.079	1827	11,908	8389	918,700	0.11
A4 1-4	9995	2.084	3654	17,357	13,973	1,295,000	0.10
A4 1-3	9995	2.156	5482	21,072	19,306	1,526,000	0.14
A4 2-1	10,022	2.120	0	3862	-	436,200	0.18
A4 2-4	10,022	2.069	1997	14,013	10,583	926,200	0.17
A4 2-3	10,022	2.091	3994	21,539	15,678	1,208,000	0.16
A4 2-2	10,022	2.096	5991	25,076	22,046	1,429,000	0.16

Table 4. Summary of Unconfined and Triaxial Compressional Tests of well D1.

Well /sample ID D1-047-02	Depth ft	Bulk Density g/cm3	Confining pressure psi	Peak Effective compressive strength psi	Effictive Residual compressive strength psi	Young's Modulus	Average Poisson Ratio psi
D1 1-2	9006	2.117	0	1040	-	135,000	0.26
D1 1-1	9006	2.122	4418	16,590 (Y)	-	1,182,000	0.10
(Multi-Stage-TXC)			6627	21,606	N.A.	1,618,000	0.18
D1 2-2	9015	1.894	1754	9129	7812	756,400	0.12
D1 2-1	9015	1.922	3507	15,333	14,034	1,093,000	0.14
D1 2-3	9015	1.909	5261	18,364	16,526	1,209,000	0.14
D1 3-1	9021	2.206	0	5922	-	1,198,000	0.33
D1 4-3	9027	2.268	1963	13,326	8540	1,291,000	0.14
D1 4-1	9027	2.237	3927	20,689	14,421	1,410,000	0.20
D1 4-2	9027	2.269	5890	28,536	23,769	2,464,000	0.16
D1 5-2	9033	2.080	0	791	-	120,100	0.30
D1 5-1	9033	2.069	3875	13,716 (Y)	-	917,200	0.12
(Multi-Stage-TXC)			5813	17,072	16,863	1,412,000	0.19
D1 6-2	9039	2.048	3720	16,371	14,955	1,154,000	0.08
D1 6-3	9039	2.055	5580	20,812	18,470	1,305,000	0.10

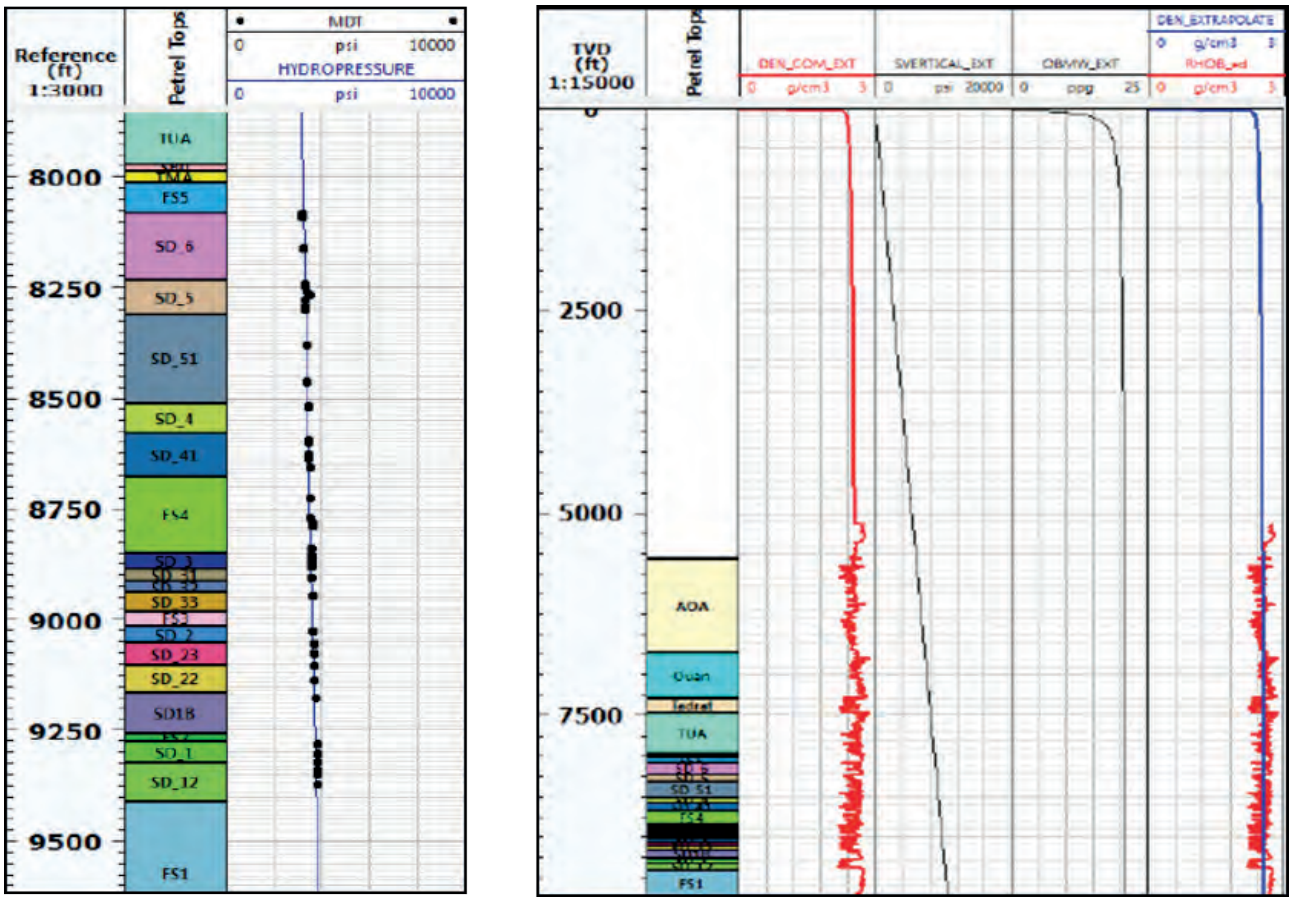


Fig. 10. Pore pressure profile in pressure (Hydropressure) against MDT measurements of well A4

Table 5. Dynamic vs. Static Mechanical properties determined during confining tests for wells A4. cells (--) shows poor S-wave data quality. Dynamic NA.

Well/ Sample ID	Depth ft	Effective confining pressure psi	Static Young's modulus psi	Dynamic Young's modulus psi	Static Poisson's Ratio (average)	Dynamic Poisson's ratio	Dynamic /static Young's Modulus	Dynamic / Static poison's Ratio
A4-047-02								
A4 1-2	9995	1827	918,700	3,022,000	0.11	0.24	3.29	2.18
A4 1-4	9995	3654	1,295,000	3,445,000	0.10	0.23	2.66	2.30
A4 1-3	9995	5482	1,526,000	3,482,000	0.14	0.24	2.28	1.71
A4 2-4	10,022	1997	926,200	--	0.17	--	--	--
A4 2-3	10,022	3994	1,208,000	--	0.16	--	--	--
A4 2-2	10,022	5991	1,429,000	--	0.16	--	--	--
Average:							**2.74**	**2.07**

Table 6. Dynamic vs. Static Mechanical properties determined during confining tests for well D1. cells (--) shows poor S-wave data quality. Dynamic NA.

Well/ Sample ID	Depth ft	Effective confining pressure psi	Static Young's modulus psi	Dynamic Young's modulus psi	Static Poisson's Ratio (average)	Dynamic Poisson's ratio	Dynamic /static Young's Modulus	Dynamic / Static poison's Ratio
D1-047-02								
D1 1-1	9006	4418	1,182,000	2,994,000	0.10	0.29	2.53	2.90
	6627	1,618,000	2,886,000	0.18	0.31	1.78	1.72	
D1 2-2	9015	1754	756,400	2,488,000	0.12	0.26	3.29	2.17
D1 2-1	9015	3507	1,093,000	2,957,000	0.14	0.23	2.71	1.64
D1 2-3	9015	5261	1,209,000	2,956,000	0.14	0.23	2.44	1.64
D1 4-3	9027	1963	1,291,000	4,897,000	0.14	0.22	3.79	1.57
D1 4-1	9027	3927	1,410,000	4,822,000	0.20	0.23	3.42	1.15
D1 4-2	9027	5890	2,464,000	5,622,000	0.16	0.20	2.28	1.25
D1 5-1	9033	3875	917,200	3,201,000	0.12	0.25	3.49	2.08
	5813	1,412,000	3,060,000	0.19	0.24	2.17	1.26	
D1 6-2	9039	3720	1,154,000	----	0.08	--	--	--
D1 6-3	9039	5580	1,305,000	0.10	--	--	--	--
Average:							**2.79**	**1.74**

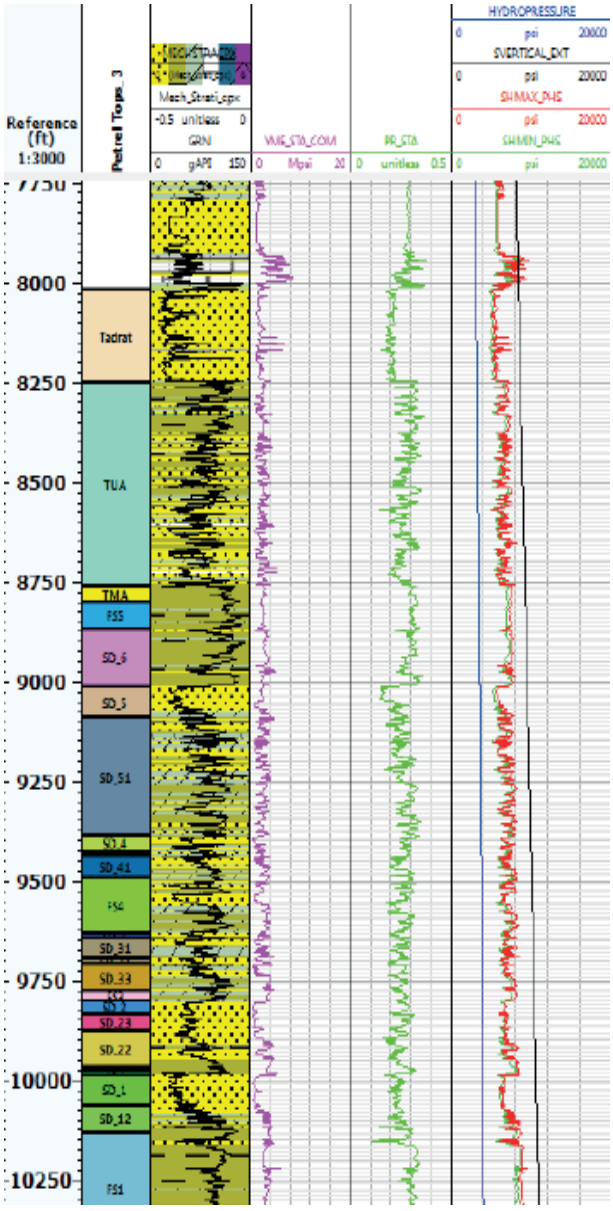


Fig. 11. Stress modeling results of well A2 (left) and well A4 (right). YME_sta_com= static young's modulus; PR_sta= static Poisson's ratio, Hydopressure= pore pressure; SHmax_phs= maximu horizontal stress, SHMIN_phs= minimum horizontal stress.

mud weight (Assif and Ni (2018). Mud weight is the output of the WBS. There are four limits defining the mud weight window. Pore pressure, breakout, mud loss and breakdown.

The result of WBS analysis for the studied well A1 shows a good match between predicted wellbore instability, calipers and drilling experimental events.

Predicted damage is also in good agreement with borehole images. FMI indicates that because of uncontrollable mud weight this well was highly affected by borehole breakout and drilling induced fractures. Most wells predicted damage reproduces satisfactory indication from calipers admitting a manageable damage of 10%.

SAND PRODUCTION ANALYSIS

Sand production analysis performed using schlumberger software Sand Management Adviser (SMA). The sand prediction model can also be used to assess changes of the critical drawdown pressure (CDD) for an open hole or perforated cased hole that may occur over the life of a field undergoing a depletion.

Fig. 12 illustrates a typical plot of single-depth sanding analysis and the definition of CDD pressure. The difference between the reservoir pressure and the bottom hole flowing pressure defines the drawdown. The boundary line between the red zone and the green zone defines the critical drawdown at different reservoir pressures. The reservoir pressure at which the boundary line crosses the diagonal is the critical reservoir pressure for sand-free production.

The CDD pressure decreases whilst the reservoir depletes and disappears at the critical reservoir pressure. The well cannot produce in the zone above the diagonal because the bottom hole flowing pressure (BHFP) is higher than the reservoir pressure in that zone. If the operation conditions lie in the green zone, the well can produce sand free. On the other hand, sand will be produced if the operating conditions lie in the red zone.

Clearly, the CDDP decreases with reservoir depletion which means the possibility for sanding to occur increases. The analysis and results allow comparison of sanding risk for different completion strategies at different stages in the life of the field. The analysis can identify high risk zones in the completion interval. These intervals should be considered for isolation because they may be expected to fail further under different production conditions.

Some of the analyzed offset seven out of thirteen wells have exhibited sand production phenomenon during Drill Stem Tests (DST). In this study, the proposal is to calibrate the sanding prediction on the produced tests to be able to apply the model to predict sand in the planned wells (Assif and Ni, 2018). An example of these results is shown in (Fig. 13). Well A1 where clearly the estimated CDD at pre-production conditions (CDDP-0) is almost the same for the three-perforation azimuth phased every 60 degrees (at 0° N, 60° N and 120°N). Figure 13 also indicates that four out of five DST,

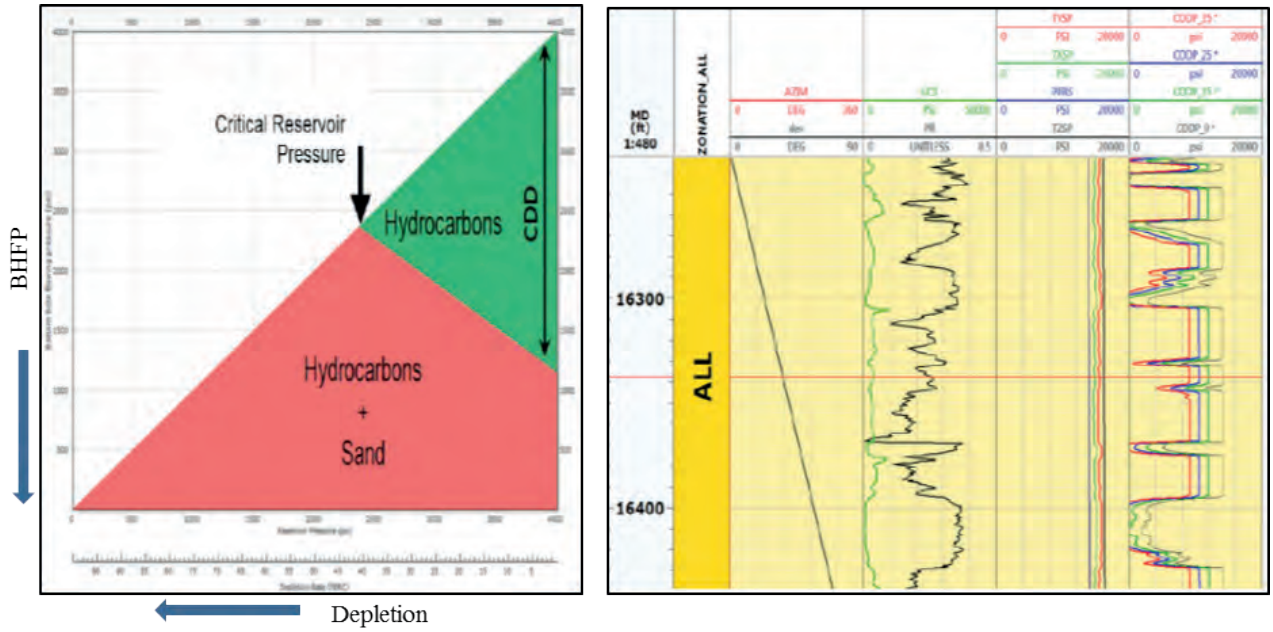


Fig. 12. Typical plot for sand prediction for single depth analysis (left) for an interval analysis (right), CDDP are calculated for different reservoir states corresponding in this case to 0%, 15%, 25% and 35% of deletion.

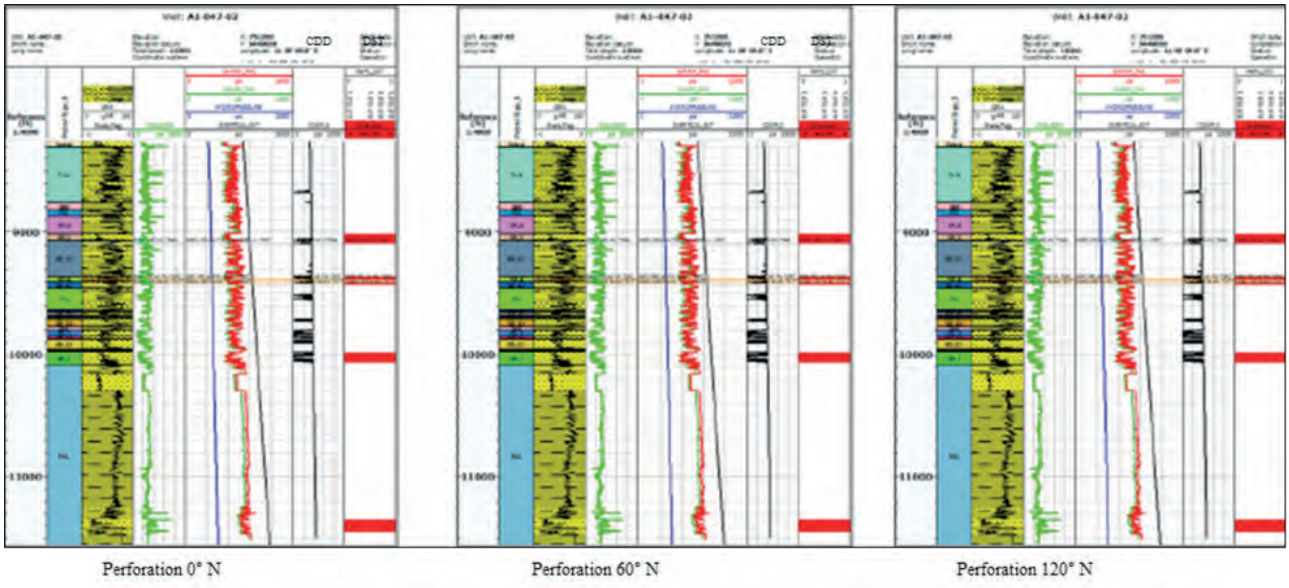


Fig. 13. Critical drawdown pressures computed for different perforation tunnel azimuth. DST perforation intervals (red last track) show sand production in agreement with the computed CDD.

the model predicted sand production. Results of the other wells with respect to sanding are in a good agreement with the computed critical drawdown. Well B2 for instance, doesn't appear in the list of the wells were sanding was produced during DSTs. However, computed CDDP predicted some sanding at the depth of the perforation (Zahirin *et al*, 2010).

CONCLUSIONS

Geomechanical studies of the available thirteen wells have been performed. The mechanical earth model and wellbore stability analysis performed to assess mechanical properties and stresses that have been used for sanding analysis. A preliminary petrophysical and rock physics analysis of log data from these wells allowed to calculate synthetic logs where data are missing. The main results are:

Phase 1: Data Audit & Rock Physics

Good logging coverage: Density, GR, CAL, VCL, PHIE, SW available for all wells, P-Sonic available for 11 wells, S-Sonic for 4 wells. Editing performed to fill gaps and correct bad obvious

reading. Synthetic curves generated using Neural Network technique. For the overburden, synthetic density logs have been generated.

Phase 2: 1D Mechanical Earth Models and Wellbore Stability Analyses

Different correlations have been used to calculate the mechanical properties (elastic and strength). Used correlation from the dynamic to static Young's modulus well fits laboratory tests results. Correction from the dynamic to static Poisson's ratio in sands not applied given the high dispersion and low correlation of experimental data Calibration of strength properties (UCS, FANG) in sands has been performed based on tests results.

Wellbore stability models are in agreement with reported drilling events. It is observed that some manageable wellbore damage has been generated during drilling, damage can be quantified at about 10% (Depth of Damage).

Wells stress models are calibrated on wellbore stability analyses. Direct measurements of the least principal stress at casing point leak off test (LOT, ELOT) were not available in any of the 13 wells. Only formation integrity tests (FIT) were performed. To improve the reliability of the least principal stress (minimum horizontal stress) estimation and reduce uncertainty appropriate stress measurements are necessary.

Phase 3: Sanding Analysis

Laboratory tests results rank Lower Acacus sands from very weak to weak. Grain size is a fundamental input parameter in sanding analysis. In order to include Grain Size variability along the analyzed sections Neural Networks method has nine (9) sanding analyses have been performed, all analyses confirm occurrence of sanding in some critical sections at actual reservoir pressure. Predicted sanding on existing wells is in a good agreement with observation from DST.

No influence of perforation orientation is observed due to a very limited stress anisotropy inferred from the stress model calibrated on wellbore stability analyses. Sanding is mainly controlled by UCS.

REFERENCES

Assef, M. H. and Ni, Q. (2018). Numerical Modeling of Onset and Rate of Sand Production in Perforated Wells. *Jour. Petr. Explor. Prod. Tech.,* **8 (4)**: *https://doi.org/10.1007/s13202-018-0443-6.*

Binti, A. I. A.; Brandt, I.; Gunasekera, D.; Hatveit, B.; Havre, K.; G. Weisz and Xu., Z. G. (2015) Multiphase Flow Simulation Optimizing Field Productivity. *https://www.slb.com/~/media/Files/resources/oilfield_review/ors15/spr15/03-multiphase-flow. The Oil field Review,* **(1)**: 26–37.

Case Study-Brazil (2013). Petrobras Enhances Reservoir Performance With Geomechanics Evaluation in Water Injection Operation. *http://www.slb.com/resources/case_studies/dcs/reservoir_consulting/geomechanics_offshore_brazil_cs.aspx.*

Gang, H.; Shepstone, K.; Harmawan, I.; Jusoh, U. H.; Sue Lin, L. and Pringle, D. (2011). A Comprehensive Study of Sanding Rate from A Gas Field: from Reservoir to Completion, Production, and Surface Facilities. *SPE Journal,* **16 (2)**: *463–81. https://doi.org/10.2118/123478-PA., 2011*

John, C.; Frederiksen, R. A.; Hasbo, K.; Green, S.; Judzis, A.; Martin, J. W. and Suarez-Rivera, R. (2007). Rocks Matter: Ground Truth in Geomechanics. *https://www.slb.com/~/media/Files/resources/oilfield_review/ors07/aut07/rocks_matter.pdf Oilfield Review* **19 (3)**: *36–55., 2007*

Kumar, S. S.; De Groot, L. and Graven, H. (2014). An Innovative Approach for Sand Management with Downhole Validation. *Soc. Petr. Eng.,* **15 (2)**: *https://doi.org/10.2118/168178-MS.*

Zahirin, R. M.; Frydman, M.; Sepulveda, W.; Garcia, G.; Benavides, M. and Matulevich A. (2010). Integrated Approach: Perforation System Optimization for Sand Prevention. *Soc. Petr. Eng.,* **14 (1)**: *https://doi.org/10.2118/128569-MS.*

CHARACTERIZATION OF LIBYAN CRUDE OILS AND ITS HEAVY FRACTIONS

Abdurazag A. Shebli* and Alhadi A. Elakrimi**

Abstract: Characterization of crude oil and its heavy fractions is a necessity to understand and predict their behavior. During production, transportation and processing, various problems such as solids deposition, clogging and coking can occur due to the presence of heavy components in oil. When it comes to the heavier fractions of petroleum, modern analytical methods are not able to fully isolate and characterize the molecules. Crude oils from different origins (Breaga, Sirtica and Bouri) were used in this study. Breaga and Sirtica crude oils are classified as an intermediate crude oils while Bouri crude oil is classified as a heavy one that has shown asphaltene deposition problems. The softening point for the vacuum residues of the three crudes was determined and it was found 42, 40 and 60 for Breaga, Sirtica and Bouri respectively. Compositional studies and structural characterization of the original crude oils and their asphaltenes and maltenes fractions were carried out to study a possible relationship between their properties and asphaltene deposition behavior. Structural characterization is carried out using various techniques including Fourier Transform Infrared Spectroscopy (FT-IR), Softening Point (SP) and Thermogravimetric Analysis (TGA and DTA).

Based on the FT-IR results, the asphaltenes have the highest degree of the aromaticity followed by the maltenes and parent crude oils, respectively. Among the asphaltenes materials studied, Bouri asphaltene has the highest aromatic nature as deduced from the absorption at 1600 and 700-900 cm-1.

The TGA results show that the weight loss of samples decreased with the increase of the heavy fractions. The asphaltenes sample exhibits a relatively lower weight loss comparing to the rest of samples over the whole temperature interval studied. This agrees with the fact that these samples have the highest heavy fraction, which indicates the presence of less volatile constituents than the other samples. This finding is consistent with the FT-IR analyses.

Keywords: Libyan Crudes, heavy fractions, Asphaltenes and Maltenes.

INTRODUCTION

Petroleum is a fossil fuel formed through millions of years under the earth's surface. Dead animals, plants and other microorganisms decayed and buried under sedimentary rock. When these are subjected to heat and pressure over time, petroleum is formed Petroleum is a naturally occurring, yellowish-black liquid found in geological formations beneath the Earth's surface. It is commonly refined into various types of fuels. Components of petroleum are separated using a technique called fractional distillation (www.differencebetween.com/difference-between-crude-oil-and-vs-petroleum, 2018; en.wikipedia.org/wiki/Petroleum, 2018).

*Libyan Petroleum Institute, P.O. Box 6377, Tripoli, Libya.
Email: a.shebli@lpilibya.com
**Department of Chemical Engineering, University of Tripoli, Libya.

The hydrocarbons in crude oil are mostly alkanes, cycloalkanes, various aromatic and a small amount of asphaltenes and resins. Its compounds contain nitrogen, oxygen and sulfur, and trace amounts of metals such as iron, nickel, copper and vanadium. Petroleum is vital to many industries and can be defined as a mixture of hydrocarbons with various molecular weights. These hydrocarbons may be aliphatic, aromatic and branched or un-branched. Hydrocarbons with a lower molecular weight (ex: methane, ethane, propane and butane) form the gases while hydrocarbons (ex: pentane, hexane and so on) form the liquids and solids. Paraffin and waxes are an example of solid hydrocarbons in petroleum. The proportion of each compound in petroleum differs from one crude to another.

Crude oil is a complex mixture of hydrocarbons and heteroatomic organic compounds of varying

molecular weights and polarity. Crudes with high levels of sulfur are known as sour crudes, whilst those with low levels are known as sweet. Heavy fractions of crude oils at atmospheric pressure and ambient temperature can be separated into four groups: saturates (alkanes, paraffins & naphthenes), aromatics, resins, and asphaltenes (Alsaffar *et al*, 2001 and Freitag & Verkoczy, 2005).

During production, transportation, various problems such as solids deposition, clogging and coking occur due to the presence of heavy components in oil. In addition, asphaltene precipitation is a common problem in oil industry throughout the world. In many instances, these deposition phenomena render in complete clogging of flow lines and serious damage to storage vessels and processing equipment. Consequently, characterization of crude oil and heavies is necessary to be able to understand and predict their behavior. Molecules in the heaviest fractions of petroleum cannot be fully isolated and characterized by modern analytical methods. Instead, they are fractionated and classified into different categories which lead merely to definitions that are workable, but they are far away from identifying exact structures.

The number of individual components in a hydrocarbon cut increases rapidly with its boiling point and the family analysis is given by mass spectrometry, one may prefer a distribution by type of carbon. This can be done by infrared absorption spectrometry which also has other applications in the petroleum industry. While a set of structural patterns can be detected by Nuclear Magnetic Resonance (NMR) of hydrogen (or carbon); this can thus describe the average molecule in the fraction under study. Characterization can be based on single carbon number or on compound class. A compound class characterization common in industry is SARA (Saturate, Aromatic, Resin and Asphaltene) characterization (Kiefer, 2015 and Hao *et al*, 2017).

Heavy oil is about 70% of the total crude oils (James, 1996). Asphaltenes are possibly the most studied fraction and yet it is the least understood materials in the petroleum industry. Everything about asphaltenes appears to be non-conclusive, elusive, and complex. However, asphaltenes have attracted numerous researchers with varied views and research approaches, varying from practical modelling approach to ivory tower study of asphaltenes molecular structures. It is considered the least valuable component of the crude oils. The presence of asphaltene cause a marked increase in crude oil viscosity, making it difficult to transport and process. Characterization of crude oil and heavies is necessary to be able to understand and predict their behavior, some analysis of typical asphaltenes samples from various sources illustrate significant and characteristic difference between the compositions of asphaltenes derived from several different sources. Maltenes remained after the precipitation of asphaltenes by n-alkanes are subjected to liquid chromatography the components eluted by the more polar solvents are called resins.

The aim of this work is to characterize some of Libyan crude oils (Brega, Sirtica and Bouri) and their heavies in terms of chemical structure by various characterization techniques such as thermogravimetric (TGA), Fourier transform infrared spectroscopy (FTIR) spectroscopy and general crude oil tests (API gravity, pour point, asphaltene contents and n-Heptane insoluble, etc.).

The characterization data obtained for the heavy components of crude oils and residues namely asphaltenes and maltenes can be used to improve thermodynamic model being developed for wax precipitation. Its applicability to other predictive models is also possible.

EXPERIMENTAL WORK

Bouri, Brega, and Sirtica crude oils and their vacuum residues are used in this study. They are selected as part of a program oriented to evaluate the feasibility of producing carbon fiber precursors from Libyan oil residues. Some properties of those crude oils and their vacuum residues are compiled in Tables 1 and 2, respectively (Petroleum Research Centre, Internal Report, 1994).

Vacuum Residues Preparation

25 liters of each crude oil were distilled in the Kontes Martin (ASTM D2892) apparatus under atmospheric pressure to 175^{o}C and then under vacuum at a pressure of 10 mm Hg to 400^{o}C. The vacuum is distilled on the Sarina High Vac (ASTM P196) still at 0.3mm Hg to 565^{o}C. The vacuum residues obtained from these three crude oils (Bouri, Breaga and Sirtica) were coded as (BVR, BrVR and SVR).

Asphaltene Precipitation

Separation of asphaltene content from the samples, the vacuum residue of Bouri (BVR), Brega (BrVR) and Sirtica (SVR) was carried out as follows:

Table 1. General characteristic of BCO, BrCO and ACO

Property	*Bouri Co.*	*Sirtica Co.*	*Briga Co.*
API	25.86	41.11	42.44
Asphaltene	3.3	0.46	0.16
Total Sulfur	1.86	0.42	0.22
Pour Point °C (°F)	+9 (+48)	-9 (+16)	-9 (+16)
kinematic viscosity (υ) At 100°F	18.62	2.935	2.696
n.-Heptane Insoluble	21.3	0.84	0.41

Table 2. General characteristic of BrVR, SVR and AVRTable.3A Bouri Crude Oil General Tests

Property	*Bouri VR*	*Sirtica VR*	*Briga VR*
API	4.30	9.39	11.78
S	3.36	1.38	0.74
PP °C	+69	+51	+51
V & N (ppm)	60 & 69	11.3 & 28.4	7.8&4.7
HI	81.8	1.7	0.64
Aspaltenes	14.4	3.2	2.7
Yield %	25.1	12.6	10.1

Keys *VR Vacuum Residue*, PP Pour: Point (°C), S: total Sulfur, HI: n Heptane Insoluble, V: Vanadium, N: Nickle

n- heptane is used as a solvent for the precipitation of the asphaltenes from the crude oil sample. A 40: 1 ratio of n- heptane to sample is used then digested in an ultrasonic path for 24 hours, until the precipitation occurs.

It is important to remember that asphaltenes are a solubility class. Initial sample weight of up to 35 grams. Precipitated asphaltenes are separated by vacuum filtration, dried in an oven and weighed. Maltenes are isolated from the filtrate by rotary evaporation. Figure 1 shows schematic of apparatus used for Separation of Asphaltene.

Infrared spectroscopy

The IR spectra were used for characterization of the molecular nature of the samples; Bouri Crude Oil (BCO), Breaga Crude Oil (BrCO) and Sirtica Crude Oil (SCO) together with their asphaltenes and maltenes, where obtained with IFS-25IR spectrophotometer. The solid and viscose samples are measured and placed uniformly on pre-weighed KBr windows. While the liquid ones are measured in IR cuvettes. IR spectra where used for a qualitative comparison of molecular nature of the samples.

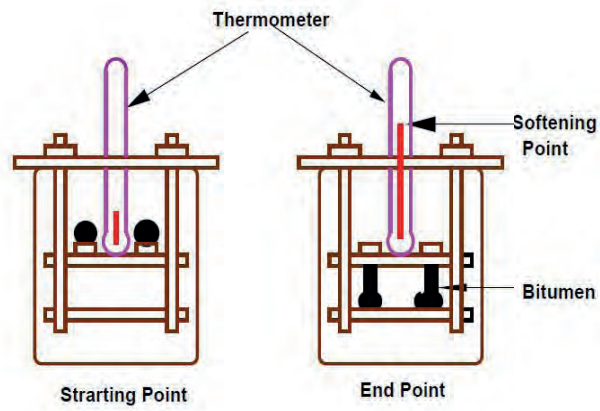


Fig. 1. Schematic of apparatus used for separation of asphaltene.

Thermogravimetric analysis

To gain a better knowledge of the chemical composition of the samples above stated in IR spectroscopy, the samples were characterized with thermogravimetric analysis. TGA/DTG measurement was conducted in DTG50. At the samples were deposited on Aluminium cell, using samples mass of ~ 10mg, with heating rate of 10c/min over the 293-873k° (20-600°C) temperature intervals.

Softening point

Generally, there are several methods such as Mettler Softening Point, Hot Stage Microscopy and Ring-and-Ball method for determining the softening temperature and the temperatures measured by these different methods vary to some extent from each other. In this study, the softening point of pitches was determined by a ring-and-ball method according to a standard ASTM procedure (D36-86). Two horizontal disks of pitches (2gr.), cast in shouldered brass rings, are heated at controlled rate in a liquid bath (glycerin) while each supports a steel ball. The softening temperature is reported as the mean of the temperatures at which the two disks soften enough to allow each ball, enveloped in pitch sample, to fall a distance of 25mm. Figure 2 shows assembly of the apparatus of softening point measurements used in this study.

RESULTS AND DISCUSION

Materials

The parent crude oils (Bouri, Brega and Sirtica) and their vacuum residues were subjected to different characterization analysis, the results of which are compiled in Tables 3 and 4 (Petroleum Research Centre, Internal Report, 1994).

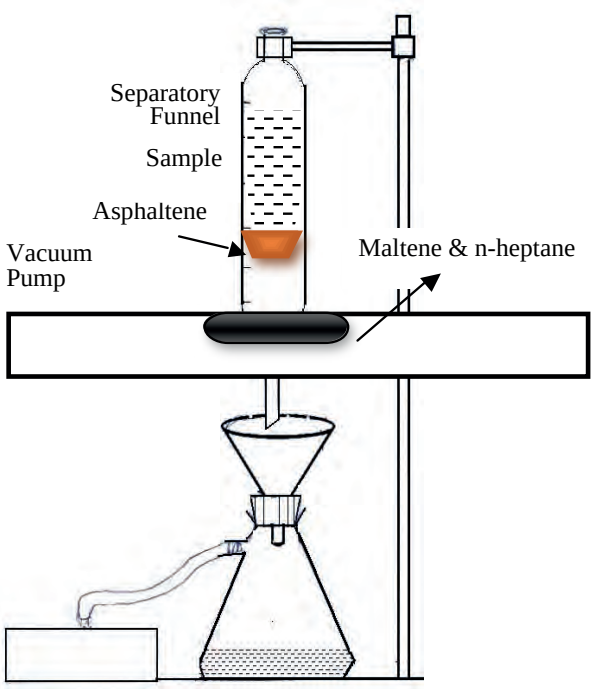


Fig. 2. Assembly of the apparatus used for softening point measurements.

Bouri Crude Oil

Bouri is close to Middle-East than N. African crude. It is classified as an intermediate crude oil having a gravity of 25.9°API and a total sulphur content of 1.86wt%.

Bouri crude has a pour point of 9°C and a kinematic viscosity of 57.4cSt at 21.1°C. For a heavy crude, both vanadium, nickel and conradson carbon content are moderate at 28ppm and 2.3wt% respectively. However, compared to other heavy crudes, Bouri has an unusually high n-heptanes insolubles content of 21.3wt%. The crude contains about 2vol% pentane and lighter components and has a Reid vapor pressure of 3.3psi (Table 3).

Bouri Vacuum Residue

Table 4 shows the general properties of Bouri vacuum residue. In addition to its extremely high n-heptanes insolubles content (approx. 80wt%), Bouri vacuum residue also has a high pour point of 69°C. Since it cannot be used as visbreaker feedstock, it is only possible to produce reduced pour point heavy fuel oils if a considerable amount of middle-distillate is used as cutter stock.

It may not be possible to produce a vacuum residue cut point as high as 565°C without encountering some coking problems in the vacuum heater or in the vacuum column due to asphaltene precipitation.

Table.3. Bouri Crude Oil General Tests.

Property	Result	Method
Density @ 15°C g/ml	0.8987	IP 365/D4052
Specific Gravity @ 60°F	0.8992	Calculation
API Gravity @ 60°F	25.86	Calculation
Characterisation Factor	11.7	Calculation
Total Sulphur % wt.	1.86	IP 336/D4294
Mercaptan Sulphur ppm wt.	46	IP 342 Mod/ D3227 Mod
Total Nitrogen % wt.	0.169	IP 379 Mod/ D4629 Mod
Pour Point °C (°F)	+ 9 (+ 48)	IP 15/D97
Viscosity @ 70°F, cSt	57.41	IP 71/D445
Viscosity @ 100°F, cSt	18.62	IP 71/D445
Vanadium ppm wt.	14.0	IP 377 Mod
Nickel ppm wt.	12.6	IP 377 Mod
Sodium ppm wt.	5.7	IP 377 Mod
Calcium ppm wt.	3.7	IP 377 Mod
Potassium ppm wt.	0.3	IP 377 Mod
Conradson Carbon % wt.	2.3	IP 13/D189
Asphaltenes % wt.	3.3	IP 143
n-Heptane insolubles % wt.	21.3	D893
Reid Vapour – Pressure KPa (psi)	23 (3.3)	IP 69/D323
Flash Point °C (°F)	< –20 (< – 4)	IP 170
Hydrogen Sulphide ppm wt.	< 1	IP PM – BJ
Neutralisation Number, mg KOH/g	0.07	IP 177/D664
Bottom, Sediment and Water % vol.	< 0.05	IP 359/D4007
Ash content % wt.	< 0.01	IP 4/D482
Salt (as NaCl) mg/litre (lbs/1000 bbls)	1.8 (0.63)	D3230

In practice it is possible that the vacuum residue cut point may have to be restricted to 500°C (or less). Only a commercial operation could determine this practical cut point, as laboratory testing is not representative.

Providing a market can be found for high sulphur coke, Bouri vacuum residue could be used as coker feedstock for the production of fuel grade coke. Due to its low penetration value it is unlikely that Bouri vacuum residue could be used as feedstock for bitumen manufacture. However, it is possible that a blend of Bouri and other Libyan vacuum residues (i.e. Es Sider) could be used as bitumen plant feedstock.

Table 4. Bouri Yields and Inspections of vacuum Residue.

Property	Result	Method
Boiling Range °C	565+	Method
Vol. % on Crude	21.7	
Wt. % on Crude	25.1	
Density @ 15 °C g/ml	1.0413	IP 365/D4052
Gravity°API	4.30	Calculation
Specific Gravity @ 60° F	1.0419	Calculation
Total Sulphur % wt.	3.36	IP 336
Pour Point °C (°F)	+69	IP 15/D97
Viscosity @ 100°C, cSt	13,230	IP 71/D445
Nickel ppm wt.	60.3	IP 377 Mod
Vanadium ppm wt.	69.3	IP 377 Mod
Micro Carbon Residue % wt.	28.4	ASTM D4530
Asphaltenes % wt.	14.4	IP 143
n-Heptane insolubles % wt.	81.8	ASTM D893
Molecular Weight	> 500	Calculation
Calofric Value MJ/Kg gross	41.52	Calculation
Calofric Value MJ/Kg gross	9917	Calculation
Sodium ppm wt.	24.3	IP 377 Mod
Calcium ppm wt.	14.0	IP 377 Mod
Potassium ppm wt.	1.1	IP 377 Mod
Ash content % wt.	0.036	IP 4/D482

Breaga Crude Oil

Table 5 shows the general properties of Breaga crude oil. It is classified as a paraffinic intermediate crude oil having a gravity of 42.4°API and a total sulphur content of 0.22wt%. The crude is lighter than some other Libyan crudes and therefore, its product quality and structure is closer to that of an Algerian rather than a North Sea crude. The crude flows readily at room temperature with a viscosity of 5.3cSt at 21.1°C and a pour point of -9°C. A nickel and vanadium content are 0.5 and 0.8ppm respectively are extremely low even for a light, low sulphur crude. The conradson carbon residue content of 1.5wt% is about average for this type of crude, approximately 7.6vol% of the crude consists of pentane and lighter components. The Reid vapour pressure is 7.8psi.

Breaga Vacuum Residue (BrVR)

Table 6 shows the general properties of Breaga vacuum residue. Due to its low sulphur and metals content, Breaga vacuum residue is excellent coker feedstock for anode grade production. Due to its high penetration value, Breaga vacuum residue is not suitable as feedstock for bitumen manufacture.

Table 5. Brega Crude Oil General Tests.

Property	Result	Method
Density @ 15°C g/ml	0.8131	IP 365/D4052
Specific Gravity @ 60°F	0.8135	Calculation
API Gravity @ 60°F	42.44	Calculation
Characterisation Factor	12.2	Calculation
Total Sulphur % wt.	0.22	IP 336/D4294
Mercaptan Sulphur ppm wt.	44	IP 342 M/ D3227 M
Total Nitrogen % wt.	0.09	IP 379 Mod/ D4629m
Pour Point °C (°F)	- 9 (+ 16)	IP 15/D97
Viscosity @ 70°F, cSt	5.293	IP 71/D445
Viscosity @ 100°F, cSt	2.696	IP 71/D445
Vanadium ppm wt.	0.8	IP 377 Mod
Nickel ppm wt.	0.5	IP 377 Mod
Sodium ppm wt.	2.5	IP 377 Mod
Calcium ppm wt.	1.5	IP 377 Mod
Potassium ppm wt.	0.3	IP 377 Mod
Conradson Carbon % wt.	1.50	IP 13/D189
Asphaltenes % wt.	0.16	IP 143
n-Heptane insolubles % wt.	0.41	D893
Reid Vapour – Pressure KPa (psi)	54 (7.8)	IP 69/D323
Flash Point °C (°F)	< –20 (< –4)	IP 170
Hydrogen Sulphide ppm wt.	< 1	IP PM – BJ
Neutralization Number, mg KOH/g	0.09	IP 177/D664
Bottom, Sediment and Water % vol.	< 0.05	IP 359/D4007
Ash content % wt.	< 0.01	IP 4/D482

Sirtica Crude Oil (SCO)

Sirtica is classified as an intermediate crude oil having a gravity of 41.1°API and a total sulphur content of 0.42wt% (Table 7). Its product quality and structure are close to that of Zuetina, except it is a little more naphthenic. Sirtica Crude Oil has a pour point of -9°C and a viscosity of 4.5cSt at 21.1°C and flows readily at room temperature. Its conradson carbon residue content of 2.1wt% is about normal for this type of crude. Approximately 7.1vol% of the crude consists of pentane and lighter component sand it has a Reid vapor pressure of 7.8psi.

Sirtica Vacuum Residue

Sirtica vacuum residue has a nickel +vanadium content of approximately 40ppm, a Sulphur content of 1.38wt% and a pour point of 51°C (Table 8).

Table 6. Brega Yields and Inspections of vacuum Residue.

Property	Result	Method
Boiling Range °C	565+	Method
Vol. % on Crude	8.3	
Wt. % on Crude	10.1	
Density @ 15 °C g/ml	0.9870	IP 365/D4052
Gravity°API	11.78	Calculation
Specific Gravity @ 60° F	0.9876	Calculation
Total Sulphur % wt.	0.74	IP 336
Pour Point °C (°F)	+51	IP 15/D97
Viscosity @ 50°C, cSt	30,000 *	D341
Viscosity @ 80°C, cSt	-	IP 71/D445
Viscosity @ 100°C, cSt	565.4	IP 71/ D445
Nickel ppm wt.	4.7	IP 377 Mod
Vanadium ppm wt.	7.8	IP 377 Mod
Micro Carbon Residue % wt.	16.7	ASTM D4530
Asphaltenes % wt.	2.7	IP 143
n-Heptane insolubles % wt.	0.64	ASTM D893
Molecular Weight	590	Calculation
Calofric Value MJ/Kg gross	43.35	Calculation
Calofric Value MJ/Kg gross	10354	Calculation
Sodium ppm wt.	25.0	IP 377 Mod
Calcium ppm wt.	15.0	IP 377 Mod
Potassium ppm wt.	0.9	IP 377 Mod
Ash content % wt.	0.021	IP 4/D482

* No Flow at temperature / Extrapolated using D341

Table 7. Sirtica Crude Oil General Tests.

Property	Result	Method
Density @ 15°C g/ml	0.8194	IP 365/D4052
Specific Gravity @ 60°F	0.8198	Calculation
API Gravity @ 60°F	41.11	Calculation
Characterisation Factor	12.1	Calculation
Total Sulphur % wt.	0.42	IP 336/D4294
Mercaptan Sulphur ppm wt.	110	IP 342 Mod/ D3227 M
Total Nitrogen % wt.	0.12	IP 379 Mod/ D4629 M
Pour Point °C (°F)	- 9 (+ 16)	IP 15/D97
Viscosity @ 70°F, cSt	4.534	IP 71/D445
Viscosity @ 100°F, cSt	2.935	IP 71/D445
Vanadium ppm wt.	1.5	IP 377 Mod
Nickel ppm wt.	3.5	IP 377 Mod
Sodium ppm wt.	18.6	IP 377 Mod
Calcium ppm wt.	4.7	IP 377 Mod
Potassium ppm wt.	0.4	IP 377 Mod
Conradson Carbon % wt.	2.1	IP 13/D189
Asphaltenes % wt.	0.46	IP 143
n-Heptane insolubles % wt.	0.84	D893
Reid Vapour – Pressure KPa (psi)	54 (7.8)	IP 69/D323
Flash Point °C (°F)	< –20 (<–4)	IP 170
Hydrogen Sulphide ppm wt.	< 1	IP PM – BJ
Neutralization Number, mg KOH/g	0.10	IP 177/D664
Bottom, Sediment and Water % vol.	< 0.05	IP 359/D4007
Ash content % wt.	< 0.01	IP 4/D482

However, heavy fuel oils of reduced point can be made by using vacuum residue as visbreaker feedstock and back blending, the visbreaker residue with FCC light cycle oil and decant oil. Despite its metal content, Sirtica vacuum residue has a relatively high carbon residue content and is therefore, suitable as coker feedstock for the production of anode grade cock. Sirtica vacuum residue has both moderate penetration value and asphaltenes content. If required, it be used as feedstock for bitumen manufacture. However, due to its superior quality it is unlikely that its use as bitumen feedstock could be economically justified.

Characterization of Samples by Thermogravimetric (TGA)

Thermogravimetric analysis records the weight loss of a sample as the temperature is raised at uniform rate. Figure 3 shows TGA of the parent crude oils. For all the three crude oils weight loss occurs as first stage beginning at temperature 26C° and ending at 600°C. The values of weight loss at 600°C, 94.54% BCO, 97.33% BrCO and 100% for SCO. The weight loss of BCO was lower than the weight loss of BrCO and (SCO). As expected these results indicated that Bouri Crude Oil consists of a higher percentage of heavy fraction (i.e. asphaltene).

Figure 4 shows TGA of Bouri crude oil (BCO) and its asphaltene, maltene and vacuum residue. In this case, weight loss occurs as a multiple step beginning at temperatures in the range 50-400°C and ending at 570-600°C. The magnitudes of weight loss at 600°C was 94.54% (BCO), 48.96% asphaltene (BA), 94.04% maltene (BM), and 83.35% Bouri vacuum residue. These results indicated that the magnitudes of weight loss at

Table 8. Sirtica Yields and Inspections of vacuum Residue.

Property	Result	Method
Boiling Range °C	550+	Method
Vol. % on Crude	10.3	
Wt. % on Crude	12.6	
Density @ 15 °C g/ml	1.0038	IP 365/D4052
Gravity°API	9.39	Calculation
Specific Gravity @ 60° F	1.0042	Calculation
Total Sulphur % wt.	1.38	IP 336
Pour Point °C (°F)	+51	IP 15/D97
Viscosity @ 50°C, cSt	100,000 *	D341
Viscosity @ 100°C, cSt	1108	IP 71/D445
Nickel ppm wt. Vanadium ppm wt.	28.4 11.3	IP 377 Mod IP 377 Mod
Micro Carbon Residue % wt.	16.5	ASTM D4530
Asphaltenes % wt.	3.2	IP 143
n-Heptane insolubles % wt.	1.7	ASTM D893
Molecular Weight	530	Calculation
Calofric Value MJ/Kg gross	42.85	Calculation
Calofric Value MJ/Kg gross	10,235	Calculation
Sodium ppm wt.	25.4	IP 377 Mod
Calcium ppm wt.	10.9	IP 377 Mod
Potassium ppm wt.	0.6	IP 377 Mod
Ash content % wt.	0.012	IP 4/D482

600°C increase in the order of parent crude oil< maltene< asphaltenes, respectively. It should be noted the same trend for the Breaga and Sirtica crude oils and their fractions have been observed as shown in (Figs. 5 and 6).

As expected, the weight loss of samples decreased with increase in the heavy fractions. The asphaltene sample exhibits a relatively lower weight loss than the rest of samples over the whole temperature interval studied. This agrees with the fact that this sample has the highest heavy fraction, which indicates the presence of less volatile constituents than the other samples. This finding is consistent with the IR and NMR analysis.

Characterization by Infrared Spectroscopy

Infrared spectroscopy (IR) has found increasing use as instrumental analysis methods for coal, pitch, carbon fiber, and other carbon materials (El Akrami *et al*, 1997; Putzig *et al*, 1992; Guillien *et al*, 1992). This spectroscopy has been used to identify various types of hydrocarbons (aliphatic,

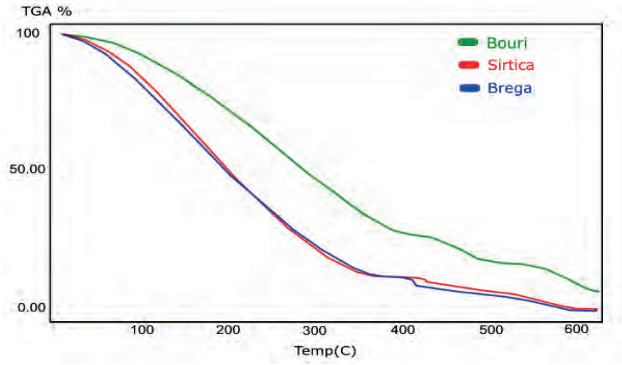


Fig. 3. TGA of the parent crude oils (Breaga, Sertica and Bouri).

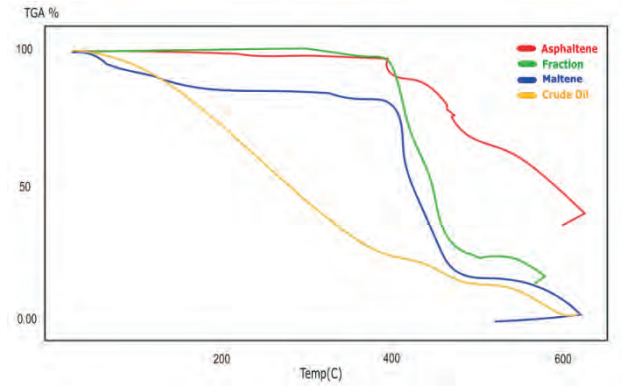


Fig. 4. TGA of Bouri crude oil (BCO) and it's asphaltene (A), maltene (M) and vacuum residue (Fraction F).

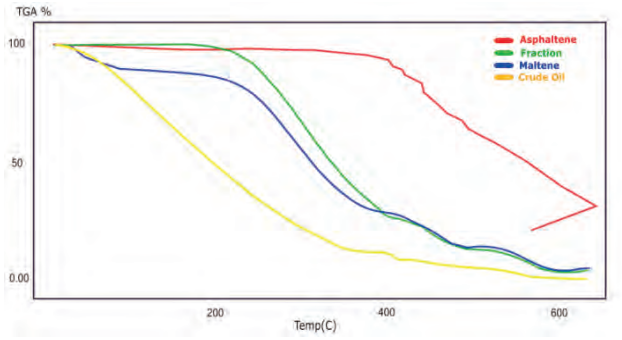


Fig. 5. TGA of Breaga crude oil (BrCo) and it's asphaltene (A), maltene (M) and vacuum residue (Fraction F).

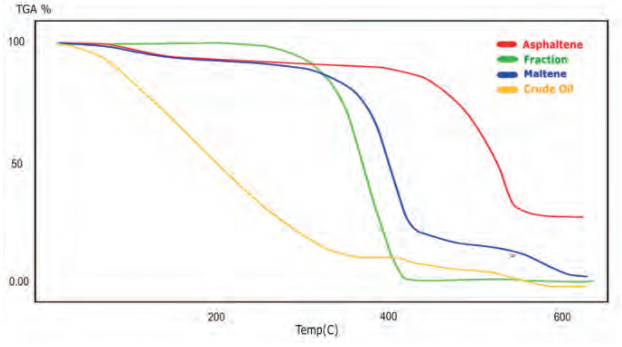


Fig. 6. TGA of Sirtica crude oil (SCO) and it's asphaltene (A), maltene (M) and vacuum residue Fraction (F).

aromatic, etc.) and functional groups that are present overlapped bands.

Figure 7 shows the IR spectra of the parent (BVR) and solvent extracted fractions (asphaltene and maltene). The spectra show characteristic absorption bands corresponding to aromatic structures at (3050, 1600, 870, 810,750cm-1) and aliphatic structures at (2960, 2922, 2855, 1450, 1379cm-1) Reference (El Akrami *et al*, 1997) The bands at 3050cm-1 in the spectra are mainly attributed to the stretching mode of C-H aromatic hydrocarbons, while the bands in the 1600cm-1 region are assigned to the stretching of aromatic C=C groups. Bands in the region 900 to 700cm-1 are usually assigned to the out-of-plane bending of aromatic C-H groups. The bands in the 2970-2700 and the bands in the 1450-1377cm-1 are due to the stretching and bending modes of saturated aliphatic hydrocarbons, respectively (El Akrami *et al*, 1997). The broad strong band observed at 1400-1600, and the sharp strong bands at 2150 and 2300 cm-1 are due CS_2 which was used as solvent for some of the samples. It should be noted that the bands at 1600 and 1450cm-1 are overlapped.

Compared to asphaltene fraction, the maltene, which constitute the bulk of the BVR, appear to have a lower degree of conjugation (or ring condensation) and less substitution on the aromatic rings in view of the higher hydrogen aromaticity as inferred from the higher intensity of the composite bands at 700-900cm-1. The maltene fraction was found to be more paraffinic than the asphaltene fraction. The whole BVR gave a spectrum that is very similar to that of the maltene. The asphaltene, on the other hand, is the most aromatic fraction of the BVR sample, as can be seen from the comparison of the intensities of the respective aliphatic and aromatic with those of other samples. In Figure 8 the IR spectra of parent crude oils showed that the relative intensities of aliphatic C-H bands (CH_2 and CH_3; 3000-2850cm-1) were stronger than those of aromatic C-H band (around 1600cm-1), and CH_2 bands (around 2927cm-1) stronger than those of CH_3 bands (around 2954cm-1). This indicates that these materials contained significant amounts of aliphatic components, especially naphthenic rings (Seshadri *et al*, 1985). The sharp strong bands at 2927cm-1 clearly arise from the saturated C-H stretching vibrations of alkyl substituents (methylene groups -CH_2) and the very weak bands near 3050cm-1, suggests that the aromatic rings are highly substituted. In general, the absorbances at 3050 and 2927cm-1 allow evaluation of the concentrations of aromatic and aliphatic bonds in the samples (Seshadri *et al*, 1985).

Figure 9 shows the infrared spectra of the asphaltenes fractions. Sirtica asphaltene exhibited a very weak band at 1600cm-1, the intensity of which is higher for the Bouri and Breaga asphaltenes Moreover the aliphatic C-H bands (2855-2960cm-1) and methylene/naphthenic C-H bending bands (1450cm-1) of Sirtica asphaltene were more intense than those of the Bouri and Breaga asphaltenes, indicating that most of the alkyl groups are in methylene or naphthalene form. Among the asphaltenes materials studied, Bouri asphaltene showed the highest aromatic nature as deduced from the absorption at 1600 and 700-900cm-1.

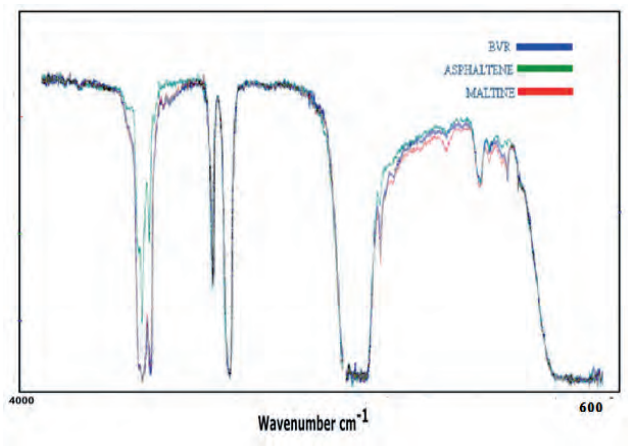


Fig. 7. IR spectra of the parent (BVR) and solvent extracted fractions.

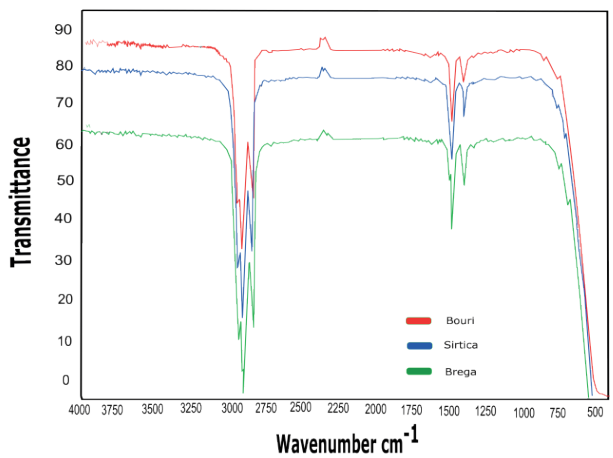


Fig. 8. IR spectra of the parent crude oils (Bouri, Sirtica and Brega).

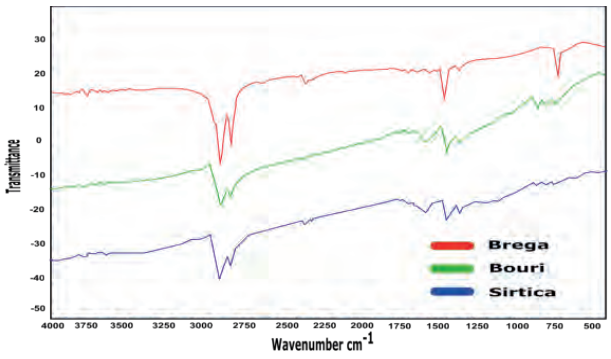


Fig. 9. IR spectra of the asphaltenes fractions.

CONCLUSIONS

Based on the results obtained in this study and the conditions under which they are obtained the following conclusions can be drawn.

- Due its high softening point and asphaltene content the Bouri vacuum residue is promising material as carbon fibre precursors.
- Due to its low sulphur and metals content, Breaga vacuum residue is excellent coker feedstock for anode grade production.
- Sirtica vacuum residue has both moderate penetration value and asphaltenes Content. It is possible that it could, if required, be used as feedstock for bitumen manufacture.
- Providing a market can be found for high sulphur coke, Bouri vacuum residue could be used as coker feedstock for the production of fuel grade coke.
- Vacuum distillation was an effective method in increasing the softening point of the crude oils.
- Vacuum distillation promoted the dehydrogenation and aromatization through reduction of aliphatic hydrogen.
- Structural characterization by softening point and IR showed that distillation of lighter fractions increased the softening point and dehydrogenation raised their aromaticity.

REFERENCES

Alsaffar, H. B., Hasanin, H., Price, D. and Hughes, R. (2001). Oxidation reactions of a light crude oil and its SARA fractions in consolidated cores. *Energy Fuels*, **V. 15**(1):182-188.

Difference Between Crude Oil and Petroleum [WWW Document] *http://www.differencebetween.com/difference-between-crude-oil-and-vs-petroleum 2018.*

El akrami, H. A., Yardim, M. F., Akar, A. and Ekinci, E. (1997). FT-IR Characterization of Pitches Derived from Avgamasya Asphaltite and Raman-Dincer Heavy Crude Oil. *Fuel*, **V. 76(14/15)**: 1389-1394.

Freitag, N. P. and Verkoczy, B. (2005). Low-temperature oxidation of oils in terms of SARA fractions: why simple reaction models don't work. *J Can Pet Technol*, **V. 44**, 54–61.

Guillien, M. D.; Iglesias, M. J.; Dominguez, A. and Blanco, G. (1992). Semi-Quantitative FT-IR Analysis of a Coal Tar Pitch and its Extracts and Residues in Several Organic Solvents. *Energy & Fuels*, **V. 6**: 518-525.

Hao, J. H.; Che, Y. J.; Tian Y. Y.; Li, D. W.; Zhang, J. H. and Qiao, Y. Y. (2017). Study on Thermal Cracking Characteristics and Kinetics of Oil Sand Bitumen and its SARA Fractions by TG–FTIR. *Energy Fuels*, **V. 31(2)**:1295-309.

James, G. S. (1996). Petroleum and Refining, *Western Research Institute*, Laramic, Wyoing U.S.A, **15**: 3-5.

Kiefer, J. (2015). Recent Advances in the Characterization of Gaseous and Liquid Fuels by Vibrational Spectroscopy. *Energies*, **8**: 3165-3197.

Petroleum [WWW Document] *https://en.wikipedia.org/wiki/Petroleum 2018.*

Petroleum Research Centre (1994). Evaluation of Libyan Crude Oils. *Internal Report*: 132p.

Putzig, C. L.; Leugers, M. A.; Mckelvy, M. L.; Mitchell, G. E.; Nyquist, R. A.; Papenfuss, R. R. and Yurga, L. (1992). Infrared Spectroscopy. *Analytical Chemistry*, **V. 64**: 270-302.

Seshadri, K. S.; Young, D. C. and Cronauer, D. C. (1985). Characterization of Coal Liquids By 13C N.M.R. and FT-IR Spectroscopy-Fractions of Oils of SRC-I and Asphaltenes and Preasphaltenes of SRC-I and DRC-II. *Fuel*, **V. 64**: 22-28.

EXOTHERMIC CHEMICAL TREATMENT (ECT), TOWARDS OPTIMIZING HEAVY CRUDE PRODUCTION OF AL HARAM FIELD, CONCESSION 47, SIRT BASIN, LIBYA, USING ECT TECHNOLOGY

Abdelgader Kernaf and Ales Mrkva*

Abstract: In today's oil and gas world, there is an ongoing demand for Enhanced Oil Recovery Techniques (EOR). Operators look for the best available solutions to optimize production from heavy crude fields which were not put on production due to lack of technologies suitable for the individual field nature, type of reservoir, pressure and most important of all, technologies that are economically feasible and environmentally friendly. Libya's capability to boost its oil production is strongly dependent on innovative extraction technologies. Particularly in the case of the 1billion barrel Al Haram Field. Many years of scientific research and technical innovation gave birth to the Exothermic Chemical Treatment (ECT) by New Oil Generation (NOG). This EOR technology is a modern method for thermal stimulation of oil reservoirs containing crude oil ranging from 10 to 30 API. ECT uses Binary Mixtures of Chemicals, containing non-explosive and non-hazardous aqueous solutions, injected to the wellbore into the pay zone within the production or injection well to stimulate the reservoir. Chemical reaction generates three key components: heat, nitrogen and pressure, which leads to increasing reservoir pressure and lowers the viscosity of heavy oil. Thus, ECT achieves rapid improvement of oil production. On line monitoring and controlling system of temperature and pressure in the reaction zone, provides efficiency coefficient of Binary Mixtures reaction that are close to 1. Successful application of ECT in Russia and USA, proved the technology as the most cost- effective method at the present day. Comparing the geology and nature of reservoirs of the case histories on which ECT was applied, they are found to be very similar to those of the Al Haram Field. That makes ECT the most invaluable technology to assist Libya in boosting its heavy crude oil production in the safest and most economical way.

Keywords: Binary mixture, exothermic chemical treatment, oil well stimulation, enhanced oil recovery, case study.

INTRODUCTION

The one billion barrel Al Haram Field in Libya (Fig. 1) has been a challenging one for heavy crude production since many years. It is not only containing heavy crudes which are difficult to produce using conventional production methods, moreover, these heavy crudes are of a waxy nature causing them to jam when transported through production lines and when is under room temperatures.

Charged by Sirte Shale, main reservoirs at the Al Haram Field are Rachmat Carbonate, and Bahi/ Hufrah clastics and Hufrah quartzites. Source rocks of lacustrine nature are thought to be the main cause for the waxy oils at Al Haram, with critical times at Eocene to Oligocene (Hallet and Clark-Lawes, 2016).

Arabian Gulf Oil Company (AGOCO), one of Libya's major National Oil Corporation Exploration and Production Companies was looking for an Enhanced Oil Recovery method suitable for the field nature. Reservoir conditions and simultaneously an economically feasible method to extract heavy oils in the field with minimum cost, and in light of the today's world of rapidly changing oil prices. In the past, Libya has applied basic forms of EOR on most of the pressure declined fields which are no longer capable to maintain production on the prevailing conditions. These forms of EOR as the so called primary Enhanced Oil Recovery Techniques or methods such as Water Injection, gas injection and sometimes pumps were deployed in Libya and Particularly in Concession 103 Intisar D reef which is part of the prolific Sirt Basin where water flooding and gas injection were used.

*New Oil Generation, U Laboratore 1102/2, Prague, Czech Republic.
Email: info@newoilgeneration.com

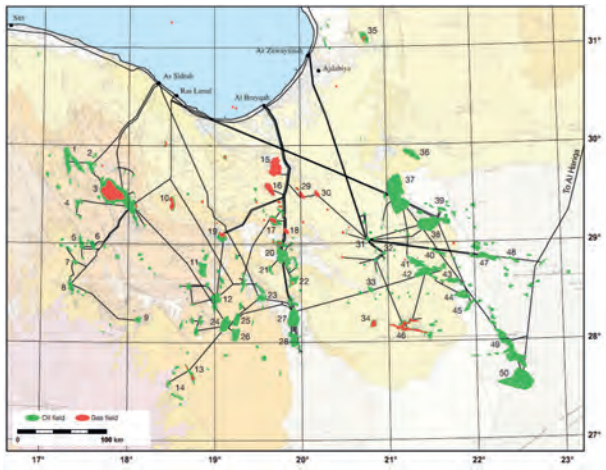


Fig. 1. Location map of the Al Haram Field among the neighbouring fields in Libya. Highlighted with a blue square and numbered 11 on the map (Source: Nubian Consulting Ltd., Geological map of Libya, 1985).

Nowadays, the Al Haram Field requires a more sophisticated technological innovation to produce the waxy heavy oils and maintain production rates at the field. This is where Exothermic Chemical Treatment (ECT) proved to be the most viable solution. Taking into account the nature of the Carbonate reservoir which is very similar to both Oil Field in Turkey and Tatarstan which undergone successful ECT application in recent years. (ECT) is offering a new technology of EOR, which brings the adequate response to production improvement, where issues encountered by operators are dealt with such in the case of production drop.

Important economy driver of the ECT is the high efficiency of impact combined with low costs in comparison with other EOR methods. The time needed for deployment of EOR system in the field is counted in weeks only. However, the effect is instantaneous and tangible improvement of production is immediately noticed.

The technology is often referred to as Binary Mixture-Technology (BM-Technology) which stimulates oil reservoirs by producing heat and pressure and by an oil combustion chemical reaction (oxidizing process with the oil). Therefore, it is a multiple stage enhanced oil recovery technology. In combination with high pressure generated during the chemical reactions and heat in the reservoir, the viscosity of oil is lowered and oil flow is increased in productive wells or renewed in non-productive or stripper wells. Hence, ECT solution is very effective in old wells where they could be rejuvenated putting back on production. The technology was developed and tested in Russia and Europe for more than 15 years. The method and technology itself have been patented globally.

Single EOR treatment could be done during the standard service works on the well to spare the time of a workover rig and shorten the service time when the borehole is unproductive as much as possible. Table 1 shows the range of use of the ECT method that combines effects of three other EOR methods. ECT as a thermal EOR method is comparable primarily with steam stimulation. Table 2 shows comparison between ECT and CSS EOR method especially in terms of energy consumption and harmful gases (greenhouse gas) emission.

Theory of Exothermic Chemical Treatment

Principle of the Exothermic Chemical Treatment (ECT) technology is based on a chemical reaction called Binary Mixture (BM). Binary Mixtures are special designed water solutions of the chemicals in specific concentrations. The composition of these chemicals has been tested for a long period to maximize the energy efficiency of the components on the oil reservoir taking into consideration preserving the economy and using available chemicals in conventional chemicals markets. Through the reaction of Binary Mixtures in the production well or injection well, high amount of heat, gas and pressure are generated. One of these chemicals acts as fuel in this process and the second chemical as an oxidizer. Additional heating proceeds due to the fact that oxygen produced in a heated bed oxidizes the fraction of oil within the formation.

TESTS AND PROCEDURES

The initial laboratory tests of reaction of Binary Mixtures were performed in Russia and in the field in 2007. Operating formulations and 1st generation of the system of continuous monitoring and optimization of BM reaction in the wells has been developed and were then successfully applied in the fields of the Perm region and the Komi Republic - Usinsk deposit oil field. It has also been granted permission to pump BM into the well without limiting its mass. In 2014, an experimental study was conducted of the conditions of exothermic reaction of BM and its effect of reaction products on oil at high temperatures and pressures. This study includes experimental laboratory tests in a specially designed, high pressure chamber, where reservoir conditions were simulated during the BM reaction in the oil formation. The study also dealt with the

Table 1. The range of the ECT method.

Thermal EOR	Gas EOR	Chemical EOR	Hydrodynamic EOR
• Steam treatment (cycling injection or continuos steam injection) • In situ combustion • Hot water flooding • Cyclingsteam treatment	• Air injection • Light hydrocarbons injection • Carbon dioxide injection • Nitrogen, flue, and others gases injection	• Surfactant flooding (including foam) • Polymer displacement • Alkaline displacement • Acid displacement • Chemicalreagents displacement (includingmicellar polymer flood, etc.) • Microbiological treatment	• Surfactant flooding (including foam) • Polymer displacement • Alkaline displacement • Acid displacement • Chemical reagents displacement (including micellar polymer flood, etc.) • Microbiological treatment

ECT

corrosion effect of components and reaction products where an assessment of safety and environmental risks was made with a proposal to minimize them. The basic components of BM are chemicals that are used by ECT technology on oil well stimulation which are essentially in aqueous solution. Due to the specific characteristics of BM chemicals, safety regulations for handling BM Chemicals were elaborated clearly. The produced document has been prepared by a specialized company, which provides the industrial safety assessments. Moreover, due to the possible corrosive effects of BM on metal well completion components, extensive BM tests were performed at certain pressure and temperature.

Used Equipment

ECT technology is designed to stimulate heavy oil wells by Huff & Puff or Injection / Production method. The basis of this technology is pumping two aqueous solutions of chemicals into the well through separate channels (tubing in tubing) and their reaction bellow the packer in special designed (NOG) Injection Spearhead, generating heat, gas and pressure. Specific proportions of Binary Mixtures are pumped simultaneously into the well. After pumping all the chemicals, minimal amount of water is used to remove all chemicals from tubing. The used equipment is divided into two parts:

Table 2. Comparison of ECT technology and CSS stimulation.

Parameter	CSS	ECT	Unit
Oil Production	1	1	m^3 / day
Water consumption	3,05	0,08	m^3 / day
Fuel consumption for 1 m^3 of oil	8-10	0,4	GJ / m^3
SOR	3	0,08	m^3 / m^3
Water losses in reservoir (10%)	0, 3	0	m^3 / day
CO_2 Emission	0,6	0	kg / day
SO_2 Emission	0,01	0	kg / day
NO_x Emission	0,08	0	kg / day
Water recycling	85	90	%

NOG Surface Equipment:

- Compact mobile high pressure pumping system.
- Quick and safe connection to tanks with chemicals and well through the NOG Interface.
- Electronic monitoring and controlling system – SW and HW tools for the process management, real time data collection from downhole pressure and temperature sensors and pumping control.

NOG Bottom Hole Assembly (BHA):

- Mechanical set packer integrated with NOG Data Concentrator.
- NOG Injection Spearhead.
- Pressure and temperature sensors above the packer.
- Pressure and temperature sensors below the packer.
- Temperature sensor in reaction zone.

Operator contributions are work over rig, tubing, wellhead and ESP cable.

Conducted Technology Tests

The technology was tested in laboratory conditions and in real downhole conditions during the first pilot tests. The laboratory tests were

mentioned above. After every downhole application, the state of technology was thoroughly assessed and all technology parts were evaluated in terms of mechanical wear and the influence of high pressure and temperature and also corrosive effect.

Equipment Evaluation

Based on this technology field test, the technology was developed and a compact mobile high pressure pumping system with electronic monitoring and controlling system accompanied the evolution of technology. Real time data collection from downhole pressure, temperature sensors and pumping control including specially integrated bottom hole assembly were evolved and approved too. Technology has been recently successfully tested on heavy oil fields in Turkey, USA and Russia in the year of 2012-2017 and assisted in elevating production rates effectively.

RESULTS

The typical pilot of ECT oil well stimulation is prepared in four steps:

1. Data collecting: Gatehering all reservoir and well available data.
2. NOG analysis: The well treatment programme is prepared including the expected effect on increased oil production.
3. NOG on location: NOG team together with engineer and geologist will consult and agree on the "treatment issues" and finally approve the progress of the work and submit the treatment documentation.
4. NOG conduct ECT: Treatment on the oil well according to the agreed procedure, following that NOG submits the final report on the application with a proposal for further potential stimulation.

Of the previously implemented applications we have chosen stimulation performed on the deposits of similar type to the Al Haram Heavy Oil Field, the main field of the Kotlah Graben, with Rachmat Carbonate. These two ECT stimulation were performed on Oil Filed in Turkey and in Russia. In Table 3 we provide basic stratigraphic data about oil reservoirs. Reservoir in Lower Carboniferous, the chosen case history reservoirs mentioned earlier, have characteristics relatively well comparable with Al Haram Field reservoirs. Garzan Limestone in Turjey has a reefal origin and a fractured, vuggy character. Average porosity of 18% and is mainly vugular and fissured in type. Average matrix permeability determined from cores is -16mD. Well tests indicate 200 to 500mD effective permeabilities, confirming the contribution of secondary porosity. The layer of Tournai Series is composed of fractured and cevernous-porous limestone. Separate interlayers are dolomitized with stylolite sutures. Average porosity is 16 % and is mainly porous and fissured in type. Average matrix permeability is determined from cores to be -70mD. Well tests Effective permeabilities from well test vary from 100 to 180 mD. Basic reservoir characteristic are given in Table 4.

Al Haram Field was discovered in the early1960s. First exploration well was D1 in Concession 47 and S1 was the first development

Table 3. Basic Stratigraphic Data.

System / Period	Epoch	Formation	Lithology	Reservoir
Upper Cretaceous	**Mastrictian** **Camoanian** **Santonian** **Conician** **Turonian**	**Garzan** **Rakhmat**	**Limestone** **Carbonates**	**Turkey** **Haram**
Jurassic				
Triassic				
Permian				
Lower Carboniferous	**Tournaisian**	**Tournai Series**	**Limestones**	**Russia**

Table 4. Basic Reservoir Characteristics of Oil Fields.

Reservoir	Turkey	Russia
Type of reservoir	Oil Saturated	Oil Saturated
Net Pay (m)	40	8
Depth (m)	1300	1380
Reservoir temperature (°C)	65	26
Reservoir pressure (MPa)	12,4	10,3
oAPI	12	22
GOR (m3/m3)	5	8
Porosity (%)	21	16
Permeability (mD)	60	70
Oil Saturation (%)	76	74
Gas Saturation (%)	11	12
Water Saturation (%)	13	14
WOC	6	5
Initial Oil Production	12,5	14

well which was drilled 3 years later than D1 well. Two years later more wells were drilled. The field was never put on production due to the at the time uneconolical nature of the heavy crudes within. High viscosity of (27cp at reservoir temperature of 81 and 380cp at `38), 21.9oAPI and a pour point of 21. The OOIP for Haram Oil Field is estimated as high as 950 MMSTB. All these put the Al Haram Field on hold for production until a new technology arises and a change in the industry takes place enabling successful production at reasonable production costs. The field consists of three reservoir horizons, starting with Gargaf at the bottom and the oldest in age. These three horizons are:

1. The Gragaf Group which is a fractured quartizite and is of (Cambro-Ordovician) age.
2. Bahi Formation is a quartzitic sandstone comprising the middle reservoir unit or horizon and is (Upper Cretaceous) in age.
3. The Haram Members (Tagrifet) are bioclastic limestones which are (Upper Cretaceous) in age as well and which the field was named after.

Haram reservoir is very similar in characteristics to the case histroy reservoirs in Turkey and in Russia. This is a very encouraging factor in deploying ECT in the Al Haram Field as it will definatly give great results and will boost and maintain commercial production rates. There are two assumptions as for the origin of the waxy heavy crudes in terms of occurance which are thermal maturity and biodegradation. Having the Al Haram Field at shallower depth than the neighbouring fields within Concession 47 gives favor to the first assumption of decreased thermal maturity and depth of burial of the kichens. That led to the waxy heavy crudes in addition to the lacustrine deposits (Source rocks) out of which the the hydrocarbons had formed.

As shown in the tables parameters of the treated oil fields are similar to those of the Al Haram Oil Field, therefore, we consider the Al Haram Oil Field appropriate for the pilot test. To support this assumption, we further outline the case study results of ECT application on oil field in Russia. The pilot test was performed in 2016. The total duration of the test, including well completions for applications and putting back into production lasted 7 days. This application achieved all treatment objectives with regards to temperature and pressure profiles as well as treatment duration profiles. Overall, it was concluded that the test was performed successfully within the parameters defined. only standard oil well operator equipment workover rig, hook load 40t, pump track, geophysical log truck, swabbing unit work over rig crew and the service facilities were used for the treatment: low and high pressure chemicals pumps, downhole pressure and temperature sensors, control unit, bottom hole assembly-packer, injection spearhead and BM chemicals. The volume of 33tons of BM was pumped into the well in 55 hours and these maximum values of temperature and pressure were reached in the reaction zone-temperature 278°C and pressure 17.6MPa. Two breaks were made during the application. Firstly, in order to check reaction control-immediate stop of reaction and restart-with successful results. Secondly, the reaction was stopped due to surface tubing valve leakage, tubing valve leakages were fixed quickly by the well operator and the reaction started again successfully. After the application, the downhole parameters were monitored and then the bottomhole assembly was pulled out of hole and the well was completed by PCP pump and put back to production. In (Fig. 2) treatment measured data is shown. In this case, 64 GJ of heat energy was released, 550 m3 of gas. The Production was increased up to 10 times from 1.5 to 15m3/day. The effect of production increasing lasted 107 days.



Fig. 2. Treatment Measured Data.

CONCLUSIONS

- Good results were achieved on carbonate reservoir oil fields with production rates enhanced substantially.
- All performed processes and procedures achieved major treatment objectives with regard to temperature and pressure profiles as well as treatment duration profiles.
- Theoretically, predicted parameters during the application and the results were obtained and confirmed with the production history after stimulation.
- During application, there were no difficulties or system failures detected and the whole system were found to be reliable, safe and encouraging to be deployed in other similar parameter oil fields.
- Oil production increased from heavy / medium oil reservoirs and was 6 – 10 times confirmed increase.
- When the heavy oil field in Turkey was treated, significant contribution of gas was seen generated during ECT increasing oil production. The field had experienced large scale applied CO^2 flooding reservoir stimulation.
- Al Haram Heavy Oil Field exhibits very similar petroleum system. This makes it a suitable candidate field for ECT technology deployment capable of lifting and mobilizing crudes with magnificent amounts which cannot be obtained otherwise.
- The three reservoir horizons of fractured quartizites, quartzitic sandstone and bioclastic limestones are favourable for ECT application. Fractures here communicate chemicals between layers and aid in the overall thermal heating of the heavy crudes and thus, increase production.

ACKNOWLEDGEMENT

The Authors are indebted to CEO of New Oil Generation S.R.O Czech Republic Mr Jakub Hodinar for the continuous support and the spirit of sharing knowledge and technical innovation with academia and the industry.

REFERENCES

Geological Map of Libya (1985). *Nubian Consulting Ltd.*

Hallet D. and Clark-Lawes D. (2016). Petroleum Geology of Libya, **2nd Edit**., 392p. Elsevier.

DISPLACEMENT OF HEAVY OIL BY CARBON DIOXIDE IN A TUBE

Mohammed Almabrouk A. Ahmad* and Parthasakha Neogi**

Abstract: After using primary and secondary oil recovery methods, about two third of the original oil in place is left behind in the reservoir. Enhanced Oil Recovery (EOR) methods are being used to recover that oil. Carbon dioxide (CO_2) flooding is one of the enhanced oil recovery (EOR) methods that is used to recover the oil. The interest here lies in recovery of heavy crude oil in a capillary tube with a radius of micrometer scale and that oil is displaced by carbon dioxide (CO_2). The dissolution of CO_2 in oil reduces oil viscosity and swells it, making it easier to displace the oil. In immiscible displacement of viscous liquid (heavy crude oil) in a tube by a gas with lower viscosity than the liquid (Carbon dioxide CO_2), a gas bubble moves steadily and leaves behind a thin liquid film of thickness h_∞, which is known as the Bretherton problem.

ANSYS® FLUENT software is used to solve the problem of CO_2 displacing heavy oil in a tube. Different velocities, capillary numbers (Ca) and different tube radii are used as an input into ANSYS® FLUENT software to solve different cases. The oil film thickness that left behind (h_∞) is reported both without mass transfer and with mass transfer.

The oil film thickness that is left behind, h_∞ (in the case of fluid mechanics) is decreased when capillary number/bubble velocity is decreased. That was the case for all different radii and different velocity inputs. When there is no mass transfer, the non-dimensional film thickness left behind h_∞/R plotted against capillary number fits Bretherton line. With a small capillary number and a radius of 1μm, the shape of the profile of the CO_2 bubble is a hemisphere and the oil film thickness that is left behind (h_∞) is very small. At large capillary number (10^{-1} for R= 1μm) and small radius (0.1μm), the profile shape of the CO_2 bubble is pointed. At the center-line of the tube there is no pressure drop in the gas phase nor in the liquid phase, however, most the pressure drop takes place across the interface. Even under mass transfer of CO_2 into oil, bubbles show Bretherton-type behavior. The thickness of thin residual oil film decreases in the presence of mass transfer, leading to an increase in oil recovery. In addition, the oil film thickness that is left behind (h_∞) with mass transfer is less than the oil film left behind without mass transfer. Convection in this case opposes the mass transfer and limits how much CO_2 can dissolve in oil.

Keywords: Bretherton problem, carbon dioxide (CO_2) flooding, Enhanced Oil Recovery (EOR), heavy oil.

INTRODUCTION

Primary and Secondary Oil Recovery

Crude petroleum is found in underground reservoirs in sandstone or limestone rock formation. The rock are porous, of pores ~ 1μm. In the first stage of oil recovery, the oil is displaced from the reservoir into the wellbore and up to the surface under its own pressure. Initially, the reservoir pressure is considerably higher than the bottomhole pressure inside the wellbore. This high natural differential pressure drives hydrocarbons toward the well and up to surface. However, as the reservoir pressure declines because of production, so does the pressure differential. To reduce the bottomhole pressure or increase the differential pressure to increase hydrocarbon production, it is necessary to implement an artificial lift system, such as a rod pump, an electrical submersible pump or a gas-lift installation. Production using artificial lift is considered primary recovery. The primary recovery stage reaches its limit either when the reservoir pressure is so low that the production rates are not economical, or when the proportions of gas or water in the production stream are too high. During primary recovery, only a small percentage of the initial hydrocarbons in place are produced.

The second stage of hydrocarbon production during which an external fluid such as brine is injected into the reservoir through injection wells

*Raslanuf Oil and Gas Processing Company, Libya, m_almabrook85@yahoo.com
**Missouri University of Science and Technology, Department of Chemical Engineering, MO, USA.

located in rock that has fluid communication with production wells (Craig, 1971). The purpose of secondary recovery is to maintain reservoir pressure and to displace hydrocarbons toward the wellbore. The secondary recovery stage reaches its limit when the injected fluid brine is produced in considerable amounts from the production wells and the production is no longer economical.

One of the limitation of both primary and secondary recovery is about two third of the original oil in place is left behind in the reservoir. Of about 649 billion barrels of oil still in the reservoirs in the United States, 22 billion barrels only are recoverable by conventional means (Aladasani and Baojun, 2010). Thus, the target for enhanced oil recovery processes is a large one, indeed. With these kinds of shortcomings, plus the increasing global demand for oil, producers must look for enhanced methods of oil recovery.

Enhanced Oil Recovery

The development of enhanced oil recovery (EOR) processes has been ongoing since the end of World War II, when operators who owned reservoirs with declining reserves recognized sufficiently quantities of oil remained in the reservoirs after primary and secondary recovery. Research and field activity increased as production from main reservoirs declined, worldwide consumption increased, and discoveries of major new reservoirs become infrequent (Green and Willhite, 1998).

EOR processes can be classified into five categories: mobility-control, chemical, miscible, thermal, and other processes. Each process has its own history, potential, technology, opportunities and obstacles. Various types of EOR methods are described below in brief (Green and Willhite, 1998 and Fig. 1).

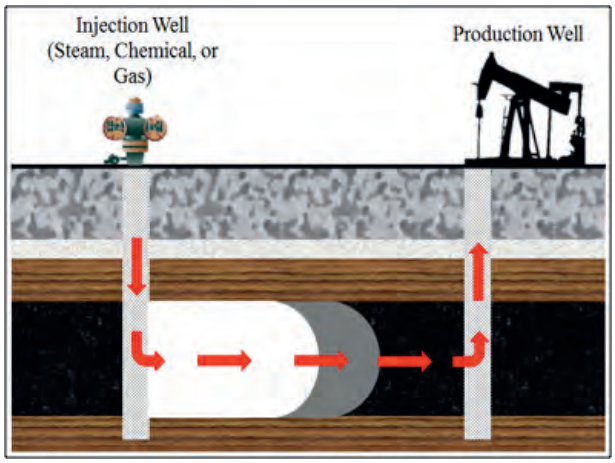


Fig. 1. Enhanced oil recovery methods.

Steam Flooding: This enhanced recovery method is used in heavy-oil reservoirs containing oils where the viscosity is a limiting factor. High temperature steam is generated on the surface then continuously introduced into a reservoir through injection wells. As the steam loses heat to the formation, it condenses into hot water, which, coupled with the continuous supply of steam behind it, provides the drive to move the oil to production wells.

In Situ Combustion: Heat can also be generated in the reservoir by injecting air and burning part of the hydrocarbon (in-situ combustion). Fortunately, only the coke formed from thermal cracking of the most viscous components gets burned. All the lighter components are swept to production by the remaining nitrogen from the injected air. This method is sometimes applied to reservoirs containing oil too viscous or "heavy" to be produced by conventional means. By burning some of the oil in situ (in place), a combustion zone is created that moves through the formation toward production wells.

Alkaline: An enhanced oil recovery technique in which an alkaline chemical such as sodium hydroxide is injected during polymer flooding or water flooding operations. The alkaline chemical reacts with certain types of oils forming surfactants inside the reservoir. Eventually, the surfactants reduce the interfacial tension (IFT) between oil and water and trigger an increase in oil production.

Surfactants: Surfactants can also be injected to reduce the IFT. Good recovery is seen when the IFT reaches ultralow values. By lower IFT gives rise to higher capillary numbers and higher recovery.

Polymers: This has been the most successful chemical EOR case. It enhances the mobility ratio and provides significantly between sweep. However, larger pressures are required. Some loss of polymer during the process is to be expected.

Carbon Dioxide Flood: Carbon dioxide (CO_2) is a common material normally used in the form of a gas and can be sometimes used to enhance the displacement of oil from a reservoir. It can be generated by burning some of the oil produced. It can also be obtained as a by-product from chemical and fertilizer plants, or it can be manufactured or separated from power plant stack gas. The latter case can be coupled to CO_2 sequestration plans (Meyer & Attanasi, 2003; Kovscek, 2002).

Even though CO_2 is not miscible with oil on first contact, when it is forced into a reservoir a miscible front is generated by a gradual transfer of smaller, lighter hydrocarbon molecules from the oil to the CO_2

and the transfer of CO_2 into oil by dissolution. This miscible front is in essence a bank of enriched gas consisting of CO_2 and light hydrocarbons.

This initial CO_2 slug is followed by alternate water and CO_2 injection, with water serving to improve sweep efficiency, that is, make the displacement more stable, and to minimize the amount of CO_2 required for the flood. As reservoir fluids are produced through production wells, the CO_2 reverts to a gaseous state there and provides a "gas lift". On the surface, the CO_2 can be separated from the produced fluids and may be re-injected helping to reduce the amount of new CO_2 required for the project; thus, the CO_2 can be re-cycled.

The main reason why CO_2 was introduced was that with multiple contacts miscibility could be reached (Hutchinson & Braun, 1961). This is not possible when the oil is heavy oil since heavy oil does not evaporate significantly. However, there are some other benefits in general mentioned earlier. When CO_2 dissolves in oil, it swells the oil, thus squeezing it out from narrow capillaries. In addition, on dissolution of CO_2 in oil, its viscosity decreases up to one order of magnitude (Chung *et al*, 1988). Of course, it is also the least expensive of all EOR processes. As a consequence CO_2 is being tried in oil fields even though CO_2 flooding is the most unstable and requires high pressure.

To quantify CO_2 flooding it is necessary to first know the physical properties of CO_2-oil mixtures. This has been addressed by many investigators and recently (Tran *et al*, 2012) have correlated the data of (Chung *et al*, 1988) using free volume theory. Such data are useful and can be used to study the displacement process.

Instead of simulating the displacement process in a reservoir, we have studied the displacement process in a single cylindrical pore. In the present system as CO_2 displaces heavy oil in a cylindrical capillary, CO_2 dissolves in the oil. This mass transfer process is accompanied by a rise in CO_2 diffusivity in oil, a lowering of viscosity of the oil and increasing in the volume of the oil. Thus, the problem is a moving boundary problem in fluid flow and mass transfer.

Fluid Mechanics

A key factor in brine flooding is the effect of brine-oil surface tension which gives rise to a large retention of oil. One process that has been suggested to recover the remaining oil is CO_2 flooding. Some oil evaporates into the gas phase and some CO_2 dissolves in the oil, leading to miscibility (Hutchinson & Braun, 1961). Miscibility cannot be attained in many heavy oil reservoirs however there are some advantages in using CO_2 flooding. CO_2 swells the oil squeezing it from narrow pores and crevices and it reduces the viscosity of the heavy oil by up to a factor of 10, thus decreases the pressures needed to move the oil. We analyze here the case of CO_2 displacing heavy oil in a single model pore.

When a gas flows into a tube filled with a liquid, it does so in form of a finger (Bretherton, 1961; Miller and Neogi) considered other cases available in literature, a liquid displacing a gas and liquid displacing another immiscible liquid, and summarized the results are shown in [Fig. 2 "A" is the displacing fluid (CO_2 here) and "B" is the displaced fluid (heavy oil)]. Fig. 2 (a) is at equilibrium and the rock is assumed to be preferentially wet by *A*. As the velocity of displacement is increased, the equilibrium contact angle increases from zero in (a) to a dynamic contact angle of more than 90º (as measured through phase *A*) in (b) and finally to 180º in (c). At yet higher velocities entrainment takes place as shown in (d).

A number of additional observations are:

(i) If the rock is preferentially wet by *B*, then the system starts from equilibrium at (b) and moves down to (c) and (d) with increasing speed.

(ii) The viscosity ratio is χ = viscocsity of A/ viscosity of B. If χ is near zero (as for a gas displacing a liquid), the transition to (d) occurs at such low velocities that (a)-(c) are practically not

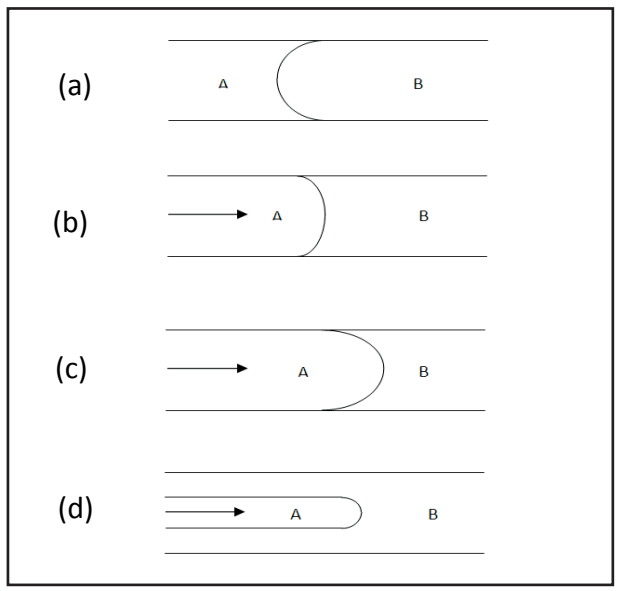


Fig. 2. Fluid B is being displaced by fluid A. (a) shows equilibrium and that B is fully non-wetting. (b) and (c) show the dynamic contact angles α (measured through A) increases with increasing displacement velocity U. Finally in (d) the contact line has entrained.

observed. Conversely, if χ is very high (as for a liquid displacing a gas), the transition occurs at very high velocities.

The problem shown in Fig. 2 (d) is called the Bretherton Problem (Bretherton, 1961) who showed that the thickness of the film of *B* left behind was determined by hydrodynamics.

The Model: Fig. 3 shows a sketch of the Bretherton problem: a tube with radius R, an inlet pressure p* drives a CO_2 finger with viscosity μ_1 and density ρ_1 into a fluid (heavy oil) of viscosity μ_2, density ρ_2, and surface tension γ. Carbon dioxide enters to the tube at steady speed U and leaves a film of thickness h_∞ behind. It is been assumed that the system remains symmetric about the tube's centerline.

Modeling Setup: The mesh of the computational domain for this problem was created in the preprocessor (GAMBIT 2.4.6). For ease of design, the geometry of the mesh was created with R equal to 1μm and L equal to 20μm and then it can be scaled up or down in FLUENT. The geometry of the computational domain is shown in (Fig. 4). After creation of the geometry, the boundary types were specified. As illustrated in the figure, the tube has four edges: inlet, outlet, wall and centerline, it is half tube and then it can be axisymmetric in FLUENT to have whole tube. The inlet edge set to be 0.4 μm. After creation of the geometry, the boundary types were specified.

A good mesh should not contain any distorted elements as the CFD analysis can be used only for regular element shapes. The mesh was then exported to FLUENT. The exported mesh was opened in FLUENT 14; there it can be scaled up or down to the required dimensions.

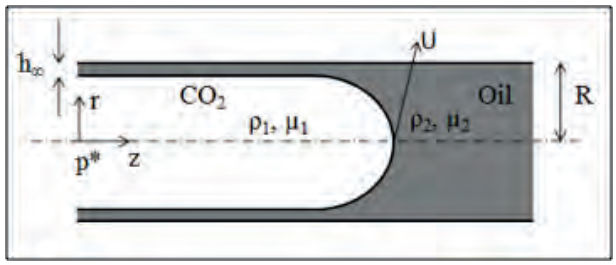


Fig. 3. A sketch of the model problem: a CO2 finger propagates into a Oil-filled tube.

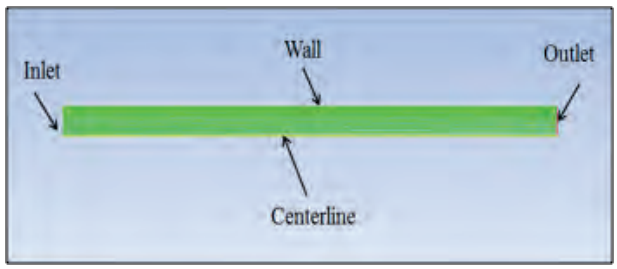


Fig. 4. The mesh and the edges of the tube.

Fluid Flow: Bretherton, 1961solved this problem approximately. As the interest here is in mass transfer and the changes that occur in the physical properties from it, the problem is solved numerically using FLUENT. Also, inertia is included which has not been taken into account by Bretherton. Bretherton's result is:

$$\frac{h_\infty}{R} = 0.643(3Ca)^{\frac{2}{3}} \quad (1)$$

Where h_∞ is the thickness of the thin film that left behind and the capillary number $Ca = \mu U/\gamma$ where μ is the viscosity of liquid to be displaced and γ is the surface tension. *U* is the rate of movement of the gas bubble. Bretherton (1961) however, worked with tubes of large radii. In the porous rock formation that contains the crude oil, the lower pore radii drops to ~0.1μm and sometimes even lower. Here, the thin films will be greatly influenced by the disjoining pressure (Morrow, 1991). Teletzke *et al* (1988) solved the Bretherton Problem numerically where they included the disjoining pressures. They found that at very low displacement velocities, the effect of disjoining pressure dominates, but at larger velocities Bretherton's fluid mechanical results prevailed. Disjoining pressure has not been included because the interest in this work lies in larger capillary pressures that lead to thicker films that are left behind. Kreutzer *et al* (2005) have presented both experimental and theoretical results for movement at higher velocities. It appears from their profiles that the front of the gas-liquid interface is not a hemisphere but slightly pointed at high velocities.

Formulation for Fluent: The method used by FLUENT to solve free surface problems is the finite volume method (Wesseling, 2001) where the interface is neither sharp nor continuous. Near the interface, we have to have small volume elements otherwise the interface becomes too thick (Fig. 5). The interface is a wide band with varying volume fraction of the gas phase made narrow by decreasing the size of the volume elements.

As a result, whereas width of the elements in *z*-direction non-dimensionalized by *R* the tube radius, is kept at 0.1, the ones in *r/R* progressively shortened. From the centerline the cell size moves outwards in 0.1 nine times. The last section next to the wall is further divided ten times at 0.01 each, and again the last segment is again subdivided ten times with cell sizes of 0.001, and in one case the process repeated once again with a size of 0.0001. The reason for small

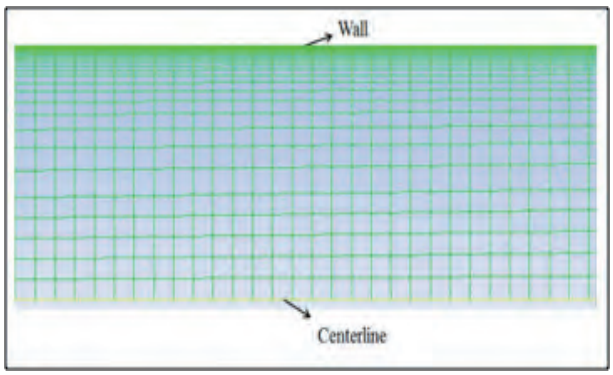


Fig. 5. The size of the volume elements in the mesh which getting smaller near the wall.

volume elements in the *r*-direction next to the wall is that the interface lies in this region and small elements makes the interface sharp. In addition, h_∞/R is a small number and smaller volume elements are needed to calculate this quantity accurately.

Physical Problem Formulation: The problem is treated as an unsteady state problem where CO_2 is introduced at the entrance in a tube of $L/R = 20$, filled with heavy oil. After initial transients, the gas finger moves at a steady rate U into the tube original filled with oil and leaving behind a lubricating layer of thickness h_∞. To keep the finger speed U steady, CO_2 is introduced at a constant volumetric flow rate at the entrance. Since this opening is kept smaller than the tube cross-section, U has to be measured separately by locating the nose tip of the finger ($z = z^*$) at different times and taking the slope. This slope is seen to be a constant. U is used to calculate the capillary number Ca.

This approach has a drawback that we cannot plan ahead to come up at a predetermined value of capillary number. We would like to take capillary number from 10^{-8} to 10^{-2} however it takes a very long time to work at small capillary numbers, so work was confined to 10^{-4} to 10^{-1} in keeping with the needs in EOR.

MASS TRANSFER

Carbon dioxide dissolves in oil that is being displaced, but oil is taken to be heavy oil and is assumed not to evaporate into the gas phase. Heavy oil has a specific gravity greater than 0.921 and viscosity greater than 100cp (Tran *et al*, 2012). The important feature is that when CO_2 dissolves in oil and the effect of mass transfer, thermodynamic and transport properties change significantly. Chung *et al* (1988) have reported detail data on the properties of Bartlett crude with and without CO_2. Tran *et al* (2012) have correlated these properties with free volume theory. Only one temperature 297.1K (75ºF) is considered and their results are:

Henry's law constant:

$H = 6.544 \times 10^4$ Pa(CO_2)/(kg/m^3)

Concentration of CO_2 in the oil at saturation in kg/m^3: $c_{sat} = p_{CO_2} / H$

and volume fraction:

$$\phi_{sat} = 1.06x10^{-3} p_{CO_2} / H$$

where p_{CO2} is the gas pressure in the Pa abs.

Swelling factor:

$$SF = \frac{1 - 5.917x10^{-5} p}{1 - \phi}$$

Where p is total pressure in atm.gage

Density in g/cm^3:

$$\rho = \frac{\phi}{1.06} + \frac{0.94921}{SF}$$

where $\phi = 1.06x10^{-3} c$ and c is the concentration in kg/m^3.

Viscosity in Pa.s:

$$\ln \mu = \ln(14.8435) + [\frac{1}{f + \phi 4.5244x10^{-2}} - 47.89]$$

Free volume fraction without CO_2 is:

$f = 0.02088 - 5.915 \times 10^{-5} p$

Diffusivity in m^2/s:

$$D = 5.14x10^{-13} e^{2.659c}.$$

The surface tension is (Rojas & Ali, 1988) in mN/m

$$\gamma = 22.626 + 2x10^{-5} p_{CO_2} - 8x10^{-10} p_{CO_2}^{\ 2}$$

Briefly, they show that oil swells under CO_2, viscosity decreases by up to one order of magnitude, and the diffusivity increases by an order of magnitude or more.

Consider Fig. 6. If it is assumed that there is no flow in the liquid film left behind, then

$$\pi R^2 < v > = \pi (R - h_\infty)^2 U \qquad (2)$$

where $<v>$ is the average velocity far from the nose of the bubble. In this region, the flow profile can be assumed to be the parabolic profile of Hagen-Poiseuille's flow. To consider the overall rate of mass transfer, a moving coordinate system can be envisioned.

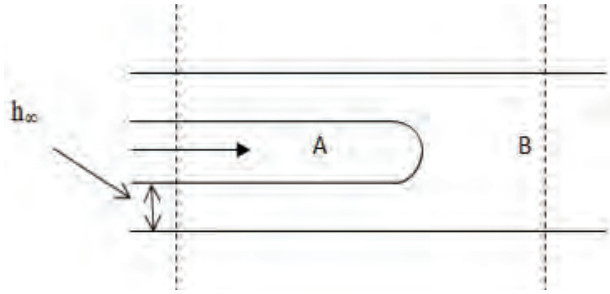


Fig. 6. A model of moving coordinate system.

CO_2 does not reach the station at the front, hence the only place CO_2 leaves the system is with the thin liquid film which can be considered to be saturated and velocity profile has a plug flow backwards at *U*. Hence the rate of mass transfer in mol/s:

$$M = \pi \left[R^2 - (R - h_\infty)^2 \right] . U c_{sat} \qquad (3)$$

where c_{sat} is the saturation concentration.

The Model

The model for the mass transfer is imposed on the fluid mechanics. Fig. 7 shows a sketch of the problem: a tube with radius *R*, an inlet pressure *p** drives a CO_2 finger with using coordinates (say affixed to the nose of the meniscus). It is possible to say that for steady displacement, no dissolved CO_2 would have reached the station downstream, all of the liquid upstream would be saturated and if there is zero shear at the liquid-gas interface then the velocity in the liquid would be plug flow at *U* backwards. Viscosity μ_1 and density ρ_1 into a fluid (heavy oil) of viscosity μ_2, density ρ_2, and surface tension γ. Also, it shows the gas volume fraction (ϕ_g) which set to be equal to 1.0 in the gas phase and it equals to 0.0 in liquid phase as it shown in (Fig. 7).

It also shows c_{sat} which is the concentration at the interphase. Carbon dioxide enters to the tube at steady speed U and leaves a film of thickness h_∞ behind.

Finite Volume

As mentioned earlier, when space is discretized into small volume elements, the exact location is of the interface lost. The gas phase is characterized by gas volume fraction ϕ_g = 1.0. The liquid phase by ϕ_g = 0.0. Across the interface, ϕ_g takes fractional values. Since the interface has disappeared, it no longer represents a discontinuity or singular surface (Slattery, 1999) hence no jump conditions are needed. In addition, the surface tension is included as a body force (Brackbill *et al*, 1992).

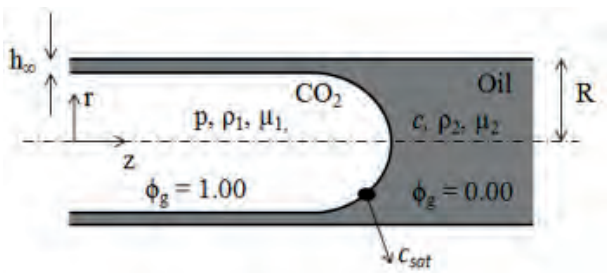


Fig. 7. A sketch of the model problem in presence of mass transfer.

The method used by FLUENT to solve free surface problems is the element of volume or the finite volume method (Wesseling, 2001). It uses a continuous variable ψ, which is 0 in the CO_2 phase and 1 in the oil phase. Since ψ changes continuously, the interface is a wide band which can be made narrow by decreasing the size of the volume elements (Gupta *et al*, 2009). Now, the interface *h* is located here by locating the element where $\psi \approx 0.5$. FLUENT calculates curvature 2*H* using a method that does not need *h*(*z*). It then uses -2*Hγ* where γ is the surface tension, which is the Laplace pressure, but it is not used as a surface force in the normal stress balance but it is used as a body force a weight that is proportional to the gradient of ψ (Brackbill *et al*, 1992).

Formulation

The equations of motion, continuity and conservation of species (CO_2) with continuous changes in properties across the interface, are solved to obtain, the velocity ***v***, pressure *p* and concentration *c*.

The fluids have been considered to be compressible, the viscosity and diffusivity dependent on the local pressure and concentration of CO_2, and the surface tension at the CO_2-oil interface and solubility of CO_2 there, have been taken to depend on CO_2 pressure. The expressions for the physical properties given above to be included in FLUENT as user define functions (UDF).

There is one exception to this. The outlet pressure in the fluid mechanical problem is set to zero. The net pressure difference is approximately estimated as $2\gamma/R^*$ where $R^* = R - h_\infty$, the radius of the gaseous tube. If *R** is approximated as *R* which is taken to be 1μm, then the upstream gas pressure is estimated to be about 0.5 atm. To keep the gas pressure down, at least in these calculations the reference viscosity of the heavy oil has been reduced to 1.5 Pa.s and not 14.8435 Pa.s as indicated above. Nevertheless, the flow remains in the low Reynolds number region and explicit algorithm is used.

As mentioned previously, at the entrance ϕ_g is forced to be 1.0 over an inner radius of 0.4μm for 1μm radius. This forces the gas into the system. At the interface, ϕ_g changes continuously but quickly to zero. Hence, in the algorithm in FLUENT for updating the concentrations is overridden to say that updated *c* is set to zero, if $\phi_g > 0.7$, $c = c_{sat}$ if $0.4 < \phi_g < 0.7$, but the updating is as is if $\phi_g < 0.4$. That is 0.4 to 0.7 is taken to be the interface.

Further, the knowledge of not only c_{sat}, but also of other quantities like γ, depends on the gas pressure at the interface. It was observed, that when the profile

is Bretherton-type (Fig. 6), the gas pressure at the interface is not significantly different from that at the entrance, that is $p(0,0)$, and this is the value used. Eventually, once the mass transfer iterations are completed, it is necessary to find h_∞/R to use in Eq. (3).

To obtain how the concentration of CO_2 varies in oil requires that we solve the conservation of species equation subject to the boundary condition that the concentration is c_{sat} at the gas-liquid interface. Instead of working with concentration c, we multiply the entire conservation of species equation with v = 1.06 cm^3/g, the specific volume of CO_2 in oil that was determined earlier for this crude oil (Tran *et al*, 2012). The result is that c is converted to volume fraction ϕ, and with a saturation value of ϕ_∞. In FLUENT, we set the inlet concentration to be ϕ_∞. After a time step, the new ϕ is reset to ϕ_∞ but only up to the interface. Thus, the hypothetical concentration of CO_2 "dissolved" in CO_2 is constant at ϕ_∞ right up to the interface beyond which conventional diffusion equation applies. The concentration on the right exit is set to zero.

RESULTS AND DISSCUSION

Fluid Flow Results

The procedure explained earlier was used to determine the profile shape of the CO_2 bubble in the tube with different tube radii and determine the film thickness that left behind, h_∞. It also calculated the pressures, in particular the centerline pressure as a function of axial position z. Note that the outlet pressure is set to zero, hence the pressures are all pressure drops and can also be taken to be the gage pressures. The relationship between capillary number and h_∞/R is also noted. In the calculations, three different radii have been used 10μm, 1μm, and 0.1μm with three different inlet velocities: 0.00168, 0.000168, and 0.0000168m/s. These two quantities were the main inputs to the FLUENT. Based on these inputs, the values of pressure (p), capillary number **(**Fig. 8). Profiles of the meniscus at Ca = 1.85x10^{-4} and R = 1μm (Ca), and the film thickness that left behind (h_∞) were seen to change. Additionally, the shapes of the profiles had different radii and moved with different velocities, when these inputs changed.

The results showed that h_∞ decreases as capillary number decreases in all cases. Also at large capillary numbers, the profile shape is pointed and for that case h_∞ cannot be measured because there were steps in the profile which never steadied upstream. Furthermore, small tube radius (0.1 μm) showed a fingering profile

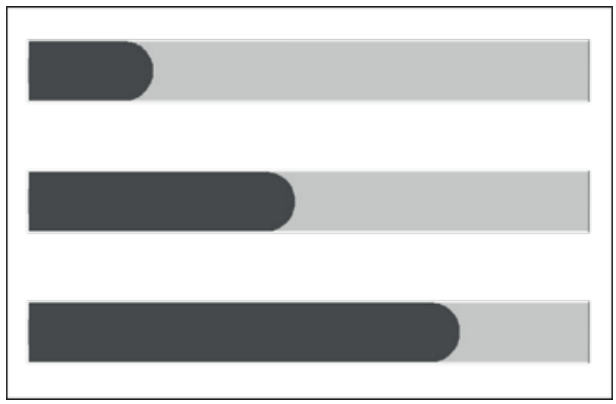


Fig. 8. Profiles of the meniscus at Ca = 1.85x10-4 and R = 1 μm.

even with same value of capillary number that gave good results with larger radius.

The shapes of the profiles for Ca = 1.85x10^{-4} and R = 1μm are shown in (Fig. 8) at different times, that is, the outline of the CO_2-oil bubble is shown at different positions. The head is a hemisphere, a feature that does not change as long as Ca remains small, and with radius 1μm and low capillary number the thickness of the deposited film h_∞ is very small such that h_∞ cannot be shown at this scale. The tip of the advancing meniscus is a spherical cap with a radius ≈ R.

As expected there is practically no pressure drop in the gas phase. Thus, instead of using the pressure of CO_2 at the interface to calculate the surface tension and the solubility, the pressure at the entrance $p(0,0)$ that is, p at $z = 0$ and $r = 0$ is used, since the gas-liquid interface is not so easily located. The outlet pressure has been set to zero and the inlet pressure adjusts itself as the inlet velocity differed. The center-line pressure $p(z,0)$ has been shown in dimensionless form in (Fig. 9) as a function of position z for the same capillary number at different times and with radius equal to 1μm. Linear pressure drop and Hagen-Poiseuille flow with parabolic profiles were verified in the liquid phase sufficiently far from the head. It is seen that the pressure neither drops significantly in the gas phase, nor in the liquid phase. Most of the pressure drop takes place across the interface.

The Laplace pressure across the hemispherical cap is approximately 2γ/R. Thus, if pressure is non-dimensionalized to $p(z,0)R/\gamma$, it should reach a value slightly in excess of 2. With this result in mind we have plotted the inlet pressure $p(0,0)$ in dimensionless form in (Fig. 10), for three different tube radii, all at a time where the menisci are at z^*/R in the tube, all with inlet velocity equal to 0.000168 m/s, and capillary numbers are all comparable (but not equal). Since the

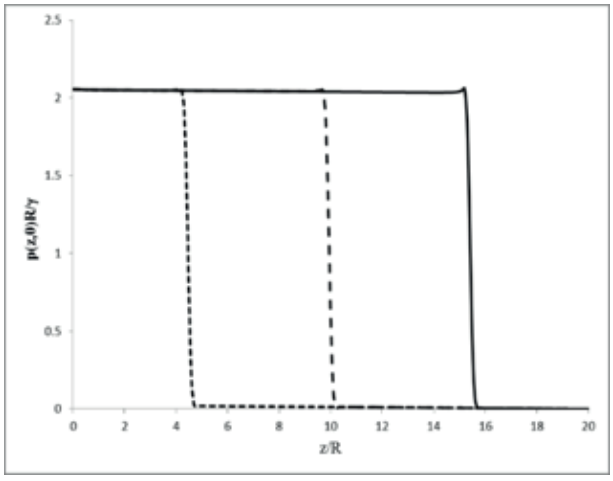


Fig. 9. Non-dimensional Center-line pressure p(z,0) versus position z for same capillary number at different times and R = 1 μm.

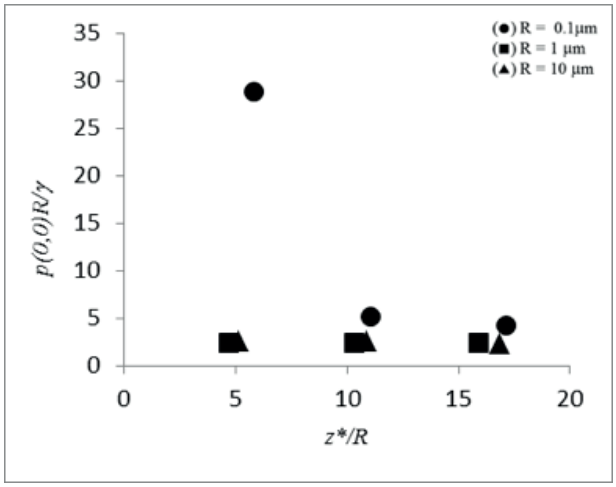


Fig. 10. Non-dimensional inlet pressure p(0,0) for three different tube radii, at a time where the menisci are at z*/R.

pressure drop across the menisci, contribute to nearly all of the pressure drop, $p(0,0)$, the total pressure drop, is as expected ~2 in dimensionless form. This is indeed the case for R = 1μm and R = 10μm. However, it is much larger when R = 0.1μm. So we looked at how the profile for the gas finger looked for R = 0.1μm which is shown in (Fig. 11).

A much sharper head is seen. Therefore, we conclude that in small tubes, the pressure drops in the gas phase and the liquid phase become quite large as R is decreased below 1μm. A point is reached where these large forces work to streamline the shape of meniscus such that the total pressure drop is reduced. No change was seen where L/R, which is otherwise = 20 in all cases, was increased to 40. The velocity of the nose was also found to be a constant.

In (Fig. 12), non-dimensional film thickness that left behind h_∞/R has been plotted against capillary number Ca, and they have been compared with Equation (1). A radius of 1 μm was used in FLUENT with three different velocities which were represented three different capillary numbers: 1e-2, 1e-3, and 1e-4. The squares stand for h_∞/R versus Ca, and the straight line represented Bretherton equation. The figure showed that the numerically calculated results were almost as same as Bretherton results. It also verified that film thickness that left behind h_∞ was decreasing when capillary number deceased.

It has been mentioned above that the ratio between the length and the radius of the tube (L/R) was = 20, with this ratio and for capillary number of 10^{-1} the h_∞ cannot be measured because there were a steps in the profile. So, the ratio was increased to 40 to see if there would be any difference (Fig. 13). However, the graph showed the same results and there was no difference. So far, only the fluid mechanics have been considered. next, the effects of mass transfer will be discussed.

Mass Transfer Results

The results of mass transfer calculations have been plotted in (Figs. 14 & 15), against capillary number Ca and Peclet number $Pe = \frac{U2R}{\bar{D}}$ respectively,

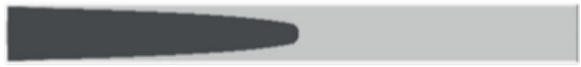


Fig. 11: Profile for gas finger with R = 0.1 μm.

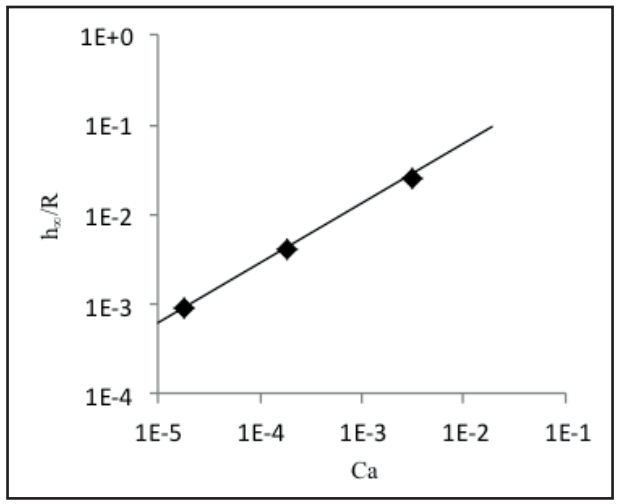


Fig.12. Non-dimensional film thickness that left behind h∞/R plotted against capillary number Ca and compare them with Equation (1).



Fig.13. Profile of capillary number equal to 10-1 and with 40 L/R ratio.

where $\overline{D}$ is an average diffusivity, averaged from p_{sat} to zero. The diffusivity is:

The average is given by:

$$\overline{D} = \frac{5.14\times10^{-13}}{4.063\times10^{-5}}\left(e^{\left(4.063\times10^{-5}\,p_{sat}\right)} - 1\right) \qquad (4)$$

In both cases, Bretherton equation, Equation (1) is used as a basis for comparison. From Equation (3), it is possible to show that for small values of h_∞/R, the dimensionless mass transfer rate is:

$$\frac{M}{\pi R^2 c_{sat} U} = 1-(1-h_\infty / R)^2 \approx 2h_\infty / R \qquad (5)$$

Thus, the dimensionless mass transfer rate is proportional to h_∞/R. If we consider the special case where the concentration of dissolved CO_2 is very low throughout, then the fluid flow will not change and the calculated h_∞/R and Ca pair will fall on the Bretherton line. Thus, the Bretherton equation provides a basis for comparison.

Non-dimensional film thickness that left behind h_∞/R has been plotted against capillary number Ca, in (Fig. 14), and they have been compared with Equation (1) in presence of mass transfer. Two different radii 10μm and 1μm were used with four different velocities. The straight line represented Bretherton equation, the squares stand for 10μm and the triangle stand for 1μm. The figure verified that film thickness that left behind h_∞ in presence of mass transfer was decreasing when the capillary number decreased. What is observed in (Figs. 14 & 15) is that convection decreases the mass transfer, quite contrary to intuition. However, the mass transfer is seen to decrease with convection from a low value and it is mainly in (Fig. 15), that a limit is observed.

That is, reaches the lowest possible value and does not change anymore with increasing Pe. On returning to (Fig. 14), it is seen that at large capillary numbers both cases of two tube radii, lead to the same asymptote that parallels Bretherton's case. Also, it showed that the oil left behind (h_∞) with mass transfer is less than the oil left behind without mass transfer.

The explanation of the negative impact of convection lies in the fact that in the front of the bubble, convection is in the direction opposite to the direction of diffusion. Increasing convection also squeezes the domain through which the CO_2 penetrates the oil at the tip of bubble. In fact, we were unable to draw the contour plots of CO_2 in oil in a meaningful way due to the very large compaction. However, the decrease in mass transferred is not without limits.

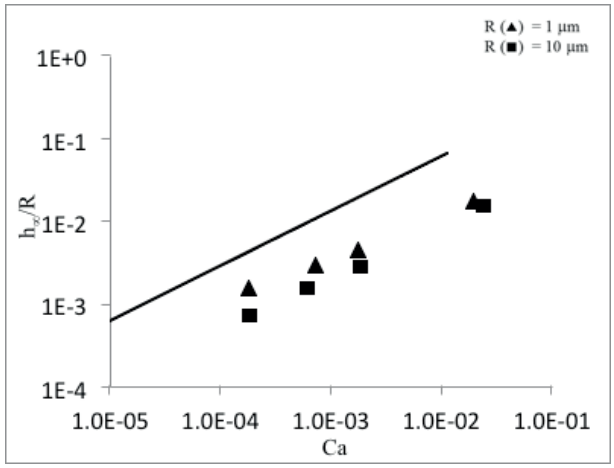


Fig. 14. Non-dimensional film thickness that left behind h∞/R plotted against capillary number Ca in presence of mass transfer, with R = 10 and 1 μm, and compare them with Equation (1).

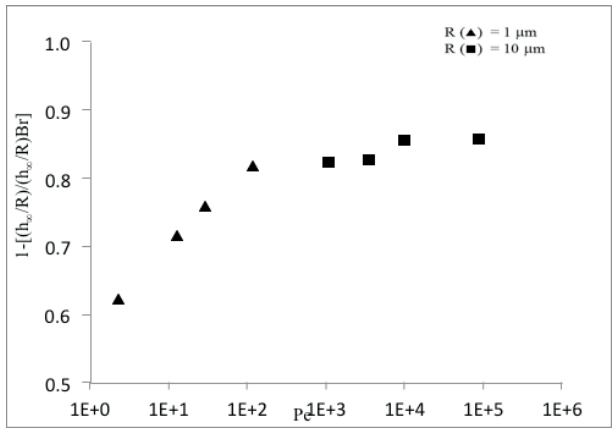


Fig. 15. Dimensionless film thickness as a function of Peclet number Pe. Mass transfer (dissolution CO_2 in oil) falls when the trend rises.

More squeezing increases the concentration gradient and diffusion flux, reaching limits in a manner similar to concentration polarization.

CONCLUSIONS

In fluid mechanics case, the oil film thickness that left behind, h_∞ is decreasing when capillary number/ bubble velocity decreases. That was the case for all different radii and different velocity inputs. The h_∞/R versus *Ca* and Bretenton line are almost identical. At large capillary number (10^{-1} for R= 1μm) and small radius (0.1μm), the profile shape of the CO_2 bubble is pointed.

Even under mass transfer of CO_2 into oil, the profile shape of the CO_2 bubbles show Bretherton-type profiles. The oil film thickness left behind (h_∞) with mass transfer is less than the oil left behind without mass transfer. The mass transfer decreases with

increasing convection as the convection is opposed to the direction of diffusion and the preferred direction of mass transfer. The fluid flow alters considerably from Bretherton type at small capillary radius and at large velocities, in same manner.

ACKNOWLEDGMENT

Author wishes to thank his company Raslanuf Oil and Gas Processing for its help and support. Also, he would likes to express his sincere thanks to his adviser Dr. Parthasakha Neogi, Truynh Tran (his research mate), and the Missouri University of Science and Technology for the constant guidance, opportunities, support and encouragement they have given to complete this study.

REFERENCES

Aladasani, A. and Baojun, B. (2010). Recent Developments and Updated Screening Criteria of Enhanced Oil Recovery Techniques. *SPE 130726*: 24p.

Brackbill, J. U.; Kolthe, D. B. and Zemach, C. (1992). A Continuum Method for Modeling Surface Tension. J. Comp. Phys., **100**: 335-354.

Bretherton, F. P. (1961). The Motion of Long Bubbles in Tubes. *J. Fluid Mech.,* **10**: 166-188.

Chung, F. T. H.; Jones, R. A. and Nguyen, H. T. (1988). Measurements and Correlations of Physical Properties of CO_2/Heavy-Crude-Oil Mixtures. *SPE Res. Eng.,* **3**: 821p.

Craig, F. F. Jr. (1971). The Reservoir Engineering Aspects ofWaterflooding. *Monograph Series, SPE*, Richardson, Texas 3.

Green, D. W. and Willhite, G. P. (1998). Enhanced Oil Recovery. *Soc. Pet. Eng.,* **V. 6**: 545p.

Gupta, R.; Flecture, D. F. and Haynes, B. S. (2009). On the CFD Modeling of Taylor Flow in Microchannels. *Chem. Eng. Sci.,* **64(12)**: 2941-2950.

Hutchinson Jr., C. A. and Braun, P. H. (1961). Phase Relations of Miscible Displacement in Oil Recovery. *AICHE*. J. **7**: 64p.

Kovscek, A. R. (2002). Screening Criteria for CO2 Storage in Oil Reservoirs. *Pet. Sci. Tech.,* **20**: 841p.

Kreutzer, M. T.; Kaptejin, F.; Moulijn, J. B.; Klein, C. R. and Heiszwolf, J. J. (2005). Inertial and Interfacial Effects on Pressure Drop of Taylor Flow in Capillaries. *AICHE. J.,* **51**: 2428-2440.

Meyer, R. F. and Attanasi, E. D. (2003). Heavy Oil and Natural Bitumen-Strategic Petroleum Resources. *(http://pubs.usgs.gov/fs/fs070-03/fs070-03.html, accessed 07/03/12).*

Miller, C. A. and Neogi, P. (2008). Interfacial Phenomena, Static and Dynamic Aspects, *2nd ed.,* Boca Raton, FL: CRC Press: 421p.

Morrow, N. R. (1991). Interfacial Phenomena in Oil Recovery. New York, NY; Marcel Dekker: 446p.

Rojas, G. A. and Ali, S. M. F. (1988). Dynamics of Subcritical CO2/Brine Floods for Heavy Oil Recovery. *SPE Res. Eng.,* **3**: 35-44.

Slattery, J. C. (1999). Advanced Transport Phenomena, Cambridge University Press: 709p.

Teletzke, G. F.; Davis, H. T. and Scriven, L. E. (1988). Wetting Hydrodynamics., *Reveue Phys. Appl.,* **23**: 989-1007.

Tran, T.; Neogi, P. and Bai, B. (2012). Free Volume Estimates of Transport and Thermodynamic Properties of Heavy Oils with CO_2. *Chem. Eng. Sci.,* **V. 80**: 100-108.

Wesseling, P. (2001). Principles of Computational Fluid Dynamics, Springer: 644p.

ANALYTICAL MODELLING OF ATTENUATION OF VOLATILE PETROLEUM HYDROCARBONS IN THE VADOSE ZONE

Elazhari Ali, Abdulmagid*, Russell Davenport** and David Werner***

Abstract: We applied the measured kapp and Kd parameter values in an analytical model to estimate the extent of the volatile petroleum hydrocarbons from a known source zone, and to compare the model analyses results based on batches experimental data with results based on parameters determined in a field lysimeter experiment. The analytical results of how far a constituent can migrate from a 50cm source zone before its attenuation, based on the field lysimeter date, the distance (r 95%) ranged from 75cm to 350 cm away from the source zone. 75 to 100cm distance from the source zone illustrates the 95% attenuation of toluene and n-octane respectively. While the attenuation distance of cyclohexane and methylcyclopentane was 200 and 250cm respectively, n-pentane, n-hexane and iso-octane have 95% attenuation distance of 350, 200 and 225cm respectively. These data suggest that the significant differences in the attenuation distance from the source zone between the laboratory data and the field data was related to the difference in the apparent biodegradation rates, which were faster for the soil investigated in the laboratory in this study. The data presented illustrate the phenomenon of biodegradation and sorption of VPHs in the unsaturated zone and the analytical model analyses data results demonstrate the VPHs extent of migration form source zone under different scenarios (source zone radius, biodegradation rate and sorption distribution coefficients). All data show that biodegradation by indigenous microorganisms is the key parameter controlling the fate and transport of contaminants in the subsurface.

Keywords: Biodegradation; petroleum volatile hydrocarbons; analytical model.

INTRODUCTION

An important topic in groundwater and soil quality management is natural attenuation. It has been reported that the efficiency of natural attenuation is impacted by three key processes, diffusion, sorption and biodegradation (Karapanagioti *et al*, 2001).

Material and Methods

This study simulated the migration and the fate of 12 VOCs vapours mixture in the unsaturated zone. In order to examine the efficiency of the indigenous microorganisms in degrading VOCs, the apparent biodegradation rates and the sorption coefficients were determined. The experiment was performed by setting-up two laboratory batch microcosm experiments. The first set contains live sand, and abiotic controls were prepared by autoclaving the sand for the second set. Then, 1ml of the headspace gas of a vial containing the fuel mixture at 25^{o}C was injected into the batches and VPHs concentrations were monitored for up to 7 days.

In order to establish a comprehensive understanding of the soil and groundwater risks for VPHs, it is useful to assess the degradation rate by including it in an analytical model that can calculate the attenuation of the vapour concentration C_a with radial distance r, from the source zone. For this purpose Equation (1) from (Hohener *et al*, 2006) is applied.

For a constant spherical source with radius r_0 in a homogenous infinite porous medium, the

*Petroleum Training and Qualifying Institute, P.O Box 6184, Tripoli, Libya, a.elazhari@ptqi.edu.ly
,*School of Engineering, Newcastle University, Newcastle upon Tyne, NE1 7RU, UK.

attenuation of the vapour concentration C_a with radial distance r is:

$$C_a(r,\infty) = \frac{C_{a0} r_0}{r} e^{-\sqrt{\frac{k_{app}}{D'}}(r-r_0)} \quad (1)$$

Where:

$Ca(r,\infty)$: The steady-state vapour concentration as a function of distance from the source

C_{a0}: The concentration near the source

r_0 [cm]: The radius of the source

r r [cm]: The distance from the source

K_{app} [s^{-1}]: the apparent biodegradation rate in the batch experiments

D': The sorption-affected gas-phase diffusion coefficient can be calculated as:

$$D' = f_a \tau_a D_a \quad (2)$$

Where:

τ_a denotes the tortuosity factor τ described by the model of (Millington and Quirk, 1961).

$$\tau_a = \frac{\theta_a^{2.33}}{n_{tot}^2} \quad (3)$$

D_a $\left[\frac{cm^2}{s}\right]$ the molecular diffusion coefficient in air can be calculated according to the method of Fuller as outlined in (Schwarzenbach *et al*, 1993).

f_a: the mass fraction of the compound in the soil air can be calculated according to the method of (Werner and Hohener, 2003):

$$f_a = \frac{1}{1 + \frac{\rho_s (1-\theta_t)}{K_s \theta_a} + \frac{\theta_w}{H\theta_a}} \quad (4)$$

Where, θ_a θ_w and θ_t denote the air-filled, the water filled, and total porosity respectively, and ρ_s denotes the density of the solids.

K_s $\left[\frac{mol\, cm^{-3}\,(air)}{mol\, g^{-1}\,(solid)}\right]$ denotes the air-solid partitioning coefficient, which can be defined as the ratio between the Henry's law constant and the solid-water partitioning coefficient K_d.

RESULTS AND DISCUSSION

Solid-water distribution coefficient determination

The measured K_d values ranged from 0.90 ± 0.6 for m-xylene to 377 ± 103 for n-octane. The K_d results demonstrate that the monoaromatics have the lowest measured K_d values because they are more soluble than alkanes. On the basis of the water solubility and volatility it is expected that each compound will be sorbed or partition into either soil solids, soil air and/or soil water (Christophersen *et al*, 2005; Karapanagioti *et al*, 2005).

The maximum vapour-phase concentration of the most VPHs was recorded just 4 hrs after incubation, and then most of the PP constituents' mixture decreased continuously until day 3. The differences between sterile and live soil demonstrates that the vapour concentration of these compounds decreased because of biodegradation.

The measured K_d values ranged from 0.90 ± 0.6 for m-xylene to 377 ± 103 for n-octane. The K_d results demonstrate that the monoaromatics have the lowest measured K_d values because they are more soluble than alkanes. On the basis of the water solubility and volatility it is expected that each compound will be sorbed or partition into either soil solids, soil air and/or soil water (Christophersen *et al*, 2005; Karapanagioti *et al*, 2005).

Apparent biodegradation rate determination k_{app}

The measurement of biodegradation rates by indigenous microorganisms is the first step in microbiological characterization. These measurements can be complicated by low microbial population or by the absence of species capable of degrading contaminants. In addition, optimum conditions of temperature, oxygen nutrients supply, and contaminant availability due to low solubility or strong sorption can limit degradation rates, especially in early tests where these limiting factors are not well defined (Providenti *et al*, 1993).

The main objective of microbial degradation tests is to determine whether the indigenous microorganisms are capable of bioremediation when condition are optimized.

A variety of mathematical expressions have been suggested to describe the kinetics of biodegradation reactions. These models have been increasing in complexity as they attempt to accommodate the numerous variables that can affect the biodegradation rate in the natural

environment. However, the main limitation of some of the VOC transport models is that they have not included biodegradation at all. Additionally, other transport models limitations have been using simplified representations such as first-order reaction kinetics, or Michaelis-Menten kinetics. First-order reactions, which assume a constant biomass, are normally observed in short incubation studies conducted at low chemical concentrations.

The data measured in the live microcosms were significantly different to those in abiotic soil within the first 5 days. The compounds showed a faster decrease in live microcosms compared to abiotic microcosms.

Profiles of vapour-phase concentrations of the VOCs in live soil are shown in Fig. 2. It can be seen that the vapour-phase concentration of these compounds decreased sharply within 50 hours. The maximum vapour-phase concentration of the most VOCs was recorded just 4 hrs after incubation, and then most of the PP constituents' mixture decreased continuously until day 3. The differences between sterile and live soil demonstrates that the vapour concentration of these compounds decreased because of biodegradation. The measured vapour-phase concentration in Figure 2 was used to

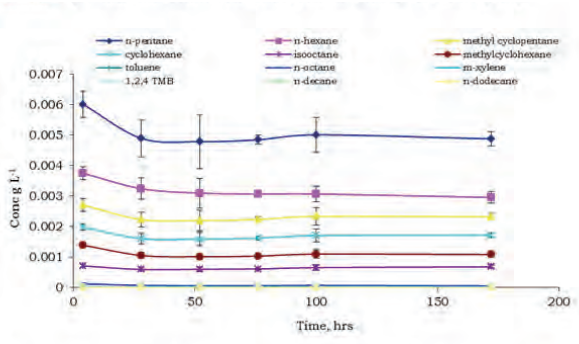


Fig.1. Comparison of fuel vapour-phase concentration in the autoclaved sand batches, as a function of time. Error bars: ±1 standard deviation (SD, n=3).

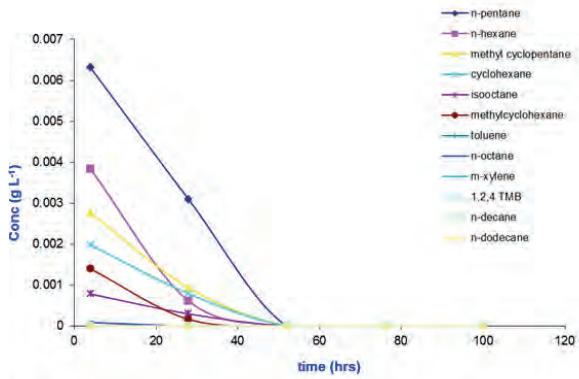


Fig. 2. Vapour-phase concentration of VPHs in live sand batches.

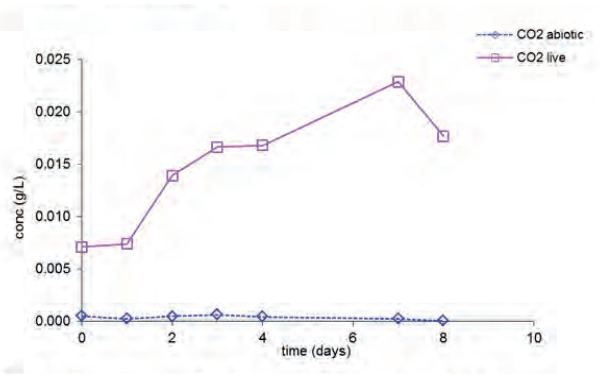


Fig. 3. Concentration profiles of CO2 in the live and autoclaved sand.

estimate the half-life rate for each constituent. From the measured half-life, the first order apparent biodegradation rate was estimated.

This approach assumes first order decay and it does not allow for an initiation or lag period during which the microbial community becomes activated or acclimated. First-order kinetics has been found to be a good approximation for most of the VPHs studied in both batch and column experiments. For all highly-volatile VPHs, the concentration decreased in the live sand was significantly different to that in abiotic sand within the first 7 days, indicating rapid biodegradation has occurred. For less-volatile VPHs constituents, the concentration decreased even faster than the highly VPHs in the live sand, in particular the aromatics (this decrease was significantly different in comparison with that in abiotic sand within the first 3 days).

For the was significantly different in comparison with that in abiotic sand highly VOCs the apparent half-lives are in the order of 0.5-1.2 days, which translates into an apparent first-order biodegradation rate kapp of 1.2 to 0.6 per day, and for the aromatic VOCs the concentration decreases and biodegradation rates are even faster. This is comparable to the biodegradation rates determined by (Providenti *et al*, 1993; Pasteris *et al*, 2002) for sand in a lysimeter.

Oxygen and Carbon dioxide

Profiles of the concentrations of CO_2 in the batches for both live and abiotic sands are shown in Fig. 3. CO_2 plots in the abiotic control were relatively stable through the incubation period and the concentration remained within 82 ± 26 % from its initial concentration. For the live sand batches a CO_2 production increase was clearly seen in the headspace (Fig. 3). From the plots it can be seen that CO_2 production started immediately after vapour

injection without any significant lag phase period. On day 0 the CO_2 concentration in the live sand increased significantly from 0.0070g/L, to reach a concentration of 0.017g/L on day 7. The increasing of CO_2 in the live sand batches which were observed after the vapour injection illustrates metabolic activity of soil microorganisms and demonstrates the active biodegradation process. Both, VOCs biodegradation and background soil respiration contribute to the observed increase in CO_2.

Analytical model results using experimental data

Results of the analytical model based on measured first order apparent biodegradation rates and solid-water distribution coefficients are shown in (Fig. 2). The results show the concentration attenuation of VPHs as they diffuse away from the source zone. Fig. 4, illustrates the rapid attenuation of the concentration of the VPHs as a result of biodegradation, and eventually the pollutant levels reach near zero concentration within a very short distance. The no biodegradation data in the plot confirms that the VPHs concentrations also decrease with distance solely as a result of the dilution process.

Fig. 5 illustrates the distance $(r_{95\%})$, ranged from 75cm to 350cm away from the source. 75-100cm distance from the source zone illustrates the 95% attenuation of toluene and n-octane respectively. While the attenuation distance of cyclohexane and methylcyclopentane was 200 and 250cm respectively, n-pentane and n-hexane and iso-octane have 95% attenuation distances of 350, 200 and 225cm respectively. These data suggest that the significant differences in the attenuation distance from the source zone between the laboratory data and field data was related to the difference in the apparent biodegradation rates, which were faster for the soil investigated in the laboratory in this study.

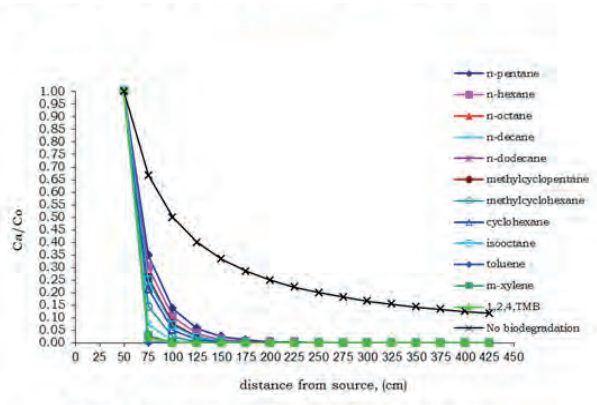


Fig. 4. Attenuation of VPHs released from a 50cm source zone.

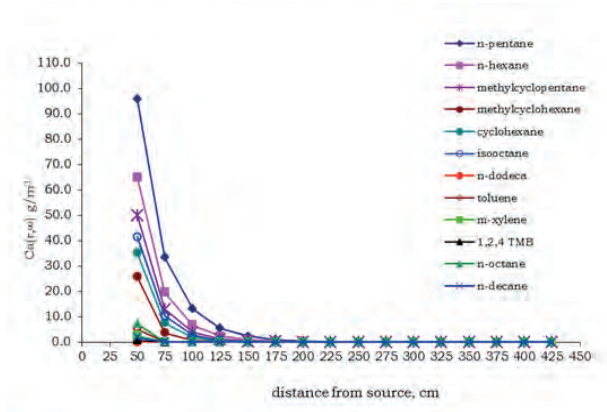


Fig. 5. Attenuation distance of VPHs from the source zone.

Analytical model results comparison between experimental batches and field lysimeter data

To validate and fine-tune numerical models for comparison reason, comprehensive data sets are required from a field experiment. Here, the data from a lysimeter test performed to quantify biodegradation of VOCs of an artificial fuel mixture are used for a comprehensive understanding of the attenuation distance from a source zone in a real field scenario. Data from the lysimeter experiment include apparent biodegradation rates and solid-water distribution coefficient (Pasteris *et al*, 2002). Data have been applied to the analytical model in order to compare the batches results and the field data model results.

The analytical results of how far a constituent can migrate from a 50cm source zone before its attenuation, based on the field lysimeter data are shown in (Fig. 7). Fig. 8 illustrates the distance (r_ (95%)), ranged from 75cm to 350 cm away from the source. 75-100 cm distance from the source zone illustrates the 95% attenuation of toluene and n-octane respectively. While the attenuation distance of cyclohexane and methylcyclopentane was 200 and 250cm respectively, n-pentane and n-hexane and iso-octane have 95% attenuation distances of 350, 200 and 225cm respectively. These data suggest that the significant differences in the attenuation distance from the source zone between the laboratory data and field data was related to the difference in the apparent biodegradation rates, which were faster for the soil investigated in the laboratory in this study.

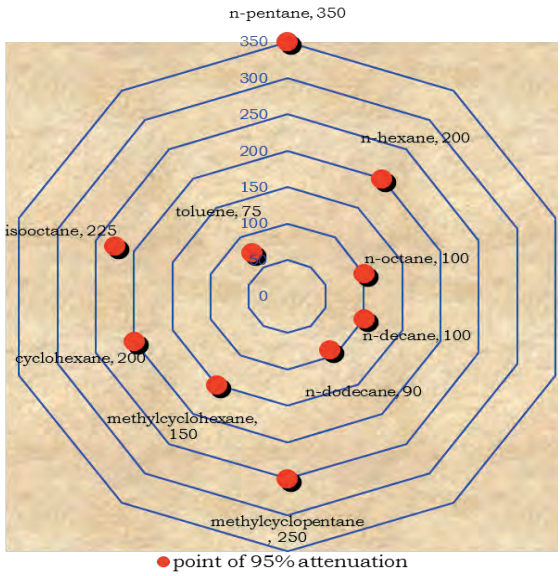


Fig. 6. VPHs attenuation from a 50 (cm) source zone (Lysimeter data).

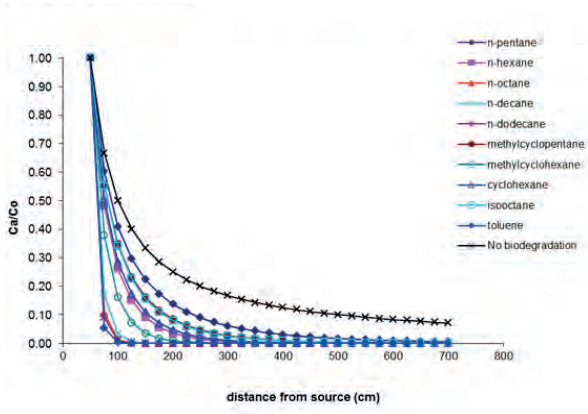


Fig. 7. Attenuation distance of VPHs released from a 50cm source zone.

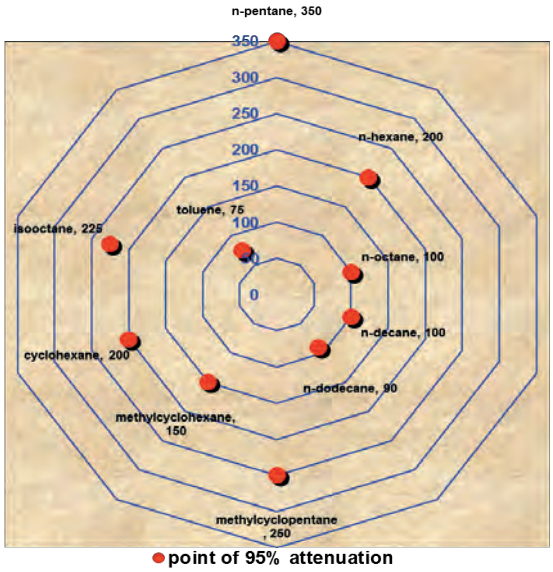


Fig. 8. VPHs attenuation from a 50 (cm) source zone (Lysimeter data).

Analytical risk assessment of VPHs source in the subsurface

Based on the lysimeter data for the 50cm source zone (Fig. 4) one could assume as a scenario that a groundwater table is just 100cm in the vertical direction (r_1) and a residential or industrial property basement just 200cm (r_2) away from the source zone. In this case (r_1) is shorter than (r_2). As a result the receptor at (r_1), which is the groundwater table, will be significantly affected, because it is within the reach of most VPHs, except toluene which has been attenuated at 80 cm. The contaminants when they reach the groundwater table are reduced to less harmful concentrations of approximately 5% of their initial concentration. Similarily, n-octane, n-decane, n-dodecane, methylcyclopentane, toluene and 1, 2, 4 TMB will not reach the (r_2) receptors.

CONCLUSIONS

In summary the data presented in this part illustrate the phenomenon of biodegradation and sorption of VPHs in the unsaturated zone and the analytical model analyses data results demonstrate the VOCs extent of migration from source zone under different scenarios (source zone radius, biodegradation rate and sorption distribution coefficients). All data show that biodegradation by indigenous microorganisms is the key parameter controlling the fate and transport of contaminants in the subsurface, and in the absence of effective biodegradation another parameter may become most important in particular sorption and partitioning (Schwarzenbach and Westall, 1981).

REFERENCES

Christophersen, M.; Broholm, M. M.; Mosbaek, H.; Karapanagioti, H. K.; Burganos, V. N. and Kjeldsen, P. (2005). Transport of Hydrocarbons from an Emplaced Fuel Source Experiment in the Vadose Zone at Airbase Vaerlose. *Denmark. Jou. Contam. Hydr.*, ***81(1-4)***: 1-33.

Hohener, P.; Dakhel, N.; Christophersen, M.; Broholm, M. and Kjeldsen, P. (2006). Biodegradation of Hydrocarbons Vapors: Comparison of Laboratory Studies and Field Investigations in the Vadose Zone at the Emplaced Fuel Source Experiment, Airbase Vaerlose *Denmark. Jou. Contam. Hydr.*, ***88(3-4)***: 337-358.

Karapanagioti, H. K.; Gossard, C. M.; Strevett, K. A.; Kolar, R. L. and Sabatini, D. A. (2001). Model Coupling Intraparticle Diffusion/Sorption, Nonlinear Sorption, and Biodegradation Processes. *Denmark. Jou. Contam. Hydr.*, ***48(1-2)***: 1-21.

Karapanagioti, H. K.; Sabatini, D. A. and Bowman R. S. (2005). Partitioning of Hydrophobic Organic Chemicals (HOC) into Anionic and Cationic Surfactant-Modified Sorbents. *Water Research,* ***39(4)***: 699-709.

Millington, R. J. and Quirk, J. P. (1961). *Permeability of porous solids* Transactions of the Faraday Society. ***57***: 1200-1207.

Pasteris, G.; Werner, D.; Kaufmann, K. and Hohener, P. (2002). Vapor Phase Transport and Biodegradation of Volatile Fuel Compounds in the Unsaturated Zone: A Large Scale Lysimeter Experiment. *Environmental Science & Technology,* ***36(1)***: 30-39.

Providenti, M. A.; Lee, H. and Trevors, J. T. (1993). Selected Factors Limiting the Microbial-Dedradation of Recalcitrant Compounds. *Jour. Indus. Microb.*, ***12(6)***: 379-395.

Schwarzenbach, R. P. and Westall, J. (1981). Transport of Nonpolar Organic Compounds from Surface Water to Groundwater. Laboratory Sorption Studies. *Environ. Sci. Technol.,* ***15(11)***: 1360-1367.

Schwarzenbach, R. P., Gschwend, P. M. and Imboden D. M. (1993). Environmental Organic Chemistry. New York: J. Wiley. X.: 681p.

Werner, D. and P. Hohener (2003). In Situ Method To Measure Effective and Sorption-Affected Gas-Phase Diffusion Coefficients in Soils. *Environ. Sci. Technol.*, ***37(11)***: 2502-2510.

THERMAL ANALYSIS OF A CLAD PIPE USING SIMULATION

Hala Y. Hamad*

Abstract: Cladding is a process where one material covers another for protection or to obtain a specific property that is not exist in one of the two materials, but exist in the second material. The use of clad pipes provide an optimum and the cost-effectiveness solution when operating under highly corrosive conditions (crude with H2S, CO2, or in offshore area) or in high pressure operations. This paper introduces briefly the clad pipes and presents the results of thermal behaviour simulation of the clad pipe which utilized to perform a mesh sensitivity study. A (10″) Stainless Steel clad pipe, which consists of a thin-walled inner Stainless Steel pipe and an outer Carbon Steel pipe, was used as a model in the current study. Finite element analysis was used as an experimental method to determine the stresses and the deformations on the clad pipe due to applied tensions and heat. In addition, the clad pipe was put under the same temperature conditions during the winter and summer times that in Sarir Oil Field to show the heat flux and the temperature gradient across the cross section of the clad pipe. Abaqus software was used to simulate the process. The results of thermal behaviour simulation of the clad pipes were obtained for different mesh types and sizes. A comparison between the different mesh types was carried out to determine the appropriate mesh type for the model. A mesh sensitivity study was performed to obtain the most accurate results. The simulation results show that the most appropriate mesh type for the current model is Tet (free), C3D4T: A 4-node thermally coupled tetrahedron, linear displacement and temperature (model 3). Because it has the maximum S (max) value (2.900E + 09Pa), and most accurate results are obtained when the global mesh size range is from (≤0.02 for the outer pipe and from ≤ 0.009 for the inner pipe).

Keywords: Clad Pipe, Thermal Analysis, 3D Finite Element Modelling.

INTRODUCTION

Pipe Cladding

Combines the advantage of a high strength carbon steel outer pipe (backing steel) with an inner layer of corrosion resistant alloy, yielding improved pipeline (Berg and Schnaut, 2009). Clad pipes are widely used in oil and gas industry, they are produced by cladding of a thin Corrosion Resistance Alloy (CRA) pipe and a thick carbon steel pipe by different manufacturing methods. The use of clad pipes provides an optimized and cost-effectiveness solution when operating under highly corrosive conditions (crude with H_2S, CO_2, or in offshore area) or in high pressure operations.

For example, The problems associated with the corrosion in pipelines due to the presence of hydrogen sulfide in crude oil in some of AGOCO`s oil fields (Nafoora Field GOSP 1, 7, 9, and Beda Field) can be avoided by using clad pipes instead of addition of expensive chemicals (which costs millions $ every year). Table 1 shows H_2S concentrations in pipeline system from Beda & Nafoora oil fields to Ras Lanuf in 2008.

CRA clad pipe can be classified into two types depending on the method used to bond the two materials, metallurgical bond (CRA clad pipe), and mechanical bond (CRA lined pipe).

Metallurgical bond (CRA clad pipe)

Metallurgical bond can be created by hot rolling, explosive bonding or weld overlay, and co-extrusion, the metallurgical bond clad pipes are expensive and there are only few suppliers who have the ability to produce these pipes.

Mechanical bond (for CRA lined pipes)

Two major methods are used to create the mechanical bond between the steel and a CRA

*AGOCO, Benghazi, Libya, Email: halayousef14678@gmail.com

material, the expanded lined and rolled lined steel pipe.

DESCRIPTION OF NUMERICAL SIMULATION

Based on the finite element (FE) analysis package ABAQUS, a 3D model was developed to provide two analyses for a clad pipe (coupled temperature and displacement analysis & heat transfer analysis). The main purpose of the simulation is to perform a mesh sensitivity study, and to show the temperature gradient across the cross section of a clad pipe, the max. stress & heat flux.

The model is a (10″) stainless steel clad pipe, which consists of two pipes, a thin-walled inner stainless steel pipe of thickness (2mm), and diameter (254mm) the inner pipe is the "liner" pipe (it works as a coating to protect the main pipe from corrosion. In this model, the outer pipe is a carbon steel with a thickness (10mm). The 3D model for the stainless steel clad pipe is shown in (Fig. 1).

Coupled Temperature and Displacement Analysis

The 3D model clad pipe was kept fixed at one end and, at the other end a tensile load of 350 kPa was applied. The clad pipe is at 317.15K, which is the ambient temperature (max temperature at Sarir Oil Field 44°C), the internal surface of the clad pipe was at 339.15K (66°C), due to the hot crude oil flow in the clad pipe, all other sides are supposed to be insulated. The clad pipe expands due to the heat flow, the numerical modelling involved two steps, the initial step (which is automatically created by Abaqus) and step-1 (at which the load was applied). At the initial step the boundary conditions for the fixed end of the clad pipe were applied. Whereas, the boundary conditions for the free end of the clad pipe and the tensile load were applied at step-1. The solution processes for Coupled Temp- Displacement Analysis are shown in (Fig. 2). Table 2 shows the properties for the used materials (Carbon Steel & Stainless Steel).

Different mesh types were examined by copying the 3D model twice (Model- 2 & Model- 3) to run the job for three different mesh types. Table 3 and Fig. 3 show the three mesh types.

Mesh Sensitivity Study

To change the mesh density, model 3 has been copied to create seven new models. The size of the mesh has been changed, and the results have been compared to carrying out the mesh sensitivity study. Table 4 shows mesh sizes for the eight models.

Table 1. H_2S Concentrations in Pipeline System from Beda & Nafoora oil fields to Ras Lanuf in 2008.

Location	API Gravity (at 60o F)	S.G. Of Oil (at 60o F)	H_2S in Oil (mg/liter)
Beda	34.5	0.852	229
Nafoora	35.7	0.846	210

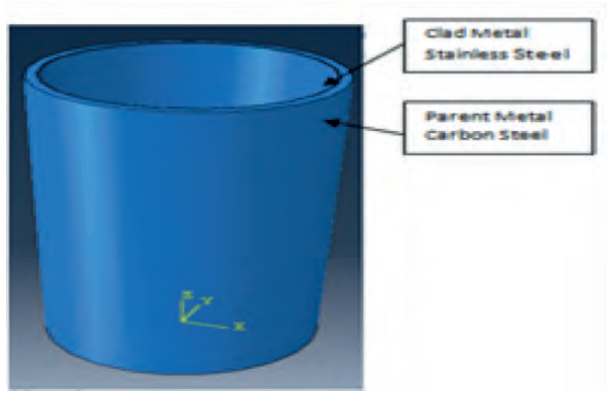


Fig. 1. The 3D Model.

Heat Transfer Analysis

The same 3D model was used to perform the following heat transfer analyses, all heat transfer analyses were performed assuming (no winds), wind velocity was neglected:

Steady state heat transfer analysis: For this analysis two BCs were created to verify the temperature gradient across the cross section of the clad pipe during winter and summer times in Sarir oil field.

Steady State and transient heat transfer analyses: Assuming that the clad pipe is not thermally isolated during two seasons, winter and summer, (conduction, convection and radiation were taken into consideration). For these heat transfer analyses one BC was created (the temperature for the hot crude oil 66°C), predefined field was created in the initial step, conduction, convection and radiation were simulated by creating interactions.

Table 5 shows the boundary conditions for the steady state heat transfer analysis (BC1 is the maximum and minimum temperature degrees in Sarir Oil Field during the summer and the winter), BC2 is the oil temperature.

Table 6 shows the created interactions for the non isolated pipe heat transfer analyses. For conduction heat transfer, tie constraints has been created to

Table 2. Thermal and Mechanical Properties for Carbone Steel & Stainless Steel.

	Property	Value
Parent Metal (Carbon steel)	Young's Modulus	200GPa
	Poison's ratio	0.3
	Density	7850 kg/m3
	Thermal Conductivity	42 W/m.k
	Specific heat	490 j/kg.k
	Thermal expansion Coeff.	0.000014 (m/m.°C) *14e-6*
Clad Metal (Stainless Steel)	Young's Modulus	197.5 GPa
	Poison's ratio	0.27
	Density	7970 kg/m3
	Thermal Conductivity	15 W/m.k
	Specific heat	510 j/kg.k
	Thermal expansion Coeff.	0.000016 (m/m.°C)

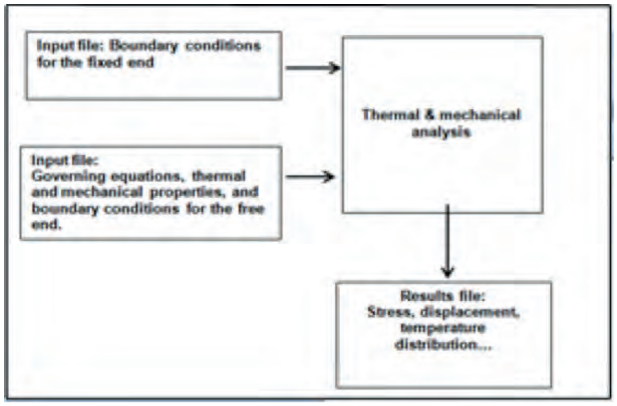


Fig. 2. The Solution Processes for Coupled Temp- Displacement Analysis.

Table 3. Mesh Types.

Model	Mesh Type
Model- 1	6840 Linear hexahedral elements of type C3D8T
Model- 2	12149 Linear wedge elements of type C3D6T
Model- 3	38453 Linear tetrahedral elements of type C3D4T

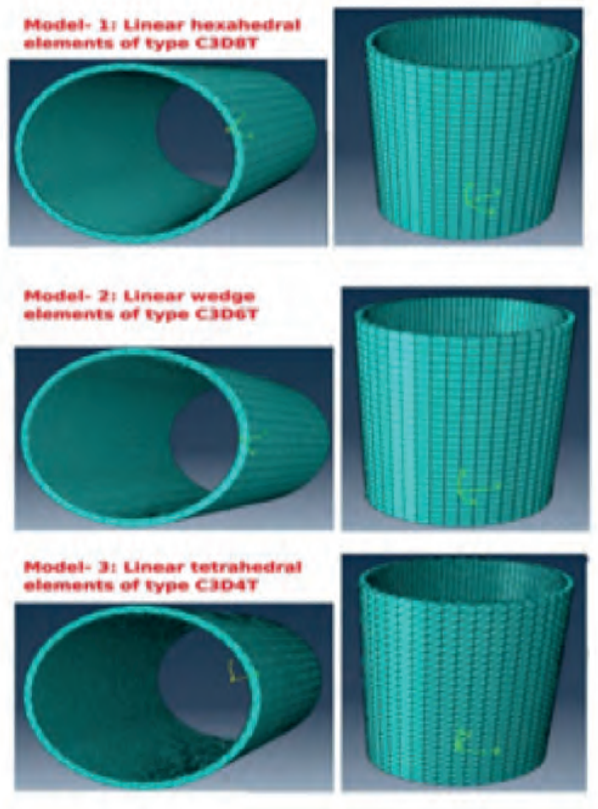


Fig. 3. The Mesh Type.

identify the surface connection between the two metals (CS & SS).

The value of Stefan- Boltzmann Constant is 5.67 E-008, and the Emissivity for the carbon steel is 0.63. The natural convection heat transfer coefficients during summer and winter were determined by using excel spreadsheets, the natural convection heat transfer coefficient correlations (S.I. units) was calculated by using the following correlations:

$$Nu = \{0.6 + \frac{0.387\, Ra^{1/6}}{[1 + (0.559/Pr)^{9/16}]^{8/27}}\}^2$$

$$Gr = \frac{D^3 \rho^2 g \Delta T \beta}{\mu^2}\ ,\ Nu = \frac{h D}{k}\ ,\ Pr = \frac{\mu C_P}{k}$$

For Ra , Ra = Gr Pr

Natural convection heat transfer coefficient during summer and winter for air in Sarir Oil Field were found about 3.94W/m^2-K, and 5.62W/m^2-K respectively.

Steady state heat transfer analysis: While the hot crude oil is flowing in the clad pipe, the properties of Sarir crude oil, according to AGOCO`s Operation Department are shown in (Table 7). The specific heat of Sarir crude oil was determined as a function of API gravity and Temperature by using the following formula (Bengtson, 2013):

$$C_p = (-1.39\times10^{-6}\times T + 1.874\times10^{-3})\times API + (6.312\times10^{-4})\times T + 0.352$$

Where: C_p = btu/ (ibm. °F), T = °F.

The specific heat of Sarir crude oil is 0.5079 btu/(lbm. °F, which is equal to 2.1265 K.j/KG. K The thermal conductivity for Sarir crude oil was determined by using the following formula:

$$k = 0.118\, \rho^{-1}[1 - 0.00054(T - 273)]\times10^3$$

Table 4. Mesh Size.

Model	Inner pipe mesh size	Outer pipe mesh size	Number of Elements
Model 3- b	0.01	0.03	27624
Model 3- a	0.0095	0.025	31385
Model 3	0.009	0.02	38453
Model 3- 1	0.0085	0.015	47306
Model 3- 2	0.008	0.01	75068
Model 3- 5	0.0077	0.007	145182
Model 3- 4	0.0076	0.006	182366
Model 3- 3	0.0075	0.005	257920

Table 5. Boundary Conditions for the Steady State Heat Transfer Analysis.

Season	BC1 Temp. (°C)	BC2 Temp. (°C)
Summer	44	66
Winter	0	66

Table 6. Interactions for the Non Isolated Pipe Heat Transfer Analysis.

Heat Transfer Method	Interaction	Type of Interaction
Convection	Int-1	Surface Film Condition
Radiation	Int-2	Surface Radiation

Table 7. Sarir Crude Oil Properties and flow Information.

Property	Value
Flow type	Turbulent
Re	4600
Density	837 kg/m^3
API	36.5
Viscosity	1.1e^{-5} m^2/s

The thermal conductivity for Sarir crude oil at 66 °C is 135.96 m.W/(m K).

The heat transfer coefficient for Sarir crude oil was determined by using excel spreadsheet, h = 103 kJ/hr-m^2-K, which is equal to 28.611 W/m^2-K. Since Prandtl Number, Pr = 26.9 and Re = 4600, the following correlation was used to determine the heat transfer coefficient for Sarir crude oil:

$$Nu_o = \frac{\left(\frac{f}{8}\right)(Re - 1000)Pr}{1 + 12.7\left(\frac{f}{8}\right)^{0.5}\left(Pr^{\frac{2}{3}} - 1\right)}$$

Where $f = (0.790 \ln Re - 1.64)^{-2}$

For: $0.5 < Pr < 2000$

$3000 < Re < 5\times10^6$

RESULTS

Comparing the Different Mesh Seizes

The jobs have been created, submitted and running to get the result of the three models. The results are shown in (Figs 4, 5 & 6 and Table 8).

The maximum stress values for the three models have been compared and it has been found that the best type of mesh for the current project is: Tet (free), C3D4T. A 4-node thermally coupled tetrahedron, linear displacement and temperature. which is for model 3. Because it has the maximum S (max) value, thus the meshes will converge faster.

Mesh Sensitivity Study Results

The jobs have been created for the different mesh size models, the simulations have been run, and the results are represented in (Table 9). The relations between the number of elements and the maximum stress, and the number of elements and the deformation (Figs. 7) are shown in (Figs. 8 & 9).

Heat Transfer Analysis Results

For the thermally isolated, steady state heat transfer analysis the temperature gradients during the winter and the summer are shown in (Fig.10). For the non isolated, steady state and transient heat transfer analyses (where the heat applied with no crude oil flowing inside the clad pipe) the maximum heat fluxes during the winter and the summer are shown in (Table 10).

From the transient analyses, the number of nodes has been selected to plot the relation between the temperature and the time, in summer and winter times, to verify how the temperature changing during the time until reaches the steady state. The relation between temperature and time is shown in (Figs.11 and 12). The times needed to reach the study state in winter and summer were found 214.1s, and 201.3s respectively.

For the non isolated, steady state heat transfer analysis, with the crude oil flowing inside the clad pipe, the maximum heat fluxes during the summer and the winter are shown in (Figs.13 & 14).

CONCLUSION

Two types of thermal analysis, (coupled temperature and displacement analysis and heat transfer analysis), have been carried out on a 10″ stainless steel clad pipe, thickness, 2mm for SS, and 10mm for CS. The aim of these thermal analyses

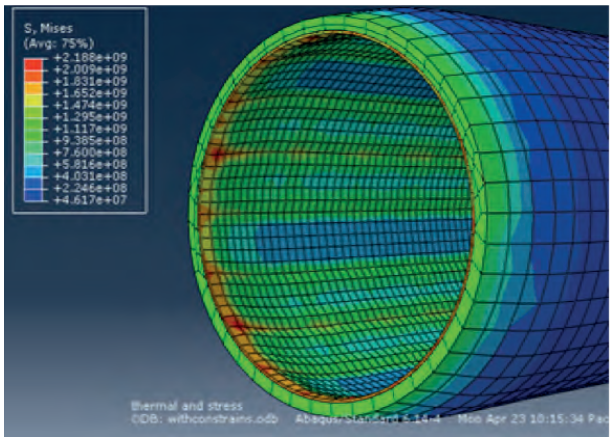


Fig. 4. Model 1, Stress Results.

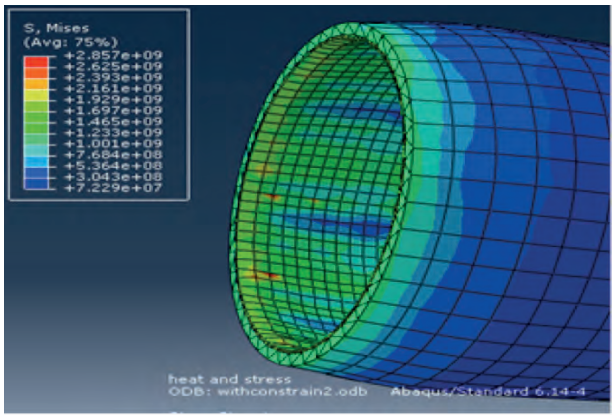


Fig. 5. Model 2, Stress Results.

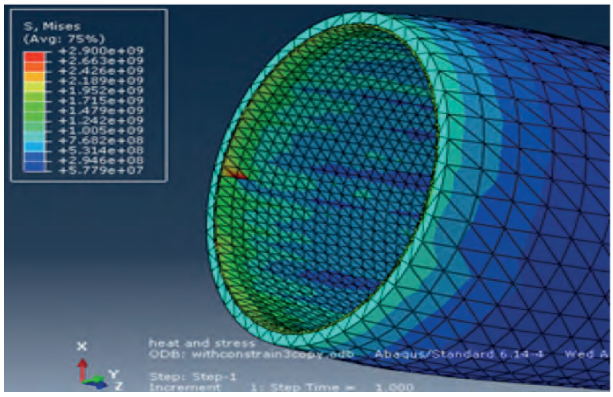


Fig. 6. Model 3, Stress Results.

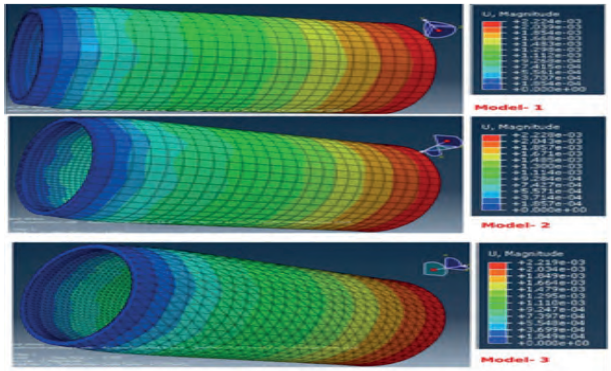


Fig. 7. Deformation.

Table 8. The Results for Model 1, 2, & 3.

Model	Number of Elements	S (max) Pa	U (max) m
Model 1	6840	2.188E+09	2.224E-03
Model 2	12149	2.857E+09	2.228E-03
Model 3	38453	2.900E+09	2.219E-03

Table 9. Mesh Sensitivity Study Results.

Model	Number of Elements	S (max) Pa	U (max) m
Model 3-b	27624	2.02E+09	2.22E-03
Model 3-a	31385	3.17E+09	2.22E-03
Model 3	38453	2.90E+09	2.22E-03
Model 3-1	47306	2.67E+09	2.23E-03
Model 3-2	75068	1.66E+09	2.21E-03
Model 3-5	145182	1.63E+09	2.21E-03
Model 3-4	182366	1.66E+09	2.21E-03
Model 3-3	257920	1.54E+09	2.21E-03

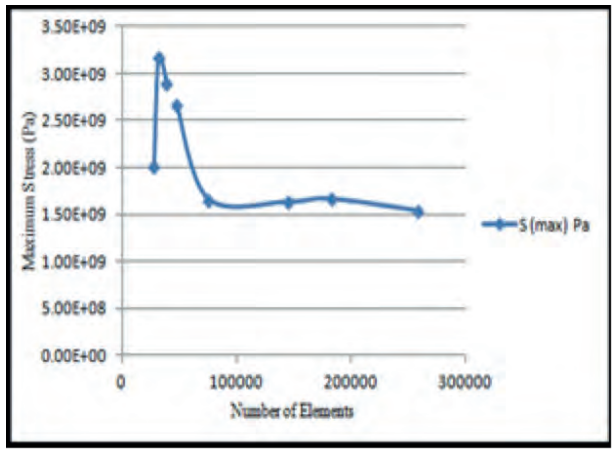


Fig. 8. Relation between the Number of Elements and the Maximum Stress.

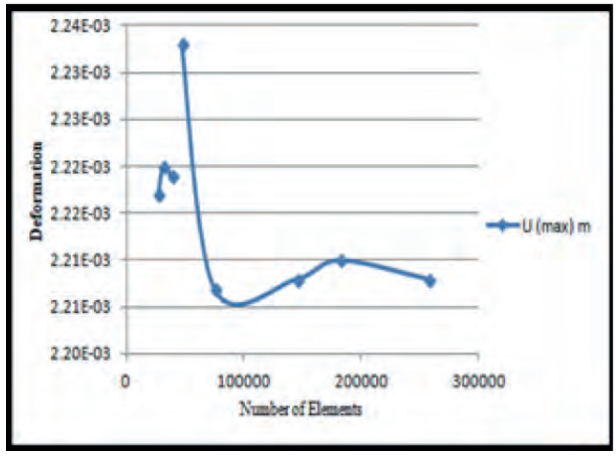


Fig. 9. Relation between the Number of Elements and the Deformation.

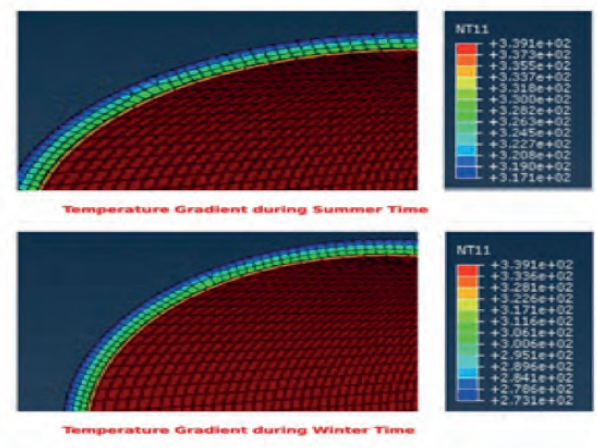


Fig. 10. Temperature Gradient.

Table 10. Maximum Heat Flux for Non Isolated Heat Transfer Analysis.

Heat Transfer Method	Interaction	Type of Interaction
Convection	Int-1	Surface Film Condition
Radiation	Int-2	Surface Radiation

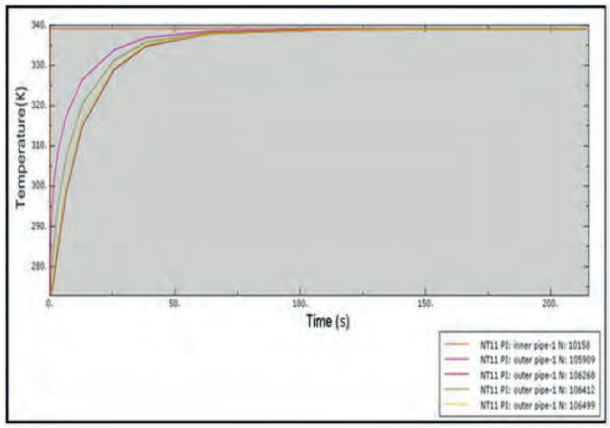


Fig. 11. Time Needed to Reach Thermal Equilibrium in Winter.

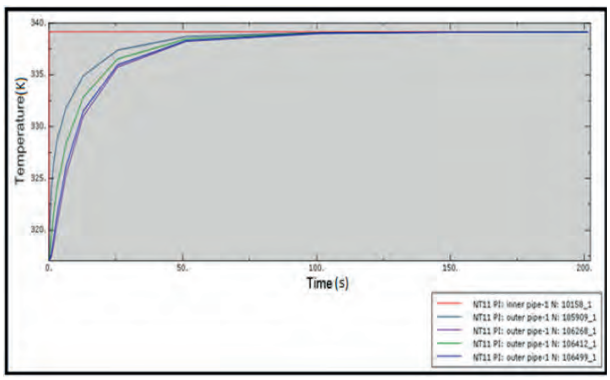


Fig. 12. Time Needed to Reach Thermal Equilibrium in Summer.

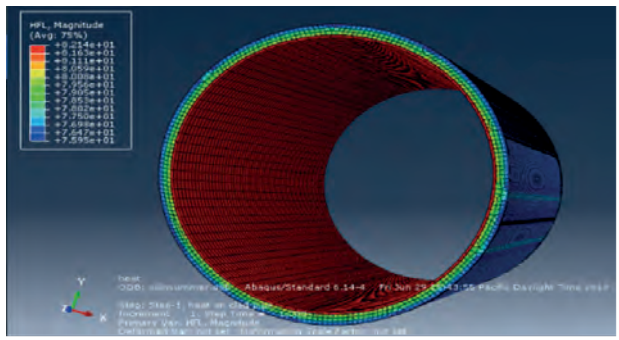


Fig. 13. The Non Isolated, Steady State Heat Transfer Analysis (with oil) in Summer.

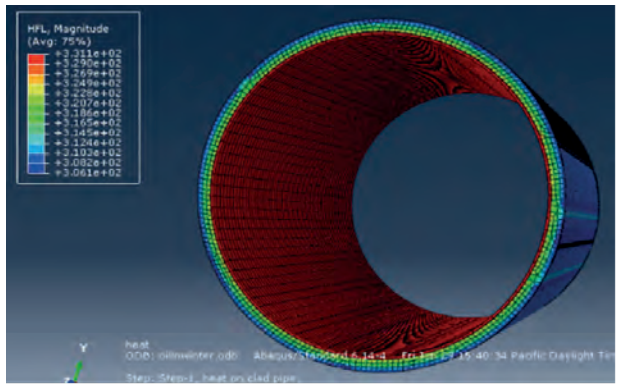


Fig. 14. The Non Isolated, Steady State Heat Transfer Analysis (with oil) in Winter.

is to verify the thermal behavior of the clad pipe when it's used in the Sarir Oil Field instead of the current carbon steel pipe. An FEA model has been developed using the Abaqus software. In the coupled temperature and displacement analysis, the accurate results were obtained by carrying out a mesh sensitivity study. In addition, the temperature gradient, heat flux values, and the transient curves also obtained from the heat transient analyses. The best type of mesh for the current project is: Tet (free), C3D4T; A 4-node thermally coupled tetrahedron, linear displacement and temperature (model 3) because it has the maximum S (max) value (2.900E+09Pa). The accurate results were obtained when the mesh size was not larger than 0.02 for the outer pipe (CS) and 0.009 for the inner pipe (SS).

Three heat transfer analyses were carried out:

- Steady state heat transfer analysis to verify the temperature gradient during the summer and winter times by applying two boundary conditions, the temperature gradients were obtained and showed in figures.
- Steady state and transient heat transfer analysis to determine the heat flux during the two seasons, the heat applied as a BC on the inner

surface of the clad pipe (no oil is flowing in the clad pipe), the heat flux results were obtained.

- The transient heat transfer analysis results show that the clad pipe will reach the thermal equilibrium when heated until 66°C during 214.1s in winter, and 201.3s in summer where Sarir`s temperature conditions were applied.

Finally, a steady state heat transfer analysis to determine the heat flux while the hot oil is flowing in the clad pipe during summer and winter times in the Sarir oil field, the heat flux results were obtained.

NOMENCLATURE

AGOCO	Arabian Gulf Oil Company
BC	Boundary Condition
CM	Clad Metal
CRA	Corrosion Resistance Alloy
CS	Carbon Steel
FE	Finite Element
FEA	Finite Element Analysis
PM	Parent Metal
SS	Stainless Steel
Gr	Grashof Number
Nu	Nusselt Number
Pr	Prandtl Number
Ra	Rayleigh Number
Re	Reynolds Number

REFERENCES

Bengtson, H. (2013). Excel Spreadsheets to Calculate Natural Convection Heat Transfer Coefficients, www.brighthubengineering.com/.

Berg, B. and Schnaut, U. D. (2009). Pipeline Technology Conference in A new production method for CRA Lined Steel Pipe based on sheet metal: 1-13.

OPTIMAL DESIGN AND SIMULATION OF SOLAR PHOTOVOLTAIC POWERED CATHODIC PROTECTION FOR UNDERGROUND PIPELINES IN LIBYA

Dr. Mustafa A. Al-Refai*

Abstract: In Libya, pipelines are being used as means of transferring hydrocarbon from wellheads to export sea ports, refineries, storage tanks, steel factory and power plants. Steel pipeline is widely used because it is of the safest means of transporting hydrocarbon and other oil products as well as its cost effective. However, one of the challenges facing oil and gas sector is corrosion on infrastructure facilities and processing units. Cathodic-Protection (CP) is an electrical method used to protect metallic body in contact with the earth from corrosion. A photovoltaic (PV) provides a reliable solution for powering remote CP stations, enabling the placing of CP units in any location along the underground pipeline, thus ensuring optimal current distribution for the exact protection requirements. In this paper the sizing of the system is determined based on the electrical power needed for the catholic protection, characteristics of the used PV module and the meteorological data of the installation site. Math/Lab Simulink and PvsystV6.43 software's are used as tools for optimal design, sizing and simulation of the PV powered cathodic protection system components. In addition to that estimation of system cost was investigated and compared with the conventional system. The results show that using solar energy powered cathodic protection system for underground pipelines is practical and very beneficial besides being economical, especially considering the rapid decreasing in the prices of PV systems components and the increasing of its efficiencies and reliability.

Keywords: Libya, PV, cathodic protection, solar energy, Matlab/Simulink, Pvsyst.

INTRODUCTION

Crude oil and natural gas transfer pipelines pass through Libyan's desert areas where a frequent problem in Cathodic Protection (CP) is that extending the normal electric power supply from the utility grid would be very costly.

Libya is blessed with a rich and reliable supply of solar energy and with an average sunshine duration of more than 300 days per year. In this paper, the study has been conducted for a pipeline cathodic protection site Ras-Lanuf which is located on the Gulf of Sirt of Libya. The pipeline 36" is running from Amal Field to Ras Lanuf Tank Farm for a distance of approximately 273km, and buried in the desert sand. With coordinates are 30°.19' N latitude and 18°.5' E longitude.

By using solar photovoltaic (PV) system provides a reliable solution for powering remote cathodic protection stations, enabling the placing of cathodic protection units in any location, thus ensuring an optimal current distribution for the exact protection system requirements.

Corrosion is defined as an electrochemical process in which a current leaves a metal body at the anode area, passes through an electrolyte, and reenters the metal structure at the cathode area. Corrosion in pipeline leads to material loss, gas and oil leakage, and interruption in gas and oil supply. In addition, problems and failures of pipeline networks not only have an economic cost; it can also present a threat to life and the environment (Beavers & Neil, 2006; Yang, 2008).

Cathodic-Protection (CP) is an electrical technique used to protect metallic bodes in contact with the earth from corrosion by minimizing the potential difference between anode and cathode. This is achieved by supplying electrical current to the

*Electrical and Electronic Department, Faculty of Engineering / Tripoli University, Libya.

structure to be protected from some outsider source. When enough current is applied, the whole structure will be at one potential level; thus, anode and cathode will disappear. The simplest method to apply cathodic protection is by connecting the metal body to be protected with another more easily corroded metal to act as the anode of the electrochemical cell (Edward and Winston, 2010). There are two main types of cathodic protection systems one is the galvanic cathodic protection systems and the other is the impressed current cathodic protection (ICCP) systems. Both types have anodes (from which current flows into the electrolyte), a continuous electrolyte from the anode to the protected metal structure, and an external metallic connection. The potential for the use of ICCP was first recognized by (Baboian, 1974). Since that time, the performance and development of various platinum surfaced anodes has been widely covered in the literature (Baboian, 1974). The correct application of cathodic protection can extend the design life of oil, gas and water underground pipeline networks, saving the energy and the money necessary to build a new one. Therefore, cathodic protection is a tool to achieve energy efficiency. In the impressed current cathodic protection system, it is possible to use the photovoltaic system as a power supply.

The objectives of this paper are designing, and simulation of solar photovoltaic powered cathodic protection system for underground pipelines transporting hydrocarbon and other oil products in Libya. The design was based on the pipeline dimensions, the percentage of protected surface area, the electrical parameters of pipeline surrounding environments, characteristics of the used PV module and the meteorological data of the site of installation. ICCP system design calculation methodologies adopted a step-by-step approach and to validate the design a simulation is carried out using Matlab/ Simulink and Pvsyst 6.43 software's.

PRINCILPES OF CATHODIC PROTECTION

Oil and gas pipelines have been made from its primary ore metal oxides with to a natural tendency to revert to that state under the action of oxygen and water. This behaviour is called corrosion. This is an electrochemical process that involves the passage of small scale electrical currents (Mathiazhagan, 2010). The change from the metallic to the combined form occurs by an "anodic" reaction:

$$Fe \rightarrow Fe^{++} + 2e- \quad (1)$$

This reaction produces free electrons, which pass within the metal to another position, on the metal surface (the cathode), where it is consumed by the cathodic reaction.

In acid solutions the cathodic reaction is (Ronald, 2001):

$$2H^{+} + 2e- \rightarrow H2 \quad (2)$$

Corrosion occurs at the anode but not at the cathode. The anode and cathode in a corrosion process may be consisting of two different metals connected together forming a bimetallic couple, or, as with rusting of steel, they may be close together on the same metal surface. The principle of cathodic protection is in connecting an external anode to the metal surface to be protected and passing of an electrical dc current such that the whole area of the metal surface become cathodic and hence corrosion do not occur. The external anode may be a galvanic anode, where the current is a result of the potential difference between the two metals, or it may be an impressed current anode, where the dc current is impressed from an external power supply (Euring, 1981).

In electrochemical process, the electrical potential between the metal and the surrounding electrolyte with which it is in contact is made more negative, by supplying negative charged electrons, to a value at which the corroding (anodic) reactions are suppressed and only cathodic reactions can take place.

Components of the ICCP System

The main components of the ICCP system powered by PV solar energy are PV generator to supply dc current, DC-DC, converters used to increase or decrease the voltage produced by the solar array, batteries storage system, coated pipeline structure system and impressed current anodes. Figure.1 shows block diagram for the whole PV powered ICCP system.

Design of Cathodic Protection Systems

The design process for cathodic protection of underground pipelines network includes the various necessary input parameters such as soil resistivity, current density protection criteria and design life. Soil resistivity is a function of soil moisture and the concentrations of ionic soluble salts and is considered most comprehensive indicator of a soil's corrosively. Typically, the lower the resistivity, the higher will be the corrosively as indicated in (Table 1).

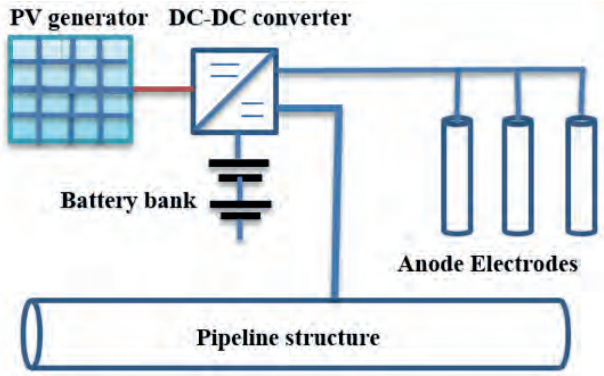


Fig. 1. Block diagram of ICCP system powered by PV.

In this paper, a design was carried out for Harouge Oil Operations' Ras-Lanuf, which is located on the Gulf of Sirt of Libya. The pipeline 36" is running from Amal Field to Ras Lanuf Tank Farm for a distance of approximately 273 km, and buried in the desert sand. In this design an assumptions of coating efficiency 90%, design life 35 years and pipe joint length is 4m are considered. The electrical parameters for pipeline, anode and surrounding environments are shown in (Tables 2 & 3) (Sami, 2008).

Design of the impressed current cathodic protection system was carried out based on the pipeline information and Tables (1 to 3). The procedure for the design starting with calculating the current required to catholically protect the pipeline under consideration or change its potential to minimum value of 0.85 volts. The current requirement depends on pipe coating quality, soil resistivity of pipeline route and total external surface area of the pipeline.

Corrosion Current Calculation

Design of ICCP starting with calculating the current required to catholically protect the pipeline under consideration or change the structure potential to minimum value of 0.85 volts. The required DC current to prevent corrosion is calculated based on the quantities of current density (which is the minimum quantity of electrical current required to prevent corrosion from occurring on the pipeline steel surface), coating quality, and soil resistivity (along the right of way and total external surface area of the pipeline; Ezeiel, 2015). The required current IR was calculated using the following equation:

Table 1. Soil Resistivity Vs Degree of Corrosively.

Soil resistivity (ohm-cm)	Degree of corrosively
0–500	Very corrosive
500–1,000	Corrosive
1,000–2,000	Moderately corrosive
2,000–10,000	Mildly corrosive
Above 10,000	Negligible

Table 2. Electrical Parameters of Pipeline Surrounding Environments.

Soil resistivity (ohm-cm)	Degree of corrosively
0–500	Very corrosive
500–1,000	Corrosive
1,000–2,000	Moderately corrosive
2,000–10,000	Mildly corrosive
Above 10,000	Negligible

Table 3. Anode Data.

Anode material	Platinum clad
Current density	30mA/m^2
Design life	35 years
Anode dimension	0.75m x 0.75m x 3.00m
Utilization of platinum clad	65% kg/amp-yr
Weight of anode	30kg
Backfill length surrounding anode	0.5m
Backfill diameter surrounding anode	0.15m
Cable wire specification	0.0212 ohms per 100ft

$$I_R = A_t \times j_c \quad (3)$$

Where, A_t is the total external pipeline surface area and Jc the current density.

The total external surface area of the pipeline can be determined using the following equations which is applied on cylindrical shape as the distributed pipeline depending on the length of the pipeline (L) and the diameter of the pipeline (D), Surface area of pipeline. And considering the coating efficiency ηc = 0.9 based on the total external surface area of the pipeline is estimated as following:

$$A_t = \pi \times D \times L \times \eta c \quad (4)$$

Where; D = 0.762m (36"), and L=273,000m.

$$\therefore = 3.142 \times 0.9144 \times 273 \times 1000 \times (1 - 0.9) = 78434.123 m^2$$

The total current required for ICCP IR using based on the pipe surface area and current density jc in Table 1 for desert environment yield.

$$I_R = 0.0004 \times 78434.123 = 31373.649\ mA$$

Next step is calculating the required number of anodes needed to meet current density limitation specified by the manufacturer which is found as follows

$$N_A = \frac{I_R}{A_t \times J_c} \quad (5)$$

Where NA is the required number of anodes and A_t , is the anode surface area estimated using Table 2 as:

$$A_a = \pi \times d \times l = 3.142 \times 0.75 \times 3 = 7.1 m^2 \quad (6)$$

Therefore,

$$N_A = \frac{I_R}{A_t \times J_c} = \frac{31373.649}{7.1 \times 30} = 148\ anodes \quad (7)$$

Then required number of anodes needed to meet 35 years intended design life based on the required current was calculated using the following formula (Dwing, 1936).

$$N_A = \frac{D_L I_R}{1000 \times A_W} \quad (8)$$

Where DL the design life and AW the anode weight

Therefore

$$N_A = \frac{35 \times 31373.649}{1000 \times 30} \cong 37\ anodes \quad (9)$$

Additionally, anode spacing is an important design parameter that is used to ensure maximum allowable voltage drop is not exceeded. The anode spacing can be reduced if the permissible voltage drop is exceeded by choosing anode with lower weight or increasing the number of anodes. The anode spacing (AS) is estimated with the following equation:

$$A_S = \frac{Pipeline\ length}{N_a} = \frac{273 \times 1000}{37} \cong 7378.378 m \quad (10)$$

Next is calculation of interval of pipe joint to determine interval of anode bracelet that will be placed. The interval of pipe joint is given as:

$$interval = \frac{A_S}{average\ length\ of\ pipe\ joint} = \frac{7378.378}{4} = 1844.595\ joint \quad (11)$$

Furthermore, anode to electrolyte resistance known as resistance to earth remains a critical parameter in cathodic protection system design evaluation in predicting anode current output. The other resistances include structure to electrolyte and cabling resistance and are often neglected in design for offshore location. The resistance of a single vertical anode R_A was calculated using the following equation (Abdulamer, 2013):

$$R_A = 0.00512 \times \rho \times \frac{\left[\ln\left(8 \times {A_l}/{A_d}\right) - 1\right]}{A_l} \quad (12)$$

Where, A_l is the anode length plus backfill, A_d is the anode diameter plus backfill and ρ is the average soil resistivity taken as 65 Ω.m against taking the lowest value since there was no significant variations of the values.

$$R_A = 0.0052 \times 65 \times \frac{\left[\ln {\{8 \times (3 + 0.5\}}/{\{0.75 + 0.15\})} - 1\right]}{(3 + 0.5)} = 0.24\ \Omega \quad (13)$$

Anode lead wire cable was supplied in ohms per 100ft per manufacturer's specification and the cable wire resistance was computed with equation:

$$R_W = \frac{\Omega\ L}{100 ft} \quad (14)$$

Where, is the length of structure (pipeline) measured in ft.

$$\therefore\ R_W = \frac{0.00212 \times 328 ft}{100 ft} = 0.070\Omega \quad (15)$$

The structure to electrolyte resistance (Re) is calculated as following:

$$R_e = \frac{R_c}{A_C} \quad (16)$$

Where, R_c is the coating resistance and AC is the area of the coated pipeline surface. The entire pipeline length under consideration has been coated. So, AC = AT

$$\therefore\ R_e = \frac{18}{86405} = 0.0002\Omega \quad (17)$$

The total circuit resistance was estimated using the follows formula (Abdulamer, 2013):

$$R_T = R_G + R_W + R_e \quad (18)$$

$$\therefore\ R_T = 0.24 + 0.070 + 0.0002 = 0.3102\Omega$$

The voltage requirement was calculated with following equation:

$$V_T = I_T \times R_T \times 150\% \quad (19)$$

Where, V_T is the voltage output requirement and the 150% represent design factor to ensure supply voltage not below the needed voltage:

$$V_T = \frac{31373.649 \times 0.3102 \times 150}{100} = 14598.159\, m\,V \quad (20)$$

PV Generator Sizing

ICCP system needs an external current source, the PV generator is used as a current source for the ICCP system. The PV station is constructed in one place per each section of which means that each media has PV station and the station is including the anodes and batteries in the same place of PV station.

Required Power And Energy For ICCP System: The required power PR for ICCP system can be calculated using the following in the equation;

$$P_R = I_R \times V_R \quad (21)$$

$$\therefore \; P_R = 31.374 \times 14.598 = 457.998\text{Watt}$$

Therefore the required energy ER needed for ICCP system in one day can be found using the as following:

$$E_R = P_R \times 24 \quad (22)$$

$$E_R = 457.998 \times 24 = 10991.944wh$$

Power Produced From PV Generator: The power produced PPV from PV generator can be determined using the following equation.

$$P_{PV} = \frac{E_R}{\eta_C} \times 1.15 \times \frac{1000W}{5400Wh/day} \quad (23)$$

$$\therefore P_{PV} = \frac{10991.944}{0.9} \times 1.15 \times \frac{1000}{5400} = 2601W$$

Number of Modules: Factors affecting the selection of a PV module are the efficiency of the module and its cost. To decide whether to use poly-crystalline or mono-crystalline modules is not easy; it requires weighing costs against efficiencies. PV modules are sized depending on the peak power of one module Pmax under Standard Testing Conditions (STC). Specifically, STC are 1,000 W/m2 solar irradiance and 25°C.

In this design, the Canadian solar power of 400 Wp production is selected and adopted. The parameters of the chosen PV module are given in Table 4, (WWW//us.sunpower.com).

The number of modules Nm is calculated in equation 21 depending on the peak power of one module Pmax which is taken as 435W, this value referred to:

$$N_M = \frac{P_{PV}}{P_M} \quad (24)$$

$$\therefore \quad N_M = \frac{2601}{435} \cong 6$$

Battery Sizing and Selection

A battery bank is used as a backup system and it maintains constant voltage across the load. It is used to power the ICCP, when the solar power is not available basically during night time and cloudy days. The energy required by ICCP was calculated and equal to 10991.944wh and the battery operating voltage is 12V. The required battery capacity in ampere hour CAh was calculated based on the values of DOD of the battery (0. 85) and its average (efficiency =78) using the following equation:

$$\text{Battery capacity in Ah} = \frac{autonomy\ days \times E_R}{V_{battery} \times DOD \times \eta_{Battery} \times \eta_{inverter}} \quad (25)$$

Where:
Autonomy days =1
Eload = energy consumption Wh/day

Table 4. Specifications for Solar Panels.

Electrical Specifications (Standard Test Conditions = 25 ؛C, 1000W/m² irradiance and AM=1.5)	
Model	**SPR-E20-435-COM**
Max System Voltage	1000 V
Max Peak Power PmaX	435 W (±3%)
Maximum Power Point Voltage Vmpp	72.9 V
Maximum Power Point Current Impp	5.97 A
Open Circuit Voltage Voc	85.6 V
Short Circuit Current Isc	6.43 A
Module Efficiency (%)	20.3%
Temperature Coefficient of Voc	--235.5mV%°C
Temperature Coefficient of Isc	2.6mA% / °C
Temperature Coefficient of Pmax	-0.35% /C

DOD=battery Depth of Discharge =0.75

ηBattery = efficiency of battery =85%

$$\therefore battery\ capacity\ Ah = \frac{1\times10991.944\text{Wh}}{0.78\times0.85\times12}$$

$$= 1381.592Ah \approx 1382\text{Ah}$$

Two 400Ah, 6V batteries in series yields 12 V at 400 Ah.

$$\text{series battery capacity,} = \frac{1382}{400} = 3.455 \approx 4\ batteries$$

Therefore, the total number of batteries in a battery bank (consisting of 4 batteries) will provide a capacity of 1600Ah.

SIMULINK OUTPUT OF DESIGNED GRID-CONNECTED PV PANEL

A block diagram of the PV model using Simulink is given in (Fig. 2). The block contains the sub models connected to build the final model. Variable temperature (T), and variable solar irradiation level (G) are the inputs to the PV model. The equation of the PV output current is expressed as a function of the array voltage as follows:

$$I = I_{ph} - I_D = I_{ph} - I_{sat}\left[e^{\frac{q(V+IR_S)}{nkT}} - 1\right]. \quad (26)$$

Where:

Iph the light current [A], Isat the diode reverse saturation current [A], Rs, the series resistance [Ω], V the operation voltage [V], and I the operation current [A].

q = charge of one electron($1.602\times10^{-19}C$),

n= Diode idealizing factor, and k= Boltzman's constant (1.38×10^{-23} J/K).

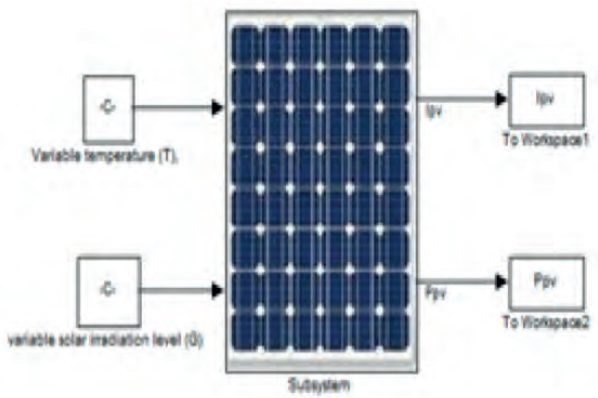


Fig. 2. Simulink model of PV module.

T=Junction temperature in Kelvin.

The modeling of the PV array for Matlab/Simulink environment is discussed in (Al-Refai, 2017). The final PV system design consists of six modules connected in parallel with manufacturer's specified nameplate as shown in Table 4. The I-V and P-V outputs characteristics of PV module with varying irradiation and constant temperature are shown in Figures 3 and 4. The P-V and I-V outputs characteristics of PV module with varying temperature at constant irradiation are shown in (Figs. 5 and 6). The results are verified and found matching with the manufacturer's data sheet output curves.

DESIGN AND SIMULATION OF PV SYSTEM USING PVSYS SOFTWARE

The final system design is performed using the Pvsyst V 6.43 simulation software (Fig. 7).

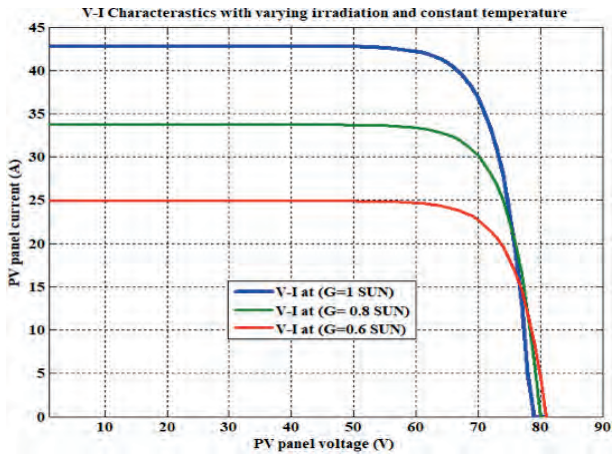


Fig. 3. V-I Characteristic curves at different insolation levels (G= 0.6 SUN, 0.8 SUN, 1 SUN) for 6 module in parallel.

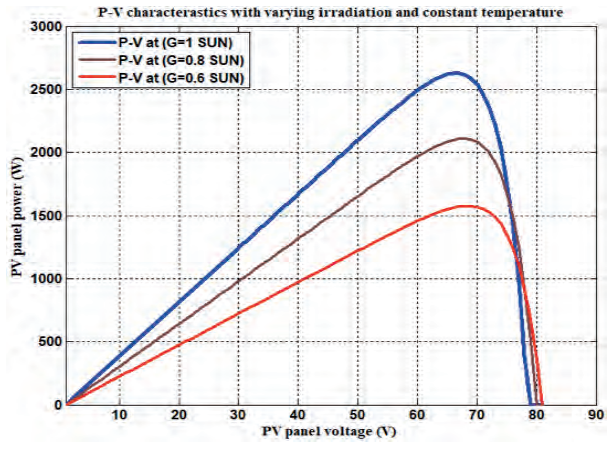


Fig. 4. P-V Characteristic curves at different insolation levels (G= 0.6 SUN, 0.8 SUN, 1 SUN) for 6 module in parallel.

PVSYST software is a PC package for analyzing the potential of a photovoltaic system at a known location. It consists of both meteorological data and the possibility to select system components from various manufacturers. The simulation results of designed PV system are displayed comprehensively through the created report by PVSYST.

Figure 8 gives the PV module and battery specification for modeling of standalone system. As per technical specification battery used is 12V, 296Ah, which can store energy of 1.184Kwh and number of battery required is 4. The PV module selected is of 435Wp, 61.5V with array voltage 61.5V, array current 36.9A, Array power (STC) generated is 2.6 kWp .The number of modules required as per calculation is 6. Design of solar PV standalone system evaluation mode as shown in (Fig. 9). PVsyst provides a detailed analysis of all losses flow diagram of the system as shown in (Fig. 10).

Figure 11 gives the normalized power production and loss factor which is yield annually. Table 5 gives the balance and main result, annual global horizon is 2121.8, available solar energy is 4588.8, unused energy is 451.93, and load connected is 4029.6.

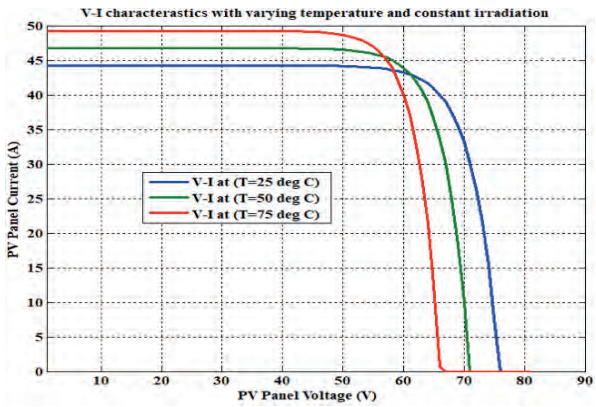


Fig. 5. V-I Characteristic curves at different cells working temperature (TC =25OC, 50OC, 75OC) for 6 module in parallel.

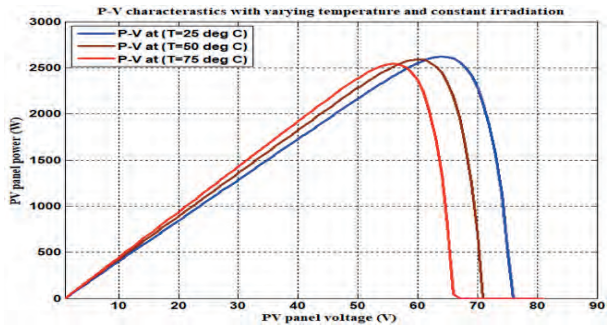


Fig. 6. P-V Characteristic curves at different cells working temperature (TC =25OC, 50OC, 75OC) for 6 module in parallel.

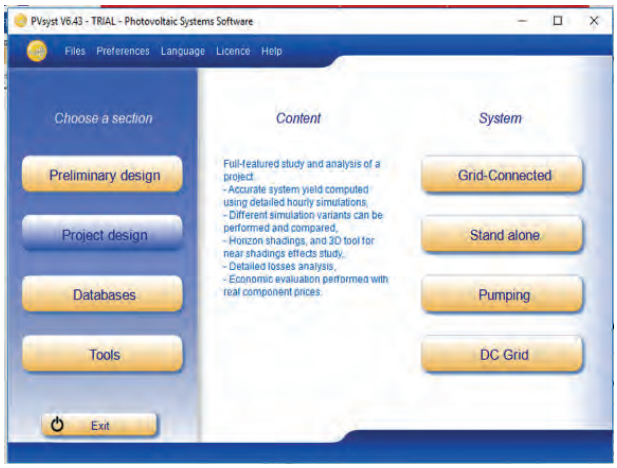
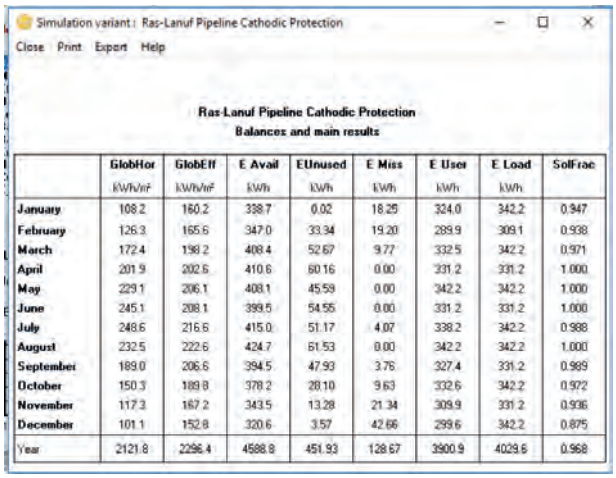


Fig. 7. PVSYST V6.43 Simulation software.

CONCLUSION

The proposed renewable supply is most viable solution for powering impressed current cathodic

Table 5. Balance and Main Results.



	GlobHor kWh/m²	GlobEff kWh/m²	E Avail kWh	EUnused kWh	E Miss kWh	E User kWh	E Load kWh	SolFrac
January	108.2	160.2	338.7	0.02	18.25	324.0	342.2	0.947
February	126.3	165.6	347.0	33.34	19.20	289.9	309.1	0.938
March	172.4	198.2	408.4	52.67	9.77	332.5	342.2	0.971
April	201.9	202.5	410.6	60.16	0.00	331.2	331.2	1.000
May	229.1	206.1	408.1	45.59	0.00	342.2	342.2	1.000
June	245.1	208.1	399.5	54.55	0.00	331.2	331.2	1.000
July	248.6	216.6	415.0	51.17	4.07	338.2	342.2	0.988
August	232.5	222.6	424.7	61.53	0.00	342.2	342.2	1.000
September	189.0	206.6	394.5	47.93	3.76	327.4	331.2	0.989
October	150.3	189.8	378.2	28.10	9.63	332.6	342.2	0.972
November	117.3	167.2	343.5	13.28	21.34	309.9	331.2	0.936
December	101.1	152.8	320.6	3.57	42.66	299.6	342.2	0.875
Year	2121.8	2296.4	4588.8	451.93	128.67	3900.9	4029.6	0.968

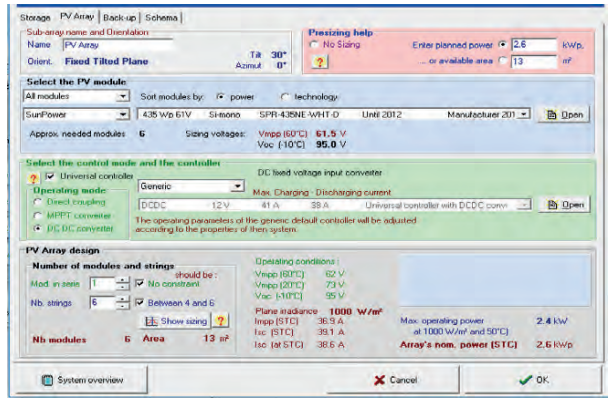


Fig. 8. System design in PVsyst.

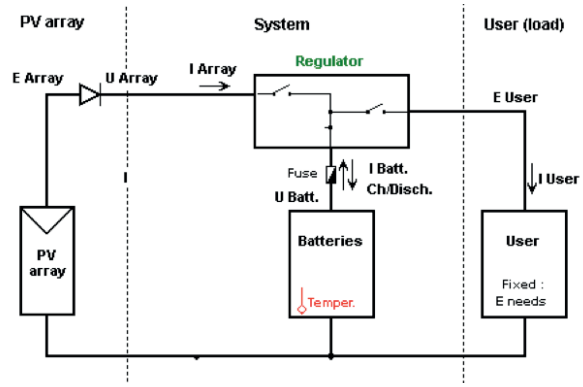


Fig. 9. Typical layout of PV system.

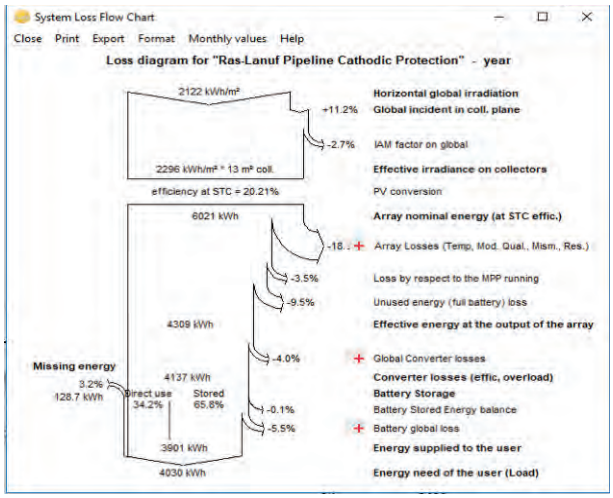


Fig. 10. System loss flow diagram.

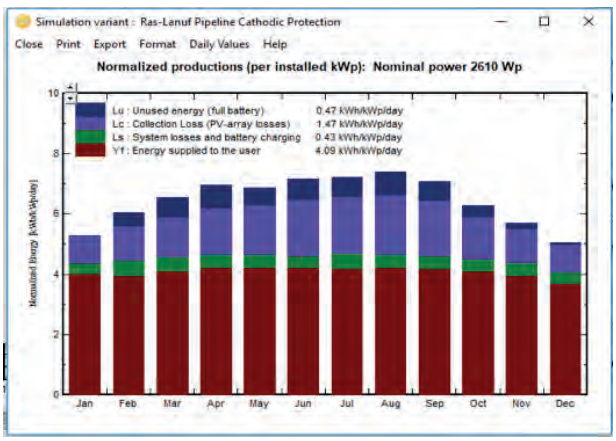


Fig. 11. Normalized production per installed KWP.

protection (ICCP) system, which is available throughout the year. This paper shows that using solar photovoltaic powered cathodic protection for buried pipelines transporting hydrocarbon and other oil products in Libya is feasible. The design was based on the pipeline dimensions, the percentage of protected surface area and the electrical parameters of pipeline surrounding environments.

This paper, also describe that numerical calculation and simulations can be useful tool in the design and evaluation of the cathodic protection of buried pipeline networks. The results show that using solar energy powered cathodic protection system for underground pipelines is practical and very beneficial besides being economical, especially considering the rapid decreasing in the prices of PV systems components and the increasing of its efficiencies and reliability. In addition to that powering ICCP of the pipeline by renewable energy system, will reduce the carbon and other harmful gases emission.

REFERENCES

Abdulamer, D. N. (2013). E ect o Soil Resistivity or Different Geometry Anodes on Design Photovoltaic or Cathodic Protection. *Journal of Global Research Analysis*, **2**: 2277-8160.

Al-Refai, M. (2017). Design and Simulation Analysis of 100MW Grid-Connected Solar Photovoltaic Power System at Tripoli-Libya. *International Journal of Electrical and Electronic Engineers*, **9** (2): 402-416.

Baboian, R. (1974). Chlorine Bicentennial. *The Electro-Chemical Society Princeton*, **9**: 158.

Beavers, J. A. and Neil, G. (2006). Thompson, CC Technologies External Corrosion of Oil and Natural Gas Pipelines. *ASM Handbook*, **13**: (C), *Corrosion: Environments and Industries*: 1015-1025.

Dwing T, H. B. (1936). Calculation of Resistance to Ground. Electrical Engineering: 1319-1329.

Edward, G. and Winston, R. (2010). Corrosion Resistance of Aluminum and Magnesium Alloys Understanding, *Performance, and Testing*: 752p.

Euring, R. L. and Davies, K. G. (1981). Kean of ARK Corrosion Services. Cathodic Protection: 1-8.

Ezeiel, E. (2015). Introduction to Electrical Design or Cathodic Protection Systems. *Ezeiel Enterprises, LLC, rticle's Review*.

https://us.sunpower.com/sites/sunpower/files/uploads/resources/sp-e20-435-helix-ds-en-ltr-pv4s-521912.pdf

Mathiazhagan, A, (2010). Design and Programming of Cathodic Protection for SHIPS. *International Journal of Chemical Engineering and Applications*, **1 (3)**: 2010-0221.

Ronald, L. (2001). Bianchetti Control of Pipeline Corrosion NACE *International the Corrosion Society 1440* South Creek Drive Houston, Texas **77084**.

Sami, M. (2008). Computer Application in pipeline Cathodic Protection *Design. Proceedings of XI. International Corrosion Symposium*, Dokuz Eylul University, Izmir, Turkey: 22-25.

Yang, L. (2008). Techniques for corrosion monitoring. Houston Woodhead Publishing: 712p.

MODELING AND PREDICTION OF HIGH TEMPERATURE OXIDATION OF STEELS USED IN PETROLEUM REFINERY HEATERS

Naji Abdelwanis*, Abdelrahman S. Sultan**, Omar M Elmabrouk***, and Farag A. Maetouq****

Abstract: This paper implements Response Surface Methodology (RSM), with rotatable Central Composite Design (CCD), in modeling and prediction of high-temperature oxidation of steels used in petroleum refinery heaters. A mathematical quadratic model was developed for modeling and prediction of the relationship between the weights gained of the oxidized steel and condition parameters, namely chromium percentage, temperature and exposure time with a range of, 0-5wt%, 450-500°C, and 0-40hrs respectively. Also, the surface plots and response surface contour plots were constructed for investigating the simultaneous effect of the condition process parameters on the weights gained from the oxidized steel and determining the optimum values of the parameter conditions. The Mean Absolute Error (MAE) between the actual and predicted weights gained from the oxidized steel values was calculated to test the validity of the developed mathematical model. The value of the (MAE) was 0.42 which indicates that the developed mathematical model have good agreement with the actual. The statistical analysis of variance (ANOVA) was also utilized to analyze the effect of the investigated parameter condition, this analysis results demonstrated that chromium weight percent and temperature have the most significant effect on the weights gained oxidation of steels used in petroleum refinery heaters followed by exposed time.

Keywords: Modeling; Prediction, RSM, High temperature corrosion.

INTRODUCTION

For oil refinery heaters (furnaces) are used to preheat feedstock to reaction or distillation temperatures. The fluid heaters are designed to increase the temperature to about 510°C (950°F) maximum. Based on economic assumptions, operating conditions, and emission requirements, the fuel burned may be remaining fuel oils, refinery gas, natural gas or combinations. The gaseous combustion products, which are mixtures of mainly; carbon dioxide, water, and nitrogen are surrounded by the steel pipes used in heaters. Additionally to other specifications, corrosion allowance the selection of heater tubes and their thicknesses are necessary (API standard 530, 2003). Due to the fact that the corrosion during operation leads to decrees the tube thicknesses. Also, for many industrial engineering and in many domains of material science e.g. high-temperature processes in petroleum industry or metal production and fabrication, the oxidation behavior of materials at elevated temperatures became of crucial importance. Moreover, to investigate and analyze the kinetics of the oxide film growth is very essential to control high-temperature oxidation (Knoll *et al*, 1999*)*.

Thermogravimetric analysis (TGA) technique was used to investigate the oxidation behaviors of three different steel, C-5, P-11 and P-22, used in the construction of petroleum refinery heaters in two different environments namely air and $O_{22}H_20O_7$-$52N_2$. The temperature of the gas composition which simulates the combustion products of natural gas were 450 and 500°C (Sultan *et al*, 2012). The diffusional transport associated with high-temperature corrosion processes using numerical modeling was studied. The external scale formation and internal subscale formation during oxidation, coating degradation by oxidation

*Department of Mechanical Engineering-Omar Al-Mukhtar University. E-mail: nabdelw@g.clemson.edu.ly
**Department of Chemical and Petroleum Engineering-Elmergib University. E-mail: assultan@elmergib.edu.ly
***Department of Industrial &Manufacturing Systems Engineering-Benghazi University. E-mail: omar.elmabrouk@uob.edu.ly
****Department of Industrial &Manufacturing Systems Engineering-Benghazi University. E-mail: farag.maetouq@uob.edu.ly

and substrate inter diffusion, carburization, sulfidation and nitridation were included in the corrosion processes. The complexities such as concentration-dependent diffusivities, cross-term effects in ternary alloys, and internal precipitation where many compounds of the same element may form (e.g., carbides of Cr) or several compounds exist instantly (e.g., carbides containing varying amounts of Ni, Cr, Fe or Mo) were reviewed. Large number of boundary conditions that differ with time and temperature were also included. Either the solute or corrodant transport was modeled using finite- difference (F-D) techniques. High temperature corrosion modeling studies using F-D were also considered (James, 1995).

In the potential geological repository at Yucca Mountain, the chosen materials for the outer barrier of nuclear waste packages are wrought and cast low-carbon steel. The potential declination mode for these materials at the moderately high temperatures assumed at the container surface, e.g. 323-533K (50-260°C) is the dry oxidation. The prediction of the dry oxidation of iron and low-carbon steel was numerically predicted based on both the experimental data and the theory of parabolic oxidation. The Forward Euler approach was applied in the numerical method and applied to integrate the parabolic rate law for arbitrary and complex temperature histories. The assumption of the growth of a defect free, adherent oxide, the surface penetration of a low-carbon steel barrier following 5000 years of exposure to a severe, but repository-relevant, temperature history were predicted to be only about 0.127mm, less than 0.13% of the expected container thickness of 10cm.

The predicted metal penetration values were raised by permitting the oxide to spall when getting to a critical thickness, however degradation was still calculated to be negligible. According to the model calculations, dry oxidation was not expected to effectively degrade the performance of thick, corrosion tolerance barriers constructed of low-carbon steel (Henshall, 1996).

Very limited researches have been directed toward the modelling and prediction of the high temperature oxidation behavior of the steels used in petroleum refinery heaters using RSM. In this paper, the effect of the most significant oxidation process parameters namely, the temperature, time and chromium weight percent on the high temperature oxidation of the steels used in petroleum refinery heaters has been investigated and mathematically modeled using Response surface methodology (RSM) allowing with CCD. The model used to predict the oxidation behavior and validated using Mean Absolute Error (MAB).

EXPERIMENTAL WORK

Sample preparation

In this study, C-5, P-11, P-22 and P-5 steels have different chromium content as given in (Table 1) were used for air oxidation experiments. These steels are used in the construction of petroleum refineries pipes and equipments. Test specimens were cut and machined into 50mm x 25mm x 2mm steel pieces. The steel specimens were kept at 700°C for 1 hour and then let them to cool inside the furnace. The steel samples were prepared with 3mm diameter used to suspend them with quartz hook to the electro balance during the oxidation experiments.

Grinding without polishing was recommended to provide a surface that favored the nucleation of oxides and result in dense adherent scales. So, using SiC papers, the steel samples were ground sequentially starting from 120 grit and following 220, 320, 400 and 600 grits. The samples were ultrasonically cleaned and degreased by using alcohol to remove SiC and the steel particles left from the grinding. The surface areas of samples were calculated after measuring the dimensions of the samples with the aid of a micrometer. Table 1 shows the Chemical composition of the steel samples.

Thermogravimetric analysis (TGA)

A CAHN C-1000 electro balance was used for the thermogravimetric analysis in this study. The sample weight change during oxidation was detected and converted to an electrical signals (voltage) output. These output signals were read and converted to weight change on a digital computer through a data obtaining unit. At the start of each experiment, the weight was zeroed by mechanical and electronic taring of the balance. The steel samples were hanged to the balance by a quartz hook in the middle of a Pyrex reaction tube in the hot zone of the furnace. The reaction tube had a diameter and a length of 5 and 80cm respectively and it was extended out of a vertical split furnace from both ends. The upper end of the reaction tube was connected the electro balance and the lower end was left open to the atmosphere.

Table 1. Chemical composition of the steel samples.

Steel	ASTM	C%	n%	P%	S%	Si%	Cr%	Mo%	V%
C-5	A 106	0.5	0.5	0.07	0.05	0.11	--	--	--
P-11	A 335	0.5	0.5	0.03	0.03	0.77	1.25	0.57	--
P-22	A 335	0.5	0.47	0.03	0.03	0.45	2.25	1.0	--
P-5	A335	0.4	0.5	0.03	0.03	0.45	5.0	0.55	--

Air oxidation

The oxidation tests of four different steel samples were done in air at 450°C, 475°C and 500°C (temperature range depends on the designed by the program means it is optional). The durations changing between 35 to 96 hours were used. It was found that the nature of the oxides did not change for long and short oxidation periods, and 48 hours of oxidation period was selected for most of the tests in this study.

During the oxidation tests, the air flow rate was brought into the reaction chamber through the upper part by means of an air pump and controlled to be equivalent to 120 cm/min gas velocity in the reaction chamber. Figure 1 illustrates the schematic representation of setup for air oxidation (Khanna and Kofstad, 1990; Sultan *et al*, 2012).

To provide an inert atmosphere and to assure that the sample was not oxidized during heating, the reaction tube and the balance were flushed by a flow of nitrogen gas. Furthermore, the weight changes of the samples subjected to oxidation were recorded by using a PCLD 711 analog-to-digital (A/D) converter via a computer system. In this study, a 100 milligram recording range (with an accuracy of 0.1% of recording range) was used for 48 hours oxidation experiments with overall accuracy of ±0.2mg. A basic computer code was used to program the computer to get a reading from the data acquisition unit for every minute. After each experiment, the supply of the oxidizing gases was cut, but the continuous flow of the N_2 gas was conserved through the reaction tube until the system was cooled down. After cooling the furnace, the samples were taken out from the furnace and kept in desiccators for consecutive analysis of the oxidation products.

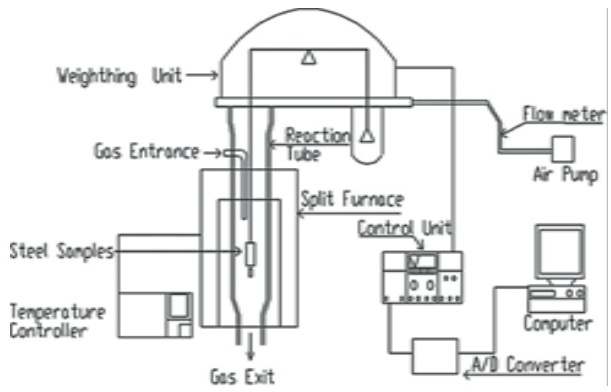


Fig. 1. Location map of the study area in NW Murzuq Basin, SW Libya.

RESPONSE SURFACE METHODOLOGY

Modeling and prediction the effect of process parameters using response surface methodology involves five major steps, these steps are (1) statistically design the experiments, (2) performing experiments practically or using simulation technique, (3) determining the coefficients in a mathematical model, (4) predicting the response and (5) validate the model by calculating the difference between the actual or simulating response and the predicted response (Geoge *et al*, 2012).

Central composite design (CCD) has been employed in this paper to model and predict the effect of high temperature oxidation process parameter, namely the temperature, the exposed time and the weight percent chromium on the steel oxidation. CCD has been widely utilized for fitting a second-order model from experimental runs. The design consists of a 2n factorial or fraction (coded to the usual ±1 notation) augmented by 2n axial points (±α, 0, 0,..., 0), (0, ± α, 0,..., 0),..., (0, 0,..., ± α), and center points (0, 0, 0,..., 0). In this case, the main effects and interactions may be obtained by fractional factorial designs running only a minimum experimental runs.

The responses and the corresponding parameters were modeled, analyzed and optimized using analysis of variance (ANOVA) approach to estimate the process parameters by means of response surface methodology (RSM).

RSM is statistical and mathematical techniques that widely used to develop, improve, optimize processes and evaluate the behavior of different influencing parameters (Raymond *et al*, 2009). RSM could also be defined as the most frequently used method of RSM is CDD, it is applicable for fitting a quadratic surface and helps to optimize the effective process parameters with a minimum number of experiments, as well as analyzing the interaction between these process parameters.

The application of RSM is achieved with measurable input parameters, the response surface can be expressed, in Equation 1, as follows (George *et al*, 2012):

$$Y = f(X_1, X_2, X_3, X_4, \ldots, X_n) \quad (1)$$

Where Y is the output or response of the process, Xi is the input process parameters and n is the number of parameters. The aim of the RSM is to mathematically model and predict the response variable (Y) and search for a suitable approximation of the functional relationship between the input measurable parameters and the output or response surface. Second degree quadratic model as given by Equation 2 was utilized for creating the model formation.

The maximum and minimum values of the independent measurable parameters values are given in (Table 2), α is 2n/4, n= number of variables (Hussein, 2015).

(In this study; α is 23/4 = 1.68).

$$Y = \beta_o + \sum_{i=1}^{n} \beta_i x_i + \sum_{i=1}^{n} \beta_{ii} x_i^2 + \sum_{i=1}^{n} \sum_{j=i+1}^{n} \beta_{ij} x_i x_j + \varepsilon \quad (2)$$

Where Y is the predicted response calculated values using the mathematical model, xi and xj are the input variables, β0 is the constant coefficient, βi , βii and βij are the inter-action coefficients of linear, quadratic, and the second order terms, respectively, and k is the number of studied factors. For statistical analysis, Xi are the actual experimental variables (Hussein, 2015).

The analysis of variance (ANOVA) was utilized to determine the lack of fit and the effect of linear, quadratic and interaction terms on response variables y. MINITAB (version 16) statistical analysis software was used to design the experiment, to analyze the experimental data and to plot the response surface and contour plots and to obtain the mathematical model. Table 2 shows the different variables used in the experiment and their levels, and Table 3 shows the planning matrix of the experiment with the experimental weight gained.

It is observed from the adequacy test by ANOVA that linear terms %Cr, interaction term %Cr with Temp. and Time with %Cr and Temp. with Time and square terms Time2 are significant. The levels of significant are illustrated in the Table 4. The fit summary recommended that the quadratic model is statistically significant for analysis of wt. gain. For the relevant fitting of

Table 2. Different variables used in the experiment and their levels.

Variable	Coding	Level		
		1	2	3
Cr (%wt)	A	0	2.5	5
Time (hr)	B	0	24	48
Temperature (°C)	C	450	475	500

Table 3. The planning matrix of the experiment with the experimental weight gained.

wt.gain (g)	Temp. (Co)	Cr (%wt)	Time (hr)
0	450	5	0
0.254087	475	2.5	24
0.254087	475	2.5	24
0.254087	475	2.5	24
0	450	0	0
0.254087	475	2.5	24
0.15242	450	5	48
0.117983	475	5	24
0.375659	475	0	24
0.177854	500	5	48
0.254087	475	2.5	24
0.311769	450	0	48
0.350096	500	2.5	24
0.158262	450	2.5	24
0.644323	500	0	48
0	500	5	0
0	500	0	0
0.254087	475	2.5	24
0	475	2.5	0
0.359333	475	2.5	48

wt. gain. the non-significant terms (p-value is greater than 0.05) are eliminated by backward the elimination process.

The ANOVA Table for the curtailed quadratic model for wt. gain is illustrated in (Table 4), the reduced model results demonstrate that the model is significant (R2 and adjusted R2 are 95.99% and 92.37%, respectively), and lack of fit is non-significant (p-value is less than 0.05). After eliminating the non-significant terms (Table 5), the final response equation for weights gained is given as follows.

wt. gain = -2.41496 + 0.29693% Cr - 0.00014 Time2- 0.00061 Temp.*%Cr + 0.00007 Temp.*Time - 0.00130% Cr*Time

The last model tested for variance analysis (F-test) found that the adequacy of the test is established. The computed values of response parameters, model graphs are generated for the further analysis in the next section. Table 6 shows the analysis values for weight gained mathematical model.

RESULTS AND DISSCUSION

The effect of the high temperature oxidation process parameters (chromium weight percentage, temperature and exposed time) on the response variables high temperature oxidation (weight gain per unit surface area) have been investigated by conducting experiments as described previously in the experimental work section.

Minitab software 16 was used for further analyze the results. The second-order mathematical model was proposed in find the correlation between the weight gain per unit surface area and the oxidation process parameters taken into account.

The analysis of variance (ANOVA) was utilized to evaluate the sufficiency of the second-order mathematical model. The results obtained from the experiments were compared with the predicted values calculated from the model as shown in (Table 7).

Table 4. Anova table for wt.gain (before elimination) Estimated Regression Coefficients for MRR.

Term	Coef	SE Coef	T	P	
Constant	-2.41496	9.89535	-0.244	0.812	non significant
Temp.	0.00827	0.04172	0.198	0.847	non significant
%Cr	0.29693	0.12453	2.384	0.038	Significant
Time	-0.01875	0.01297	-1.446	0.179	non significant
Temp.*Temp.	-0.00001	0.00004	-0.152	0.882	non significant
%Cr*%Cr	-0.00184	0.00439	-0.42	0.684	non significant
Time*Time	-0.00014	0.00005	-2.867	0.017	Significant
Temp.*%Cr	-0.00061	0.00026	-2.386	0.038	Significant
Temp.*Time	0.00007	0.00003	2.781	0.019	Significant
%Cr*Time	-0.0013	0.00027	-4.862	0.001	Significant
S = 0.0455052 R-Sq = 95.99% R-Sq(adj) = 92.37%					

Table 5. ANOVA table for MRR (after backward elimination.

Term	Coef	SE Coef	T	P	Remark
Constant	31.162	1.1599	26.867	0.00	(most significant)
Ip	11.012	0.9115	12.08	0.00	(most significant)
Ton	14.405	0.9115	15.803	0.00	(most significant)
Toff	-5.21	0.9115	-5.715	0.00	(most significant)
Ip×Ip	-3.553	0.9136	-3.889	0.002	(significant)
Ton×To n	-2.205	0.9136	-2.414	0.033	(significant)
Ip×Ton	6.959	1.1768	5.913	0.000	(most significant)
Ton×Tof f	-2.959	1.1768	-2.514	0.027	(significant)
S = 3.328 R-Sq = 97.6% R-Sq(adj) = 96.2%					

Table 6. Analysis of Variance for wt. gain mathematical model.

Source	DF	Seq SS	Adj SS	Adj MS	F	P
Regression	9	0.495272	0.495272	0.05503	26.58	0
Linear	3	0.379119	0.016101	0.005367	2.59	0.111
Square	3	0.039388	0.039388	0.013129	6.34	0.011
Interaction	3	0.076766	0.076766	0.025589	12.36	0.001
ResidualErorr	10	0.020707	0.020707	0.002071		
Lack-of-Fit	5	0.020707	0.020707	0.004141	*	*
Pure Error	5	0	0	0		
Total	19	0.51598				

Table 7. The predicted weight gained, the actual weight percent, the absolute error and the mean absolute error.

Predicted Wt. gained	Actual Wt. gained	Absolute error
0.015	0	0.015
0.256	0.254	0.001
0.256	0.254	0.001
0.256	0.254	0.001
0	0	0
0.256	0.254	0.001
0.098	0.152	0.054
0.156	0.117	0.038
0.333	0.375	0.042
0.221	0.177	0.0431
0.256	0.254	0.0019
0.354	0.311	0.0422
0.307	0.350	0.0430
0.197	0.158	0.0387
0.631	0.644	0.013
0	0	0
0.056	0	0.056
0.256	0.254	0.001
0.013	0	0.013
0.342	0.359	0.017
MAE		0.42

It is clear that the regression the values of mathematical model is reasonably well fitted with the observed values. The mean absolute error is calculated as the mean absolute difference between the predicted and observed values as 0.42.

Figure 2. shows the estimated response surface for weight gain per unit surface area in relation to high temperature oxidation process parameters of chromium weight percentage and temperature. It is clear from the figure that, the weight gain per unit surface area tends to increase, significantly with increase in temperature and lower value of chromium weight percentage. Hence, maximum weight gain per unit surface area is obtained at high peak temperature (500°C) and chromium weight percentage, as shown by the arrow in (Fig. 2), this is due to lost effect of the chromium, in other words, in high temperature working condition, the lower content of chromium steel should not be selected.

Figure 3 represents the weight gain per unit surface area as a function of chromium weight percentage and exposed time, whereas the temperature remains constant in its higher level of 475°C. The results show that the highest weight gain per unit surface area values occurred at the higher time and lower chromium weight percentage.

The direction of further improvement is illustrated in the counter plots presented as arrow. This is the direction taken in further experimentation. From this observation, it can be concluded that exposed time is directly and chromium weight percentage is inversely proportional to the weight gain per unit surface area for the studied range of the conducted experiments

Additionally, The effect of the temperature and the exposed time is on the estimated response surface of weight gain per unit surface area is shown in (Fig. 4), the chromium weight percentage is hold constant in its average value of 2.5%. The results show that the weight gain per unit surface area increases when the temperature

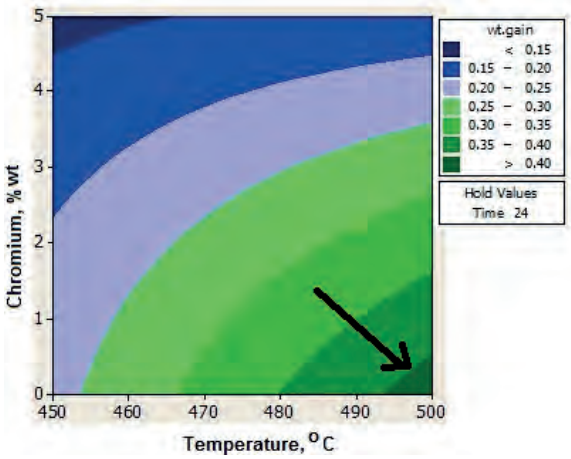


Fig.2. The estimated response surface for weight gain per unit surface area in relation of chromium weight percentage and temperature.

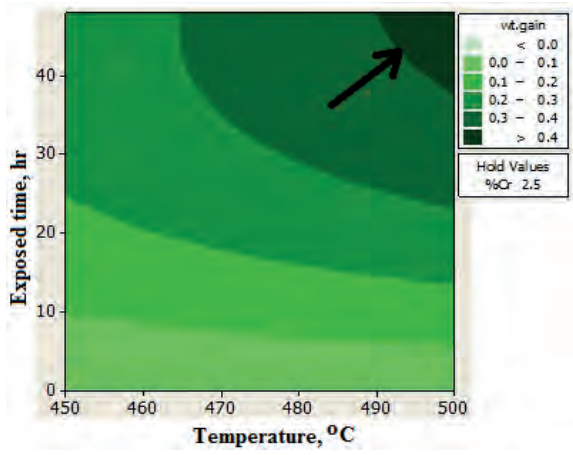


Fig.4. The estimated response surface for weight gain per unit surface area in relation of temperature and exposed time.

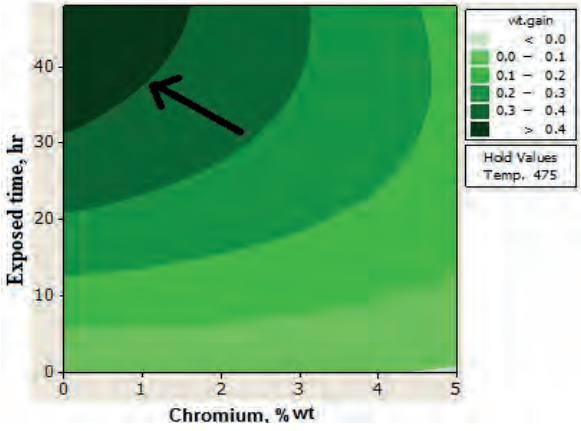


Fig.3. Estimated response surface for weight gain per unit surface area in relation of chromium weight percentage and exposed time.

and the exposed time increase, as indicated by the arrow shown in (Fig. 4). The reason is the same as explained previously, however with the increase in temperature, weight gain per unit surface area increases, this is highly expected because the oxidation processes is highly controlled by the diffusion processes of the oxygen ions. The higher the temperature, the higher the diffusion rate.

CONCLUSIONS

In this study, the mathematical models for three input parameters namely temperature, exposed time and chromium weight percent for the high temperature oxidation process of steel using response surface method was developed and introduced. The second-order response models have been validated using analysis of variance and evaluated using the mean absolute error. It is found that all the three input parameters and some of their interactions have significant effect on weight gained per unit area investigated in the present study. This is also concluded the response surface method is a powerful tool to model and predict the high temperature oxidation processes.

REFERENCES

API Standard 530, (2003). Calculation of Heater Tube Thickness in Petroleum Refineries. *5th Edn., American Petroleum Institute*, Washington DC.

George, E.; Dieter, L. and Schmidt, C. (2012). Engineering Design, *5th edition*, New York, McGrawHill.

Henshall, G. A., (1996). Numerical Predictions of Dry Oxidation of Iron and Low Carbon Steel at Moderately Elevated Temperatures. In: *MRS Symposium Proceedings*, Boston, MA, December 1996.

Hussein. A. K. (2015). Application of Response Surface Methodology for Modelling and Optimization of Hot Corrosion Rate of Nimonic 75 Coated by Ce-doped Aluminizing-Titanizing. Al-Nahrain University, *College of Engineering Journal (NUCEJ)*, ***18***: 240-249.

James, A. (1995). Numerical Modeling of High-Temperature Corrosion Processes, Oxidation of Metals, ***44 (1&2)***: 309–338

Khanna, A. S. and Kofstad, P. (1990). Microscopy of Oxidation. Presented at *International: Conference on Microscopy of Oxidation*, London, England: 113-118.

Knoll, A.; Smigiel, E.;Broll, N and Cornet, A. (1999). JCPDS-International Centre for Diffraction Data 1999 ISSN 1097-0002, Advances in X-ray Analysis, ***4***.

Raymond, H.; Montgomery, D. C. Christine, M. and Anderson, C. (2009). Response Surface Methodology: Process and Product Optimization Using Designed Experiment. A Wiley Interscience Publication. *3rd Eddition:* 282p.

Sultan, A.; Karakaya, A. I. and Erdogan, M. (2012). Influence of Water Vapour on High Temperature Oxidation of Steels used in Petroleum Refinary Haeters. *Materials and Corrosion*, ***63 (2)***: 119-126.

INVESTIGATION OF WAX DEPOSITION DEVELOPMENT IN SARIR-TOBRUK PIPELINE

Hamza E.Almansour*, Sabri M. Mrayed** and Ezeddine E. Zorgani***

Abstract: Wax deposition in pipelines is one of the biggest flow assurance challenges in the oil industry. The need for understanding deposition becomes greater as hydrocarbons are being transported over increasingly greater distances. Transportation of waxy crude oil in a cold environment can result in wax depositions on the pipe wall. The problem of wax deposition seriously adversely affects the normal operation of a pipeline that might lead to a complete shutdown in some cases and imposes considerable loses in production. This study takes a look at the wax deposition phenomena which has been experienced recently in the onshore Sarir-Tobruk pipeline. The pipeline carries an average of 200,000 barrel per day from Sarir Field to the Al-Hariga Port at Tobruk (514km). The study aims to understand the behavior and mechanism of wax deposition in the pipeline and how it is influenced by the operational parameters. Software HYSYS was used to examine the effects of inlet operation conditions including inlet crude oil temperature and flow rate and environmental conditions (ambient temperature) on wax deposition development in the pipeline. It also aims to investigate the energy requirement for heating the crude before it is pumped into the pipeline in both winter and summer seasons. Important results of wax deposition have been reported from the simulation. Increasing of inlet crude oil temperature and time duration cause increases of wax thickness layer. However, increases of ambient temperature causes decreasing of wax thickness layer. The temperature effect of both inlet crude oil and ambient indicates that wax deposition development is predominantly thermally driven. Also, investigation of energy requirement shows that 130ºF is suitable inlet operation temperature, especially in the winter season to avoid any jelly formation phenomena for the crude oil before reaching its destination at Al-Hariga Port. The effect of flow rate showed that increasing of flow rate causes an increase in the wax thickness layer. This result relates to the fact that models based on molecular diffusion do not account for the shear forces where the effects of shear removal start to act. It is recommended to conduct further studies incorporating other methods and compare with real operating data once the pipeline is taken for maintenance or renewing; wax thickness measurements become possible and the real wax profile can be obtained.

Keywords: Wax Deposition, Sarir-Tobruk Pipeline.

INTRODUCTION

Crude oil is a complex mixture of hydrocarbons consisting of paraffins, aromatics, naphthenes, resins and asphaltenes. Among these groups of hydrocarbons, high molecular weight paraffins (interchangeably referred to as waxes) are responsible for some of the problems that are encountered during transportation and processing of the crude oil (Singh & Venkatesan, 2001).

Wax deposition is a mainly problem in oil transportation pipelines either in subsea or land. The problem of wax deposition begins when the inner wall temperature of the pipe falls below the wax appearance temperature (WAT); wax deposition occurs and paraffin components present in crude oil precipitate and deposit on the cold pipeline wall. If remediation or prevention techniques are not used regularly, wax deposit will accumulate in the pipeline wall, and wax gel layer will grow rapidly in thickness and impedes the flow of oil due to the flow restriction, as shown in (Fig. 1).

*University of Benghazi1/ Chemical Engineering Department, Benghazi, Libya.
**University of Tripoli. Chemical Engineering Department, Tripoli, Libya.
***National Oil Corporation (NOC) Planning and Studies Department, Tripoli, Libya. Email: hamza.almansouri@uob.edu.ly



Fig. 1. Wax deposit reducing the effective diameter in a retrieved pipeline (Singh et al, 2000).

This paper aims to understand the behavior of wax deposition in the system of pipelines named Sarir-Tobruk and how it is influenced by the operational parameters. Moreover, in this paper, the ASPEN Tech. HYSYS is used to examine the effect of inlet conditions (such as T, P, and Flow rate) and environmental conditions (ambient temperature) on wax deposition. The HYSYS pipe module contains wax deposition models. The wax deposition model in HYSYS uses a theoretical approach that based on molecular diffusion. It uses a wax attribute in HYSYS called *Profes* method, which is described in the HYSYS User Guide, it evaluates the concentration by calculating equilibrium wax quantities at the two different temperatures involved, the temperature at the wall and the temperature in the bulk fluid.

PHYSICS OF WAX DEPOSITION PHENOMENON

At reservoir temperatures (70-150ºC) and pressures (55-103MPa), wax molecules are dissolved in the crude oil. Once, the crude oil leaves the wellhead and flow through pipelines, its temperatures beings to drop because of heat losses to the surroundings (Singh & Venkatesan, 2001). The Temperature loses is the most common cause of wax deposition because wax solubility in hydrocarbon fluids decreases as the temperature is lowered. Consequently, a radial temperature gradient over the cross section area of the pipe is established, reaching a minimum value at the pipeline wall. Because the concentration is temperature dependent, a concentration gradient is established by the temperature gradient. If the temperature of a wax-oil mixture drops below the solubility limit of wax, also known as Wax Appearance Temperature (WAT), the waxy components start to precipitate out of the crude oil and form solid crystals in the solution as shown in (Fig. 2). If the temperature of the bulk reaches the minimum ambient temperature, that is the wall temperature, there will no longer be a radial temperature gradient across the pipe section, and the precipitation of wax ceases from this point on. Similarly, if all the wax molecules initially dissolved in the solution has precipitated out, further solidification is not possible (Sircar & Gupta, 2015).

WAX PRECIPITATION CURVE (WPC)

Wax precipitation curve or wax solubility curve gives the amount of wax that precipitates from the crude at different oil temperatures. It is an important parameter for wax deposition model, which is necessary for accurate prediction of wax deposition (Han *et al*, 2010). The wax solubility curves (plots of solubility versus temperature) are widely used to quantify wax deposition process. Typical solubility curves are shown in (Fig. 3). As seen here, the solubility curves can be concave upwards or downwards. Its concavity depends on the crude oil composition. The Shape of solubility curve has a significant effect on wax deposition process, especially on the effect of crude oil temperature on wax deposition as explained in the study of (Huang *et al*, 2012). A number of techniques have been developed to determine the amount of precipitated

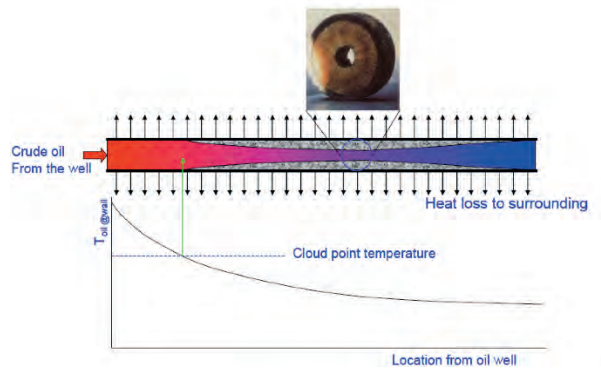


Fig. 2. Wax deposition occurs when the inner wall temperature is below the cloud point temperature.

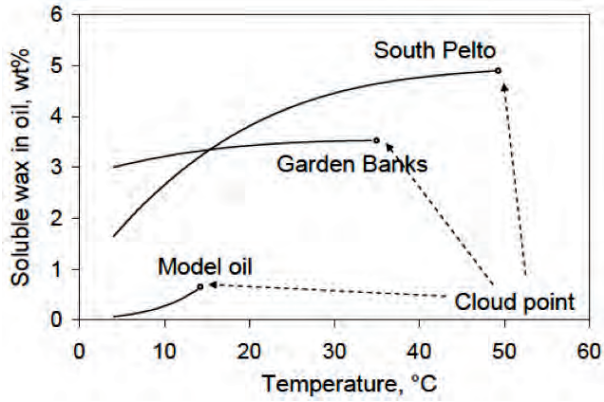


Fig. 3. Solubility curves for different crude oils.

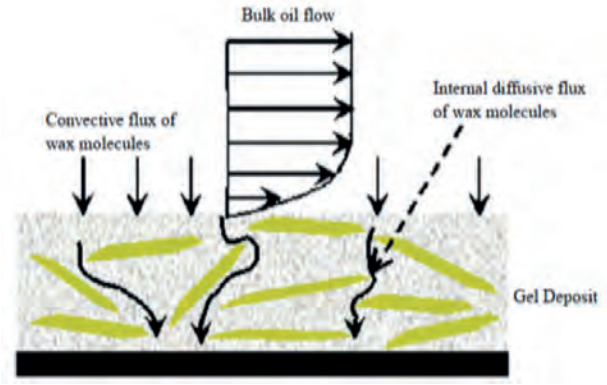


Fig. 4. Show how wax molecules diffuse into the deposit.

wax in crude oil at different temperatures, including Differential Scanning Calorimetry (DSC), Fourier Transform Infrared Spectroscopy (FTIR), Nuclear Magnetic Resonance (NMR), High-Temperature Gas Chromatography (HTGC), filtration and centrifugation.

WAX DEPOSIT AGING

The work by (Singh *et al*, 2000) showed that an external convective mass flux of wax molecules from the bulk oil flow towards the cold wall and an internal diffusive flux within the gel layer are responsible for the growth and aging of the gel deposits (Singh *et al*, 2000). This internal diffusion and subsequent precipitation of wax molecules inside the gel layer leads to an increase in the wax fraction in the deposit (Huang *et al*, 2012 and Fig. 4). The wax fraction is an indicator of gel strength which is an important parameter for designing remediation methods such as pigging (Huang, 2011). The phenomena of wax aging were quantitatively studied by (Singh *et al*, 2000), as shown in (Fig. 5). According to (Singh *et al*, 2000) the wax content of the deposit increases as time goes and wax diffuse into the deposit and oil is squeezed out. However earlier studies have assumed that the wax fraction in the deposit is constant during the wax deposition process.

REVIEW OF PREVIOUS WORK

To study the wax deposition in the pipelines, many experimental and theoretical studies have been carried out under different operating conditions. A quick review of the most common studies is made below.

Creek *et al* (1999) did a series of experiments in flow-loop apparatus to study the effect of crude oil temperature and flow rate on the deposition rate. They studied the temperature gradient by varying the temperature difference between the oil and coolant/ wall. They found that greater temperature difference between oil and wall gave a greater deposition rate. The second portion of experiments was to study the effect of flow rate on wax deposition where five different flow rates were studied while the temperature difference was constant. They found that wax deposition rate decreases with increasing flow rate. Jennings *et al* (2005) found similar results using a coldfinger apparatus to study wax deposition for different coolant temperatures and different stirring speeds. For studying the effect of flow rates, both Creek *et al* (1999) and Jennings *et al* (2005) attributed the reason to the ''shear removal'' due to sloughing where a layer of deposit is suddenly removed especially in high velocity.

Bidmus *et al* (2009) used a flow loop experiment based on heat transfer to investigate solids deposition on the pipe wall. They studied the effect of inlet

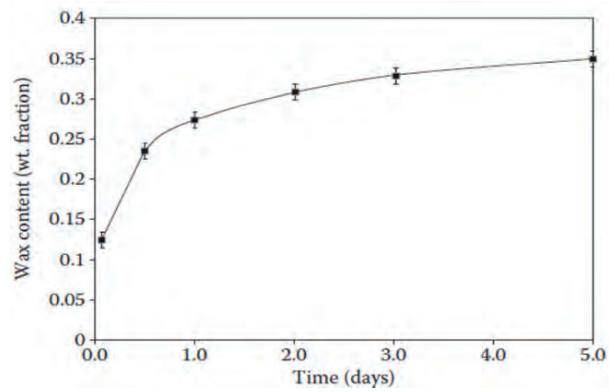


Fig. 5. Evolution of wax fraction in the deposit observed by Singh et al (2000).

temperature of crude oil on wax deposition where four different inlet temperatures were examined while the coolant temperature was kept constant. It was found that a decrease in the oil temperature (decreasing thermal driving force) to near ambient or pipe-wall temperatures could substantially decrease the wax deposition tendency. Similar results were found on the study of (Lashkarbolooki *et al*, 2010) used a crude oil with a 13°API from the Kermanshah Oil Field in a flow loop experiment. They found that wax deposition was decreased with increasing coolant temperature. On other hands wax deposition increased with increasing the inlet crude oil temperature. They concluded that the wax thickness was highly dependent on the temperature difference between the inlet oil and coolant temperatures (ΔT).

Hoffmann & Amundsen (2010) did a series of experiments used a flow-loop to investigate wax deposition under different temperature and flow conditions. Two series of experiments were carried out. The first series of experiments the oil temperature was increased with constant temperature difference with the coolant. In a second series, oil flow rates were varied to measure the influence of shear forces on the wax thickness. Firstly, they studied the effect of the gradient of solubility curve (dC/dT) on the total concentration gradient [dC/dr=(dC/dT)*(dT/dr)] by keeping temperature gradient (dT/dr) constant while absolute temperature was varied. They found that wax thickness was decreased with increasing temperature measured. The result from large flow-loop apparatus was compared with a small scale lab method Differential Scanning Calorimetry (DSC), where the wax deposition in term of mass precipitation was also decreased. This similarity showed that wax solubility gradient is one of an important parameter for wax deposition. Moreover, they examined the effect of oil temperature while the coolant temperature was constant. They found that wax thickness increased faster at low temperature. This result was consistent with the solubility curve that showed the highest gradient in the low-temperature region. Secondly, they studied the effect of flow rate on wax deposition and they observed that wax thickness decreased with increasing flow rate. However, the total concentration gradient was increased in the high flow rate. They attributed the reason for decreasing wax thickness because of increasing shear stress at the oil deposit interphase.

Huang *et al* (2012) studied the effect of changing oil/coolant temperatures on wax deposition rate in a series of flow loop experiments. They found that wax deposition decreased with increasing oil temperature while an increase in coolant temperatures led to decrease wax deposition. They attributed the reason to mass driving force, not to thermal driving and they found that a higher mass driving force a greater increase in the deposition rate. In order to make a theoretical analysis of these trends, they compared the experimental results with a wax model called Michigan Wax Predictor (MWP), which showed a good agreement with experimental results. They studied the importance of the shape of the wax solubility curve on the effects of oil temperatures on wax deposition by comparing the results from two different crude oil using the MWP. Two different crude oil has different solubility curves, one is a straight line and the other is a concave curve. They showed that the difference in the solubility curves could be led to getting opposing trends for studying the effect of Toil. Results from MWP showed a major difference in the wax deposition with changing the temperature conditions between two crude oil. They found that increasing Toil lead to decrease wax deposition of the crude oil has a concave curve while wax deposition increased with increasing Toil for crude oil has straight line solubility curve. They concluded that the shape of solubility curve can greatly affect the mass driving force by affecting the equilibrium concentrations of wax in the bulk oil (Coil(eq)) and at the wall (Cwall(eq)), where the changing in the equilibrium concentrations leads to a difference in the behavior of mass driving force which explains the opposing trends in the amount of deposit between two crude oil. Therefore, they thought that the mass driving force for wax deposition is a more appropriate parameter to quantify the temperature effects of wax deposition in comparison to the thermal driving force.

(Lu *et al*, 2012) showed that other effects focus on the heat and mass transfer phenomena at the oil–deposit interface may affect wax deposition when the oil flow rate is changed and may either increase or decrease the growth rate of the deposit. They identified three effects that give rise to an alternative explanation that has been overlooked in previous studies. They found that these three effects include the effect of the boundary layer thickness on mass transfer (effect 1), the diffusivity at the interface on mass transfer (effect 2), and the interface wax concentration on mass transfer (effect 3). Both effects 1 and 2 tend to increase the growth rate of the wax deposit, while effect 3 tends to have the opposite effect. The overall growth behavior of the

wax deposit is the result of the competition between these three effects. They found that effect 1 changes insignificantly with time, while effect 2 weakens with time and effect 3 strengthens as time increases because of the insulation effect by the buildup of the wax deposit on the wall. Therefore, they found that effect 3 eventually dominated the competition over the other two as time progresses. Therefore, they summed up that, the reason for decreasing wax deposition with increasing flow rates in the flow-loop apparatus was not the shear removing mechanism as claimed in many previous studies. They attributed the reason to the heat and mass transfer phenomena at the oil-deposit interface was not a viewpoint to those studies.

Shahrabadi *et al* (2013) used model oil prepared by solving paraffin wax into toluene solvent, with different wax content in a flow-loop apparatus to investigate the wax deposition on the pipe surface under different conditions. They observed that wax deposition was increased with increasing temperature difference and time residence. This was because of increasing time leads more heat loss, which leads to reduce crude oil temperature, therefore, cause increasing in a wax deposition. But it was reported that as the time progress wax deposition was decreased because of the increasing wax thickness layer on the pipe wall led to an increase the insulation effect, therefore, decreased the heat transfer rate. Also, they studied the effect of flow rate which found to be depended on flow regime. They found that wax deposition increased in laminar flow whereas it decreased under turbulent flow. However, they did not give an explanation for decreasing wax deposition in turbulent flow they believed in the three effects were identified by (Lu *et al*, 2012).

Wang *et al* (2015) used an oil sample with 7.1 mass% of wax dissolved and WAT of 20ºC in a small- scale flow loop apparatus in combination with DSC technique, to examine the effects that effect on wax deposition. They studied the influence of oil temperature, wall temperature and the flow velocity. For a deposition experiment at a constant wall temperature, they observed that an increase in the oil temperature resulted in a higher deposition rate, whereas an increase in the wall temperature for a constant oil temperature led to a lower deposition rate. All of the above observations were compared with wax solubility curves (WPCs) generated from the DSC technique which showed a remarkable similarity with flow-loop experiments. Hence, they concluded that the wax solubility curve and its gradient (dC/dT) was greatly affected the wax deposition as the thermal driving force ΔT. In addition, they studied the effect of flow velocity on the wax deposition where it found to be decreased with increasing flow velocity. They thought the reason for this trend that because of the adhesion of lighter hydrocarbons was so low that was easily stripped down by the flow shear due to the sloughing effect, therefore, the mass percentage of the heavier hydrocarbons in the deposit becomes relatively higher which may lead to an increase of deposit hardness. For every flow velocity investigated, the results obtained were explained in term of wax deposit composition (WPCs shape). The WPCs also showed that for the higher operating flow velocity the wax species deposited changed toward a higher carbon number (a higher molecular mass distribution).

DESCRIPTION OF STUDY

Current Study

Nowadays Libya exports about 1 Million BPD of crude oil according to National Oil Corporation (NOC). The oil is normally carried across several terminals through different pipelines which represent the most economic and safest carriage system for mineral products (Shamekh *et al*, 2014). One of those pipelines is Sarir/Tobruk Pipeline, which is the target of this study (Fig. 6). The study aims to investigate the wax deposition phenomena in Sarir/Tobruk pipeline, where the crude oil is shipped from Sarir field to the Al-Hariga port at Tobruk (a distance of 514km). Sarir crude is waxy crude which has a wax content range from (13-24)%wt. (Shamekh *et al*, 2014). Thus, it is important to study wax deposition in this pipeline where the deposition is certain to occur. This pipeline is considered as one of

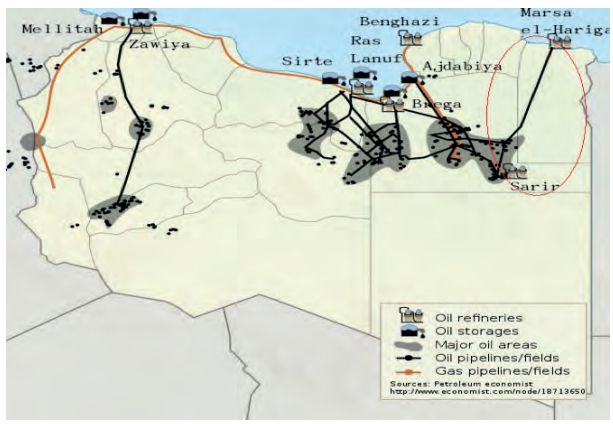


Fig. 6. Show systems of pipelines of gas and oil around the Libya.

the important pipeline in Libya. Economically, this pipeline was the only artery which kept uninterrupted and provides continuous flow of crude during the conflict in the country as it maintained an average of 200,000BPD.

Sarir Field (SF)

Sarir Field (SF) was discovered in southern of Cyrenaica area during 1961 and is considered to be the earliest and the largest oil field in Libya. It is operated by the Arabian Gulf Oil Company (AGOCO), a subsidiary of the state-owned National Oil Corporation (NOC). The field has estimated oil reserves of 12Gbbl, 6.5Gbbl ultimate recoverable reserves and 312,500BPD maximum production rate.

Characterization of Sarir Crude Oil

Sarir crude is classified as paraffinic crude oil having a gravity of 36.5°API and a total sulphur content of 0.12wt%. The crude is paraffinic in nature in the middle and upper part of its boiling range, although it is less paraffinic in the lower boiling range. Sarir crude has a high pour point of (+21ºC) and a kinematic viscosity of 10.63cSt at 37.7ºC. In addition, the experimental work done by (Alghanduri *et al*, 2010), gave us good knowledge about characterization of waxy of Sarir crude oil such these important information the WAT and wax content. According to (Alghanduri *et al*, 2010) the WAT of Sarir was (48.7± 0.36ºC/ 49.6± 0.1ºC), measured using the differential scanning calorimetry (DSC) with two different cooling rates and wax content was 13.6% wt. determined by the UOP 46-64 method.

Table 1. Sarir Crude Oil Properties (Alghanduri et al, 2010 and Shamekh et al, 2014).

PROPERTY	VALUE	REF.
Density @ 15°C g/ml	0.8415	[28]
API gravity @60°F	36.5	[28]
Sulphur Content, wt.%	0.120	[28]
Asphaltenes Content, wt.%	0.20	[22]
Mercaptan Sulphur ppm wt.	8	[22]
Water and Sediment Content, vol.%	0.05	[27]
Wax Content, wt.%	13.6	[27]
Cloud point/WAT °C	48.7 - 49.6	[27]
Pour point °C (°F)	+21(+70)	[27]-[28]
Melting point of wax °F	127	[22]
Viscosity @100°F cSt	10.63	[28]
Avg. Molecular Weight Mw	244.7	[27]

RESULTS AND DISCUSSIONS

This section presents the summary results of the main parameter examined by HYSYS simulation (V9, 2016). All the presented data and findings will be mentioned and discussed further, in the following sections.

The following (Fig. 7) shows the simulation of elevation profile of Sarir/Tobruk pipeline which has been used in the following calculations. The pipeline go through different elevations, approximately 90 meter (296ft) at Sarir Field and 98 meter (321ft) at Tobruk Terminal and cross through the highest point at the line which is 188 meter (617ft).

Temperature Profile

Figure (8) shows the temperature profile of Sarir/Tobruk pipeline. As shown in the figure the temperature of crude oil decrease gradually along pipeline due to heat losses to the surrounding. This temperature profile has been calculated in case of winter season where ambient temperature considered to be the lowest temperature compared to other seasons. The crude oil pump at 125ºF

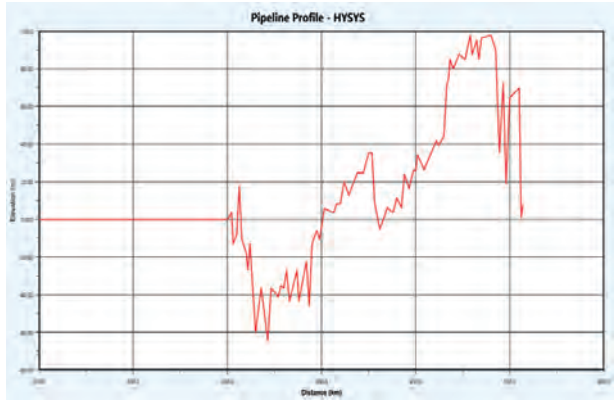


Fig. 7. Elevations Profile of Sarir-Tobruk Pipeline in HYSYS.

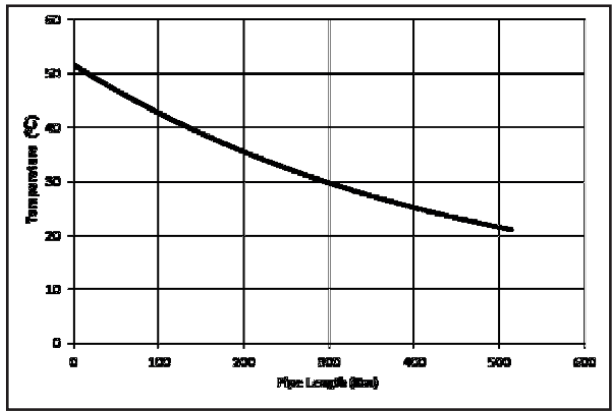


Fig. 8. Temperature Profile along the Sarir-Tobruk Pipeline.

(51.67ºC) in Sarir Field reaches to Tobruk at 70ºF (21ºC). The outlet temperature of the crude oil was calculated using HYSYS and was found to be in a good agreement with the measured field value according to AGOCO Operations Department and T.A.D. The final temperature where found to be the temperature of crude pour point. The crude oil is then heated in the storage tanks to increase the crude oil temperature above the pour point to prevent any possible blockage in the last section of the delivery system in Tobruk terminal.

Pressure Profile

Figure (9) shows the simulated pressure profile along the pipeline. The overall pressure is decreased along the pipeline, however, some points in the profile show increase in the pressure due to the hydrostatic pressure. This variation of pressure caused by the topography, where the pipeline goes through different elevations as shown in (Fig. 5). The Crude oil pump at 475psi (3275kpa) in Sarir Field reaches to Tobruk at 152.4psi (1054.54kpa) with overall pressure drop equal 322.6psi (2220.46kpa).

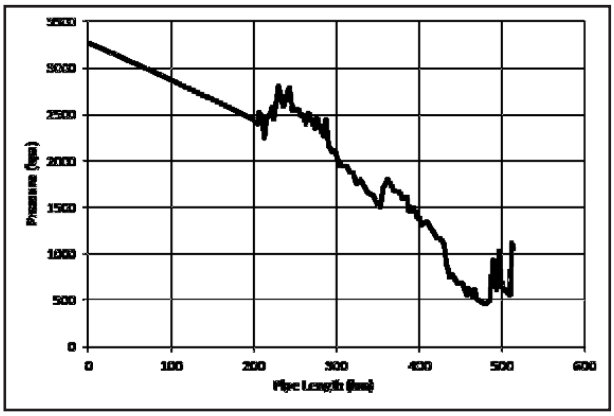


Fig. 9. Pressure Profile along the Pipeline.

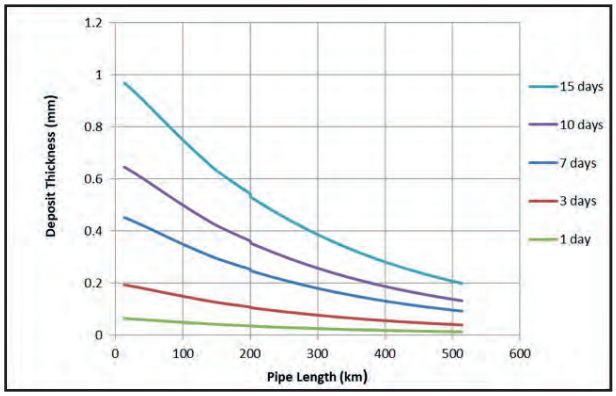


Fig. 10. Wax Thickness Layer along the Pipeline at different simulation times.

Wax Thickness Layer Profile

Figure (10) shows the change of wax thickness layer along the pipeline at different simulation times. Wax thickness layer is the only variable that changes with time in HYSYS simulation and even in other recognized wax simulations, in contrary to other variables. Therefore, different simulation times were conducted and the results show a significant difference between them and it should be mentioned that the subsequent calculations are based on three days simulation time. From observing (Fig. 10) the wax thickness layer changes gradually along the pipeline and wax deposition seems to be steady at 400km. Figure (11) shows the change of wax thickness layer with different times simulation at the different locations in the pipeline, where the wax thickness is increased with an increasing time duration. A similar observation has been found in the experimental study of (Creek *et al*, 1999; Hoffmann & Amundsen, 2010; Lashkarbolooki *et al*, 2010 and Huang *et al*, 2011). This may be because of increasing time leads more heat loss, which leads to reduce crude oil temperature, therefore, cause increasing in a wax deposition. This phenomenon is known as ‘’deposit’s aging’’, where was quantitatively studied by (Singh *et al*, 2000), which showed that the wax content of the deposit increases as time goes and wax diffuse into the deposit and crude oil is squeezed out. That means to reduce the amount of entrained crude oil in the deposit, thereby, lead to more wax species available to produce wax crystal within the deposit itself (Fig. 4).

Effect of Crude Oil Inlet Temperature on Wax Thickness Layer

According to AGOCO Operations Department and T.A.D, the crude oil inlet temperature range from 130ºF to 120ºF in summer and winter seasons. Thus, we have examined the development of wax thickness layers with four different inlet crude temperature including the operation temperatures range, while the ambient temperatures is kept constant. Figure (12) illustrates the wax deposition along the pipeline increases with increasing inlet crude temperature. More illustration in (Fig. 13) which shows wax thickness wax increase with increasing inlet crude oil temperature. Similar trend have been found in work of (Creek *et al*, 1999; Bidmus *et al*, 2009; Lashkarbolooki *et al*, 2010 and Wang *et al*, 2015). They found that a decrease in the oil temperature (decreasing thermal driving force) could result in decreasing wax deposition. However,

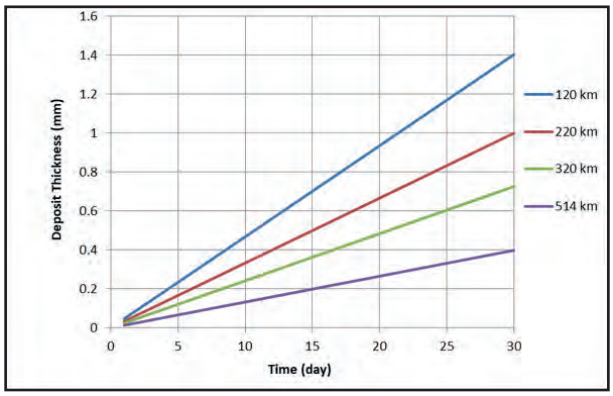


Fig. 11. Wax Thickness Layer versus Time at Different Locations in the Pipeline.

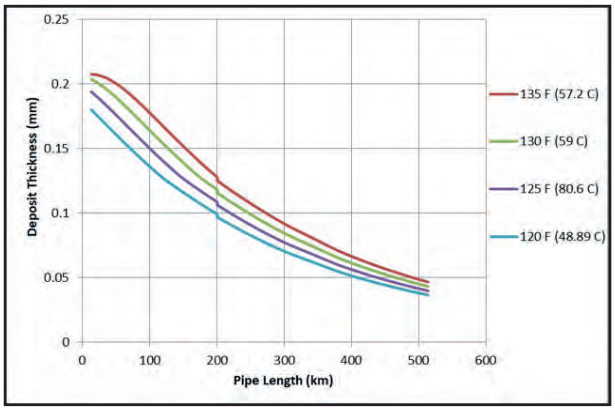


Fig. 12. Effect of inlet crude temperature on wax thickness layer along the pipeline.

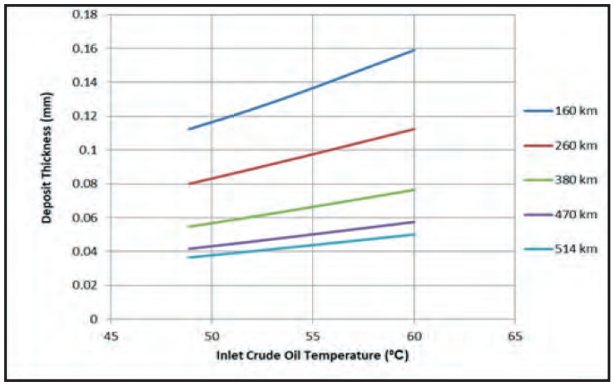


Fig. 13. Wax thickness layer versus inlet crude oil temperature at different locations in the pipeline.SW Libya.

study of (Hoffman and Amundsen, 2009) and (Huang *et al*, 2011) showed opposing trends, where wax deposition was decreased with increasing oil temperature.

Effect of Ambient Temperature on Wax Thickness Layer

Four different ambient temperatures have been examined, and 7ºC ambient temperature is chosen to

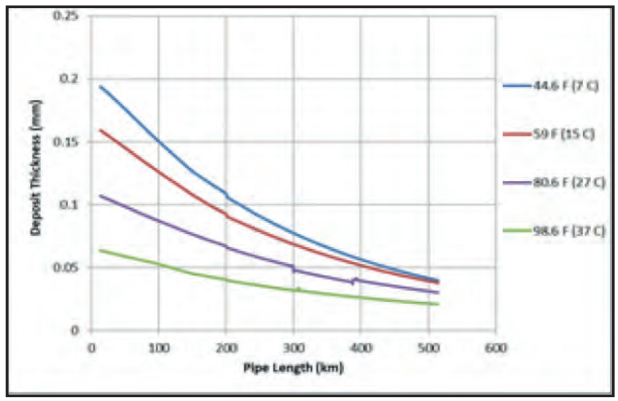


Fig. 14. Effect of ambient temperature on wax thickness layer along the pipeline.

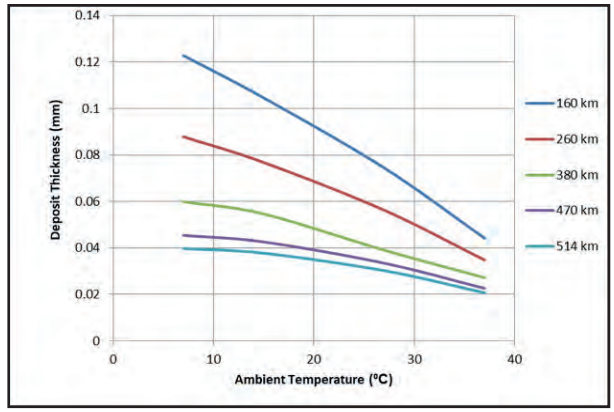


Fig. 15. Wax thickness layer versus ambient temperature at different locations in the pipeline.

be the lowest temperature as the worst case for wax deposition occurrence (as mention previously). Figure (14) shows the change of wax thickness layer along the pipeline at different ambient temperatures. This figure exhibits that the wax deposition along the pipeline decreases with increasing ambient temperature. More illustration in (Fig. 15), which shows wax thickness decreased with increasing ambient temperature. Similar trends have been observed in experimental work done previously by (Creek *et al*, 1999; Jennings *et al*, 2005; Lashkarbolooki *et al*, 2010; Huang *et al*, 2011 and Wang *et al*, 2015). In their work they found that deposit thickness decreased when the coolant temperature increased (increasing ambient temperature).

In all the above results, a generalization was made that the deposit thickness decreases when thermal driving force decreases (decreasing ΔT). The focus on the thermal driving force for wax deposition is based on the fact that molecular diffusion was assumed to be the main mechanism for wax deposition. In this mechanism, the concentration gradient is established by thermal gradient, which

means that more wax molecules can precipitate and form thicker deposits with increasing temperature gradients. Thus, increasing inlet crude temperature and decreasing ambient temperature, lead to increase the thermal driving force ΔT and, that is, explained the behavior we obtained above. Many previous studies were based on the fact that thermal driving force on molecular diffusion equation are response to decrease or increase wax deposition (Creek *et al*, 1999; Jennings *et al*, 2005; Bidmus *et al*, 2009; Lashkarbolooki *et al*, 2010 and Wang *et al*. 2015).

Although the study of (Huang *et al*, 2011 and Hoffman & Amundsen, 2010) showed that solubility gradient (dC/dT) has a significant effect on wax deposition as the thermal gradient. (Huang *et al*. 2011) made a comprehensive study to examine the effect of the shape of solubility curve. The study showed that mass driving force and shape of solubility curve were affecting the deposition rate rather than thermal driving force. They found that the shape of the solubility curve had a major impact to affect the change in characteristic mass flux for wax deposition when the oil and the coolant (ambient) temperatures are changed.

Effect of Crude Oil Inlet Temperature on Energy Requirement

To investigate the possibility of heating the inlet crude oil to a temperature at which the pour point temperature (PPT) of the crude oil is avoided two cases are studied in both winter and summer season, where the ambient temperatures are 44.6ºF (7ºC) and 98.6ºF (37ºC) respectively. Figures (16 & 17) show temperature profile for different inlet crude oil temperature in both winter and summer season. As shown in the figures there is a significant

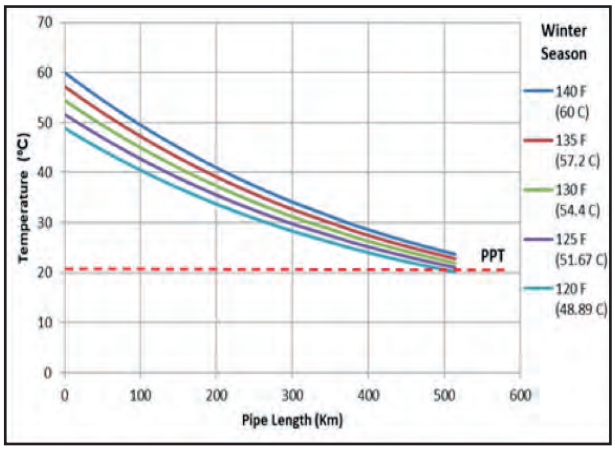


Fig. 16. Effect of inlet crude temperature on temperature profile along the pipeline in winter season.

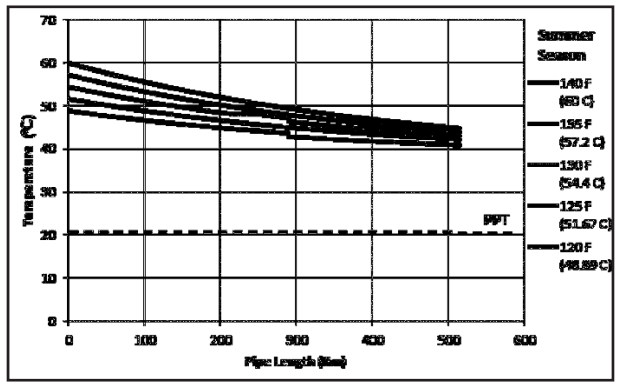


Fig. 17. Effect of inlet crude temperature on temperature profile along the pipeline in summer season.

difference between two seasons. In the summer season, the output crude oil temperatures for all range of inlet operating temperatures remain fairly remote from the PPT. The results show that an inlet temperature of 130ºF (54.4ºC) is high enough to avoid any possibility of jelly formation during the crude transportation in winter season while in summer season where the ambient temperature is relatively higher compared to the winter season and the rate of heat transfer as consequence is minimal, a reduction in the crude temperature along the pipeline was found to be very low and even with an inlet temperature of 120ºF (48.89ºC) the formation of jelly is not possible. The results obtained can be used to determine what inlet temperature the crude should be and how much energy that must be used to heat the inlet crude oil to the optimum temperature.

Effect of Flow Rates

The effect of crude oil flow rate on wax thickness layer along the pipeline is shown in (Fig. 18). The results show that the wax thickness layer increases with increasing flow rates. Results showed opposing trends to those have been observed in a series of experimental studies, where wax deposit reduced with an increase in the flow rate. This might be attributed to the fact that the model used in the prediction of the wax layer thickness based on molecular diffusion as the main mechanism and does not take into account the effect of shear removal. Many previous studies thought that an increase in shear stress forces at the oil-deposit interface with increasing flow rates was behind the reduction of wax thickness layer (Creek *et al*, 1999; Jennings *et al*, 2005; Hoffman & Amundsen, 2010 and Wang *et al*, 2015). However, the results obtained in the study made by (Lu *et al*, 2012) showed that other effects focus on the heat and mass transfer phenomena at

the oil–deposit interface may affect wax deposition when the oil flow rate is changed and may either increase or decrease the growth rate of the deposit. They identified three effects that give rise to an alternative explanation that has been overlooked in previous studies. They found that these three effects include the effect of the boundary layer thickness on mass transfer (effect 1), the diffusivity at the interface on mass transfer (effect 2), and the interface wax concentration on mass transfer (effect 3). The overall growth behavior of the wax deposit is the result of the competition between these three effects.

Although wax deposition decreases with increasing flow rate some other studies report that wax deposition some while increases with increasing flow rates (Jennings *et al*, 2005; Hoffman & Amundsen, 2010 and Wang *et al*, 2015). Figure (19) illustrates that wax thickness layer increased with increasing flow rates in the pipeline. This observation shows that shear removal force work as a side effect for increasing flow rate, although, recent research has an argument about the main mechanism behind the reduction in thickness of wax with increasing flow rate. The reason behind the increase of wax deposition with increasing flow rates comes from increasing wax concentration species in the deposit itself where this increasing was thought to be from the reduction in the amount of entrained crude oil in the deposit which means an increase in a wax fraction in the deposit. This was also explained by (Singh *et al*. 2000), in which he was able to show that the external convective mass flux of wax molecules from the bulk oil flow towards the cold wall and internal diffusion are responsible for the growth of wax deposits. Which means that more reduction in the amount of entrained crude oil in the deposit more precipitation of wax molecules inside the deposits layer. This phenomenon is caused by internal diffusion and well known as ‘’wax aging’’ which increases as time increases as shown in (Fig. 11).

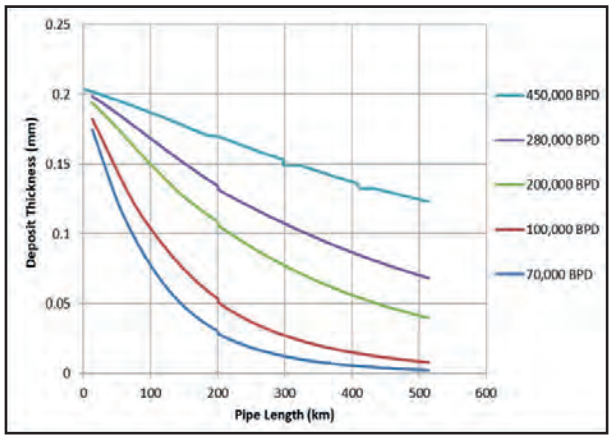


Fig. 18. Effect of flow rates on wax thickness layer along the pipeline.

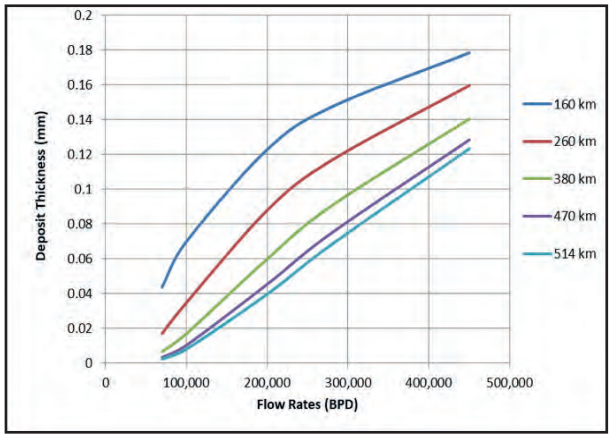


Fig. 19. Wax thickness layer versus crude oil flow rates at different locations in the pipeline.

CONCULTIONS AND FUTURE WORK

Conclusions

The wax deposition models built in the commercial software Aspen HYSYS were used to simulate the phenomena of wax deposition in Sarir/Tobruk oil pipeline. The study involved the prediction of both temperature and pressure profiles along the Sarir/Tobruk pipeline. The prediction of temperature profile showed a good agreement with operational data measured at the pipeline outlet condition.

Profes method was used to simulate wax thickness layer under different time simulations, inlet crude oil temperatures, ambient temperatures and crude oil flow rates.

Increasing of inlet temperature and elapsed time cause an increase in the wax thickness. On the other hand, increasing of ambient temperature causes decreasing of wax thickness layer.

The temperature effect of both inlet crude oil and ambient indicates that wax deposition development is predominantly thermally driven.

The effect of flow rate showed that increasing of flow rate causes an increase in the wax thickness.

Investigation of the effect of inlet temperature on the jelly formation phenomena shows that heating the crude oil to 130ºF in winter season is sufficient to avoid any jelly formation for the crude oil before reaching its destination at Al-Hariga Port in Tobruk.

Future work

Accuracy of the results obtained in this study can be improved by using the wax precipitation curve (WPC) in Aspen HYSYS simulation.

The same investigation can be carried out using computational fluid dynamics (CFD) simulation techniques for better accuracy.

Experimental techniques such as flow-loop and cold flow apparatus are strongly recommended to verify the results obtained from the simulation.

It would be better in the future when this old aged pipeline is renewed and reliable data from the actual field can be obtained and compared to simulation results to give a good approximation to what happens in the real field.

REFERENCES

Alghanduri, L. M.; Elgarni, M. M.; Daridon, J. L. & Coutinho, J. A. P. (2010). Characterization of Libyan Waxy Crude Oils. Energy & Fuels, 24: 3101-3107.

Bidmus, H. O. and Mehrotra, A. K. (2009). Solids Deposition During "Cold Flow" of Wax Solvent Mixtures in a Flow-Loop Apparatus with Heat Transfer. Energy & Fuels, 23: 3184-3194.

Creek, J.; Lund, H. J.; Brill, J. P. and Volk, M. (1999). Wax Deposition in Single Phase Flow. Fluid Phase Equilibria, 158/160: 801-811.

Han, S.; Huang, Z.; Senra, M.; Hoffmann, R. and Fogler, H. S. (2010). Method to Determine the Wax Solubility Curve in Crude Oil from Centrifugation and High Temperature Gas Chromatography Measurements. Energy & Fuels, 24: 1753-1761.

Hoffmann, R. & Amundsen, L. (2010). Single-Phase Wax Deposition Experiments. Energy & Fuels, 24: 1069-1080.

Huang, Z.; Lu, Y.; Hoffmann, R.; Amundsen, L. & Fogler, H. S. (2012). The Effect of Operating Temperatures on Wax Deposition. Energy & Fuels, 25: 5180-5188.

Jennings, D. W. and Weispfennig, K. (2005). Effects of Shear and Temperature on Wax Deposition: Coldfinger Investigation with a Gulf of Mexico Crude Oil. Energy & Fuels, 19: 1376-1386.

Lashkarbolooki, M.; Seyfaee, A.; Esmaeilzadeh, F. and Mowla, D. (2010). Experimental Investigation of Wax Deposition in Kermanshah Crude Oil Through a Monitored Flow Loop Apparatus. Energy Fuels, 24:1234-1241.

Lu, Y.; Huang, Z.; Hoffmann, R.; Amundsen, L.; Fogler, H. S. & Sheng, Z. (2012). Counterintuitive Effects of the Oil Flow Rate on Wax Deposition. Energy & Fuels, 26: 4091-4097.

Shahrabadi, A.; Sadi1, M.; Hendi, S. and Dabir, B. (2013). Modelling and Experimental Study of Wax Deposition in Transportation Line Using a Flow Loop System. Iranian Journal of Chemical Engineering (IAChE), 10(1): 3-16.

Shamekh, A.; Masheiti, S. and Ben Soud, S. (2014). A Simulation Study of the Sarir Field/Tobruk Terminal F Crude Oil Pipeline. UKSim-AMSS 16th International Conference on Computer Modelling and Simulation: 368-373.

Singh, P. and Venkatesan, R. (2001). Morphological Evolution of Thick Wax Deposits During Aging. AIChE Journal, 47: 6-18.

Singh, P.; Venkatesan, R.; Fogler, H. S. and Nagarajan, N. (2000). Formation and Aging of Incipient Thin Film Wax-Oil Gels. AIChE Journal, 46: 1059-1074.

Sircar, A. and Gupta, A. (2015). Flow Assurance and Comparison of Modeling & SCADA Results for Onshore Crude Oil Trunk Line, (IV): 2278-2540.

Wang, W.; Huang, Q.; Wang, C.; Li, S.; Qu, W.; Zhao, J. and He, M. (2015). Effect of Operating Conditions on Wax Deposition in a Laboratory Flow Loop Characterized with DSC Technique. J. Therm Anal Calorim, 119: 471-485.

NAPHTHA CATALYTIC REFORMER HYBRID MODELING

Isam A. B. Salem and Shams Khaled*

Abstract: Naphtha Catalytic reforming is a very important process because it is responsible for high percent of gasoline production in the petroleum refinery. Because of the complex nature of naphtha reforming process and its reaction chemistry, mathematical modeling of such a process with First Principle Method (FPM) will provide highly non linear relations. This nonlinearity of the developed model will reduce the prediction capability and the model results will deviate from the actual plant data.

A hybrid modeling (HYB) method adapted in this paper, which is the first principle model in parallel to neural network (ANN) model are used to simulate naphtha reformer. The aim of the HYB is to add the corrections from ANN to the deviated results obtained from FPM.

Two months of operational data of a Libyan refinery is used in this study to simulate the semi regenerative naphtha reforming reactor, each data point was properly prepared by HYSYS Software to be used as input to FPM model which is simulated by MATLAB Software.

The paper focused on one output variable (reactor outlet temperature Tout) from the FPM which showed high deviation between the predicted and actual data.

Also same data is also used as input to ANN model, the data is normalized, outliers removed and verified with variance and correlation coefficient to select the proper input variables. Correlation coefficients between input and output showed high dependency between the proposed variables. Different architectures of ANN are carried out using MATLAB where mean square error (mse) was used as performance parameter. The results showed that neural network with structure [4-5-1] provided best performance. This ANN provided best residual predictions to reduce the deviations in reactor outlet temperature.

Keywords: modeling, hybrid, naphtha reformer, neural and network.

INTRODUCTION

The mathematical modeling of the chemical processes is very important in many aspects such as the process optimization and control. The progress in understanding the complex kinetics and chemical mechanisms of naphtha reforming and the structure of the reactions network provided the basis to establish mechanistic models which contains the fundamentals of the process and can provide good predictions of the results, such modeling is called (white-box) or first principle modeling. The prediction capability of such models can be affected by several reasons such as the parameter estimations, deactivation of the catalyst.

Modeling with Artificial Neural network (NN) which depends on information regarding the input and output variables allowed complex chemical processes to be modeled easily. Modeling by neural network is very good in capturing the nonlinearity of the complex chemical process which some first principle model may fail, on the other hand neural networks provide good estimate in the range of the data which the model trained on but it is very weak in extrapolation. Combinations of both neural network and first principle configuration was used and tested and the main idea behind this is to take the advantages of both in modeling process.

Arrangement between first principle and neural network (hybrid modeling) can be either serial or parallel. Such combinations are well covered in the literature for different chemical process and with good results (Bhutani et al, 2006; Dimitris and Lyle, 1992).

*Department of Chemical Engineering, University of Benghazi, Benghazi, Libya.
Corresponding author: isam.salem@uob.edu.ly ; Tel: +218 913799271

Modeling napththa reforming with first principle approach is extensively studied and available in literature, but due to the complexity of process and its chemistry which resulted in deviation in the obtained results.

Many attempts like the better estimate of the kinetic parameters or detailed reaction network can be used to reduce the deviations in predictions. In this paper a hybrid model of naphtha catalytic reforming reactor was derived which contains neural network in parallel to first principle. This arrangement contains the principles governing the chemical process such as (reaction network, catalyst deactivation) and on the other it also contains the neural network which will capture the nonlinear behavior of the process.

PROCESS DESCRIPTION

The reforming process modeled in this paper starts with the feed which is straight run naphtha goes through hydrotreater. The major reforming reactions are endothermic, this will lead to temperature reduction of the feed stream and causes reaction rate to decrease, and because of this, the catalyst is distributed over two reactors. The straight run naphtha feed is mixed with recycled rich hydrogen stream and heated to desired temperature before goes to the first reactor which is called reformer. The product from the first reactor after heating enters the second reformer, the outlet from the second reactor enters a separator in which hydrogen rich gas is separated and recycled back and mixed with fresh feed to the first reactor. This type of catalytic reforming is called semi regenerative naphtha reforming (SRR).

MODEL DEVELOPMENT

First principles model

The steps to model naphtha catalytic reforming reactor which used extensively in the literature and illustrated very well in our previous paper and can be summarized as follows (Isam, 2017).

- Naphtha mixture which contains three hydrocarbon classes; naphthenes, paraffins and aromatics is lumped into psudocomponents. The proposed psudocomponents have average properties of that class.
- ASTM D86analysis of about 53 data points obtained from operation were used as input to HYSYS software to predict the average properties of each cut.
- Smith model which describe the chemical reactions network for the whole system was adapted.
- Heat and component mass balance were carried out by considering the reactor as plug flow reactor and the resulting ordinary differential equations of mass and heat balances were solved simultaneously by suitable solver.
- Data available after reactor model simulation are the temperature outlet and psudocompenents concentration in the reactor effluent.

Neural network model

Neural network is used extensively in engineering application because of its simplicity and its ability to capture the nonlinearity in the process.

The basic element of the neural network is the neuron. Layers consist of a number of neuron (nodes) which contain an ‘activation function’. Data presented to the nueral network via the first layer which is called input layer, which connected to the hidden layers where the data processing take place. The hidden layers also connected to an output layer where the data output is obtained.

Hybrid model

Three types of configuration of hybrid modeling are available in literature. Here in this paper the parallel configuration was selected because it showed better performance than the other two types (Bhutani et al, 2006). The hybrid model will contain FPM and the neural network both will simulate the reformer. The neural network will be trained to provide the difference between the calculated and the real variables. This difference is called the residual and is used as correction factor to the FPM parameters.

Model data pretreatment: the data gathered in for this study was obtained from a Libyan refinery for two months of operation of about (60 points of data set) which were properly logged.

Data Outlier detection and removal: Data that do not fit within a certain pattern of the gathered data are called data outlier. incorrect and faulty measurements can be the main source of outliers in industrial data The inclusion of such outliers in neural network will reduce the precision of the results and according to this data outliers removed with several methods . Simple technique is to plot the frequency histogram of the data, the frequency

distribution plot will provide continuous and normally distributed curve, by this outliers can be detected easily. The method used to remove outliers ensured that all data are normally distributed. This method is simple and proved high accuracy with results (Khawla, 1997). This method detected 7 points which can be considered as outliers.

Normalization: Neural networks require that their input and output data are normalized to have the same order of magnitude. Normalization is very critical; if the input and the output variables are not of the same order of magnitude, some variables may appear to have more significance than they actually do. There are several methods used for normalization such as Z-Score Normalization, Min-Max Normalization, Median Normalization, Sigmoid Normalization (Al Mahdi, 2013; Jayalakshmi, and Santhakumaran, 2011).

Here in this paper min/max normalization as in (1) this proved to provide satisfactory results with neural network.

$$y = \frac{(x - min_d) * (max_n - min_n)}{max_d - min_d} - min_n \quad (1)$$

Where
maxd is the maximum value in the data
mind is the minimum value in the data
maxni is the maximum value in the new range
minn is the minimum value in the new range
x is the input data

Input and output variables selection: Four input and one output variables where selected as the parameters of the neural network. The suitability of this selected was tested by statistical tools. Covariance and correlation analysis which is shown in Table 1. was carried out to show the dependence of the different variables.

Covariance will provide measure of the relation but on the other hand correlation coefficient (r) given as in (2) is a statistical tool to measure the strength of the relationship between two variables. They are in the range of [-1 1]; positive value indicates that one variable increases with the other while negative value indicates the opposite , and 0 shows no observed relationship between the two variables.

$$r = \frac{б_{xy}}{б_x б_y} \quad (2)$$

Where $б_{xy}$ is Covariance and $б_x$ $б_y$ Standard deviation.

Table 1. The correlation coefficient of the input and output variables.

Input variable	IBP	FBP	SG	H2
Temperature residuals	-0.41	-0.52	-0.13	-0.41

Neural network architecture: The neural network developed in this model is the feedforeward network, comprising of input layer (IP) , hidden layers (H) output layer (OP) having N_{ip}, N_h, and N_{op} nodes . Because the selection of the nodes in the hidden layer are problem dependent , the nodes Nh are adjusted by trial and error taking the advantages of the recommendation available in the literature (Su et al, 2016).

The *newff* function is used for data training. The transfer function used in the hidden layer are (tan sigmoid) tansig function in Matlab is used and output layer with linear transfer function purelin.

Training of the neueral network carried out back propagation algorithm Levenberg-Marquardt method is used *trainlm* function in Matlab also training with Bayesian regularization trainbr function was used. The performance of the neural network is based on the mean squared error and the correlation of determination and time was not used as comparison parameter because the data was small size. In this model the nodes Nh are adjusted.

RESULTS

The FPM and the HYB models both developed using Matlab, one output parameter from the FPM which is the reactor outlet temperature T_{out} where compared to the real production data, and the difference obtained is corrected by the neural network model. Different neural network architectures were tested to select best one. The selection is based on the performance of neural network which the minimum mean square error mse. Tables 2 and 3 show the results of using two different methods of training on different neural network architectures. Table 2 shows the results of using *trainlm* Matlab function on neural network with one and two hidden layer and can be observed that no constant pattern in the MSE change.

Table 3 shows the results of using trainbr matlab function on neural network with one and two hidden layer and can be observed that no constant pattern in the mse change. Neural network with structure [4-6-1] provided best performance (mse=0.01) and this neural was used to calculate the corrections. In Table 4 the error percent of (some data points) for predict outlet temperature by FPM compared to the one of the HYB and improvement in the prediction capability is very clear.

Table 2. Performance for training using "trainlm".

	Training with one hidden layer			Training with two hidden layer		
Architecture	4-4- 1	4-5- 1	4-6-1	4-4-4 1	4-4-5-1	4-6 6-1
mse	0.024	0.01	0.024	0.039	0.046	0.255

Table 3. Performance for training ann using "trainbr".

	Training with one hidden layer			Training with two hidden layer		
Architecture	4-4- 1	4-5- 1		4-4-4 1	4-4-5-1	4-6 6-1
mse	2.08	0.6		2	2.91	2.6

Table 4. Error (%) between the real outlet reactor temperature and predicted one by using the FPM and HYM.

Days of study	Error using HYB%	Error using FPM %
1	0.03	-4.85
8	0.0008	-5.3
14	-0.007	-5.1
20	0.03	-4.8
30	-0.01	-3.9
40	-0.5	-5.3
50	0.01	-5.3

CONCLUSION

HYB mode which is FPM in parallel to ANN model is constructed and tested. The neural network model was used to correct the deviations between the real data and the FPM predictions. The hybrid model prediction capability was tested over a two months of operation data collected from a Libyan refinery. The hybrid model showed good prediction capability with maximum percent error less than 0.9 for all studied data points.

REFERENCES

Al Mahdi A. (2013). Modeling of Libyan Crude Oil Using Artificial Neural Networks. *Unpublished Ph.D. Dissertation, Dept. chem. Eng. Loughborough University*: 135p.

Bhutani, N.; Rangaiah G. P. and Ray, A. K. (2006). "First Principles, Data-Based, and Hybrid Modeling and Optimization of an Industrial Hydrocracking Unit" *Ind. Eng. Chem. Res.,* **V. 45**: 7807-7816.

Dimitris C. P. and Lyle H. U. (1992). A Hybrid Neural Network-First Principles Approach to Process Modeling. *AIChE Journal,* **V. 38(10)** :1499-1511.

Isam, A. B. (2017). The Effect of Feed Characterization on Naphtha Reformer Modeling. *Saudi Journal of Engineering and Technology,* **V. 2(12)**: 499-508.

Jayalakshmi, T. and Santhakumaran, A. (2011) "Statistical Normalization and Back Propagation for Classification. *International Journal of Computer Theory and Engineering,* **V.3(1)**: 1793-8201.

Khawla, A. A. (1997). Modeling, Simulation, and Optimization of Large-Scale Commercial Desalination Plants. Unpublished Ph.D. Dissertation, Dept. Chem. Eng., *Virginia Polytechnic Institute and State University, Virginia*: 453p.

Su Xin, X.; Wu, Y.; Pei, H.; Gao, J. and Lan, X. (2016). Prediction of Coke Yield of FCC Unit Using Different Artificial Neural Network Models. *China Petroleum Processing and Petrochemical Technology,* **V. 18(3)**: 102-109.

CAUSE AND CONTROL OF SULFUR TRIOXIDE FORMATION IN WASTE GAS THERMAL INCINERATOR

W. Alzamzam*, W. Alfaghi** and S. Almabrouk***

Abstract: Sulfur recovery unit is an integral part in natural gas treatment process. In which Incineration process is used in almost sulphur recovery units in order to make the process effluents releasable into the atmosphere.

This paper studies the formation of sulfur trioxide at thermal incinerator, its cause and control depend on two main factors which are an excess air and incineration temperature. ProMax software is used in this work to simulate the different combustion air flow rate and temperature changes of incinerator. Sulfur recovery unit (SRU) at a gas processing complex is the case study, which field data has been collected from the distribution control system (DCS). The investigation of SO_3 formation will be tested for the (SRU) with and without tail gas treatment unit (TGTU). Results show that the main causes of SO_3 formation are an excess air of O_2 in flue gas, and low incinerator furnace temperature. So, that to assure an almost complete combustion of H_2S and to control SO_3 formation, furnace temperature has to be higher than 700°C and excess air between 2 & 3Vol %. Finally, it's not possible to operate SRU without TGTU due to high dangerous environmental impact even at short periods (Mawle, 2010).

Keywords: Sulfur trioxide, incinerator, combustion air, sulfur plant, reaction furnace temperature.

INTRODUCTION

Climate change & air pollution due to different pollutants in the air is one of the major concerns all around the world. The air pollution is also known to cause adverse effect on crops, trees, lakes, animals, natural environment, building, monuments and statues. It has been estimated that large amount of premature deaths and adverse health effects are linked to air pollution. Over 350 manmade contaminants such as dioxins, volatile organic compounds, persistent organic pollutants are responsible for decreased hand-eye coordination, memory, physical stamina etc (Mawle, 2010).

Oil and gas exploration and production is source of pollution which are associated with many environmental and socio-economic impacts (Baptiste and Nordenstam, 2009), despite this, many nations throughout the world would still cherish to discover oil and gas within their territories. This is due to the fact that the availability of such natural resources is seen as a point of economic transformation and development fortunes of such nations. The problem here is that most of these countries are inexperienced in the oil and gas industry and usually their decisions are mainly based on economic transformation with little consideration for environmental and social implications.

Natural gas is a source of energy, which is widely used as an industrial, commercial, and domestic fuel. To make natural gas suitable for using, it is important to purify it from all impurities such as acid gases. The acid gases of hydrogen sulfide (H_2S) and carbon dioxide (CO_2) are common impurties existing in the natural (Al-Lagtah *et al*, 2015).

Usually, the acid gases are separated from natural gas in the gas treating unit (GTU) and the separaed acid gas stream is sent into the sulfur recovery unit (SRU). Sulfur recovery unit is one of the basic units of gas refineries; this unit is very important in economic and environmental issues.

*&** Operation Department, Mellitah Complex, Mellitah Oil and Gas Company, Mellitah, Libya. Email: walzmzam@yahoo.com
Email: walid6848@yahoo.com
***Petroleum Department, Faculty of Engineering, Tripoli University, Libya.

This work is to study the formation of SO_3 via thermal incinerator at sulfur recovery unit SRU. It will be done for two different mode (TGTU on line and TGTU off line) to know how SO_3 effected by temperature of thermal incineration and excess air.

MATERIAL AND METHODS

In order to investigate the formation of sulfur trioxide via the incineration stack at SRU, a typical an exist industrial sulphur recovery unit is studied as shown in (Fig. 1). ProMax software is used in this study as a simulator of the different parameters which effect on the incinerator especially combustion air and fuel gas to investigate the SO_3 changes due to these parameters.

RESULTS AND DISCUSSION

Incineration of tail gas streams in sulphur recovery unit (SRU) is a mandatory treatment in order to meet the environmental requirements and regulations. Simulating the performance of incinerator using combustion air and fuel gas in different levels were carried out for several air levels and studied pollutants of sulphur trioxide compound in each case to be compared with air quality limits. Figure 2 represents the scheme of simulation case; in addition, all tests were carried out based on 1-3vol% of O_2 excess air. And incineration temperature gradient (400-800°C) for both cases of Tail gas treatment unit on and off SRU system.

Tail gas is Running

Figure 3 shows the furnace temperature of the incinerator at different fuel gas quantities and with different excess air volume, which is clear the temperature is directly proportional with fuel gas and inverse with excess air. Figures 4 and 5 show sulfuric compounds concentrations that are being emitted to the environment via the stack by different incinerator temperature and different excess air.

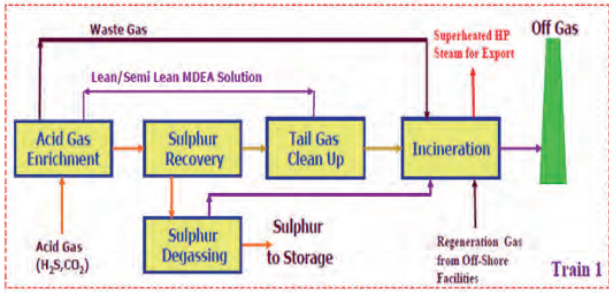


Fig.1. Scheme of sulphur recovery unit.

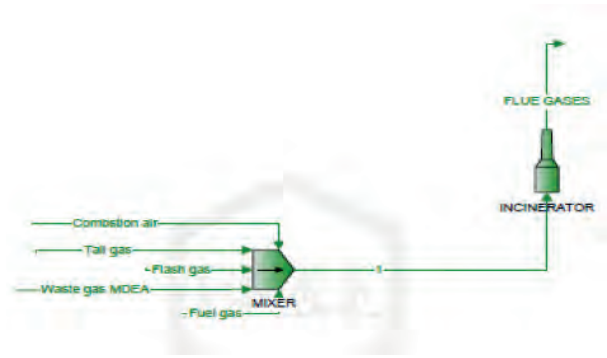


Fig. 2. Scheme simulation case (Incinerator).

Results depict that the increasing of incinerator temperature resists the formation of SO_3 especially when the temperature more than 700°C, and keeping at limit (less than 50ppm) even at excess air (1-3vol% O_2). SO_3 is more hazardous on health and environment than other sulphuric compounds, additionally, in order to obtain optimal working parameters for the case study and based on simulator results, the optimal temperature must be in range (700°C -800°C) for good environmental result and good operation conditions. On other hand the excess air is cause to increase the formation of SO_3 and reduce SO_2. This means that increasing the excess air increase the SO_3.

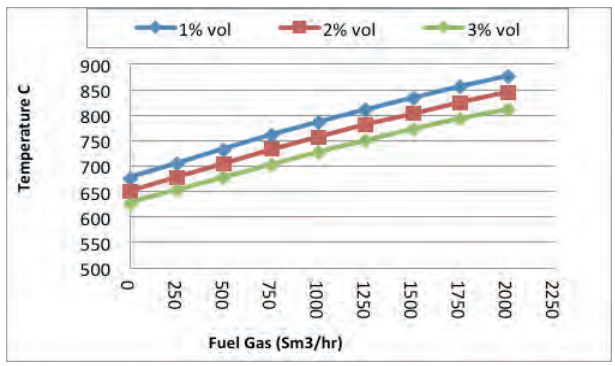


Fig. 3. Relation of furnace temperature to fuel gas and combustion air.

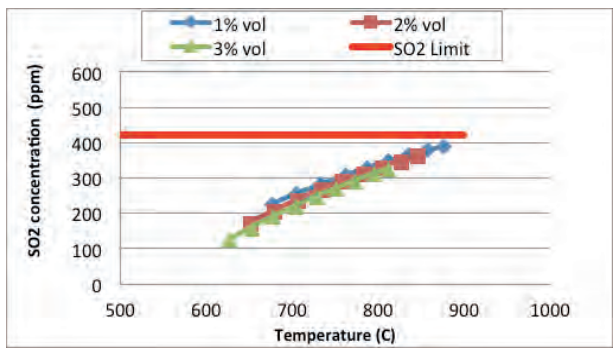


Fig. 4. SO_2 out of stack at different incineration temperature.

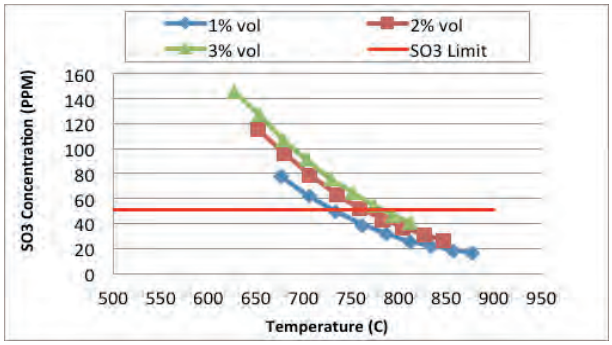


Fig. 5. SO_3 out of stack at different incineration temperature.

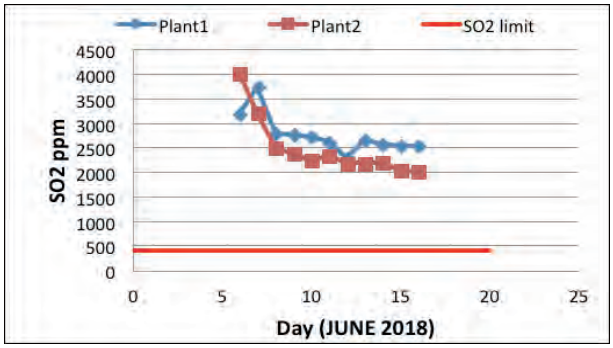


Fig. 6. SO_2 in tail gas to Incinerator (Exist SRU).

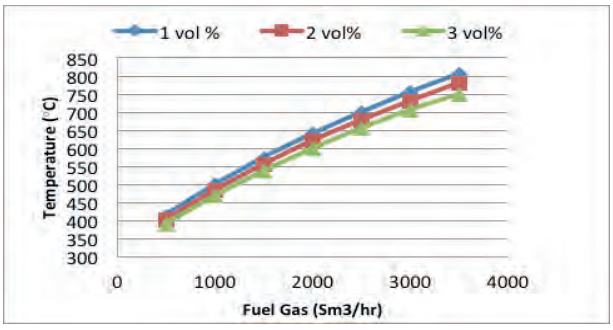


Fig. 7. H_2S in tail gas to Incinerator (exist SRU).

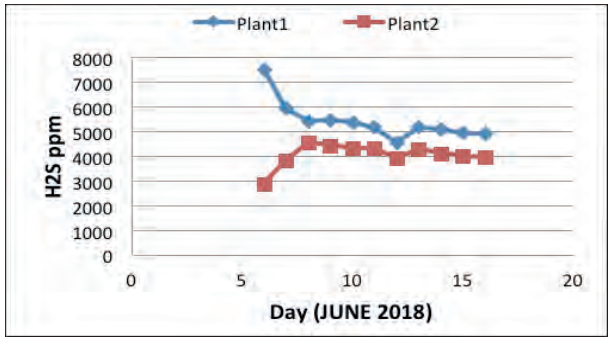


Fig. 8. Relation of furnace temperature to fuel gas and combustion air.

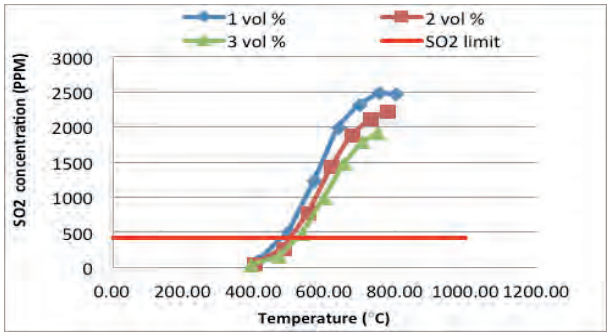


Fig. 9. SO_2 out of stack at different incineration temperature.

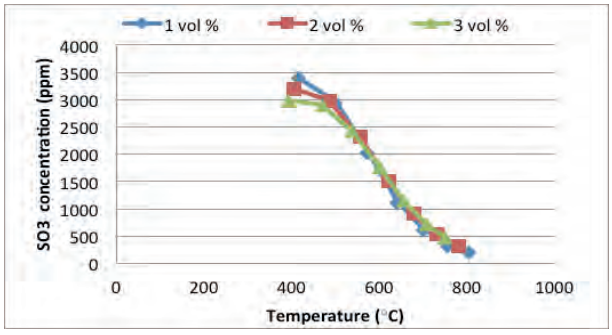


Fig. 10. SO_3 out of stack at different incineration temperature.

Tail gas out of SRU system

The tail gas stream from claus section for two exist sulphur plants contain toxic and hazardous compounds (mainly hydrogen sulphide, and sulphur dioxide) which cannot be released to atmosphere (Figs 6 and 7). So, in such emergency condition, the tail gases send to thermal incineration directly without further treatment in TGTU.

This work is done to study the pollutants vent via thermal incinerator to the atmosphere in case TGTU off, and investigate if this operation condition is possible to emitted pollutants to atmosphere.

Figure 8 shows the furnace temperature of the incinerator at different fuel gas quantities and with different excess air volume as thermal incinerator, in which it's clear that the temperature is directly proportional with fuel gas and inverse with excess air. Figures 9 and 10 show sulfuric compounds concentrations that are being emitted to the environment via the stack by different incinerator temperature.

Results show that the SO_2 is over range and does not meet the international standard which is 420ppm neither at high temperature nor at excess air. On the other hand SO_3 is over range and does not meet international standards which is 50ppm, neither at high temperature nor low excess air.

This disaster due to TGTU out of service and high SO_2, H_2S feed to incinerator from clause (Figs. 6 and 7). This work is good evidence for that Claus section must be follow by tail gas treatment unit to assure complete combustion of H_2S and to assure the other sulphur compounds (SO_2 and SO_3) on limit

with the regulations standards. So, TGTU should be lined up with the SRU system and no possibility to be out of service.

Tail gas treatment unit is very important part for SRU and the environment, it is provide up to 99% the efficiency of sulfur recovery unit. The comparison is done for incineration unit emission gases to the atmosphere in case of TGTU on line and TGTU off line. (Figs. 11and 12) represent the SO_3 out of stack at different incineration temperature with and without TGTU at excess air 1vol% and 2vol%, the result show that all level of emission gas on specification in case of TGTU on line and off specification in case TGTU offline. This proves that it is not possible to run SRU without TGTU due to high risk of harmful gases emission to the atmosphere via incinerator stack.

CONCLSION AND RECOMMENDATIONS

Furnace temperature is a very important factor for the SO_3 formation at incineration unit; another factor is excess air in fact, oxygen excess favours the oxidation of sulphured compounds, besides increasing undesirable production of SO_3. In normal SRU system (TGTU on) results show that SO_3 inverse proportional with temperature. It means that the increase of temperature in incineration furnace reduces formation of SO_3 especially (more than 700°C) leads to meet the emission standards which is 50ppm at different excess air level 1-3% vol. On the other hand, SO_2 is on limit with regulation which is less than the concentration 420ppm. It's recommended that incinerator temperature is around 750°C so that to assure complete combustion of H_2S and to assure the other sulphur compounds (SO_2 and SO_3) on limit with regulations standards. Incinerator temperatures must not be lower than 700°C, excess air increases the formation of SO_3 due to oxidation SO_2 so it must be not high to avoid SO_3.

In another case (TGTU off line), the formation of SO_3 in incineration unit is flow the same behaviour as it in (TGTU on line) with both furnace temperature and excess air but the problem is the emissions are over range for both SO_3 and SO_2. So, it's not possible to work SRU without TGTU due to high toxic environmental impact even at short time.

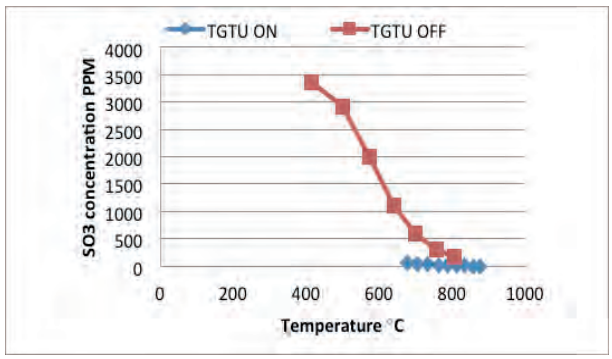


Fig. 11. SO_3 out of stack at different incineration temperature with and without TGTU at excess air (1 vol%).

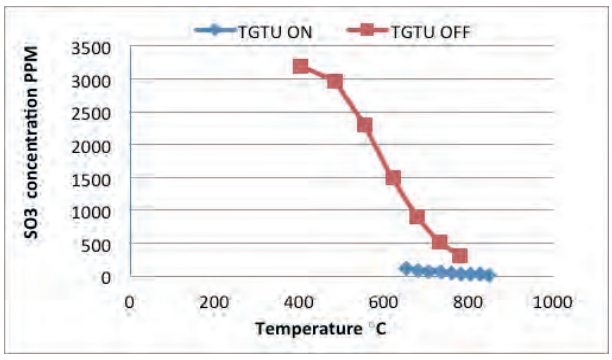


Fig. 12. SO_3 out of stack at different incineration temperature with and without TGTU at excess air (2 vol%).

ACKNOWLEDGMENT

The authors would like to thank Mellitah Oil and Gas Company, especially operation department coordinator, Superintend and complex manger whom always support us and the scientific research.

REFERENCES

Al-Lagtah, N. M. A.; Al-Habsi, S. and Onaizi, S. A. (2015). Optimization and Performance Improvement of Lekhwair Natural Gas Sweetening Plant using Aspen Hysys. Journal of Natural Gas Science and Engineering, ***V. 26***: 367-381.

Baptiste, A. K. and Nordenstam, B. J. (2009). Impact of Oil and Gas Drilling in Trinidad: Factors Influencing Environmental Attitudes and Behaviours Within Three Rural wetland communities. *Environmental Conservation*: 1-8. In Press.

Mawle, A. (2010). Climate Change, Human Health and Unsustainable Development. *Journal of Public Health Policy*: 272-277.

A CASE STUDY OF PRODUCTION OF VALUE-ADDED LIQUID PRODUCTS FROM NATURAL GAS OF MELLITAH GAS PLANT USING GTL TECHNOLOGY: A TECHNO-ECONOMICAL STUDY

Iftikhar Ahmad, Fauzi Elshawesh and Ahmed Souleman*

Abstract: Natural gas (NG) has assumed an extremely important status worldwide as both a source of clean energy and a major feedstock for a number of petrochemicals. Its global value can be assessed by the economic, environmental, and sometimes political future of countries being dependent on their possession or lack of natural gas for domestic and global demand. This paper analyzes the economic aspects of natural gas. It presents a study on the economic and profitable utilization of natural gas by its conversion into value-added products. There are four most important conversion options to convert natural gas into liquids: (a) Ammonia Production, (b) Fuels Production using GTL Technology (Fischer-Tropsch Process) or Dimethyl Ether (DME) Production, (c) Liquefied Gas Production, and (d) Methanol Production.

This paper presents an economic study of conversion of natural gas of Mellitah Gas Plant in Libya into value-added liquid products using Gas to Liquid (GTL) technology. The important GTL technology is conversion of natural gas into liquid products by Fischer-Tropsch synthesis process. It provides good and promising means to meet the energy needs with cleaner fuels. Development of GTL technology in Mellitah complex allows for more value of natural gas by production of readily transportable liquid products such as diesel and naphtha. The produced diesel is free of sulfur, contains no aromatics and polycyclic aromatics and having high cetane number. The combustion of FT diesel results in virtually no emissions of SO2, NOx and unburned hydrocarbons. Another product, F-T naphtha, is considered to be an ideal feedstock for ethylene production as compared to naphtha produced from crude oil due to the lack of aromatics. Absence of aromatics gives rise to higher ethylene yield as compared to ethylene from conventional naphtha. GTL technology is a downstream value added industry (economic enhancement) of natural gas. At present Libya is exporting natural gas which can be converted to value added liquid products. The installation of GTL plant in Mellitah complex will give employment opportunity to young Libyans. Another advantage is the produced diesel will help to reduce the import of diesel for local consumption and it will be a step towards self dependency of the country on fuel. At present Libya imports more than 50% liquid fuels for local consumption. GTL plant in Libya can also be a strategic new export industry. The capacity of GTL plant and its re-payback value has been calculated. The quality of liquid products have also been discussed.

Keywords: GTL technology, Conversion of natural gas to liquid products, F-T products.

INTRODUCTION

Libya had natural gas reserves of an estimated 1,505 billion cubic meters (bcm) as of 2016, at which point recent new discoveries and investments in natural gas exploration were expected to raise estimates of these reserves (World Oil Review, 2017). As with oil, Libyan natural gas production was almost entirely shut-in for sustained periods in 2011, but has since recovered quickly. Libya's natural gas production has grown substantially in recent past. According to EIA (U.S. Energy Information Administration), Libya natural gas production is 11.53 billion standard cubic meter in 2017.

The Western Libya Gas Project (WLGP), which is operated by Eni and NOC through the Mellitah Oil & Gas joint venture, accounts for most Libyan natural gas production growth since 2003. The

*Mellitah Oil & Gas B.V., Tripoli (Libya)
Email: ahmadift1953@gmail.com

WLGP includes Wafa and Bahr Es Salam fields. The vast majority of the gas produced from WLGP is exported via the Green Stream Pipeline. Most other natural gas in Libya is produced by NOC and its Sirte Oil Company subsidiary in the onshore Sirt Basin. Following is the description of Wafa and Bahr Es Salam fields.

Wafa Field

Wafa Field is an oil and gas field with a significant gas cap and limited quantity of recoverable oil. It is producing gas and associated condensate from the gas cap through 22 gas wells and oil with associated gas from oil zone through 15 oil wells. The production from 37 wells collected in different gathering stations (NG1, NG2, SG1, NO1 & NO2) and routed for separation and treatment at the central plant. The on specification gas is delivered to Mellitah by the 32inch diameter and 525.5km long pipeline, the average gas delivery is about 13MMSm3/day. The production of oil and condensate sent to storage tanks in Wafa, and then delivered in mixed mode with NGL coming from gas trains to Wafa Coastal Plant by 16inch diameter pipeline. Approximately 23,000bbls of NGL and 38,000bbls of oil and condensate are delivered daily to Mellitah.

Bahr Es Salam Field

It is a field where gas and associated condensate are produced from (26) wells; (15) platform wells and (11) sub-sea wells. The production is gathered on the platform where the gas is primarily dehydrated and approximately 20MMSm3/day of sour gas delivered to Mellitah gas plant for further treatment by 36 inches diameter and 110km long sea-line. The un-stabilized condensate is delivered to Mellitah process plant by the 10inch diameter sea-line for stabilization.

The National Oil Corporation (NOC) announced intentions to significantly increase the country's natural gas production. New or expanded projects to support this goal include associated oil and gas fields in various stages of development. Increased natural gas production would facilitate an expanded use of natural gas in the power sector, while maintaining and expanding existing pipelines and liquefied natural gas exports. However, like all prospective oil and gas plans in Libya, greater development of the natural gas sector is contingent upon support and certainty from the new political order. Table 1 presents the production of natural gas in Wafa Field and Bahr Es Salaam Field and its export from the Mellitha Gas Plant.

GAS TO LIQUID (GTL) TECHNOLOGY

Another important use of natural gas is to convert it into liquid products. Recently a new technology, Gas to Liquid (GTL) Technology, has been developed to convert natural gas into liquid products which can be transported easily by road tankers or pipelines. Gas to Liquid (GTL) Technologies provide good and promising means to meet the energy needs with clean fuel (Ahmad *et al*, 2002). The products are free of sulfur, metals, aromatics and asphaltenes. The two important GTL technologies are described below:

(a) Conversion of natural gas into liquid products by Fischer-Tropsch synthesis process. It is one of the leading GTL technologies to convert natural gas into high value, clean burning fuel.
(b) Another important GTL technology is the process to convert natural gas into DME (dimethyl ether). DME is a clean fuel and it can be used as a substitute for power plant fuel. DME can be used as good diesel substitute/ diesel volume extender since it has high cetane number.

GTL products will also provide significant environmental benefits (CONCAWE, 1999; El Missirie, 2000 and De *et al*, 2000) as compared to other conventional liquid fuels.

Fischer-Tropsch (FT) Synthesis Products Process

Fischer-Tropsch technology is a process that rearranges carbon and hydrogen molecules present in the natural gas. Conversion of natural gas into F-T products involves three main processing steps such as:

(a) Synthesis gas manufacture
(b) Fischer-Tropsch conversion
(c) Product upgrading

A block diagram indicating production of FT liquid products from natural gas is given in (Fig.1).

Synthesis Gas Manufacture

Synthesis gas is a mixture of hydrogen (H2) and carbon monoxide (CO). It is produced by incomplete combustion of natural gas. In addition to hydrogen and carbon monoxide small amount of carbon dioxide is also produced in synthesis gas production. The technology for making synthesis gas is a known process which has been used in many commercial

Table 1. Production and Marketed Natural Gas of Mellitah Oil and Gas B.V.

Year	Natural Gas at Mellitha Complex ($MMSm^3$)		Natural Gas Marketed ($MMSm^3$)	
	NGL from Wafa Field	Dehydrated Natural Gas from Bahr Es Salaam Field	Natural Gas Marketed in Local Market	Natural Gas Exported
2007	4,552.557	7,199.714	0	8,784.985
2008	4,569.607	7,977.396	0	9,381.145
2009	4,009.956	7,888.998	0	8,753.173
2010	4,415.734	8,185.830	501.361	8,991.064
2011	3,648.387	2,378.242	2,040.325	2,152.126
2012	4,569.708	8,128.668	2,613.495	6,252.582
2013	3,688.646	8,331.319	2,979.290	5,354.704
2014	4,200.242	8,888.807	3,127.644	6,356.750
2015	4,775.971	9,680.922	3,596.604	1,422.543
2016	4,755.913	9,703.459	5,012.205	4,635.901
2017	4,444.689	9,994.788	5,080.731	4,536.411

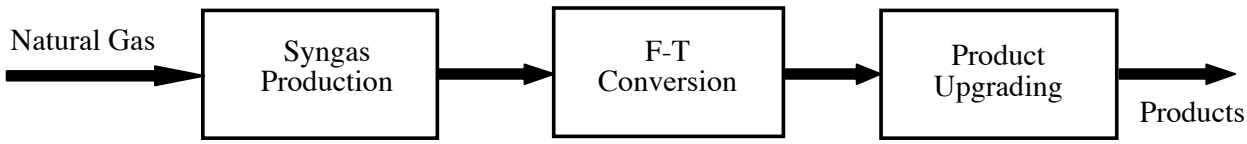


Fig. 1. Block diagram of Fisher-Tropsch process of GTL Technology.

applications as the first step for producing hydrogen, ammonia and methanol. The basic reaction is:

$$2CH_4 + O_2 \longrightarrow 4H_2 + 2CO$$

Two types of gasifiers are commonly used for the production of synthesis gas: viz. (i) partial oxidation and (ii) reforming. In partial oxidation process, natural gas is oxidized partially with pure oxygen to produce hydrogen and carbon monoxide. In case of reforming, oxygen is introduced principally through stream in presence of catalyst.

In addition to above two methods for synthesis gas production, there is one more process called autothermal reforming (ATR) which uses air directly instead of pure oxygen. Since air is directly used in this process, no dedicated oxygen generation unit like partial oxidation process is required which will reduce the plant capital cost. The process selection is based on number of factors like feedstock type, H_2 : CO ratio, etc.

Fischer-Tropsch Conversion

It converts Syngas into paraffinic and olefinic hydrocarbons of varying chain length. F-T process was first developed in 1920 by Hans Fischer and Franz Tropsch (De Klerk, 2013) for production of synthetic liquid fuel from coal. Then it was further developed by U.S. then by South Africa in 1950's due to energy security concern. GTL project based on natural gas was recently developed. F-T conversion happen at moderate temperature (200 – 300 oC) and pressure (10 – 40 bar) and uses iron or cobalt based catalysts. The simplified reaction is:

$$nCO + (2n + 1)H_2 \longrightarrow C_nH_{2n+2} + nH_2O$$

Side reactions include olefins and alcohol production. The desired H2 : CO ratio for Fischer-Tropsch reactor is about 2:1. In this step, synthesis gas flows into a reactor containing a proprietary catalyst converting into waxy hydrocarbons. Two basic types of catalysts used in the Fischer-Tropsch

reactor are cobalt and iron. The hydrocarbons are synthesized by a chain growth process, with the length of the chain being determined by the catalyst selectivity and the reaction conditions.

Product Upgrading

The waxy hydrocarbons are upgraded into F-T products in this step. Product upgradation can be done by using standard hydrocracking and hydroisomerization processes.

F-T Products: F-T products are mainly middle distillates of conventional refinery. The major F-T products are naphtha, gasoline, kerosine, jet fuel and diesel. F-T products contain predominantly paraffins and olefins with very few complex cyclic hydrocarbons and oxygenates. Further, the products are totally free of sulfur, nitrogen, nickel, vanadium, asphaltenes and aromatics that are typically found in petroleum products. The properties of F-T diesel is shown in Table 2.

Advantages of F-T products: Since F-T products are free of sulfur, nitrogen and complex cyclic hydrocarbons, its combustion results in virtually no emissions of SO_2, NO_x and unburned hydrocarbons. Also F-T products can be directly used without any purification process like hydrodesulphurization in case of crude oil derived fuels. F-T products hold a great promise in meeting the stringent exhaust emission norms. F-T naphtha is considered to be an ideal feedstock for ethylene manufacture as compared to naphtha produced from crude oil due to the lack of aromatics. Absence of aromatics gives rise to higher ethylene yield as compared to ethylene from conventional naphtha.

The attraction of FT diesel in addition to its purity is its fuel quality with respect to the cetane number. F-T diesel has a high cetane number of around 75 as compared to minimum requirement of around 50 – 58 in most of the countries. A high cetane number provides fast fuel/air mixing and reduced engine delay before ignition. The other important effect of a high cetane number is the lower flame temperature which results in the reduced formation of oxides of nitrogen (NO_x).

The physical properties of F-T products are almost similar to petroleum products. It can be transported in the same ships/tankers in which petroleum products are transported. It can be stored in the conventional petroleum product storage tanks. No special ships and storage tanks are required for storage and transportation of F-T products unlike liquefied natural gas (LNG). Hence less investment is required for shipping and transportation of F-T products.

TECHNO-ECONOMICAL STUDY

This study is based on the GTL Plant of average production of 50,000 bbl/day middle distillates (Diesel and Naphtha). Actually the natural gas at Mellitah gas plant is much more than this amount. For the sake of calculation we are considering the techno-economical study of this capacity plant. The distribution of products is shown in Table 3 and the revenue collected from the sales of products is given in Table 4.

Calculation of Amount of Gas Required for GTL Plant

50,000 bbl per day of middle distillates = 8,183,000 Liters (Since 1bbl of middle distillates-163.66 Liters), or, 6,614,319kg (Considering density of middle distillates is 0.8083g/cm^3), or, 50,000 bbl of middle distillates = 6614 Tons.

Table 2. Properties of F-T diesel.

Parameters	EU Countries	California Specifications	F-T Diesel
Cetane index	51 Minimum	48 Minimum	73
Aromatics (vol.%)	35 Maximum	10 Maximum	BDL* or 0
Sulfur (ppm)	50 Maximum	50 Maximum	BDL* or 0

Table 3. Distribution of F-T Products.

Product	Percent of Natural Gas Converted to Product	Amount of Product Produced per day (in Tons)
Flue gas	5	413
Liquid Products (Naphtha + Diesel)	80	6614
Wax	15	1240

Therefore, the amount of natural gas required to produce 6614 Tons/day of middle distillates = 8268 Tons/day (Considering 80% of natural gas is converted to middle distillates in FT-Technology), or, the amount of gas required for GTL plant is 371MMSCFT/day (Density of gas = 0.04912 lb/SCFT).

Calculation of Annual Cost of Gas Processed in GTL Plant

- The amount of natural gas processed in GTL plant per day = 371MMSCF/day, or, 378,420 MMBTU per day (Since 1MMSCFT = 1,020MMBTU).
- The cost of natural gas processed in GTL plant = US$946,053per day (Considering average cost of 1MMBTU = US $2.50).

Therefore, Annual Cost of Natural Gas Processed in GTL Plant = US$ 345.308 million.

Calculation of Plant Capacity and Cost of Plant

A number of studies5 peg the cost of the various existing F-T technologies in a range of U.S.$ 20,000 to U.S.$ 30,000 per daily barrel. A feasibility study of applying Exxon's Advanced Gas Conversion for the 21st Century (AGC-21) technology to produce 50,000B/D of middle distillates and other oil based products from 500 million cubic feet of gas was completed jointly by Exxon and Qatar General Petroleum Corp. Capital costs for the project were estimated to be $1.2 billion- or $24,000 per daily barrel (DBL) of middle distillate capacity.

- Plant Capacity = 50,000bbl per day of middle distillate.
- Plant Cost = U.S.$ 1,200 million (Considering plant cost 24,000 per daily barrel of middle distillate capacity).

Economics of GTl Plant was studied using annual expenses to run the plant and annual revenue obtained from sales of the products. The results are summarized in Table 5.

- GTL Plant Capacity = 50,000 bbl/day of middle distillate
- GTL Plant Cost = U.S.$ 1, 200 million (Based on U.S. $ 24,000 per daily barrel)

Annual Profit = U.S. $ 2,256.981 Million

Table 4. Revenue Collected by Sales of FT-Products.

Product	Annual Production (Tons)	Average Price per Ton (U.S. $)	Annual Revenue from Sales of Products (U.S. $)
Flue Gas	Utilized as fuel in the plant	-	-
Liquid Products (Naphtha + Diesel)	2,414,110	1065	2571.027 Million
Wax	452,600	536	242.594 Million

Table 5. Summary of Economics of GTL Plant.

GTL Plant Capacity = 50,000 bbl/day of middle distillate

GTL Plant Cost = U.S.$ 1, 200 million (Based on U.S. $ 24,000 per daily barrel)

Annual Expenses	Annual Revenue from Sales of Products
Annual Cost of Natural Gas Processed = U.S. $ 345.390 million Annual Cost of Plant Operation = U.S. $ 91.250 million *(based on U.S. $ 5 per barrel of middle distillate)* Annual Plant Depreciation Cost = U.S. $ 120 million *(based on 10% depreciation per annum)*	Revenue obtained from sales of middle distillates = U.S.$2571.027 Million Revenue obtained from sales of wax = U.S.$ 242.594 Million
Total Annual Expenses = U.S. $ 556.640 million	Total Annual Revenue from Sales of Products = U.S. $ 2,813.621 Million

$$\text{Repayback vale of the plant} = \frac{\text{Plant Cost in U.S. \$}}{\text{Annual Profit in US \$}} = \frac{\text{U.S.\$ 1,200 Million}}{\text{U.S.\$ 2,256.981}} = 0.53 \text{ years}$$

Therefore, Repayback value of the plant = Approximately 6 month

CONCLUSIONS

1. GTL technology is Downstream value added industry (economic enhancement) of natural gas. At present Libya is exporting natural gas which can be transferred to value added products. It can be a strategic new export industry.
2. F-T products are free of sulphur, nitrogen and complex cyclic hydrocarbons. Its combustion results in virtually no emissions of SO_2, NO_x and unburned hydrocarbons. F-T products can be directly used without any purification process like hydrodesulphurization in case of crude oil derived fuels. F-T products hold a great promise in meeting the stringent exhaust emission norms.
3. The attraction of F-T diesel in addition to its purity is its fuel quality with respect to the cetane number. F-T diesel has a high cetane number of around 75 compared to minimum requirement 50 - 58 in most of the countries. A high cetane number provides fast fuel/air mixing and reduced engine delay before ignition. The other important effect of a high cetane number is the lower flame temperature which results in the reduced formation of oxides of nitrogen (NO_x).
4. F-T naphtha is considered to be an ideal feedstock for ethylene manufacture as compared to naphtha produced from crude oil due to the lack of aromatics. Absence of aromatics gives rise to higher ethylene yield as compared to ethylene from conventional naphtha.
5. A techno-economical study was performed for GTL plant of 50,000 daily barrels capacity of production of middle distillates. The annual revenue obtained from the sales of GTL products is U.S.$ 2,813.621 million while the annual revenue obtained from the export of natural gas is U.S.$345.390 million. The net annual profit from the GTL plant will be U.S.$2,256.981 million.
6. The cost of GTL plant (50,000 daily bbl capacity) is U.S.$ 1,200 million. The re-payback value of the plant is calculated to be approximately six months. Set up GTL plant in Mellitah will be an economically viable plant.
7. The installation of GTL plant in Mellitah will provide employment opportunity to young Libyans. This will bring know-how of new GTL technology among Libyans.

REFERENCES

Ahmad, I.; Zughaid, M. and Elarafi, M. G. A. (2002). Gas to Liquid (GTL) Technology: New Energy Technology for the Third Millennium (SPE 78573), *Proceedings in 10th ADIPEC:* 839-845.

CONCAWE (1999). CONCAWE special task force AE/ STF-3, December 1999. Motor vehicle emission regulations and fuel specifications. Part 1- Summary and annual report 1998.

De Klerk, A. (2013). Fischer-Tropsch Prrocess. Kirk Other Encyclopedia of Chemical Technology. Weinheim: Wiley-VCH.

De, A. K.; Rajan, R. G.; Rao, D. V. and Sivabjarti, A. (2000). Gas to Liquid Technology Options. presented in Petrotech 2001, held at New Delhi (India) on 9-12 January, 2001.

El Missirie, A. A. (2000). Natural Gas Versus Conventional Petroleum Products: Technical, Economical and Environmental Comparison. Presented in MOC 2000 held at Alexandria (Egypt) on April 18-20, 2000.

World Oil Review (2017). World Gas & Renewables 2017.

PRELIMINARY TECHNO-ECONOMIC FEASIBILITY STUDY FOR ESTABLISHING A 250MM LB/YR POLYSTYRENE PLANT

Eltwaty, A. I, Escandarani, S.S., Akaza, Y. M., Elhouni, M. A., and Alwefally, M. O.*

Abstract: Polystyrene is a versatile plastic that is used in the manufacture of many consumer products such as appliances, electronics, car parts, foam , insulating and packaging materials .In a previous paper ,the viability of a local plant for producing styrene has been demonstrated suggesting that a techno-economic feasibility study for establishing a polystryrene plant is the next step. Here the results of this study are presented.

After surveying the literature for relevant technologies, a recent US patent was selected as a manufacturing process. The technology is based on anionic polymerization chemistry and has the advantage of recycling part of the product as a heat sink for heat generated during reaction to soften products for further processing, suggesting a three step manufacturing process: feed preparation, adiabatic reaction and product finishing sections.

In feed preparation section commercial grade styrene is inhibited and continuously treated to remove impurities that can interfere with polymerization downstream. The inhibitor is removed in one of two beds of activated alumina, the other being regenerated. Temperature is carefully controlled to prevent thermal initiation.

The adiabatic reaction section is run batch wise. It consists of low temperature initiation reactor and two anionic polymerization reactors one operating while the other is being regenerated. Sufficient amount of solid product enters the reactor to control the temperature to the desired level. The finishing section is run continuously to accomplish termination, product finishing and purification. Material and energy balances in the original patent were reproduced and a preliminary economic feasibility was undertaken. The project is promising, with an internal rate of return in the range of 30 percent for a ten year operation and a payback period of 2.3 years.

Keywords: Ordovician Succession, Mamuniyat Formation, Murzuq Basin, SW Libya.

INTRODUCTION

Polystyrene is an outcome of polymerizing styrene; styrene is derived from Ethyl Benzene. Polystyrene is an important type of polymer that is a final product of diverse chemical processes; Polystyrene is a versatile plastic used to make a wide variety of consumer products. As a hard, solid plastic, it is often used in products that require clarity, such as food packaging and laboratory ware. When combined with various colorants, additives or other plastics, polystyrene is used to make appliances electronics, automobile parts, toys, gardening pots and equipment and more.

Polystyrene follows certain polymer synthesis. For instance, Chain growth Polymerization is performed by employing free-radical polymerization and copolymerization, ionic polymerization, coordination polymerization and cationic polymerization. In the manufacturing personnel, it has been Chosen Growth Polymerization and has applied one of its techniques; Anion Polymerization.

Ionic polymerization follow the steps; initiation, propagation and termination. The initiator in an anionic polymerization may be any strong nucleophile, including Grignard reagents and other organometallic compounds like n-butyl (n-C4H9) lithium. During the initiation process, the addition of the butyl anion to styrene produces a carbanion at the head end in association with the

*M. O. Department, University of Benghazi.

positively charged lithium counterion. The chain propagates by insertion of additional styrene monomers between the carbanion and counterion. In this paper;

- The material balance and energy balance have been calculated.
- Based on material and energy balance calculations the essential units of plant have been designed.
- An estimated feasibility study was carried out for the cost of the plant and the time period during which the plant retrieves the capital.

Polystyrene plant will be a successful project in Libya because it will complete the petrochemical plants sequence in Raslanuf (ethylene plant). Moreover, if such enormous project is implemented, it may promote economy and instigate the industrial revolt in Libya.

DESCRIPTION AND APPLICATION OF EQUIPMENT AND PROCESS

The process is based on the use of recycled polymer that acts as a heat sink to control the adiabatic temperature rise to the desired final temperature. The output of this plant is 30,041lb of polystyrene per hour. The process flow sheet is shown in (Fig. 1).

The plant is segregated into three sections:

Section 100 - Feed Preparation involving removal of all polar impurities.

Section 200 - Adiabatic Polymerization to the desired finishing temperature.

Section 300 - Finishing to producing polymer for both sale and for recycle.

Section 100

Feed Preparation Styrene monomer is delivered by rail and stored in T-151. When received, it is inhibited with tertiarybutylcatechol (TBC) and is stored off-site at ambient temperature. Inhibit or level is monitored periodically and (in rare cases) may need to be added shot wise. The monomer (stream 1) is passed through E-101 Where it is heated to 50° C. and sprayed into Flash Tank, V-101, that is under reduced pressure of about 20 mm Hg. Traces of Water, oxygen, and other volatile impurities are vaporized (stream 3) and condensed in E-103. Condensate is drained to decanter V-102 Where Water (stream 5) is removed and the organic layer (stream 6) stored in T-101 to be used for fuel. TBC inhibitor is added to V-102 to prevent the possibility of polymerization of this organic layer. The styrene monomer (stream 2) is then cooled to 10° C. in E-104 then passed upward through a bed of activated alumina in C-101. The activated alumina removes the TBC inhibitor and traces of polar compounds. The clean stream is stored in Surge Tank T-102. Up to this point, the process is continuous. The next step (polymerization) is however, carried out in a batch manner. T-102 is continuously receiving cooled monomer (stream 4) but the monomer is removed batch Wise for the batch adiabatic polymerization to follow. Batch polymerization is necessary to obtain the desired narrow molecular Weight distribution. As these monomer batches are being forwarded to R-201 (stream 8), NBL initiator (stream 7) is added (as a 15% solution in ethyl benzene) and is mixed in static mixer M-101.

Section 200

Adiabatic Polymerization Low temperature initiation takes place in the Well-agitated R-101 over a period of 15 minutes. The adiabatic polymerization is carried out alternately in R-202A and R-202B. Solid polymer pellets at about 70° C. are loaded by gravity (stream 9A) into R-202A, B from Weight Tank V-201. After the Warm solid polymer addition is complete, the monomer stream from R-201, containing the NBL initiator, is added rapidly. The elevated temperature of the pellets is sufficient to increase the polymerization rate. The rapid release of the heat of polymerization causes the temperature to rise and the reaction to accelerate as it rises. The reaction is complete in less than 10 minutes. Longer reaction time is allowed primarily to assure temperature uniformity of the polymer melt, as the newly formed polymer heats the cool granules. The cool polymer pellets serve as a “heat sink” and limit the maximum temperature rise as polymerization proceeds adiabatically to completion with a target of 10 ppm of residue monomer (or 99.99999% conversion). After the polymerization cycle is complete, the molten polymer (stream 10)is removed by a gear pump and transferred to the finishing section. The R-202 reactor is then heated briefly to about 260-300° C. to thermally terminate any living ends. This heating is a precaution to prevent gel build-up on the reactor Walls and may not be required after every batch. Termination is determined with an

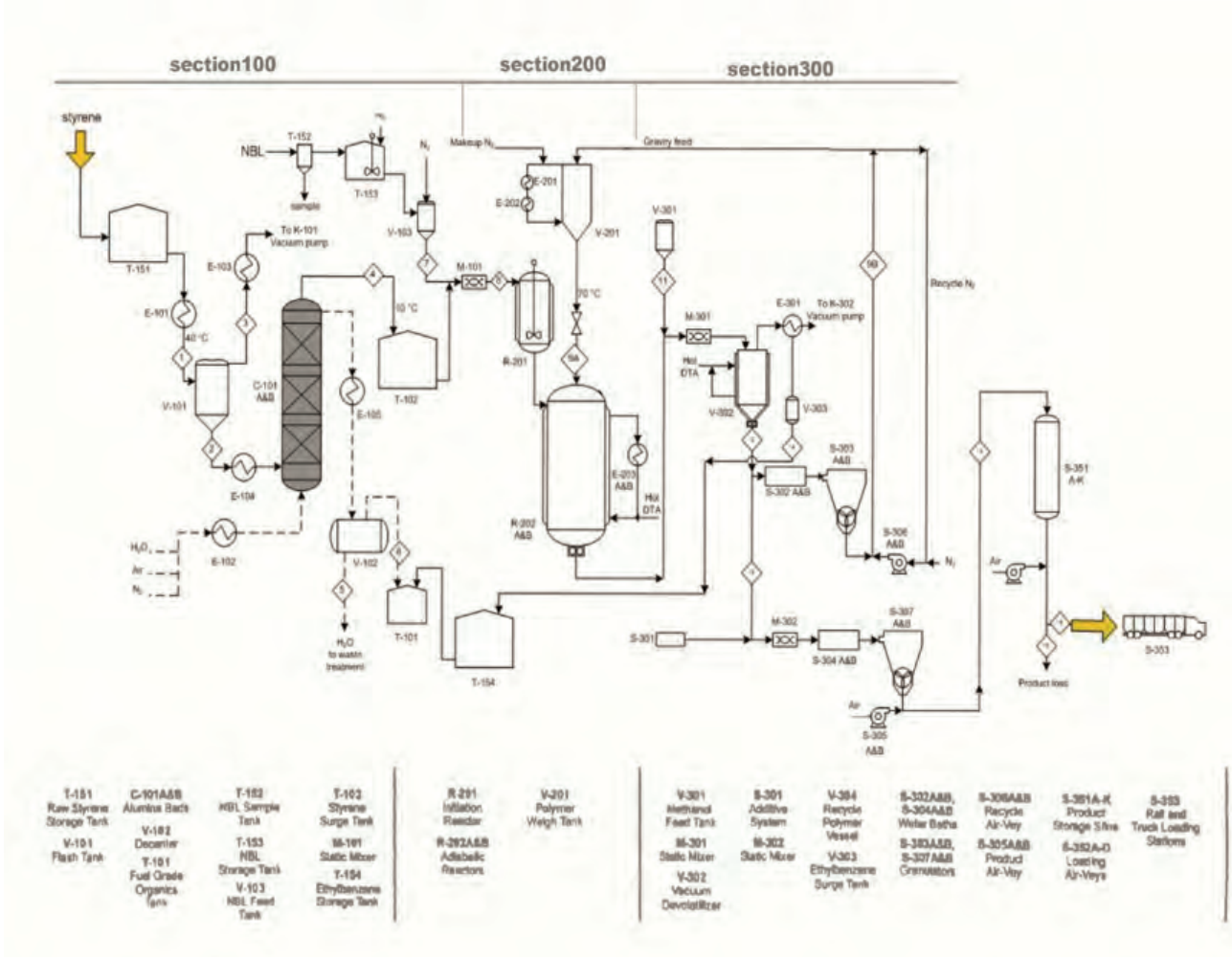


Fig.1. The process flow sheet.

instrument designed to measure the disappearance of the bright color associated with the living styryl anion.

Section 300

Finishing After polymerization in R202A, B, the next step is termination, Which is carried out on stream 10 by precise addition of a stoichiometric amount of methanol from (stream 11) V-301. The methanol is mixed (in Static Mixer M-301) into the living polymer stream where it reacts with the living styryl ends. Adiabatic polymerization has increased the polymer temperature to the 230—260° C. range required for both polymer flow and volatile removal. The small amount of residual ethyl benzene (about 0.2 Wt %)is removed in the Vacuum Devolatilizer (V-302). This very pure ethyl benzene is condensed in E-301, collected in V-303, and (stream 14) stored in T-152. When a railcar full has accumulated in, it is returned to a styrene plant for cracking to styrene. Upon entering high vacuum of V-302, the ethyl benzene vaporizes, causing foaming in the polystyrene. The ethyl benzene vapor quickly disengages from the polymer and the polymer is removed from the bottom of V-302 with gear pumps (M-302A—D). The polymer stream exiting V-302 (stream 12) is split into approximately 2 equal streams, a product stream (13) and a recycle stream (9B). The product stream has the desired additives (lubricants, flow aids, dyes, etc) introduced immediately before static mixer M-303. The polymer is then pumped through S-304A, B. Product is inserted into an extrusion unit and then pellets are the outcome. V-304. In V-201 the polymer temperature is adjusted desired value (70 c) then the polymer is transferred to R-202 by gravity flow where it serves a heat sink to limit the maximum adiabatic temperature. (Eugene, 2005)

PRESENTATION OF DATA AND RESULTS

Material balance is the principal fundament of the process design; it concludes the quantities of raw material in order to seek the necessarily required capacity.

The Material in equals Material out

The inserted quantity of raw material for the plant is 250 million lb per year, which equals 30040Ib per hour. Purification section 100 it is a continuous process, At T-151, the feed stock is inserted and add it along with TBC 12mg per kg of Styrene (Eugene, 2005). Flash Drum will release the traces of impurities in styrene it has used Antoine equation at 20mmHg pruseere and 50 C , while The Adsorber will adsorb the amount of inhibitor TBC from styrene(st4 = st2-adsorbed TBC)

Ethyl Benzene and NBL were mixed in the storage tank

To determine number of moles of NBL (initiator), n = Mass of styrene per batch/Mn. Adiabatic Polymerization section 200 It is a batch process. in Initiation Reactor R-201A, B. Each mole of initiator will react with 1 mole of monomer according to the rapid reaction and the purification of monomer, in Propagation Reactor R-202A, B The monomer Styrene will fully react, approximately 99.999% of reaction has been achieved. The length of chains is nearly equivalent according to the rapid reaction. In order to absorb exothermal heat, we should make sure that the reactor contains 50% wt of Styrene and 50% f Polystyrene. The following equation consists of number average degree of polymerization (Fried, 2014)

$$Xn=[M]0/[I]0 \quad (1)$$

The following equation consists of number-average molecular weight (Fried, 2014)

$$Mn = Xn * [Mw] \quad (2)$$

Mn = 1919.4787*104.2 = 200,000

Termination section 300: This reaction is principally terminated by Methanol, number of moles of Methanol are equivalent to number of moles of NBL which they possess similar number of chains.

We remove Ethyl Benzene by applying devolatilizer and store it in tanks in order to recycle it afterwards. Energy contradicts with material with regard to form changing status, Energy streams are not equal with respect to inlet and outlet.

Energy has multiple forms: Heat, mechanical energy and electrical, total energy is conserved regardless of its form. In process design, energy balances are made to determine the energy requirements for process heating, cooling and power. In plant operation, an energy balance on the plant will expose the pattern of energy usage, and suggest areas for conservation. Energy exists in many forms, which makes it more complex than material balance. The process is applied by following steady-state system, the processed reaction is the adiabatic reaction. Kinetic and potential energy were neglected in this process subsequently, the reaction is exothermic.

At flash drum the styrene feed stock has been inserted into a heater and was heated to 50 c , The exerted feed from flash drum was cooled to 10 c and went through absorber No temperature change is detected, nor enthalpy is changed. The inserted feed stock from ST8 has a precise temperature of 10 c, this reaction must be executed at low temperature. Initiation reaction is performed by unleashing an approximate temperature of 10C.

Enthalpy and temperature were not changed according to the low percentage of Ethyl Benzene and NBL with comparison to Styrene. At propagation Reactor R-202A, B. The process is described as adiabatic polymerization reaction, the reaction is said to be exothermic. The added feed stock from ST8 was inserted at 10C

General Energy Balance Equation:

$Q = W + \Delta H + KE + PE$

According to our assumptions, the equation will be

$\Delta H = 0$

The reaction is performed at 240C between Styrene and initial styrene. As the reaction is initiated, it occurs rapidly. Temperature rises to a higher point 360C according to the exothermic attitude, and this behavior is undesirable. In order to dominate and control this upsetting outcome is to recycle the polystyrene product as granules until the temperature becomes constant at 240C, which is the melting point of polystyrene. We also provide warmth to the recycled polystyrene at 70Co to reach the required circumstances.

As the batch is conceived, we apply thermal termination (260 to 300C) to styryl ions. The

enthalpy of polymerization reaction equals 288btu/lb. We used the jacket in order to obtain a temperature of 240C of the feed stock (Figs. 2 & 3). In order to measure heat, we must apply the following equation (enthalpy times mass).

ΔHR = - 288 btu/lb (Eugene, 2005)

We assumed that the heat capacity of the liquid is approximately equivalent to the heat capacity of the reaction temperature.

$$\Delta H1 = CP\ (Tr-T1) \quad (3)$$

Where :.
CP is specific heat of styrene at 240 c
T1 is initial temperature
Tr is the the reaction temperature

$$\Delta H2 = CP\ (Tr - Tm) \quad (4)$$

Where :.
CP is the specific heat of reacted polystyrene at 360 c
Tm is the maximum temperature

$$\Delta Hrpc = CP\ (Tr - Trp) \quad (5)$$

Where :.
CP is the specific heat at 240 c
Trp is the input temperature of recycled polystyrene
The fallowing equation excludes recycled polystyrene

$$\Delta HR = H1 + H2 \quad (6)$$

$$-\Delta HR + CP\ (Tr-T1) + CP\ (Tr - Tm) = 0 \quad (7)$$

The following equation includes recycled polystyrene :.

$$\Delta HR = \Delta H1 + \Delta HRPS + \Delta HPC \quad (8)$$

$$-\Delta HR + \Delta H1 + \Delta HRPS + \Delta HPC = 0 \quad (9)$$

Where

$$\Delta HRPS + \Delta HPC = \Delta H2 \quad (10)$$

To find out the enthalpy of phase change

$$\Delta HPC = \Delta H2 - \Delta HRPS \quad (11)$$

Devolatilizer: It has a specified function, which is segregating Ethyl Benzene from Polystyrene by high vacuum pressure at 10mmHg. The inserted

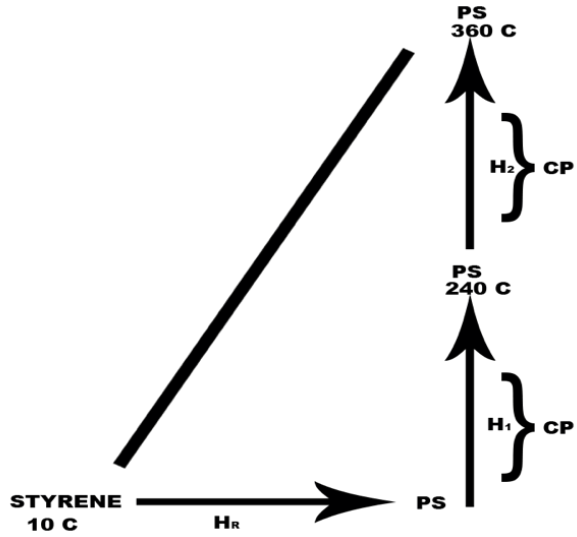


Fig. 2. Change of enthalpy without recycled polystyrene.

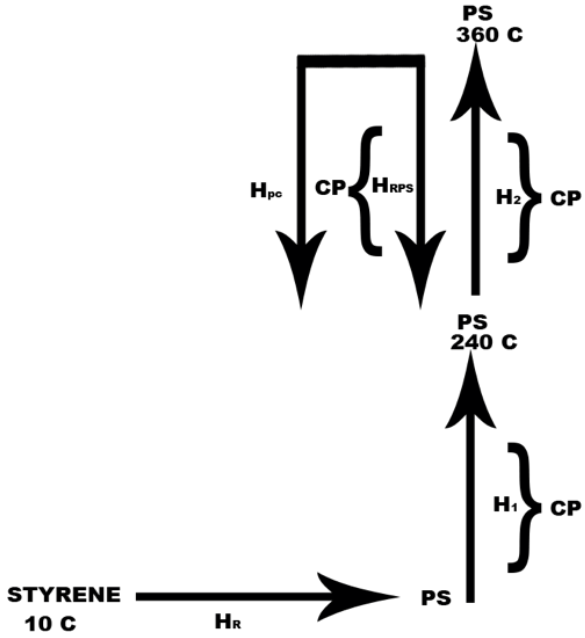


Fig. 3. Change of enthalpy with recycled polystyrene.

temperature from the devolatilizer is equivalent to the exited temperature from mixer, which is 240C.

In order to determine the outlet temperature of Ethyl Benzene, it has used Antoine equation:

$$\ln P = \mathrm{A} - \frac{B}{C+T} \quad (12)$$

The purpose of design is to determine the volume of the utilities in order to evaluate certain requirements such as, economic details. The main function of the factory is to produce polystyrene;

we previously mentioned that the factory consists of three sections. For instance, the purification section promotes the capital cost of factory. However, purification section cannot be underestimated according to its importance and role in the quality of the product and it controls its properties.

In order to distinguish between candidate reactors that may affect the design, We have selected and used packet bed reactor (batch reactor) the reaction is extremely rapid. The essential utilities include flash drum, adsorber, reactors and separators. Styrene intrudes the adsorber to remove the inhibitor (TBC) it penetrates beds that contain aluminia, alumina adsorbs TBC and we employ regeneration to this adsorber each three months because aluminia is saturated with TBC (Rivero *et al*, 2003).

To find out the volume of the adsorber we have to find the amount of alumina that adsorbed the TBC in three month per bulk density of alumina.

Mass of alumina equal amount of TBC in three months divided on q

Whereas q is Langmuir – freundich equation (13)

q = 0.00173*C^0.5/(1+0.00836*C^0.5)

Whereas, C is the quantity of TBC to styrene, Amount of TBC is equal the total mass *C

The calculated volume of the adsorbed was 1435 cubic feet. The Initiation Reactor R-201 is intrusively invaded by Styrene, NBL and EB. The reaction occurs at low temperature. The process is batch. Therefore, we assumed that the volume of the reactor equals the feedstock that entered the reactor.

Additionally, resident time of reaction is few, the total duration of process is 15 min (Eugene, 2005)

Density = M/V
Thus, Volume = Density/Mass
The total volume of feedstock = Volume of Styrene + Volume of EB + Volume of NBL
Volume of Styrene = Mass of Styrene / Density of Styrene
Mass of Styrene = 60081.712lb
Density of Styrene at reaction temperature = 44.29lb/ft3
Volume of Styrene = 1356.5 cubic feet
The volume of NBL = Mass of NBL/Density of NBL
Mass of NBL = 19.24324093lb
Density of NBL = 42.45lb/ft3 at 10C
Volume of NBL = 0.453315452 cubic feet
The volume of EB = Mass of NBL/Density of EB
Mass of EB = 180.7348004lb
Density of EB = 54.68lb/ft3
Volume of EB =3.305 cubic feet
Reactor volume = 1360 cubic feet
In order to determine the diameter of reactor, we use the following equation:
V = πr2h
We assume that the height of the reactor = 19.5 feet
D = (V / h*π)^0.5 * 2
D =9.88 feet

Propagation Reactor R-202 It is the reactor that incubates the propagation process, recycled PS is dumped from above into the reactor and it receives the feedstock, which comes from R-201. This reaction occurs rapidly and at high temperature, resident time of reaction is few. The total duration of this process is 10min (Eugene, 2005). Therefore, it has calculated the product volume to select the method that is suitable for designing the reactor. Rate equation of the reaction (Eugene, 2005)

Rp = Kp [M-][M] (14)

From the rate constant (kp=2L/mol-sec) , it is possible to calculate the approximate overall polymerization rate (Rp) for styrene and the associated heat evolution rate. The kinetics are reported to be simple second order (Eugene, R. M., 2005).

For the case of pure undiluted styrene, [M] is 8.689 mol/L and for MW=200,000, [M]=0.0004525. Then assuming that styrene acting as it's own solvent will have the same kp at 25° C. as benzene (kp=2L/mol-sec), Rp=0.0786 mol (of styrene)/L-sec .

The estimated Volume of the reactor is 1853.7 cubic feet

Diameter of reactor = (V / h*π)^0.5 * 2
We assumed that height of reactor= 32.8084 feet
D= 8.897933662 feet

In Devolatilizer; V-302 Ethyl Benzene is soluble in Polystyrene as liquid phase. As we apply de-volatilization to EB, the outcome phase is gaseous which refers to its increment in volume.

In order to determine the volume of Devolatilizer; Volume of EB Gaseous + Volume of

PS , the Volume of Gaseous EB it has used the real gas equation; PV=ZnRT

The calculated devolatilizer volume was 1426 cubic feet

The equipment size, flow rate, raw material, and ploystyrene production are a very important factor in factor in following steps.

Fixed capital cost.

- ISBL Plant Costs
- Offsite Cost.
- Engineering Cost.
- Contingency Charges.

Working Capital.

Cash cost of production.

Total cost of production.

The Cash flow in each year of the project.

The simple payback period.

The net present value with a 15% cost of capital 25 year of production.

Discounted cash flow rate of return (DCFROR) or IRR.

Taking into consideration that the factory may shutdown for 19 days for periodic maintenance or unexpected emergency cases. According to this the factor works for 346 days in a year.

The Total Fixed Capital Cost has calculated 120MM $.

The Total Working Capital has calculated 15.02 MM $ per year.

Cash flow summary of calculation (Table1): In year 1 and 2 of the project, there are capital expenses but no revenues or operating costs. The capital expenses are not operating losses, so they have no effect on taxes or depreciation. They are negative cash flows. All of the working capital must be invested. The plant incurs 100% of the fixed cost of production but only 50% of the variable cost. Because the plant makes a profit, depreciation can be charged. Using the straight-line method of depreciation with a 15-year recovery period, the annual depreciation charge is one-fifteenth of the total fixed capital investment = 120/15 = $8MM.

The effect of charging depreciation is that the table income is negative, so no taxes are owed in year 4 (taxes are paid based on the previous year's income). Simple Pay-Back Time a simple method for estimating the payback time is to divide the total investment by the average annual cash flow:

$$\text{Simple Pay} - \text{Back Time} = \frac{120}{51.67} = 2.32\text{year}$$

Table 1. Summary of calculation.

year	cap.ex	revenue	CCOP	Gr.Profit	Deprcn	Taxable inc.	Tax paid	cash flow	factor	PV of CF	NPV
1	36	0	0	0	0	0	0	-36	0.8695652	-31.30435	-31.30435
2	84	0	0	0	0	0	0	-84	0.7561437	-63.51607	-94.82042
3	15.02	96.3935	72.6355	23.758	8	15.758	0	23.758	0.6575162	15.621271	-79.19915
4		192.787	134.781	58.006	8	50.006	0	58.006	0.5717532	33.165119	-46.03403
5		192.787	134.781	58.006	8	50.006	5.0006	53.0054	0.4971767	26.353052	-19.68097
6		192.787	134.781	58.006	8	50.006	5.0006	53.0054	0.4323276	22.915697	3.2347224
7		192.787	134.781	58.006	8	50.006	5.0006	53.0054	0.375937	19.926693	23.161416
8		192.787	134.781	58.006	8	50.006	5.0006	53.0054	0.3269018	17.327559	40.488975
9		192.787	134.781	58.006	8	50.006	5.0006	53.0054	0.2842624	15.067443	55.556418
10		192.787	134.781	58.006	8	50.006	5.0006	53.0054	0.2471847	13.102124	68.658542
11		192.787	134.781	58.006	8	50.006	5.0006	53.0054	0.2149432	11.393151	80.051693
12		192.787	134.781	58.006	8	50.006	5.0006	53.0054	0.1869072	9.9070883	89.958782
13		192.787	134.781	58.006	8	50.006	5.0006	53.0054	0.162528	8.6148594	98.573641
14		192.787	134.781	58.006	8	50.006	5.0006	53.0054	0.1413287	7.491182	106.06482
15		192.787	134.781	58.006	8	50.006	5.0006	53.0054	0.1228945	6.5140713	112.57889
16		192.787	134.781	58.006	8	50.006	5.0006	53.0054	0.1068648	5.6644099	118.2433
17		192.787	134.781	58.006	8	50.006	5.0006	53.0054	0.0929259	4.9255738	123.16888
18		192.787	134.781	58.006	0	58.006	5.8006	52.2054	0.0808051	4.2184636	127.38734
19		192.787	134.781	58.006	0	58.006	5.8006	52.2054	0.0702653	3.6682292	131.05557
20		192.787	134.781	58.006	0	58.006	5.8006	52.2054	0.0611003	3.1897645	134.24534
21		192.787	134.781	58.006	0	58.006	5.8006	52.2054	0.0531307	2.7737083	137.01904
22		192.787	134.781	58.006	0	58.006	5.8006	52.2054	0.0462006	2.4119202	139.43096
23		192.787	134.781	58.006	0	58.006	5.8006	52.2054	0.0401744	2.0973219	141.52829
24		192.787	134.781	58.006	0	58.006	5.8006	52.2054	0.0349343	1.8237582	143.35204
25	-15.02	192.787	134.781	58.006	0	58.006	5.8006	52.2054	0.0303776	1.5858767	144.93792

CONCLUSION

It has selected a Polystyrene manufacturing patent and its methodology. Within reason, it has the privilege to control the properties with no complex interferences regardless of the showcased difficulties of temperature control. It has implemented the energy and material balance onto most plant equipment and has designed the prior units. The calculations of work match the guidelines of the patent, it has bonded the provided hints of patent and has obtained the results by linking our knowledge to those hints.

The industrial advantage of designing this plant is that inlet feedstock is wholly exploited to come up with a product without wasted inlet. The economic distinction of this project is that the plant is quite profitable and its capital is predictably regained after two years and three months of operating.

RECOMMENDATIONS

- Strongly recommend that the patent and its references should be studied with full concentration.
- We suggest that you take your research to an advance level by looking up to similar examples.
- The economic study lacks details about sub-utilities, because we focused on the main utilities and neglected their sub-branches.

NOMENCLATURE

PS	Polystyrene
NBL	Normal Butyl Lithium
EB	Ethyl Benzene
TBC	4-tert-Butylcatechol
Xn	number average degree of polymerization
[M]0	initial concentration of monomer
[I]0	initial concentration of initiator
Mn	number-average molecular weight
ΔHR	Enthalpy of polymerization reaction
ΔH1	Enthalpy of reaction before exothermal
ΔH2	Enthalpy of reaction after exothermal
ΔHRPS	Enthalpy of recycled polystyrene
ΔHPC	Enthalpy of phase change of recycled polystyrene
CP	specific heat
Kp	Rate constant
Rp	Rate of Reaction

REFERENCES

Eugene, R. M. (2005). United States Patent. **1 (12)**: 19-21.

Fried, J. R. (2014). Polymer Science and Technology, *Third Edition* Prentice Hall, **40 (6)**: 49-50.

Rivero, M. J.; Ibáñez, R. and Ortiz, M. I. (2003). Analysis of the Elimination Process of Polymerisation Inhibitors from Styrene by Means of Adsorption. J. Chem. *Technol. Biotechnol. Int. Res. Process. Environ. Clean Technol,* **78 (1)**: 64–72.

INTEGRATION OF AIRBORNE WIND ENERGY WITH THE OIL AND GAS INDUSTRY

Youssef Elshebani *

Abstract: The oil industry has regained a reputation of being a competitor to Renewable energy. With the ever-rising demand, towered energy and the momentum to shift into more sustainable solutions, a common ground between conventional and renewable energy production can be found by means of co-generation. This paper presents a method of integration between oil and renewable energy namely Airborne Wind Energy (AWE) focusing on Kite technology with brief introduction into the kinematics and force distribution on airborne kites. Deriving an analytical model of the so called pumping cycle kites which its principal of operation is to mechanically drive a ground based generator, an insight into crosswind motion is presented and a formula to find the mean mechanical power is obtained. Along with a wind distribution profile on various regions in Libya using a Weibull distribution model calculated by iterative techniques to specify its constants. Using the model to compute electrical power generation on board the platform, operate distant wells or pumping heads. Followed by a case study on using such technology in offshore platforms and the impact it can carry on energy consumption in such platforms, presenting results in terms of fraction of energy generated to the consumption of the platform as well as savings in CO2 emissions. Presenting the possibility of expansion and scalability of such technology and its impact on the oil and gas industry in Libya.

Keywords: Airborne energy, Wind Energy, Renewables.

INTRODUCTION

For many years, oil and gas sector was seen as a competitor for renewable energy with the prior offering practical satisfaction for energy demand while the latter focuses on sustainability, environment and planet habitation. The power generated using wind turbines increases with the cube of the wind speed, hence doubling the wind speed would increase the available power by a factor of eight times. It is this fact that motivated many researchers and engineers to propose various concepts for extracting electricity at high altitudes "1-10Km" (Bolonkin, 2004; Roberts *et al*, 2007). Such ideas manifested in attempting to locate wind turbines at high altitudes. However, in recent years several designs have been suggested to use tethered kite to collect energy at high altitude. In this paper the traction of pumping kite generator is considered. The operating principle of such a device revolves around driving a ground based electric generator using a tethered kite as an alternative to locating a wind turbine at high altitude. On the ground the lower portion of the tether is wound around a drum connected to a generator. Energy is harvested by allowing the kite to fly at high altitude in a lying eight orbit with high crosswind speed (Loyd, 1980). During the fast crosswind motion the kite develops high pulling forces unwinding the tether around the drum and thus rotates the drum generating electricity through the generator. The kite is controlled such as the pulling force is reduced during operation and the tether is wound back by operating the generator as motor. This cycle is repeated and hence the name pumping cycle. It is worth noting for generation with this system relies on kite dynamics control to obtain large and small pulling forces alternatively (Argatov *et al*, 2009).

More than two thirds of the power generated by a conventional turbine is extracted from the outer portion of its blade (Van der Vlugt *et al*, 2013). A kite represents the outer portion of the blade and hence, it generates electricity using the most active criteria

*Email: Elsehbani.youssef@gmail.com

of a wind turbine, disavowing complementary parts such hub, tower and others. These results in a sharp decrease in size required for the system.

Methods for using such a system with oil and gas production are presented and discussed. A numerical experimentation is carried out to calculate the power generated of such a system and compared with possible applications in the oil and gas industry.

KITE POWER

Kites have been seen to hold considerable application in pulling load and was refined by G. PoCock in around 1825 to as much as was technically possible at the time. However, with the rise of aerodynamics in early 1900 followed by energy crises have centred many efforts toward utilising wind energy, though kites where disregarded as mean of a viable source of energy (Schmehl *et al*, 2014).

A kite surface converts the wind energy to useful forms of energy either by housing a turbine on the kite or by driving a load on the ground e.g a generator. The latter is most interest in this paper. A motion of the kite tethered at a central point and moving downwind, will achieve a near transvers motion that will be termed as cross wind. This allows for the kite speed to increase beyond the wind speed due to the glide ratio of the kite profile CL/CD (Schmehl *et al*, 2014) thus, producing enough lift to sustain the kite airborne and generate energy.

Simple Model

As soon as kite is set to the atmosphere and allowed to move in cross direction to the wind vw with velocity va the tension in the cord noticbly increases due to increasing lift force experienced according to eq (1):

$$F_L = \frac{1}{2} p A C_L v_a^2 \tag{1}$$

Thus if a kite with is flown with velocity va that is ten times faster the air speed than a force with a factor of 100 will be produced in comparison with a stationary kite in the sky.

There are several modes where a kite can be used to generate power. One way is by having a drum on the ground attached to the kite tether the drum is coupled with a generator that turns as the tether is reeled-out. Hence the power produced will be the tension on the tether TL multiplied by extension velocity of the tether vL:

$$P = T_L V_L \tag{2}$$

As mentioned earlier the most efficient orientation would be to fly the kite in cross wind by roll controlling the kite to the desired condition to make use of the added velocity induced by lift. Such a velocity triangle is depicted in (Fig. 1).

It is noted that the velocity of wind, kite, and cross namely Vw, Va and Vc respectively form a right triangle. By using trigonometric relation, it can be shown that.

$$V_a = (V_w - V_L)\frac{L}{D_k} \tag{3}$$

Hence, the lift can be defined as

$$F_L = \frac{1}{2} p A C_L (V_w - V_L)^2 \frac{L^2}{{D_k}^2} \tag{4}$$

Now, by combining the former equation with definition of the power density in wind Pw

$$P_w = \frac{1}{2} p {V_w}^3 \tag{5}$$

A function F can be defined which describes the operation of the kite. Since we are dealing with cross wind operation it will be termed as Fc

$$F_c = \left[\frac{L}{D_k}\right]^2 \left[\frac{V_L}{V_w}\right]^2 \left[1 - \frac{V_L}{V_w}\right]^2 \tag{6}$$

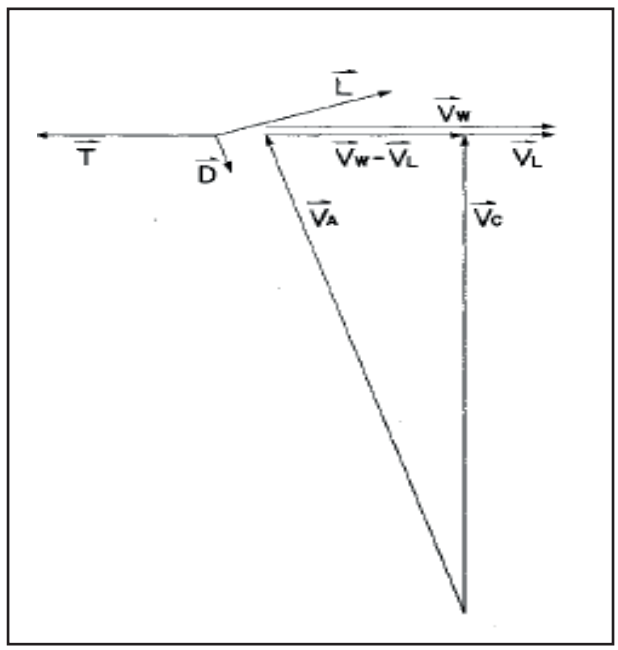


Fig. 1. A schematic of kite power systems with offshore rigs.

This allows to find the maximum point for Fc and hence power produced by the kite since power produced can be modelled as for any mode of kite operation:

$$P = P_w A C_L F \tag{7}$$

$$F_{max} \; when \; \frac{V_L}{V_w} = \frac{1}{3} \tag{8}$$

The maximum power produced is when the reeling velocity is one third of wind velocity. So, a kite with surface area of 576 m2 flying cross wind in 10 m/s wind speed would produce 22MW. Though this number presents the limit and cant actually be achieved at the moment due to tether drag, effects of gravity, cosine losses and the motion cannot be purely cross wind as assumed by the theory (Schmehl *et al*, 2014).

Advanced model

A more realistic model would account for effects of gravity and kite and tether inertia as well as centrifugal forces acting upon the kite (Argatov *et al*, 2009).

The tensions in the cable namely T:

$$T = T_1 + w_c{}^{II} + F_C{}^{II} \tag{9}$$

Where, w CII is the component of the cable weight in the direction of the tether. Where:

$$w_C^{II} = W_c cos\theta \tag{10}$$

A function FIIC is defined as

$$Fc = \frac{1}{2}\rho_a C_{II} sin^2\theta cos^2\emptyset \int_0^r V^2 (xcos\theta) dx \tag{11}$$

Where, CII is the friction coefficient with kite and tether. Assuming the kite undergoes motion in equilibrium the tension T1 can be interpreted as:

$$T_1 = F^{aero} - F^{grav} + F^{Cf} \tag{12}$$

By using the crosswind motion model provided that VII is replaced with VII-VL, then:

$$F^{aero} = \frac{1}{2}\rho_a A C_L G_E \sqrt{1 + G_E^2} (V_{ll} - V_L)^2 \tag{13}$$

Where GE is termed as the glide ratio, it represents the kite aerodynamic properties.

$$G_E = \frac{C_L}{C_D - \frac{C_{Ird}}{4A}} \tag{14}$$

The Aerodynamic force FAero is the largest active force on the kite larger than Fgrav and Fcf.

Mechanical Power generated by the kite

The mechanical power generated can be computed by substituting Eqs (13, 12 and 9 into 2) yielding

$$P_M = V_L \left(\frac{1}{2}\rho_a A C_L G_E \sqrt{1 + G_E^2} (V_{ll} - V_L)^2 + F_{cf} - F_r{}^{Grav} - w_c^{ll} + F_c^{ll} \right) \tag{15}$$

Takin PM as a function of kite velocity VL a value for the maximum of the function can be found using asymptotic analysis. Giving:

$$P_m^{max} = \frac{1}{2}\rho_a A C_L V_{ll}{}^3 k \tag{16}$$

k =Where,

$$\frac{4}{27} G_E \sqrt{1 + G_E^2} \left(1 + \frac{9}{2} \frac{F_{cf} - F_r{}^{Grav} - w_c^{ll} - F_c^{ll}}{\rho_a A C_L G_E \sqrt{1 + G_E^2}} \right) \tag{17}$$

Mean Mechanical Power

Averaging over one time period of open loop trajectory

$$\langle P_M^{max} \rangle \cong \frac{1}{2}\rho_a A C_L V^3 \cos^3(\vartheta) k_0 k_* \tag{18}$$

Where,

$$k_0 = \frac{4}{27} G_E \sqrt{1 + G_E^2} \tag{19}$$

$$k_* = 1 + \frac{2}{3} \frac{\langle F_{cf} \rangle - \langle F_r{}^{Grav} \rangle - \langle w_c^{ll} \rangle - \langle F_c^{ll} \rangle}{\rho_a A C_L k_0 V^2 \cos^2(\vartheta)} \tag{20}$$

Where the later equations can be solved numerically using an iterative software to yield a mean value for the power developed by the kite during a complete period of operation.

INTEGRATION OF KITE POWER IN THE OIL FIELD

Off shore Rigs

Decentralised power for Oil pump: One of the major losses for deep ocean oil pumps is the vast distance the electric wiring must cover which

carries much initial cost and maintenance costs not to mention complexity of such a set up, furthermore, the carbon emissions generated at the rig site of generating using turbines with a large portion going to losses.

By using a float structure set up carrying a kite power generator operating the pumps and other auxiliary machinery will achieve a much better efficiency due to minimizing of transporting losses. The intermittent power supply would not be an issue, as the pumps do not need to be continuously active, instead operate when there is power available (Nilsson & Westin, 2014 and Fig. 2). However, these systems would require a storage device but since the power, demand is not significant it could use e.g. battery. Such structures can be made on shore and towed to specified test giving ease of movement to supply many sites and provide a better settings for oil pumps scattered in large area, these structures are discussed in more details in (Korpåsa *et al*, 2012).

The Set up of such system is considered applicable and its feasibility rely on factors such as water depth, reservoir characteristics and distance from platform to injection well. Analyses deem the concept technologically achievable under certain constraints and some essential parameters must be evaluated economically prior to investing in such set up:

- Distance between platform and injection head i.e. the cost implication of the cable
- CO_2 tax
- Fuel costs for running gas turbines
- Cost for floating wind turbine

When these important parameters are taken into account the solution is deemed highly interesting. A study made by DNV GL (2014) showed that a system with raw-water injection using a 5MW pump together with a 6MW turbine could be cheaper than traditional raw-water injection already at step out distance of 20-30Km. which a kite power system can provide power cheaper than the wind turbine making such integration highly motivating. Analyses by DNV GL have shown that there are no technical difficulties and that the commercial potential looks promising (Slätte, 2014).

Direct Generation on Deck of the Rig: Floating and stationary kite power systems can be connected to the oil platform directly thus enabling direct supply of renewable energy instantly to the platform. As oil platforms are customarily located in deep waters where vast wind resources can be harnessed, providing the potential for high production and capacity factors. Though the intermittent power supply by the kite systems can cause concern, where renewable energy alone

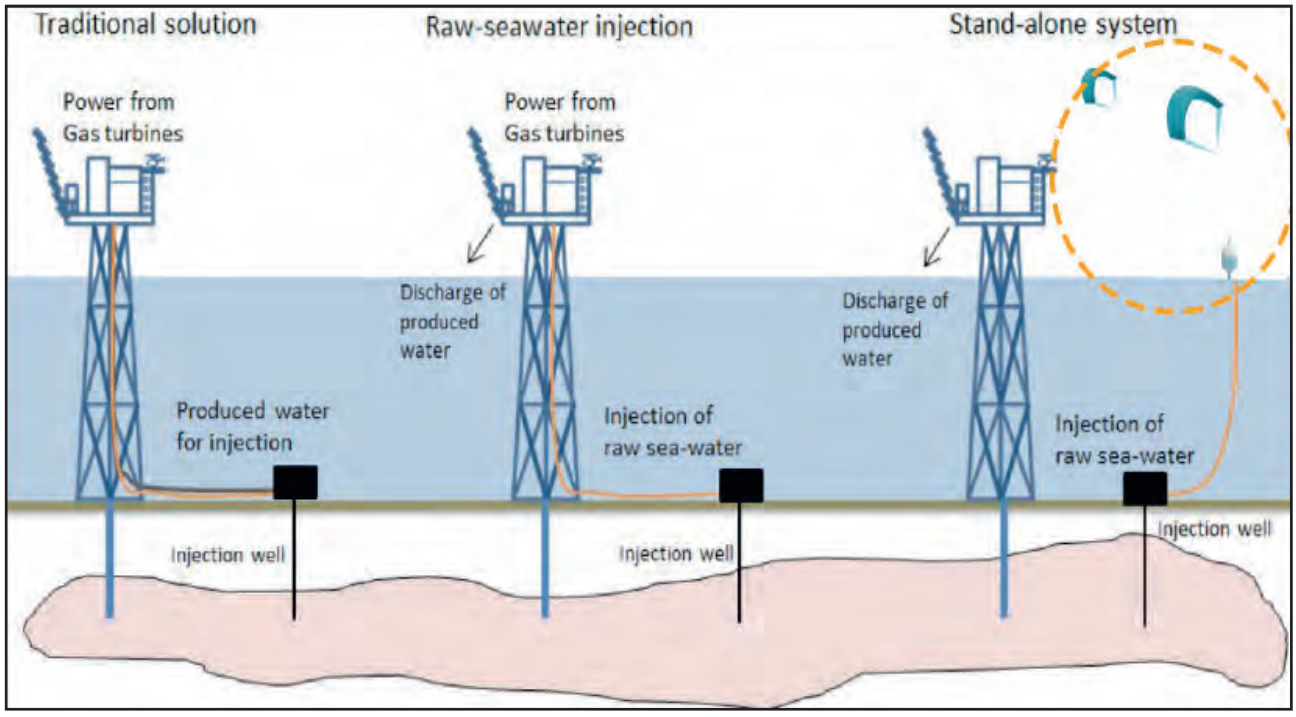


Fig. 2. Crosswind motion velocity triangle.

will not be able to supply the platform all the time (48021HI Energy, 2014). For platforms that already employ gas turbines or connected through cables to national grids these systems can work in parallel. Helping to drive fuel prices as turbines usually require high grade fuels not to mention the carbon emission reduction. One example is the Beatrice Wind farm in Norway, where two turbine systems with 5MW were connected build at a depth of 40 m and connected to a nearby oil rig providing 30% of its total energy demand. It is worth reminding that such a capacity using kite power would require less size and fewer complications as using kites have economical advantage over blades (Marvik *et al*, 2012).

Other research support the idea of integrating renewable sources with oil and gas rigs such SINTF energy research (48021HI Energy, 2014). This clearly shows that development of kite system would make a great solution to the energy demand for of shore platforms. Sue to its inherit advantages over conventional wind turbines and lower risks for equipment failure, such that if the kite is detached during rough weather it will not be such a disaster like blades of turbine failing, or a tower bending, clearly pointing to a very intriguing and potentially applicable solution.

NUMERICAL EXPERIMENTATION

As a closing remark, a value of the generated power is calculated using numerical solver octave. Using the kite parameters from (Argatov *et al*, 2009); area of the kite is 500m2, mass of the kite m is 850kg, coefficient of lift CL is 1.5, coefficient of drag CD is 0.04. average length of tether assumed to be r =1260m with a diameter of 6.7cm, normal reaction force (drag) coefficient C⊥ is 1.0 and friction coefficient Cll is 0.02. The density of the tether material pt is 1450Kg/m3 and thus the linear mass of the tether is μ=ptπ(d/2)2 the wind speed for this calculation was taken based on Ref (Argatov, I.; Rautakorpi, P. and Silvennoinen, R. (2009)) with an average value of 10m/s, and acceleration due to gravity g=9.81m/s2 and air density pa=1.23Kg/m3. The mean angle the kiteline forms with the vertical θ* is about 1.25 radians (71.61o degrees)

To calculate the mean mechanical power using eq. (18) the effective glide ration and average values of <Fcf>, <FrGrav>,<wcII> and <Fcll>. Effective glide ratios is taken from eq. (14) to be 12.2.

$$F_{cf} = mr\omega^2 \quad F_C^{ll} = \frac{1}{2} p_a C_{ll} r d V^2 cos\vartheta_*^{\,2}$$

$$w_c^{ll} = \mu r g sin\vartheta_* \quad F_r^{Grav} = mg sin\vartheta_*$$

Here ϑ_* is the mean angle of inclination of the kiteline with the horizon. Before calculating an estimation of the average centrifugal force a lying eight orbit must first be defined using equations

$$\theta = \theta_* + \frac{\pi}{18}\sin(2\tau) \quad \emptyset = \frac{\pi}{12}\sin(\tau)$$

Where τ is a parameter that goes from 0 to 2 during one period of operation.

If we define the period as:

$$T = \frac{L}{G_a V cos\vartheta_*}$$

Where; L is the length of the orbit. Next the centrifugal force is

$$F_{cf} = mr\omega^2 = \frac{mr}{T}\int_0^T \left((\theta`)^2 + (\emptyset`)^2 sin^2\theta\right) dt$$

The mean power generated by such a setting is about 5.7MW. comparing with Diehls result of 4.9MW a note must be understood, that in Diehl's model the unwinding of the tether is pulled back while in our model it is assumed that the kite is constantly pulling the tether out of the drum.

A VIEW OF THE APPLICATION

Offshore platforms come at various sizes considering the troll A platform in the Norwegian shelf close to Kollsnes where the processing plant is located. Such a platform that uses a nominal value of 100MW (ABB, 2003). A system of kite generation can be used to supply its half power with a maximum number of 11 kites which will take less size since the kites will be operating at high altitude of about 300 m and by this reduce the costs of fuel and carbon production significantly.

Using such systems to power water injection pumps on floating structures is technically feasible. Utilizing a smaller size kite systems to power the pumps and auxiliaries such as 45m kite area would be more than sufficient to supply a pump such as HP200 by Framo which is capable of providing a pressure of 2500psi at flow rate of 3960 m3/h consuming 8500KW rated (FOGPS, 2018).

CONCLUSION

Means for integrating the renewable energy sector with oil and gas production is presented with a focus on kite power. Investigating the working principle of: "traction kite power system" with a brief discussion of the crosswind motion law. Different possible application for using such a setup is explored and the following is found:

- A kite power system would provide considerable energy while using considerably less space compared with wind turbines.
- Kite power may have the possibility of in platforms to generate part of the electricity demand
- Kite power systems can work to operate distant pumps and other machinery and thus decrease the cost of transporting the energy from the platform using cables.

FUTURE WORK

More research and development is required upon this technology as it still rather new. A more detail into practical experiments are needed, comparison with numerical and analytical models for further development of the model are required. A more economical approach into the subject comparing the costs of gas turbines, grid reliance and wind turbines with kite power system is required, drawing upon the advantages of each and applicability.

REFERENCES

A Compact Means of Boosting Production. (2018). [Brochure], Framo Oil and Gas Pumping Systems, Framo Technical Description: 4-9.

ABB (2003). Powering Troll with New Technology. [online] ABB: 4-5. available at: http://clux.x-pec.com/files/fronter/ENE202%20-%20 Elkraft %20 2/H%F8st /Anvendelser / hvdcLight_powering TROLL .pdf [Accessed].

Argatov, I.; Rautakorpi, P. and Silvennoinen, R. (2009). Estimation of the Mechanical Energy Output of the Kite Wind Generator. Renewable Energy, **V. 34(6)**: 1525-1532.

Bolonkin, A. (2004). Utilization of Wind Energy at High Altitude. AIAA Paper 2004-5705: 1-13.

DNV GL. (2014). Electrifying the Future, Høvik: Energy 48021HI (2014). Talisman Beatrice Project. [Online], available at: *http://www.hi-energy.org.uk/HI-energy-Explore/talisman-beatrice-project.htm.*

Korpåsa, M.; Warlanda, L.; Heb, W. and Tandea, J. O. G. (2012). A Case-Study on Offshore Wind Power Supply to Oil and Gas Rigs. Elsevier Ltd., Trondheim:

Loyd, M. L. (1980). Crosswind Kite Power. Journal of Energy, **V. 4(3)**: 106-111.

Marvik, J. I.; Øyslebø, E. V. and Korpås, M. (2012). Electrification of Offshore Petroleum Installations with Offshore Wind Integration.

Nilsson, D. and Westin, A. (2014). Floating Wind power in Norway: Analysis of Future Opportunities and Challenges. Unpublished MSc Thesis. Lund University: 17-38, 49-57.

Pocock, G. (1827): The Aeropleustic Art, or, Navigation in the Air by the use of Kites, or Buoyant Sails. Sherwood & Co, London. *http://collections.britishart.yale.edu/vufind/Record/2033761.*

Roberts, B. W.; Shepard, D. H.; Caldeira, K.; Cannon, M. E.; Eccles, D. G. and Grenier, A. J. (2007). Harnessing High-Altitude Wind Power. IEEE Transaction on Energy Conversion, **V. 22(1)**: 136-44.

Schmehl, R.; Ahrens, U. and Diehl, M. (2014). Airborne-Wind Energy (Ch. 1 and Ch. 2). **1st ed**. Newyork, Hiedlburg: Springer.

Slätte, J. (2014). Interviewee, Senior Consultant at DNV GL-Renewables Advisory: Interview.

Van der Vlugt, R.; Peschel, J. and Schmehl, R. (2013). Design and Experimental Characterizationof a Pumping Kite Power System. In: Airborne wind energy (Ed. by: U. Ahrens; M. Diehl, and R. Schmehl), Berlin Heidelberg Springer; 403e25. *http://dx.doi.org/10.1007/978-3-642-39965-7_23*. **Ch. 23**.

CRITICAL SUCCESS FACTORS FOR SUCCESSFUL LIBYAN OIL AND GAS PROJECTS

Abdulbaset A. Frefer*, Mahmoud M. Matoug** and Haleema H. Omer***

Abstract: Libyan oil and gas companies (LOGCs) are facing many kinds of risks and challenges, which make execution of projects increasingly complex. Identification of critical success factors (CSFs) are vital to Libyan oil and gas projects success, as it allows companies to focus their efforts on these factors to ensure success. The main objective of this research is to identify the success factors, which are important for Libyan oil and gas projects success. From the literature review, thirty factors were found to be critical. To seek the opinion of clients, consultants and contractors in the Libyan oil and gas sector on the critical success factors, a questionnaire survey was conducted. The top ten critical success factors were selected based on their individual relative importance index. In addition to that, five semi-structured interviews were conducted with local experts in oil and gas projects in order to add other CSFs. These experts added ten more CSFs, so the total CSF's developed and identified was twenty-one factors. These critical success factors were classified into five groups of factors, which are critical inputs to achieve oil and gas projects success in Libya.

Keywords: Critical Success Factors (CSFs), Libyan Oil and Gas Companies (LOGCs), oil and gas projects, project success.

INTRODUCTION

The oil and gas sector is one of the largest and most important driving force behind many other sectors (Tsiga et al, 2017). The International Energy Agency (IEA, 2007) reported that the world's primary energy needs are expected to grow by 55% between 2005 and 2030 at an average rate of 1.8% per year, with the demand reaching 17.7 billion tons of oil equivalent. The challenges that oil and gas projects will continue to face, fall in the following categories: namely; Technical; Managerial; and Human resources (Badiru and Osisanya, 2013) .

Identification of critical success factors of project management can help mitigating these challenges and contributing to the success of projects. Oil and gas projects are investment projects undertaken by investors or state-owned oil companies or international oil companies with the purpose of making profits (Omer, 2017). Oil and gas projects are executed at different stages of the oil and gas industry value chain, which is broadly divided into upstream, midstream and downstream (Shuen, 2014).

This research focuses on Libyan oil and gas sector, which is considered the most important sector in the country. Libya is located in North Africa, it has the largest amount of proved crude oil reserves and the fifth-largest amount of proved natural gas reserves in Africa (USIA, 2015). Libya is a member of the Organization of the Petroleum Exporting Countries (OPEC) since 1962. National Oil Corporation (NOC) of Libya oversees the operation of the oil and gas sector, which includes implementing Exploration and Production Sharing Agreements (EPSA) and Development and Production Sharing Agreement (DPSA) with International Oil Companies (Omer, 2017).

There are many international oil companies in Libya, such as Total, Eni, Wintershall and Repsol. Tsiga et al (2017) stated that the international oil companies invest heavily in exploration and development. According to the International Monetary Fund (USIA, 2015), the Libyan oil and gas sector was responsible for 96% of the government revenue and 98% of total foreign exchange earnings in 2012. Roughly 79% of Libya's export revenue came from crude oil exports. Therefore; project

*Mechanical and Industrial Engineering Department, University of Tripoli, Tripoli, Libya; Email:drfrefer@hotmail.com
**Mechanical and Industrial Engineering Department, University of Tripoli, Tripoli, Libya; Email: mmmatoug54@ymail.com
***QA/QC Engineer/ Projects & Engineering Department, Mabruk Oil Operations, Tripoli, Libya; Email: haleema.omer@mabruk-oil.com

failure in the oil and gas project will not only affect the oil and gas companies, but the economy of the country as a whole. This highlights the need for the identification of critical success factors for oil and gas projects in Libya. Identification of critical success factors will assist the Libyan oil and gas companies in performing their projects successfully and will help them remain competitive in the international market.

The main purpose of each project is to be successful. In order to increase the chances of project success (Baccarini, 2009), it is necessary for oil and gas companies to have an understanding of what are the critical success factors, to systematically and quantitatively assess them, anticipating possible effects, and then choose appropriate methods of dealing with them.

LITERATURE REVIEW

Project Success

Project success is the most researched and discussed topic in project management area as was reported in the literature. According to Silva et al (2016), project success is an abstract concept; and to determine whether a project is successful and subjective is extremely complex. These researchers stressed that the lack of an agreed definition for project success has long been the reason for failing to define and evaluate success. Silva et al (2016), also noted that there is no such thing as an absolute success in a project and there is only perceived success. (Al-Ageeli and Alzobaee, 2016) stated that measuring the project success is a complex task since the success is intangible and hardly be agreed upon.

The role of different project management techniques to implement projects successfully has been widely established in areas, such as planning and control of time, cost, and quality (Munns and Bjeirmi, 1996). Pinto and Slevin (1988) see a project success as a complex and often-illusory construct, but nonetheless, it is of crucial importance to effective project implementation. Critical

Success Factors in Project Management

The project management is important for every project. According to PMI (Pmbokr, 2018), project management is defined as "the application of knowledge, skills, tools, and techniques to a broad range of activities in order to meet the requirements of a particular project." The appropriate application of project management will help the oil and gas companies to execute projects effectively and efficiently.

According to (Iram et al, 2016), researches conducted on project success and critical success factors are important methods through which the effectiveness and efficiency of the projects is further improved. Alias et al (2014) pointed out that the study of project success and critical success factors (CSFs) is often considered as one of the important ways to improve the effectiveness of project delivery. (Iram et al, 2016) stated that effective and efficient management of critical success factors is the basic requirement of project success. They noted that for the achievement of organizational goals, it is necessary for a manager to consider the critical success factors in his/her decision.

The field of project management has directed a significant part of their research efforts to identifying the critical success factors of projects. Despite project success being a dominant theme in the project management literature, there is still few consensuses on the factors that can lead to project success (Müller and Jugdev, 2012). The concept of "success factors" was first coined in 1961 by D. Ronald Daniel of McKinsey & Company (Daniel, 1961), it was refined into critical success factors in 1981 by John F. Rockart (Rockart & Treacy, 1981), and since then many researchers have published lists of critical success factors (Srimathi et al, 2017).

Rockart (1979) defined critical success factors as "the limited number of areas in which satisfactory results will ensure successful competitive performance for the individual, department or organization." Dvir et al (1998) defined critical success factors as "the main variables that contribute to projects' success." Amade et al (2015) stated that critical success factors are the few key variables or factors that the manager should prioritize, in order to achieve his/her goals for current or future areas of activity. Kerzner (1987) defined critical success factors as "the elements which must exist within the organization in order to create an environment, where projects may be managed with excellence on a consistent basis. According to Alias et al (2014), critical success factors are inputs to project management practice that can lead directly or indirectly to project success. Success factors contribute to the success or failure of a project, but do not form the basis for judgment.

Developing and identifying the success factors have dominated the field of project management from 1980s to 2000s. Many researchers have tried

to certain extent to identify success factors for project management. The first major contribution of Slevin and Pinto (1986) was the development of a project management tool; named, the project implementation profile (PIP) and identification of ten critical success factors (Slevin and Pinto, 1986). In the same period, Kerzner (1987) in his study identified six critical success factors for successful projects.

In the years that follow, studies have continued to generate new insights and lists with critical success factors (CSFs). Most of these studies were carried out at project level and were aimed at identifying critical success factors applicable to all projects. According to Els et al (2012) in a study they conducted on defining critical success factors based on the literature review, they suggested fifteen factors. In the study by Belassi and Tukel (1996) on critical success factors, they grouped these factors into four areas: factors related to the project; project manager and the team members; the organization and the external environment. A study by Fiberesima and Abdul Rani (2011) on critical success factors in oil and gas project portfolio in Nigeria, they showed in their findings that, thirteen critical success factors are of high importance within the deepwater oil and gas project portfolio management. Hajiagha et al (2016) in their study of critical success factors in oil and gas petrochemical projects, they identified five critical success factors.

Significant efforts were also directed towards comparing the multitude of factors with the purpose of arriving at a definitive list. A comprehensive study was conducted by Fortune and White (2006), who reviewed sixty-three publications on critical success factors (CSFs). Although many researchers have proposed various critical success factors, there is no general agreement. Table 1, shows summary of critical success factors (CSFs) from the seven literature reviews discussed in this research paper.

RESEARCH METHODOLOGY

The potential critical success factors that can be used to increase the chances of a project success were identified from literature review. These CSFs formed the basis for the questionnaire, which was used to seek the opinion of project practitioners; representing clients, consultant and contractors in the Libyan oil and gas sector on the degree of importance of the critical success factors. Through data collection and analysis, the relative importance of the critical success factors was identified using the Relative Importance Index (RII).

Critical Success Factors and Questionnaire Design

A set of 30 critical success factors were initially obtained from the literature reviews of previous studies. These factors formed the basis of the questionnaire survey. The questionnaire consists of two sections. The first section elicits information on the respondents' background, while the second section consists of questions related to the critical success factors. In order to test the clarity and comprehensiveness of the questionnaire, a pilot survey was conducted in Libya with twenty oil and gas professionals, including clients, consultants and contractors. To insure the validity of the questionnaire, it was discussed with experienced oil and gas project practitioners in the Libyan oil and gas sector, whose opinions were duly incorporated. Internal consistency of the data reliability analysis was achieved by employing Cronbach's Alpha coefficient and analysis of the data was done using Statistical Package for the Social Sciences (SPSS). Cronbach's Alpha reliability coefficient ranges from 0 to1. The closer the coefficient value to 1, the greater is the internal consistency of the data (Tsiga et al, 2017; Cronback, 1951). Cronbach's Alpha coefficient for each field of the questionnaire is 0.949, this is considered high, and the result is ensuring the reliability of each field of the questionnaire. Thereby, it can be said that it is proved that the questionnaire is valid, reliable, and ready for distribution.

The questionnaire survey was carried out in Libya in the beginning of 2017. One hundred and twenty (120) questionnaires were administered to experience project practitioners; including clients, consultants, and contractor. These experienced practitioners are working in oil and gas companies that were recommended by National Oil Corporation (NOC), as part of the most important companies, which have great experience in oil and gas projects in Libya. The respondents were requested to indicate their views on the importance of each of the critical success factors. They were asked to use five-point Likert Scale ranging from 1 to 5, where 1-represents strongly agree, 2-agree, 3-not sure, 4-disagree and 5- strongly disagree. Out of the 120 distributed by hand, eighty-eight (88) were received back. Therefore, the response rate was 73.33%.

Table 1. Summary of critical CSFs from the seven literature reviews.

Critical Success Factors \ Source	Slevin et al.	Kerzner	Hauptfleisch et al.	Belassi et al.	Fiberesima et al.	Hajiagha et al.	Fortune et al.
Support from senior management	√			√			√
Clear realistic objectives							√
Strong detailed plan kept up to date							√
Good communication and feedback	√		√		√		√
User and client involvement							√
Stakeholder management			√				
Skilled, suitably qualified team				√			√
Effective change management							√
Competent project manager				√			√
Strong business case and sound basis for project							√
Sufficient and well allocated resources					√		√
Good leadership		√	√				√
Proven and familiar technology							√
Realistic schedule					√		√
Risks addressed, assessed and managed			√				√
Project sponsor and champion				√			√
Effective monitoring and control	√	√	√				√
Adequate budget							√
Organizational adaptation, culture and structure			√	√			√
Good performance by suppliers, contractors and consultants							√
Planned close down, review and acceptance of possible failure							√
Training provision							√
Political stability in the country				√			√
Correct choice of project management methodology and tools							√
Environmental influences							√
Past experience			√				√
Project size, level of complexity and duration				√			√
Appreciating different viewpoints							√
Contractor's capability to manage the project					√		
Innovation			√				

Data Analyzes Tools

The data collected were analyzed with the aid of SPSS. Descriptive statistics were used to analyze the respondents' profiles using SPSS, whereas, Relative Importance Index (RII) used to rank the critical success factors as well. The RII for each critical success factor is calculated using the formula (1) below (Tsiga et al, 2017):

$$RII = \frac{\sum X}{Y*Z} \ (0 \leq RII \leq 1) \quad (1)$$

Where X; is the weight given to a factor by a respondent, in the range of 1 to 5. Y; is the highest score available (5 in this case) and Z; is the total number of respondents that have answered the question.

RESULTS AND DISCUSSION

The results of this research indicate that 48.86% of the respondents come from client companies, 27.27% from contractor companies and 23.86% from consultant companies. The respondents are experienced, with 56.97% having project management experience of 11 years or more. The respondents are very well educated, the highest academic qualifications of the respondents ranging from Higher National Diploma (HND) to Doctor of Philosophy (PhD). About 53.4% having Bachelor of Science (BSc) and 39.7% possess Master of Science (MSc) as their highest academic qualifications. This suggests that they understood the questionnaire, its subject matter, and its intended purpose, so, they were more objective and truthful in their responses. Therefore, and based on their project practitioners background, academic qualifications and experience, the respondents were able of providing reliable information. Table 2, presents summary of the respondents' profile.

Relative Importance Index (RII)

The main purpose of this step is to identify the appropriate critical success factors that can be used to increase the chances of oil and gas project success in Libya. From the perspective of the clients, consultants and contractors, all thirty critical success factors identified in the literature reviews were significant in the Libyan oil and gas sector, as all had RII scores above 0.7. However, the different categories of respondents seem to have different views about the most important CSFs as shown in Table 3.

Table 3, clearly illustrates that most of the respondent ranked good leadership first with (RII = 0.9535), followed by support from senior management with (RII = 0.9326); good communication and feedback was ranked the third with (RII = 0.9256), and skilled, suitably qualified team and political stability in the country, which ranked the fourth with (RII =0.9233), the fifth factor was strong detailed plan kept up to date with (RII = 0.9116). The effective monitoring and control was ranked the sixth with (RII= 0.9093); competent project manager and contractor's capability to manage the project was ranked the seventh and the eighth with (RII = 0.9070) and (RII = 0.8930), respectively. Risks addressed, assessed, managed, which was ranked as ninth with (RII = 0.8837) was followed by realistic schedule with (RII = 0.8791). Fig. 1, clearly show the ten most important critical success factors in the Libyan oil and gas projects.

In contrast with the literature review, good leadership was identified as an important critical success factor by Kerzner (1987) and Fortune and White (2006), the fact that good leadership is a tool for project managers to help achieve success. Dulewicz and Higgs (2005) emphasized that project managers who have an understanding of leadership are more likely to lead the project to success. As well as, support from senior management also identified as an important critical success factor as was suggested by Slevin and Pinto, 1986; Belassi and Tukel (1996) and Fortune and White (2006). Young and Jordan (2008) stated that the top management should make enough time to be aware of the project status and to intercede as necessary, and the time spent should be in proportion to the cost and potential of the project.

Good communication and feedback and skilled was identified as an important critical success factor by Slevin and Pinto (1986) and Fortune and White (2006). Political stability in the country was identified as an important critical success factor, and has the highest rank by respondents, this is likely due to the current political situation in Libya. Libya has been going through civil unrest that started in 2011, which caused damage to many of its oil and gas facilities and curtailed crude oil and production significantly. Elhoush and Kulatunga (2017) pointed out that due to the current risky and unsecured situation in Libya, risk management in the oil and gas sector should be prioritized.

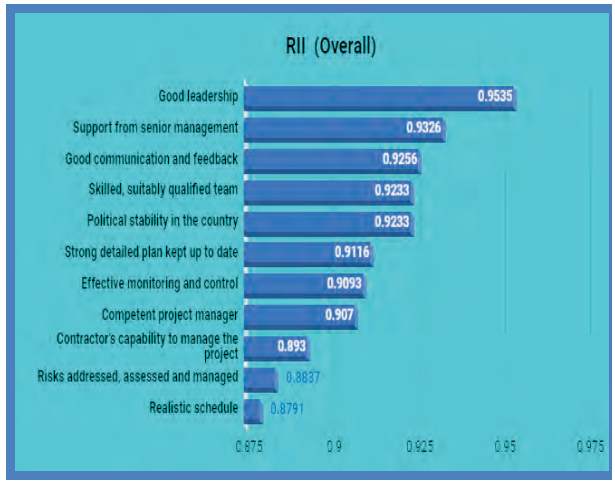


Fig. 1. The overall of most important CSF in oil and gas projects in Libya.

Table 2. Summary of respondents' profile.

Critical Success Factors	RII Client	Rank	RII Consultant	Rank	RII Contractor	Rank	Overall RII	Overall Rank
Good leadership	0.9581	1	0.9429	2	0.9182	2	0.9535	1
Support from senior management	0.9209	3	0.8857	6	0.8727	6	0.9326	2
Good communication and feedback	0.9209	3	0.9524	1	0.9000	4	0.9256	3
Skilled, suitably qualified team	0.9116	4	0.9429	2	0.9273	1	0.9233	4
Political stability in the country	0.9256	2	0.9333	3	0.9091	3	0.9233	4
Strong detailed plan kept up to date	0.8930	6	0.9143	4	0.9091	3	0.9116	5
Effective monitoring and control	0.8884	7	0.9143	4	0.8455	8	0.9093	6
Competent project manager	0.9209	3	0.9429	2	0.8818	5	0.9070	7
Contractor's capability to manage the project	0.9116	4	0.8762	7	0.8727	6	0.8930	8
Risks addressed, assessed and managed	0.8744	9	0.9333	3	0.8091	10	0.8837	9
Realistic schedule	0.8419	13	0.8667	8	0.8818	5	0.8791	10
Clear realistic objectives	0.9070	5	0.8857	6	0.8091	10	0.8767	11
Good performance by suppliers, contractors and consultants	0.8791	8	0.8667	8	0.8727	6	0.8744	12
Adequate budget	0.8791	8	0.9048	5	0.8091	10	0.8674	13
Sufficient and well allocated resources	0.8698	10	0.9048	5	0.8636	7	0.8651	14
Strong business case and sound basis for project	0.8930	6	0.8476	9	0.7818	11	0.8535	15
Correct choice of project management methodology and tools	0.8605	11	0.8286	11	0.8455	8	0.8465	16
Past experience	0.8233	14	0.8667	8	0.8182	9	0.8465	16
Proven and familiar technology	0.8233	14	0.8381	10	0.8727	6	0.8395	17
Training provision	0.7814	16	0.8286	11	0.8182	9	0.8023	18
Project size, level of complexity and duration	0.7674	18	0.8000	13	0.8455	8	0.7953	19
Environmental influences	0.7767	17	0.8381	10	0.7727	12	0.7907	20
Effective change management	0.7767	17	0.8286	11	0.7727	12	0.7860	21
Organizational adaptation, culture and structure	0.7860	15	0.7905	14	0.7364	14	0.7791	22
Stakeholder management	0.7674	18	0.7714	15	0.7091	15	0.7767	23
Planned close down, review and acceptance of possible failure	0.7674	18	0.8095	12	0.7545	13	0.7744	24
Innovation	0.7442	20	0.8286	11	0.7727	12	0.7721	25
Appreciating different viewpoints	0.7535	19	0.7905	14	0.7545	13	0.7628	26
Project sponsor and champion	0.7442	20	0.7714	15	0.7091	15	0.7419	27
User and client involvement	0.8465	12	0.8667	8	0.7818	11	0.7302	28

Table 3. Relative importance index (RII) of 30 factors.

Companies	%
Client	48.86
Consultant	23.86
Contractor	27.27

Qualification	%
HND	4.55
BSC	53.41
MSC	39.77
PHD	2.27
Other	0

Experience (years)	%
1-5	13.95
6-10	29.07
11-15	16.28
16-20	13.95
Above 20	26.74

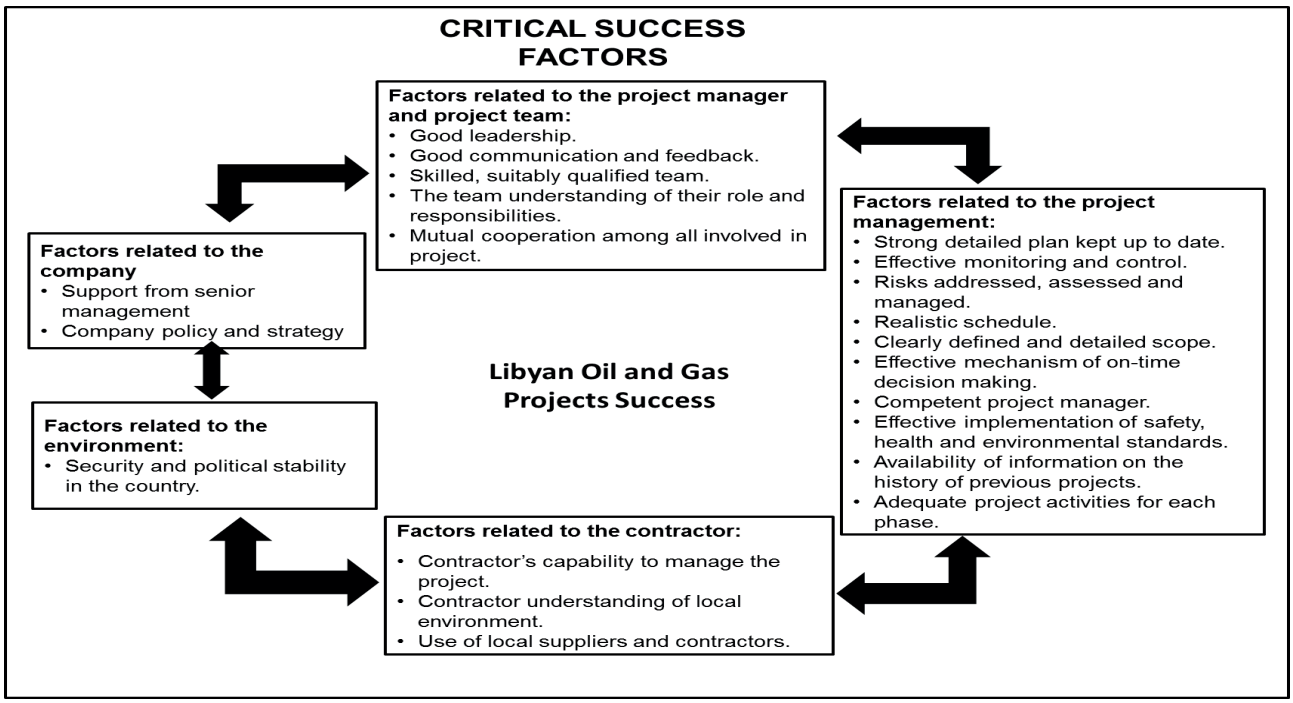


Fig. 2. The critical success factors to deliver oil and gas projects success in Libya.

Interviews

Following the analysis of the questionnaire survey results, interviews were conducted with experts in the Libyan oil and gas projects to validate the results of this research and to add any uncounted for critical success factors in the initial questionnaire survey. Semi-structured interviews were conducted based on the results of the initial survey. Eight interviews invitations were distributed by hand, out of the eight distributed, five were participated. Interviewees were selected carefully to ensure that they were experienced and professionals in their respective fields with a minimum of fifteen (15) years' experience.

Interviewees agreed with the outcome of the analysis of this research that the top ten CSFs identified for Libyan oil and gas projects and they added eleven more of CSFs: namely;

- Clearly defined and detailed scope;
- Effective implementation of safety, health and environmental standards;
- Cooperation among all involved in project;
- The team understanding of their role and responsibilities;
- Contractor understanding of local environment;
- Use of local suppliers and contractors;
- Effective mechanism of on-time decision making;
- Company policy and strategy;
- Availability of information on the history of previous projects;
- Adequate project activities for each phase, and
- Security and political stability in the country.

In fact, two interviewees commented that "security and political stability in the country" is more suitable as CSF than "political stability in the country". The results from the questionnaire survey and interviews were divided into five groups of critical success factors: namely;

1. Factors related to the company;
2. Factors related to the project management;
3. Factors related to the project manager and project team;
4. Factors related to the contractor and
5. Factors related to the environment.

These factors are critical inputs to achieve project success. Fig. 2 demonstrates the critical success factors identified in this research to deliver oil and gas projects successfully in Libya.

CONCLUSIONS

Oil and gas companies in Libya can use critical success factors to improve their project performance management, since complexities

of project management present some challenges for the success of projects in these companies. Identifying critical success factors are very important for effective project management, as well as the improvement in the critical success factors will give better results in project management success in oil and gas projects. Results indicate that the twenty-one CSFs were identified as critical success factors in Libyan oil and gas projects. These critical success factors have been grouped into five groups of critical success factors as was stated earlier, factors related to the company, factors related to the project management, factors related to the project manager and project team, factors related to the contractor, and factors related to the environment.

The most important CSFs are related to project management, project manager and project team, so oil and gas companies should have sustainable training programs in the specialist knowledge of project management and in training of soft skills. It is important to understand and implement these factors for oil and gas project management success in Libya.

ACKNOWLEDGMENTS

The authors are thankful to the Mabruk Oil Operations Company and the anonymous reviewers for their constructive feedback on this research.

REFERENCES

Al-Ageeli, H. and Alzobaee, A. (2016). Critical Success Factors in Construction Projects: *Governmental Projects as A Case Study. Journal of Engineering,* **V. 22(3)**: 129-147.

Alias, Z.; Zawawi, E.; Yusof, K. and Aris, N. (2014). Determining Critical Success Factors of Project Management Practice: *A Conceptual Framework. Procedia-Social & Behavioral Sciences,* **V. 153**: 61- 69.

Amade, B.; Ubani, E.; Omajeh, E. and Anita, A. (2015). Critical Success Factors for Public Sector Construction Project Delivery: A Case of Owerri, Imo State. *International Journal of Research in Management, Science & Technology,* **V. 3(1)**: 11-21.

Baccarini, D. (2009). Critical Success Factors in Construction Engineering Projects: A Case Study. *Proc. AIPM Conf.*: 1-14.

Badiru, A. and Osisanya, S. (2013). Project Management for the Oil and Gas Industry: A World System Approach. Chapter 10: Managing Construction Projects in Oil and Gas, *Taylor & Francis Group, London*: 273-390.

Belassi, W. and Tukel, O. I. (1996). A New Framework for Determining Critical Success/Failure Factors in Projects. *International Journal of Project Management,* **V. 14(3)**: 141-151.

Cronback, L. (1951). Coefficient Alpha and the Internal Structure of Tests. *Psychometrika,* **V. 16(3)**: 297-334.

Daniel, R. (1961). Management Information Crisis. Harvard Business Review, **V. 39(5)**: 111-121.

Dvir D.; Lipovetsky S.; Shenhar A.; and Tishler A. (1998). In Search of Project Classification: *A Non-Universal Approach to Project Success Factors. Research Policy,* **V. 27**: 915–935.

Dulewicz, V. and Higgs, M. (2005). Assessing Leadership Dimensions, Styles and Organizational Context. *Journal of Managerial Physiology*, **V. 20(2)**: 105-123.

Elhoush, R. and Kulatunga, U. (2017). The Effectiveness of Project Risk Management: A Study within the Libyan Oil and Gas Industry. *13th International Postgraduate Research Conference (IPGRC), University of Salford, UK.*

Els, M.; Merwe, V. and Hauptfleisch, A. (2012). Critical Success Criteria and Success Factors in Project Management: A Quest to Enhance Generic Professional Practice. *International Cost Engineering Council 8th World Congress, Durban, South Africa*: 23-27.

Fiberesima, D. and Abdul Rani, N. (2011). An Evaluation of Critical Success Factors in Oil and Gas Project Portfolio in Nigeria. *African Journal of Business Management,* **V.5(6)**: 2378-2395.

Fortune, J. and White, D. (2006). Framing of Project Critical Success Factors by a Systems Model. *International Journal of Project Management,* **V. 24(1)**: 53-65.

Hajiagha, S.; Shokouhinia, M. and Hashemi, S. (2016). Success Criteria in Oil, Gas and Petrochemical Projects. *Proc. EMIE Conf.*: 182-187.

International Energy Agency (2007). *World Energy Outlook. Executive Summary, China and India Insights, Paris*: 1-21.

Iram, N.; Khan, B. and Sherani, A. W. (2016). Critical Factors Influencing the Project Success: An Analysis of Projects in Manufacturing and Construction in Pakistan. *Arabian Journal of Business and Management Review*, **V. 6(2)**: 20-22.

Kerzner, H. (1987). In Search of Excellence in Project Management. *Journal of Systems Management,* **V. 38**: 30-40.

Müller, R. and Jugdev, K. (2012). Critical Success Factors in Projects: Pinto, Slevin, and Prescott- the Elucidation of Project Success. *International Journal of Managing Projects in Business,* **V. 5(4)**: 757-775.

Munns, A. and Bjeirmi, B. (1996). *The Role of Project Management in Achieving Project Success. International Journal of Project Management,* **V. 14(2)**: 81-87.

Omer, H. (2017). Assessment of Projects Using Key Performance Indicators in Oil and Gas Companies. Unpublished MSc Thesis, Engineering Management, University of Tripoli, Tripoli, Libya: 1-164.

Pinto, J. and Slevin, D. (1988). *Project Success: Definitions and Measurement Techniques. Project Management Journal,* **V. 19(1)**: 67-72.

PMBOK, (2018). *A Guide to the Project Management Body of Knowledge. 6thed, Project Management Institute, Pennsylvania, USA*: 1-569.

Rockart, J. (1979). Chief Executives Define their Own Information Needs. *Harvard Business Review*, **V. 57(2)**: 81-92.

Rockart, F. and Treacy, E. (1981). Executive Information Support Systems. *CISR Working Paper,* (65): 1-43.

Shuen, A.; Feiler, P. and Teece, D. (2014). Dynamic Capabilities in the Upstream Oil and Gas sector: Managing Next Generation Competition. *Energy Strategy Reviews,* **V. 3**: 5-13.

Silva, G.; Warnakulasuriya, B. and Arachchige, B. (2016). Criteria for Construction Project Success: A Literature Review. 13th Intern. Conf. on Business Management: 697-717.

Slevin, D. and Pinto, J. (1986). The Project Implementation Profile: *New Tool for Project Managers. Project Management Journal,* **V. 17(4)**: 57-70.

Srimathi, S.; Dinesh, S. and Sethuraman, R. (2017). A Review on Critical Success Factors in Construction Project. *International Journal of Scientific Research in Science, Engineering and Technology,* **V. 3(2)**: 478-478.

Tsiga, Z.; Emes, M. and Smith, A. (2017). CSFs for Projects in the Petroleum Industry. *Proc. ProjMAN Conf.*: 224-231.

U.S. Information Administration (2015). *Country Analysis Brief: Libya*: 1-12.

Young, R. and Jordan, E. (2008). Top Management Support: Mantra or Necessity. *International Journal of Project Management,* **V. 26(7)**: 713-725.

A FRAMEWORK FOR ENHANCING THE DECISION MAKING PROCESSES TO DEVELOP OIL AND GAS FIELDS WITHIN SOME LIBYAN OPERATING OIL AND GAS COMPANIES

Hanan Zawam Aburas* and Dr. Rajab Abdullah Hokoma**

Abstract: Decision Making Process (DMP) is considered to be as a set of connected steps, adapted to accomplish desired objectives within any organization. This paper aims to develop a framework for enhancing the DMP within some Libyan oil and gas operating companies. Required data were gathered through an intensive literature-review, personal interviews, and an intensive questionnaire. Based on data analysis, the main findings indicated that the procedures being used for making decisions related to developing oil and gas fields need to be seriously improved, well-documented, and should be designed for enhancing the quality of the DMP. One of the challenges that confronted DMP is found to be the required time for gathering and analyzing the data to make the proper decisions. For developing the framework, PDCA cycle was used, containing four phases; each curtained steps to achieve the desired goals. The framework seeks to enhance the decisions' quality in order to improve the performance throughout practicing the most effective tools and advanced techniques within this business area.

Keywords: Decision making Process, developing oil and gas fields, PDCA-cycle.

INTRODUCTION

DMP is a debatable issue for several oil and gas companies; it diverges from a company to another depending on the desired resolution and time needed to achieve targeted goals. Making a decision is a vital and difficult task for the management body; as the decision is a choice between alternatives in pursuit of objectives, where no alternatives exist no decision can be made.

In the area of making decisions specifically in the oil and gas industry, the DMP is not only a matter of having the right data or the right tool; it is an integrated approach that could be utilized.

This paper is carried out to develop a framework of DMP for developing oil and gas fields via adopting the most common tools and techniques that could be practiced to enhance decisions' quality.

*Geosciences & Reservoir Department, Mellitah Oil & Gas B.V. Libyan Branch, Email: hanan.aburas@yahoo.com
**Mechanical & Industrial Engineering Department, Faculty of Engineering, University of Tripoli, Libya, Email: r.hokoma@uot.edu.ly

An Overview of DMP within Oil and Gas Industry

It was realized that the DMP is not an easy task; as it is permeated by some complexities in the absence of required information and tools that are used for data analysis. The procedures for making decisions within most participated Libyan operating oil and gas companies could be considered as the most crucial for improving the quality of the DMP, followed by the used tools and techniques. Whereas, communications as a factor influencing the processes of making decisions is found to be at the lowest level throughout the entire decision making processes (Hokoma & Aburas, 2018).

The steps for making a decision are not independent or separate from each other as they are linked and connected. In other words, what occurs at a certain stage directs procedures and defines what occurs in the succeeding stages. Each alternative of the suggested solutions has to be evaluated separately by comparing the potential outcomes and selecting what is the most beneficial against time, cost, value of information, potential applications, safety and security perspectives Frefer (2014).

Several oil companies spend up to eighteen months in decision cycle-gathering data, analyzing information and modeling risk and uncertainty before selecting the proper production system (Ellen et al, 2001). In respect of production plan, Hokoma (2016) stated that Just-In-Time (JIT) techniques should be considered as the proper production planning and quality enhancement techniques within the Libyan oil and gas industry. It was concluded that the management body within the said industry does not have a clear strategy towards most areas that are considered as being crucial in any successful implementation of JIT techniques. Additionally, some challenges were also being pointed-out for the decision-makers to be aware of, while implementing JIT systems within the industrial environment.

In respect of different types of decisions, decision making is located between three dimensions; certainty, risk, and uncertainty. The risk is the probability of an undesirable outcome and uncertainty is the inability to predict future events. Both risks and uncertainties inherent in oil and gas industry investment that are larger at the exploration stage, but they are reducing through appraisal and development stages. It is often forgotten that the goal is to make good decisions which will lead to better outcomes, not to reduce uncertainty (Bratvold, 2012).

Frefer (2014) referred that the scientific method for making decision involves six steps. However the process is varying from one to another, and to determine whether a decision is "good" or not, it should be focused on the process of making the decision rather than the outcomes of the decision.

Bickel & Bratvold (2008) focused on an upstream oil and gas industry, and stated that the decision making taxonomy involves four different elements: complexity, task constraint, ambiguity and the information structure of the environment. However, there is no such standard taxonomy or classification scheme for making decisions. Adding to that, due to the highly complex nature of the oil industry, a single person rarely has sufficient information to make a decision, hence a group decision is very essential to make an effective decision. Moreover, it was complained that several engineers do not believe, there is enough time to follow a decision analysis approach. Consequently, companies have a challenge finding time for value creating activities. One way to address this concern is to make sure that process adds value and working on the right things at the right time.

In respect of technology and decision analysis in reservoir management, using technology & techniques to support making decisions usually costs. Thakur (1995) stated that any development of new reservoir management technology and its applications must be subjected to a thorough economic screening. However, using and supporting such a technology is justified based upon business needs.

In a strategic reservoir planning which is necessary for developing and managing oil producing asset. Gerbacia & Al-Shammari (2001) have debated that making decisions involve uncertainty parameters, such as economic factors and production potentials lead to uncertainties in predicting results as often uncertainties in the planning parameters are not recognized. Therefore, multi criteria decision making is required to identify the most influenced parameters that influence making decisions. Several attempts have been adopted to determine the proper procedures of making decisions, and how to follow-up the process. For enhancing the decisions' quality, the processes should be developed and improved continuously using the most advanced techniques and tools, sharing new ideas and learning from fault decisions which could be considered as an essential success factor for any organization (Hokoma & Aburas, 2018).

Aburas (2018) stated that several factors usually influence the quality of DMP within many companies, a many of them are procedures that has big impact, followed by with less contribution communications and tools/techniques. This relatively true to the real world as the decision is made regardless involving the whole team and using simple tools.

Parakash (2012) stated that, there is a strong correlation between process, people and technology for processing making good decisions. Therefore building and integrating approaches towards DMP should be considered as an important aspect for creating a strong decision support system. Goren and Taylor (1978) described the correct process for making decisions on large projects in the North Sea were subject to an undetected scale effect which resulted in their getting off-schedule and over-budget. An effective organizational set-up and suggest that a management scheme should include a "feedback" function which will form the basis for top level decision making and will enable the project managers to exercise control over their project.

METHODOLOGY AND DATA COLLECTION

The data were being gathered through literature reviews, direct observations, a survey questionnaire and some personal interviews; all used for gathering the required data to investigate the conducted DMP within the targeted companies.

The population size was acquired from expertise in each participated company. Sampling is chosen to shorten the time, effort and to determine the lower limit of the population sample. The sample size for this survey was calculated. 237 hard copies were distributed and a total of 216 were returned, giving a response rate of 91%.

DATA ANALYSES AND DISCUSSION

As a first stage for analyzing the gathered data, a reliability test (Cronbach's Alpha) was applied to examine the internal consistency of the entire questionnaire, and was equal to 0.839, giving a strong evidence that the questionnaire is stable and reliable enough to be analyzed.

The analysis was performed using the Statistical Package for the Social Sciences (SPSS), and it was found that who dominate the seniority managerial levels and involved in the DMP are mostly men (85%). Approximately above 90 % of the participants are well-highly qualified with BSc & MSc. degrees (Aburas, 2018). This leads to the availability of qualified people in the participated companies within almost all the related departments. The diversity in managerial levels that were participating in this study are shown in Table (1).

Table 1. The participated managerial levels.

Managerial levels	Frequency	%
Manager	32	14.8
Superintendent	29	13.4
Coordinator	42	19.4
Supervisor	14	6.5
Team Leader	4	1.9
Specialist	23	10.6
Senior	63	29.2
Other	9	4.2
Total	216	100.0

The researchers investigated the issue of how many steps of DMP are carried out in the participated companies. Table (2) shows most participants (70.8%) don't know how many steps are used for conducting the DMP in their companies. This might refer to absence of having clearly documented DMP. About 15% of participants stated that the steps of making a decision are less than four. Observingly, it was found out that some participants had just provided a rough number which might be inaccurate, meaning that the procedures of making decisions are not well-defined in their workplace.

The availability of using any specific processes in making decision for developing oil and gas fields was also investigated. Table (3) shows most participants (45.8%) don't know if there is any specific process of DMP and 19.4% of participants stated that there is no such specific process. Despite the fact that only 16.7% of participants said "Yes", but the process was unclearly provided in this study. Few participants (18 %) preferred not to provide any answer.

Proceeding to the previous discussion, some participants stated that Brain Storming technique and Decision Tree Analysis are considered as techniques and tools of DMP. Others stated the time, quality, accuracy and cost should be taken into considerations when making decisions. Besides the process of decision making is subject to the specialist to provide the conceptual basic details such developing oil and gas fields with including risk analysis. Another way of processing the decision making starts with gathering data, analyzing, screening, delivering draft report and then a final report is accepted. All in all, it was observed that past experience and key learning are being widely used in the DMP for developing oil and gas fields.

According to the statistical results and throughout reviewing the literature of DMP principles along with some used tools/techniques it can be seen that, each department has its own way to make an effective decision, and there is no specific process to make a particular decision; as some of the procedures have been inherited from previous experienced ones. One more thing, from close observations with the participants, using simple tools/techniques with less cost and more reliably are preferred to be used in the DMP.

Table 2. Number of steps conducting in the participated companies.

DMP steps	<= 4	5	6	7	8	9	10	11	>14	Don't know
As seen by participants, %	15.3	6.9	2.3	1.4	0.5	0.5	0.5	0.5	1.4	70.8

As a result, improving the quality of making decisions for developing Oil and Gas fields, requires to use different simple, understandable techniques and tools such as Brain Storming technique, (Plan, Do, Check and Action) PDCA cycle (comprehensible and simple cycling), Decision Making Matrix and feedback process. Adding to that; taking into account other factors that may influence making decision such as culture and policy of the company.

SUGGESTED FRAMEWORK FOR DEVELOPING OIL AND GAS FIELDS

Several processes of making decisions are being used in oil and gas industry have been adopted to meet corporate goals. The PDCA Cycle is broadly used to enhance the DMP quality more efficiently as it consists of four phases (Plan, Do, Check and Action); it is a circle with no end, and it should be repeated again and again for seeking continuous improvement, and each phase has certain steps, and between each phase there is a Decision Gate (DG) to go through to confirm and agree the outcomes of phase to move into the next phase, and so on. The suggested framework is illustrated in Fig. 1.

To be in mind, it is believed that the culture intervention (human factor) as well as government policy and country regulations should be taken into considerations when making decisions. The framework of DMP is illustrated and started with the following:

Phase I (Plan)

Establishing the main strategic and desired objectives of any organization should be achieved first throughout conducting several meetings among related departments; involves professional members who are being selected from reservoir engineers, operating engineers, drilling engineers, project engineers, economist, environmental, and anyone related to the project of developing oil and gas fields. The Decision Making matrix should be utilized to identify criteria of making decisions, which can be considered as an essential part in achieving the overall aspect, such as (economic, environment, political, and technological factors). The suggested DMP should employ the Brain Storming qualitative technique, throughout the DMP.

Table 3. Used process in making decisions.

Availability of specific process of DMP	Yes	No	Don't know	Prefer not to say
As seen by participants, %	16.7	19.4	45.8	18.1

Phase II (DO)

This section identifies 3 steps of the DMP to investigate and predict the reservoir performance for developing oil and gas fields.

1. Data Collection: It includes gathering the related data as; Rock and fluid data, special core analysis, well logs, the production history of the field, the entire reservoir description and a reliable existed 3D dynamic reservoir simulation model.

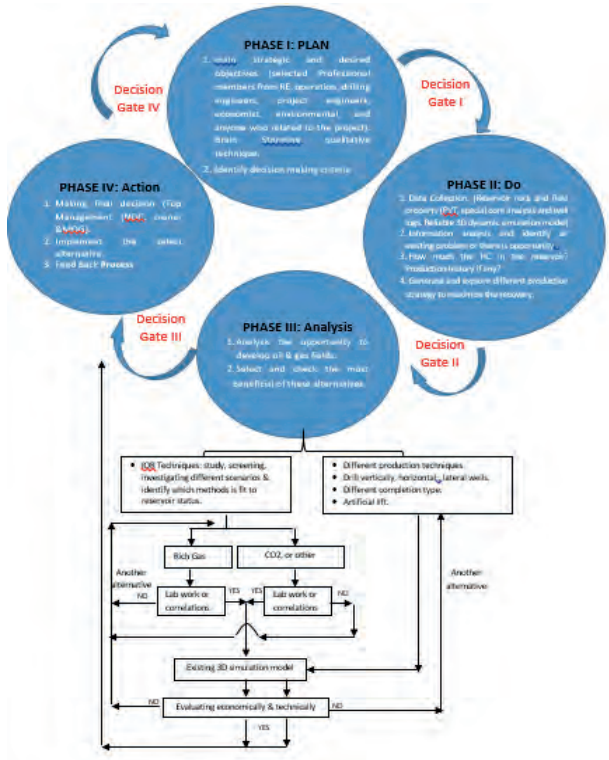


Fig. 1. Framework DMP for oil and gas fields.

2. Identify an existing problem and analysis the information: Making a decision is called a problem solving process that eliminates barriers to company goal attainment. The first step in this elimination process is identifying precisely what the problems or opportunities are that assist developing such fields. The gathered information should be analyzed in qualitative and quantitative perspective and representing in a meaningful way so that the relationships between varieties of data/ information can be detected.
3. Generate and explore alternatives: Key staff should list various possible solutions/alternatives. Then developing an action plan in order to address any obstacles/barrier that may prevent achieving the required goals. There are different production technologies to prolong the field life. For instance, in the late stage of developing oil and gas field, planning of Enhance Oil Recovery (EOR) projects may require in which involving a multiple hurdle decision making task; procedures to be undertaken in planning EOR projects is a conducted preliminary screening process and selecting the appropriate EOR techniques. Reservoir description involves reviewing comprehensively by a team of geologist, geophysicist, petrophysicist, drilling and completion engineer and reservoir engineer and to reach a total understanding of the reservoir and its performance. Then gather needed laboratory and field data and followed by field pilot testing to examine the performance of choosing a technique, which all need to be modeled and duplicated mathematically by numerical reservoir simulation, followed by performing technical/economic feasibility report.

Phase III (Check and Analysis)

This section identifies one step of the DMP. After fully understanding the entire reservoir status and the related issue, examining the possible optimum production strategy should be investigated.

4. Check and Select the most beneficial of these alternatives: Each alternative has to be evaluated separately comparing against potential outcomes, constraints, assess the risks associated with the optimum solution. Decide carefully which alternative will be implemented according to proposed decision making criteria.

A different strategic plan should be defined and different production forecasting scenarios for subjecting reservoir should be created by using existing 3D dynamic reservoir simulation tool. After acquiring the results, the risk and economic analysis should be performed accordingly. The SWOT analysis tool is valuable in this stage to investigate the strength, Weakness, Opportunity and threats of the chosen solution. Financial decision is quantitative analysis tool, deciding, whether to pass forward or stop at this stage or re-evaluate and addressing a new possible option.

Break-even analysis is used, to determine when an option becomes profitable, whereas, the Net Present Value (NPV) is an indication of how much the project will earn in comparison to putting the money in a bank that offers an interest rate equals the discount rate. Besides, Cash flow forecasting, to forecast the impact of a financial decision. The evaluation stage is significant; it is considered as it is a beginning of gaining experience/ learning to enhance the performance of making decisions in hereafter. The main decision criteria are, operational profit, project reliability, working environment, personnel safety, risk to the environment and total project cost (Thakur, 1995).

The decision making cannot be completed unless measure and assess the entire results, and which is always determined by an interactive technical and economic feasibility criterion.

Phase IV (Action)

In this phase, including two steps; implementing the selected alternative and feedback process as follows:

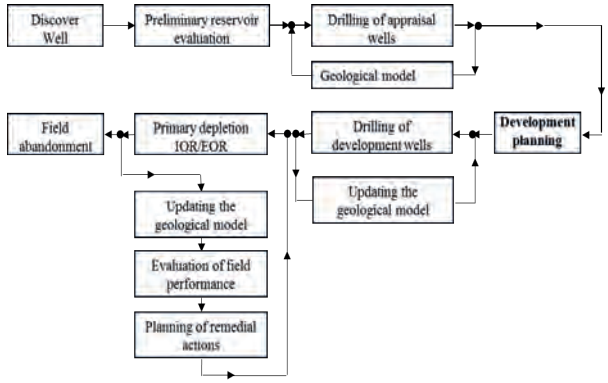


Fig. 2. Reservoir management feedback system.

5. Implement the selected alternative: This step is to put the selected alternative into the implementation stage. The implementation plan is required and containing important issues; for instance required actions to achieve the goal, create a time scale (Schedule), ways to reduce the risks to a minimum, and a remedial action should be involved in case of non-functioning of any stage as a contingency plan.
6. Feed Back Process: it is very important step; as after selecting the implemented alternative, decision makers must gather feedback to determine the consequences negatively/ positively of the implemented alternative. If the identified problem is not being solved, managers need to seek out and implement some other alternatives instead. The learning feedback system is shown in Fig. 2, as adopted by Chierici (1990).

To acquire reliable reservoir information, it should be taken into account periodically run numerical reservoir simulation model. Each step should be validated by the dynamic simulation model against actual reservoir behavior. Therefore, the feedback system should be developed with reservoir management requirements.

For each previous phase, a decision has to be taken to proceed the following phase. Eventually, after recommending the proper production strategy for developing a certain oil and gas fields, the National Oil Corporation (NOC); the company which controls and handles the oil and gas industry (upstream and downstream) exclusively make a decision at the end.

In respect of reservoir management, to be more successful managed, there was a study (Chierici, 1990) identified elements of successful reservoir management teams, the main ones as follows:

1. Cross-functional team, and empowerment and reduced routine supervision.
2. Minimum individual technical reviews by functional heads in favor of joint reviews.
3. Informal communication and clarification of priorities and periodic project reviews.
4. Quick approval process making a decision by all team members, technology transfer between various teams, and well-trained and highly motivated individuals.
5. Frequent office staff visits to the subject area and creation of interests regarding the reservoir performance among the field operators and supervisors.
6. Comprehensive and cost-effective surveillance and management program, well planned data collection and management program, and
7. Innovation and risk taking by integrating a new technology into the reservoir management program to maximize profitability and economic recovery.

CONCLUSIONS

The paper makes a contribution by developing a framework of decision making processes for developing oil and gas fields within some Libyan operating oil and gas companies which their operations' management systems are limited and governed by two parts, the owner and NOC.

After intensively investigating the conducted DMP within the surveyed companies, some concluding remarks are illustrating as following:

- There is an integrated work between relevant departments (Geology/Geoscience, petroleum, reservoir, production, and process operation specialists) to be employed intensively in the DMP for developing oil and gas fields.
- The reservoir dynamic simulation tool is considered crucial to assist decision makers in developing oil and gas fields and used mainly in the reservoir department. Hence the simulation tool is recommended to generate different scenarios of production strategies of such fields.
- Experience and practices in making decisions in similar situations help managers to make occasional decisions without going through an (a-to-z) of the DMP, as most of made decisions are regularly intuitive decisions; in other words, it is based on experience in such similar situations.
- It was realized that the decision environment within the business area is controlled by the top management body within the related companies.
- Clear procedures for making decisions within the related companies should be adopted more effectively.
- NOC is always seeking to improve the quality of making decisions to obtain valuable resolutions, and paying serious attentions for improving the whole situations.

To sum up, it is recommended to adapt the developed DMP framework for developing oil and gas fields to enhance the quality of making decision and to meet the management requirements. Furthermore, a working team approach and

integrated advanced technology should be used to seek for leading a successful reservoir management.

ACKNOWLEDGMENT

The authors would like to thank Reserves Development Department, NOC, and they also appreciate the participation and support of all the surveyed Libyan operating oil and gas companies.

REFERENCES

Aburas, H. (2018). Decision Making Process for Developing BAHR ESSALAM Field, Concession NC41, North West, Offshore, Libya. *Unpublished MsC Thesis*, Engineering Management Department, Faculty of Engineering, University of Tripoli, Libya: 120p.

Bickel, J. and Bratvold, R. (2008). From Uncertainty Quantification to Decision Making in the Oil and Gas Industry. *Energy Exploration & Exploitation*: **V. 26**: 311-325.

Bravold, R. (2012). Decision-Making in Oil & Gas, the Good, Bad, and the Ugly. University of Stavanger-Norwegian Inst. of Technology, University of Texas at Austin: 1-41.

Chierici, G. (1990). Advanced Reservoir Management Aspects of Enhanced Oil Recovery. *1st Technical Symposium on Enhanced Oil Recovery* in Libya, NOC: 239-250.

Ellen Co; Graham D., Jason M. & Erling S. (2001). Making Decision in the Oil and Gas Industry. *Oilfield Review*, Winter Schlumberger: 2-9.

Frefer, A. (2014). Decision Making, Engineering Management and Economics, *A course given at the Engineering management department, Faculty of Engineering, University of Tripoli*, Libya.

Gerbacia, W. and Al-Shammari, H. (2001). Multi-Criteria Decision Making in Strategic Reservoir Planning Using the Analytic Hierarchy Process, New Orleans, Louisiana 30 September-3 October 2001. SPE **71413**.

Goren, Y. and Taylor, W. (1978). Decision Making In Deep Sea Development Projects. *Oceaneerng International*, SPE *8043*: 43-49.

Hokoma, R. & Aburas, H. (2018). Quality Enhancement for Improving the Processes of Making Decisions within Libyan Operating Oil and Gas companies. *Journal of Engineering Research*, University of Tripoli, Libya, **V. 25**: 1-8.

Hokoma, R. (2016). A Way Forward For Implementing Just-In-Time Techniques Within The Libyan Oil and Gas Industries. *Journal of Engineering Research*, University of Tripoli, Tripoli, Libya, **V. 21**: 1-14.

Learn About Quality, Project Planning Tools, ASQ website [Online), Available: *http://asq.org/learn-about-quality/project-planning-tools/overview/pdca-cycle.html.*

Prakash, D. (2012). Decision Making in Upstream Oil and Gas Industry- An Integrated Approach, India. SPE-**154999-MS**: 637-641.

Thakur, G. (1995). The Role of Technology and Decision Analysis in Reservoir Management, Chevron Petroleum Technology Company, Bahrain. SPE **29775**: 63-79.

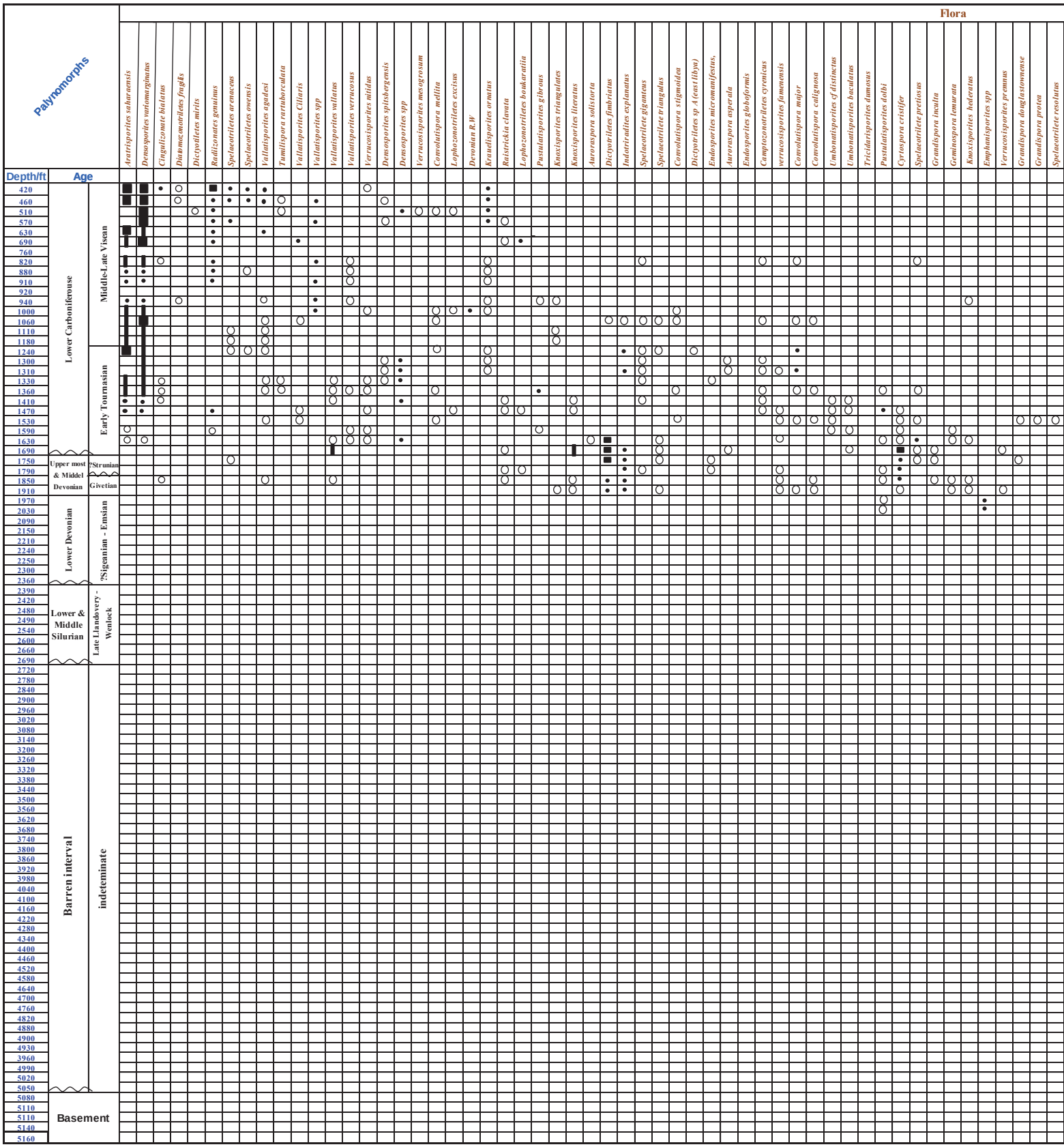
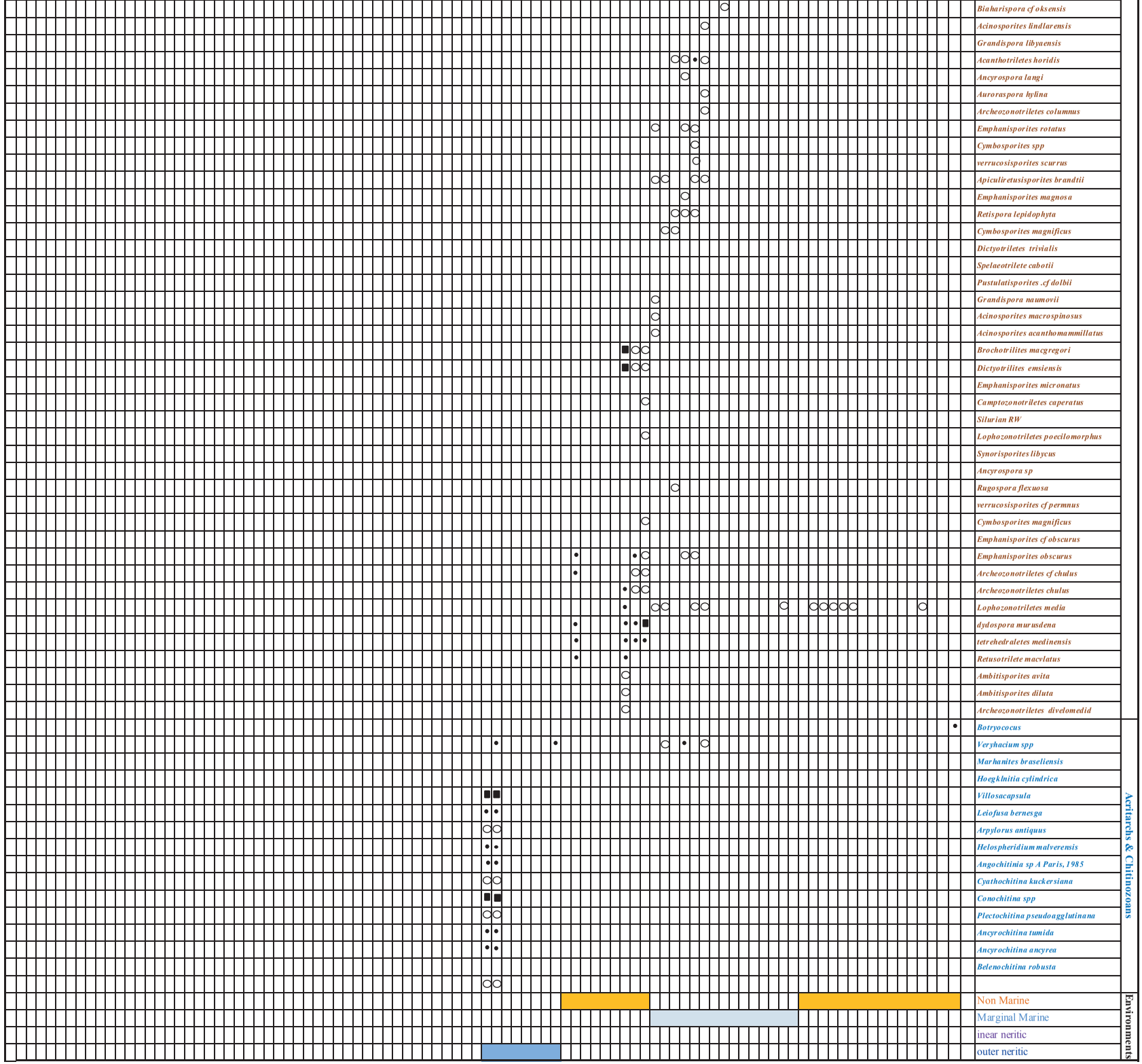


Fig. 2 Distribution of common and stratigraphically significant palynomorphs in the investigated intervals of well A1-177/01.


Biaharispora cf oksensis
Acinosporites lindlarensis
Grandispora libyaensis
Acanthotriletes horidis
Ancyrospora langi
Aurorospora hylina
Archeozonotriletes columnus
Emphanisporites rotatus
Cymbosporites spp
verrucosisporites scurrus
Apiculiretusisporites brandtii
Emphanisporites magnosa
Retispora lepidophyta
Cymbosporites magnificus
Dictyotriletes trivialis
Spelaeotrilete cabotii
Pustulatisporites .cf dolbii
Grandispora naumovii
Acinosporites macrospinosus
Acinosporites acanthomammillatus
Brochotrilites macgregori
Dictyotrilites emsiensis
Emphanisporites micronatus
Camptozonotriletes caperatus
Silurian RW
Lophozonotriletes poecilomorphus
Synorisporites libycus
Ancyrospora sp
Rugospora flexuosa
verrucosisporites cf permnus
Cymbosporites magnificus
Emphanisporites cf obscurus
Emphanisporites obscurus
Archeozonotriletes cf chulus
Archeozonotriletes chulus
Lophozonotriletes media
dydospora murusdena
tetrehedraletes medinensis
Retusotrilete macvlatus
Ambitisporites avita
Ambitisporites diluta
Archeozonotriletes divelomedid
Botryococus
Veryhacium spp
Marhanites braseliensis
Hoegklnitia cylindrica
Villosacapsula
Leiofusa bernesga
Arpylorus antiquus
Helospheridium malverensis
Angochitinia sp A Paris, 1985
Cyathochitina kuckersiana
Conochitina spp
Plectochitina pseudoagglutinana
Ancyrochitina tumida
Ancyrochitina ancyrea
Belenochitina robusta
Acritarchs & Chitinozoans
Non Marine
Marginal Marine
inear neritic
outer neritic
Environments